Perceptual Eigenmode Distortion Analysis for Motion Cueing Evaluation

in Fixed-Wing Aircraft Simulators

G.H.J. Tillema

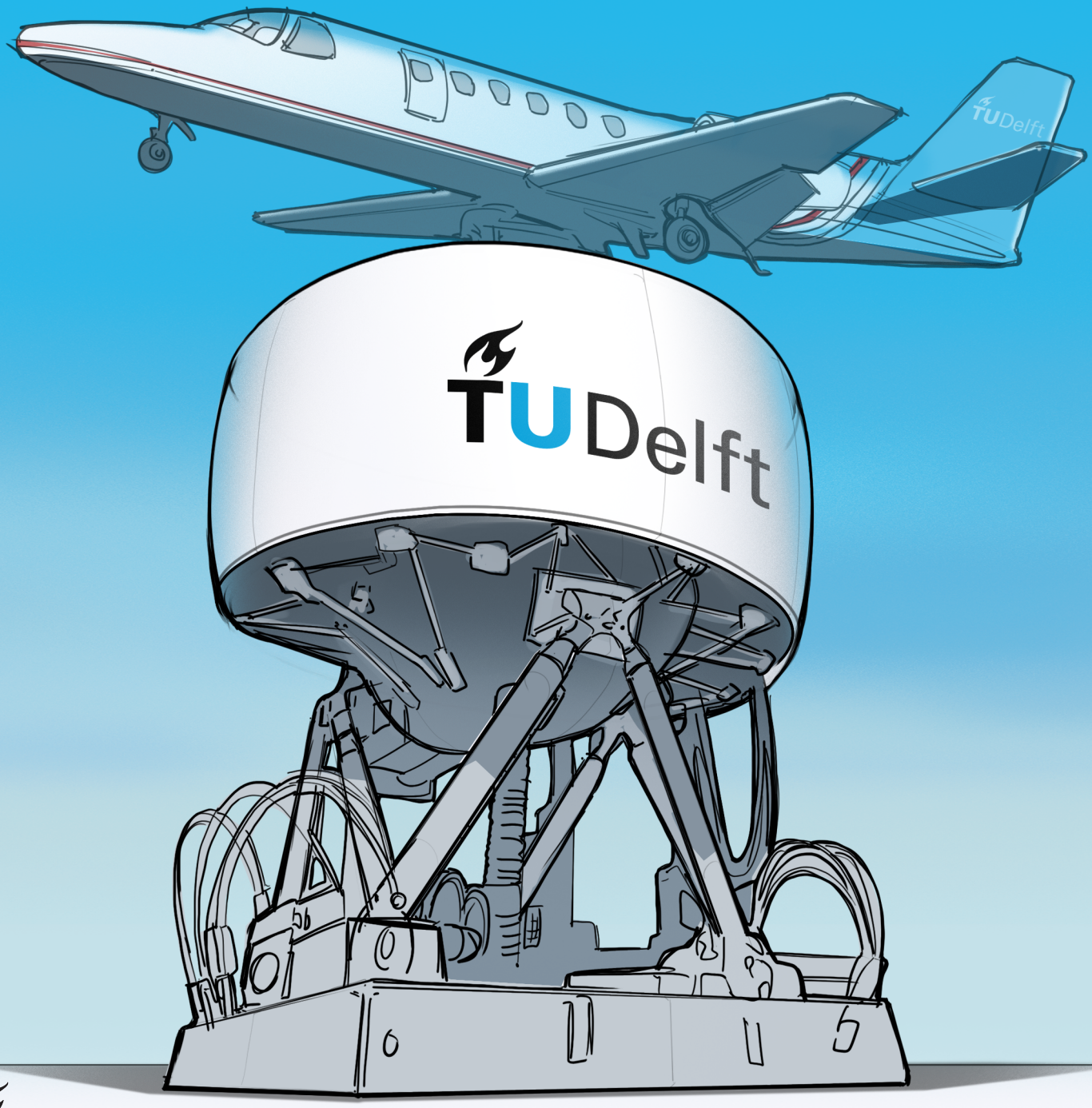

Delft University of Technology

TUDelft

This page is intentionally left blank.

Perceptual Eigenmode Distortion Analysis for Motion Cueing Evaluation

in Fixed-Wing Aircraft Simulators

by

G.H.J. Tillema

in partial fulfillment of the requirements for the degree of

Master of Science
in Aerospace Engineering

at the Delft University of Technology,
to be defended publicly on Monday April 6, 2020 at 02:00 PM.

Supervisor:	Ir. O. Stroosma	TU Delft
Thesis committee:	Prof. dr. ir. M. Mulder,	TU Delft
	Dr. ir. J.C.F. de Winter	TU Delft

This thesis is confidential and cannot be made public until December 31, 2020.

TU Delft

This page is intentionally left blank.

Preface

This thesis was written to acquire the MSc. Degree in Aerospace Engineering at the Delft University of Technology. The thesis was performed within the Control & Simulation section and was conducted from July 2019 until March 2020.

This thesis is written for aerospace student, engineers and researchers that have a sustained understanding of control theory principles and/or have an interest for getting a better insight of flight simulators.

The concepts and thoughts in this thesis are based on performed literature study, earlier research, meetings with engineers and (progress) meetings with the daily supervisor.

Acknowledgements
First, I want to express my deep gratitude to my daily supervisor Ir. O. Stroosma. His support, enthusiasm and suggestions were invaluable for the continuation of this thesis project. Furthermore, setting up and conducting the experiment would have become a mess without his support.

Second, I want to express a word of gratitude to Prof. dr. ir. M. Mulder, Dr. ir. M.M. van Paassen and Kim Johnson for reviewing my thesis.

Furthermore, a special thanks go out to the participants that participated in the experiment, spending all this time at the SIMONA and helped me with gathering data.

In addition, I would like to thank Erik ten Oever and Lars Dellemann for their time and interest in my work, the critical questions they asked and nice talks during lunch and coffee breaks. Making this thesis project more fun and less stressful.

Finally, I would like to thank my family and friends for their support during this graduation project, but also during my study. Their persistence and enthusiasm was boundless during this project.

G.H.J. Tillema
Delft, March 2020

This page is intentionally left blank.

Table of Contents

I

AIAA Paper

This page is intentionally left blank.

Perceptual Eigenmode Distortion Analysis for Motion Cueing Evaluation in Fixed-Wing Aircraft Simulators

G.H.J. Tillema*

The Perceptual Eigenmode Distortion (PEMD), an extension to the Eigenmode Distortion (EMD), is a method for objectively evaluating simulator motion fidelity, developed at TU Delft. EMD investigates motion cue distortions, imposed by the Motion Cueing Algorithm (MCA), in terms of eigenvectors, which represent the dynamic modes of a linear system. In this paper, EMD is extended by a human perception model, which was assumed to help in assessing the various motion cue contributions. Additionally, a new automatic MCA tuning approach is introduced. The method is applied to a combined linear model of the Cessna Citation 500 for asymmetrical flight and the Classical Washout Algorithm (CWA). The automatic tuning algorithm is used to create an MCA parameter set and is compared to the current state-of-the-art method for objective evaluations, the Objective Motion Cueing Test (OMCT). A pilot-in-the-loop experiment was performed, with six pilots in the SIMONA Research Simulator, to assess three CWA motion configurations, which were compared in a double-blind pairwise format. Throughout each run, the Dutch roll eigenmode was externally excited with a gust of semi-random amplitude and direction. Two hypotheses were tested using subjective preferences and through measuring the Dutch roll suppression performance. Preferences varied between pilots and within-pairs, and similar results for PEMD and OMCT were found. A significant improvement in performance was found, however, between a no-motion condition and the PEMD. Therefore, PEMD seems to have considerable potential.

Nomenclature

$\square$	=	Generic symbol placeholder
α	=	Angle-of-attack
δ_a	=	Aileron deflection
δ_r	=	Rudder deflection
$\lambda_\square$	=	Eigenvalue
$\omega_\square$	=	Break frequency of filter in CWA channel
ϕ, θ, ψ	=	Roll, pitch and yaw angle
$\zeta_\square$	=	Damping ratio of CWA channel
$\check{\square}$	=	Quantity in perception thresholds
$\dot{\square}$	=	Quantity derivative
$\square_0$	=	Quantity trim point
$\square^{EOM}$	=	Quantity augmented vehicle system
$\square^{MCA}$	=	Quantity in simulator
$A^\square$	=	System matrix
$\boldsymbol{a}_\square$	=	Actuator accelerations
$a_\square$	=	Acceleration in subscripted axis
$B^\square$	=	Input matrix
$B_\square$	=	Actuator buffer
$C^\square$	=	Output matrix
$C^\square$	=	Eigenmode cost function
$C_\square$	=	Force or moment coefficient
$D^\square$	=	Feedthrough matrix
$D^\square_\square$	=	Euclidean distance
f_y	=	Sway specific force
g	=	Gravitational acceleration
$I_\square$	=	Vehicle moments of inertia
$K_\square$	=	Gain of subscripted CWA channel
$L_\square, M_\square$	=	Non-dimensional moment derivatives
$\boldsymbol{l}_\square$	=	Actuator lengths
$l_\square$	=	Pilot station moment arms
$\boldsymbol{m}$	=	Representative manoeuvre
$\boldsymbol{p}$	=	MCA parameters
p, r	=	Roll and yaw rate
$\boldsymbol{u}^\square$	=	Input vector
u, v, w	=	Longitudinal, lateral and vertical velocity
$V_\square$	=	Matrix of right eigenvectors
$\boldsymbol{v}_\square$	=	Actuator velocities
$W^\square_\square$	=	Weight of eigenmode motion cue
x, y, z	=	Axes of reference frame
$\boldsymbol{x}^\square_\square$	=	Eigenvector
$\boldsymbol{x}^\square$	=	State vector
$Y_\square$	=	Non-dimensional lateral force derivative
$\boldsymbol{y}^\square$	=	Output vector
Z	=	Objective function
$\boldsymbol{z}$	=	Modal response

*MSc. student, Delft University of Technology, Faculty of Aerospace Engineering, Control & Simulation section, Kluyverweg 1, 2629HS Delft, The Netherlands, e-mail: g.h.j.tillema@student.tudelft.nl

I. Introduction

Full flight simulators are standalone devices to replicate all motions and forces as would be perceived by the pilot in an aircraft. Ideally, the perceived motions and forces in the flight simulator are identical to the real aircraft. However, where an aircraft has an (almost) infinite motion space, flight simulators have physical limitations.

The Motion Cueing Algorithm (MCA) has been developed to deal with these physical limits and is an algorithm between the flight model (i.e., Equations of Motion (EOM)) and a motion platform [1]. An MCA ensures that the simulated motion platform does not exceed its limits (e.g., actuator lengths).

The MCA was in the past only subjectively tuned by MCA-tuning experts, who tuned the variables of the algorithm until the pilot was satisfied. The resulting performance was generally expressed in terms of fidelity, whereby high-fidelity means a high match between simulator and aircraft. As this fidelity rating was subjective, resulting tuning variables were different per pilot, but also dependent on the task and workload of the pilot [2].

The undesirability of only subjective evaluations was already recognized in the 1970s and improved objective evaluations have been developed since, such as Sinacori [3], Schroeder [4] and Gouverneur [5].

These developments resulted in the current state-of-art method: the Objective Motion Cueing Test (OMCT) [6]. This method has improved the tuning process and gives an objective and detailed picture of the performance of the MCA and motion platform combined. This analysis is performed in the frequency domain and obtains the frequency response function, which provides magnitude- and phase distortions introduced by the MCA and motion platform.

Despite the power of OMCT, this method also has its shortcomings, such as its sine-wave input signals not representing realistic motion experienced during flight. Also vehicle dynamics are not evaluated in this test. Moreover, within OMCT, each signal is studied in isolation, while aircraft motions are linked through the vehicle dynamics.

To tackle these shortcomings, the Control & Simulation section at the Faculty of Aerospace Engineering in TU Delft has developed a novel objective evaluation method, the Eigenmode Distortion (EMD) [7]. The EMD method uses a different approach to evaluate objective fidelity. Rather than analyzing in the frequency domain, this method investigates distortions of motion cues imposed by the MCA in terms of eigenvectors, which represent the dynamic modes of a vehicle linear model. This was achieved by combining linearized vehicle dynamics and a linearized MCA, into a single combined linear time-invariant system. Initially, EMD was developed for and applied to rotorcraft simulators [8]. Recent work of Stoev et al. [9] has extended this to fixed-wing aircraft simulations applied to a linear model of the Cessna Citation 500 for symmetric flight in combination with the Classical Washout Algorithm (CWA) [1] as the MCA.

The purpose of this study is to improve the EMD method, by incorporating a human perception model, which is referred to as *Perceptual Eigenmode Distortion* (PEMD). With PEMD, contributions of individual motion cues can be better identified in an eigenmode. In this paper, EMD is applied to a lateral model of the Cessna Citation 500 for asymmetrical flight and the CWA is used as the MCA. Besides, a new automatic tuning approach is introduced and a pilot-in-the-loop experiment is conducted on the SIMONA Research Simulator (SRS) [10] at the Delft University of Technology, which evaluates the OMCT and PEMD with both subjective and objective metrics. The objective metric is designed as pilot opinions in Stoev's pilot-in-the-loop experiment were hampered by inconsistencies both between- and within subjects, which underlined the need for objective results.

This paper is structured as follows; the EMD and its implementation to the lateral model of the Cessna Citation 500 is elaborated in Section II. The EMD pilot perception model addition is elaborated in Section III, yielding PEMD. The PEMD analysis is used to derive a tuning algorithm in Section IV. The potential of PEMD is evaluated with an experiment discussed in Section V. The results of this experiment are elaborated in Section VI. Lastly, a discussion, recommendation and conclusion is given in Section VII, VIII and IX, respectively.

II. Eigenmode Distortion

A. Methodology

Despite the power of OMCT, which is at the time of writing the state-of-the-art method for evaluating objective motion cueing fidelity, the method has its shortcomings. OMCT captures the performance of the MCA and motion platform combined, however the simulated vehicle dynamics are not included. Furthermore, the simulated response to each signal is studied in isolation, while aircraft motions are linked through dynamics. It was shown that several intricate interactions between aircraft- and MCA dynamics could therefore not be captured [8].

The EMD method, developed by Miletović [7], is an objective evaluation method to address these shortcomings. EMD investigates the distortion of motion cues, imposed by the MCA, in terms of eigenmodes. Whereas eigenvalues provide information about the nature of an eigenmode, eigenvectors provide information on how different states interact in each eigenmode in terms of phase and magnitude. Moreover, these eigenvectors can be used to determine the MCA imposed motion cue distortions by taking the difference between the eigenvectors of the aircraft model and the MCA distorted equivalent.

To obtain these motion cue distortions, a combined linear model of the flight model (i.e., Equations of Motion (EOM)) and MCA is used. The linear model structure for the EOM in asymmetric flight is given in Equations 1 to 3. These EOM describe the dynamic behaviour of the aircraft and represent motion as experienced by the pilot in the aircraft.

$$\dot{\boldsymbol{x}}^{EOM} = A^{EOM}\,\boldsymbol{x}^{EOM} + B^{EOM}\,\boldsymbol{u}^{EOM} \tag{1}$$

$$\boldsymbol{x}^{EOM} = \begin{bmatrix} v & \phi & p & r \end{bmatrix}^T \tag{2}$$

$$\boldsymbol{u}^{EOM} = \begin{bmatrix} \delta_a & \delta_r \end{bmatrix}^T \tag{3}$$

Apart from the linear EOM, a linear model of the MCA is required. While the $\boldsymbol{x}^{EOM}$ state vector is known from flight dynamics, the formulation of $\boldsymbol{x}^{MCA}$ depends on the used MCA. Equation 4 formulates a generic linear MCA structure.

$$\dot{\boldsymbol{x}}^{MCA} = A^{MCA}\,\boldsymbol{x}^{MCA} + B^{MCA}\,\boldsymbol{u}^{MCA} \tag{4}$$

$$\boldsymbol{u}^{MCA} = \begin{bmatrix} f_{y_p}^{EOM} & p^{EOM} & r^{EOM} \end{bmatrix}^T \tag{5}$$

A system coupling, indicated by $\square^{COUP}$, is designed to combine the systems in the form of Equations 6 to 8.

$$\dot{\boldsymbol{x}}^{EMD} = A^{EMD}\,\boldsymbol{x}^{EMD} + B^{EMD}\,\boldsymbol{u}^{EMD} \rightarrow \begin{bmatrix} \dot{\boldsymbol{x}}^{EOM} \\ \dot{\boldsymbol{x}}^{MCA} \end{bmatrix} = \begin{bmatrix} A^{EOM} & 0 \\ A^{COUP} & A^{MCA} \end{bmatrix} \begin{bmatrix} \boldsymbol{x}^{EOM} \\ \boldsymbol{x}^{MCA} \end{bmatrix} + \begin{bmatrix} B^{EOM} \\ B^{COUP} \end{bmatrix} \boldsymbol{u}^{EOM} \tag{6}$$

$$\boldsymbol{y}^{EMD} = C^{EMD}\,\boldsymbol{x}^{EMD} + D^{EMD}\,\boldsymbol{u}^{EMD} \rightarrow \begin{bmatrix} \boldsymbol{y}^{EOM} \\ \boldsymbol{y}^{MCA} \end{bmatrix} = \begin{bmatrix} C^{EOM} & 0 \\ C^{COUP} & C^{MCA} \end{bmatrix} \begin{bmatrix} \boldsymbol{x}^{EOM} \\ \boldsymbol{x}^{MCA} \end{bmatrix} + \begin{bmatrix} D^{EOM} \\ D^{COUP} \end{bmatrix} \boldsymbol{u}^{EOM} \tag{7}$$

$$\boldsymbol{y}^{EMD} = \begin{bmatrix} f_{y_p}^{EOM} & p^{EOM} & r^{EOM} & f_{y_p}^{MCA} & p^{MCA} & r^{MCA} \end{bmatrix}^T \tag{8}$$

The output vector $\boldsymbol{y}^{EMD}$ contains the motion cues as experienced by the pilot in the aircraft and in the simulator, indicated by $\square^{EOM}$ and $\square^{MCA}$, respectively. It must be noted that the motion cues for any trajectory can be compared, but to reduce the dependence on specific trajectories only inherent eigenmodes are used.

This linear system is used for the EMD analysis. First, eigenvectors of the state matrix A^{EMD} are determined. To obtain eigenvectors expressed as pilot experienced quantities, the eigenvectors of the state matrix are multiplied with the output matrix C^{EMD}. With these eigenvectors, the imposed motion cue distortion can be determined by taking the difference between the eigenvector of the aircraft model and the coupled system, e.g., compare the individual (aircraft) components of the eigenvector with their distorted (simulator) equivalent.

B. Linearized Flight Model

In this paper, the EMD is applied to an asymmetrical flight condition. Equation 9 shows the dimensional asymmetric EOM, which can be derived from flight dynamics. After some rewriting, these equations can be expressed in state-space form presented in Equations 1 to 3.

$$\begin{aligned} W\cos\theta_0\phi + Y_v v + Y_{\dot{v}}\dot{v} + Y_p p + Y_r r + Y_{\delta_a}\delta_a + Y_{\delta_r}\delta_r &= m(\dot{v} + rV_0) \\ L_v v + L_p p + L_r r + L_{\delta_a}\delta_a + L_{\delta_r}\delta_r &= I_{xx}\dot{p} - I_{xz}\dot{r} \\ N_v v + N_{\dot{v}}\dot{v} + N_p p + N_r r + N_{\delta_a}\delta_a + N_{\delta_r}\delta_r &= I_{zz}\dot{r} - I_{xz}\dot{p} \\ \dot{\psi} &= \tfrac{r}{cos\theta_0} \\ \dot{\phi} &= p + r\tan\theta_0 \end{aligned} \tag{9}$$

Equation 9 is derived in the stability reference frame and assumes a steady, straight and symmetric flight condition with a flat non-rotating Earth. The CWA requires rotational rates and specific forces as input, which must therefore be the output of the EOM state-space system. The roll- and yaw rate are available as states, but an expression for sway specific force needs to be formulated.

Specific force is defined as the non-gravitational force per unit mass [1], which implies that the gravitational component needs to be removed from the lateral acceleration.

$$\begin{aligned} f^b_{y_{cg}} &= a^b_{y_{cg}} - g\cos\theta\sin\phi \\ &= \dot{v} + ru - pw - g\cos\theta\sin\phi \end{aligned} \tag{10}$$

The sway specific force, shown in Equation 10, is defined in the body reference frame, as required for the CWA. As the EOM in Equation 9 are defined in the stability reference frame, a transformation from stability to body frame is required. It must be mentioned that this transformation is not required if the EOM are defined in body frame or the MCA uses the stability frame as a reference.

The next step is to express the sway specific force at the pilot station. This transformation becomes increasingly important for larger aircraft. For example, for a larger aircraft, the distance between the centre of gravity and the pilot station is larger. This increased distance acts as a moment arm, giving additional experienced specific forces due to rotational rates and accelerations. For light aircraft, the pilot is sitting close to the centre of gravity, which implies that this transformation is not very important. However, for the Cessna Citation 500 (the aircraft used in this paper) this distance is not negligible. The transformation from centre of gravity to pilot station is given by Equation 11. For the Cessna Citation 500, the moment arms are $l_x = 3.2$ $[m]$ and $l_z = 1.0$ $[m]$, for horizontal and vertical distance, respectively [11].

$$f_{y_p} = f^b_{y_{cg}} + \dot{p}l_z + \dot{r}l_x \tag{11}$$

To construct the state-space output- and feedthrough matrices, C^{EOM} and D^{EOM}, respectively, linearization is required. Equation 12 shows the result of this linearization. Here, subscript 0 denotes the trim point.

$$f_{y_p} = \dot{v} - g\phi - u_0\alpha_0 p + u_0 r + l_z\dot{p} + l_x\dot{r} \tag{12}$$

As a linear expression for sway specific force is derived, the $\boldsymbol{y}^{EOM}$ can be constructed. Roll- and yaw rates are directly available as states in the state-space, and the sway specific force can be constructed as a combination of states and inputs. This concludes the derivation of the state-space output- and feedthrough matrices, where $\boldsymbol{y}^{EOM}$ is the resulting output vector, shown in Equations 7 and 8.

C. Linearized MCA

The MCA yields positions and orientations to control the motion platform. To find the motion cue distortions caused by the MCA, the inputs and outputs need to be related to each other. Specific forces and rotational rates, defined in body reference frame, are inputs to the Classical Washout Algorithm (CWA), which is the MCA used in this study. The outputs are modified to output specific forces and rotational rates instead of positions and orientations, Figure 1 depicts this modification for the lateral CWA.

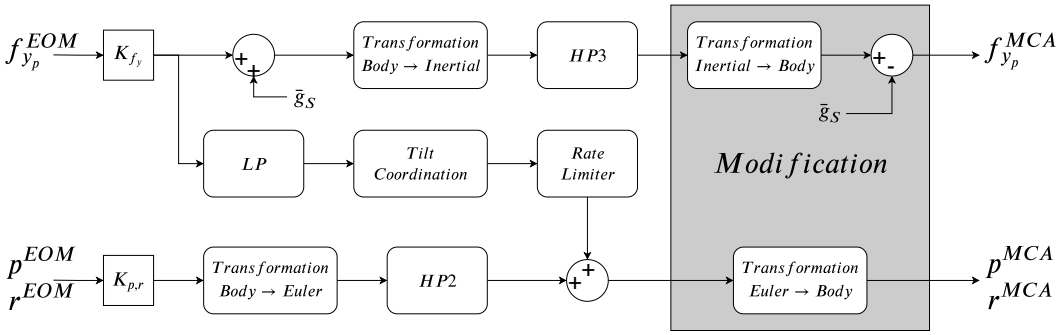

Fig. 1 The Classical Washout Algorithm Adapted for Lateral Motions [1]

The CWA is the MCA used in this paper and is constructed for lateral motions, so longitudinal channels are removed. As of nonlinearities, this CWA is linearized for the EMD analysis. Besides, a small angle approximation is used for the transformations, and the rate limiter in the tilt-coordination channel is removed. After linearization, this gives the state-space system- and input matrices, A^{MCA} and B^{MCA}, respectively.

The state-space output matrix (C^{MCA}) and feedthrough matrix (D^{MCA}) are formulated to output sway specific force, roll- and yaw rate. The resulting output vector is $\boldsymbol{y}^{MCA}$, shown in Equations 7 and 8.

D. System Coupling

To make EMD analysis possible, linear models of the EOM and MCA are combined into a single state-space system. This is possible as the outputs of the EOM are inputs to the MCA (Figure 2). So-called coupling matrices are defined to express the MCA inputs as EOM states and inputs. For this, B^{MCA} is reformulated as A^{COUP} and B^{COUP}, and D^{MCA} is reformulated as C^{COUP} and D^{COUP}. Finally, this gives a state-space system as in Equations 6 to 8.

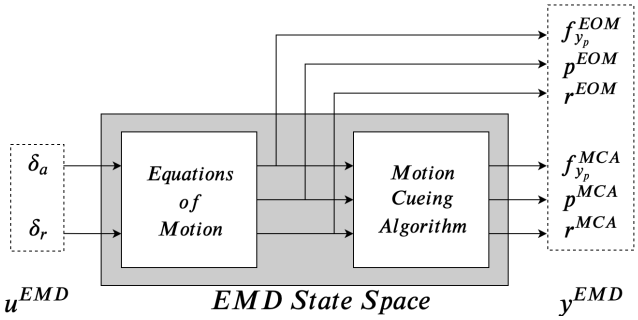

Fig. 2 EMD System Coupling

E. Eigenvector Distortion Analysis

When analyzing aircraft eigenmodes, eigenvalues are usually used, which provide information about the nature (i.e., periodic or aperiodic), timing and decay of a mode. For example, the Dutch roll has two complex poles, meaning that it is a periodic mode, whereas the spiral mode has one real pole close to the imaginary axis, meaning that it is an aperiodic mode of slow nature.

$$A^{EMD}\,\boldsymbol{x}_i^{EMD} = \lambda_i^{EMD}\,\boldsymbol{x}_i^{EMD} \tag{13}$$

$$V_{\boldsymbol{x}} = \begin{bmatrix} \boldsymbol{x}_1^{EMD} & \cdots & \boldsymbol{x}_n^{EMD} \end{bmatrix} \tag{14}$$

Additionally, eigenmodes can be analyzed using eigenvectors, which provide information on how the components of $\boldsymbol{x}^{EMD}$ interact in each eigenmode. Equation 13 presents the formulation for determining the i^{th} eigenvector and its

associated eigenvalue for an individual mode. Eigenvectors of different modes can be combined in a matrix, $V_{\boldsymbol{x}}$, see Equation 14. These eigenvectors can be used to determine motion cue distortions. First, eigenvectors of the A^{EMD} matrix are determined, which are expressed in $\boldsymbol{x}^{EMD}$ states. To obtain the motion cue distortions, these eigenvectors are multiplied with the output matrix, C^{EMD}, Equation 15.

$$V_{\boldsymbol{y}} = C^{EMD} V_{\boldsymbol{x}} \tag{15}$$

The resulting eigenvectors, expressed in aircraft and simulator cues, are shown in Figure 3 for the lateral model of the Cessna Citation 500 in cruise configuration, Table 3, and representative MCA settings. In Figure 3, the solid lines represent the motion cues as experienced by the pilot in the actual aircraft. Furthermore, the dashed lines represent the motion cues as experienced in the flight simulator. The magnitude- and phase distortions between the solid- and dashed lines are caused by the MCA and form the basis of the EMD method.

It must be stated that a comparison in magnitudes between specific forces and rotational rates has to take into account their different units. For example, the magnitude of the sway specific force components is larger than that of the roll rate. However, it would be wrong to conclude that the sway specific force is thus a more dominant motion cue in this mode. This is also the motivation for the EMD method extension described in Section III.

The magnitude distortion is defined as the ratio between the magnitudes of $\square^{EOM}$ and $\square^{MCA}$ components. Additionally, phase distortion is defined as the angle between these components. If a complex eigenvector that corresponds to the positive conjugate eigenvalue is visualized, counter-clockwise and clockwise phase distortion indicates phase lead and lag between the two components with respect to the actual aircraft, respectively.

Figure 3a depicts eigenvectors corresponding to the Dutch roll. The following observations can be made; sway specific force, $f_{y_p}^{MCA}$, has a magnitude distortion of $|f_y| = \frac{|f_{y_p}^{MCA}|}{|f_{y_p}^{EOM}|} = 0.64$ and a phase distortion of $\angle f_y = 16.3°$ lead (counter-clockwise) for this tuning. Furthermore, the roll rate, p^{MCA}, has a magnitude distortion of $|p| = 0.62$ and phase distortion of $\angle p = 18.1°$ lead. Finally, the yaw rate, r^{MCA}, has a magnitude distortion of $|r| = 0.69$ and phase distortion of $\angle r = 24.5°$ lead. These observations are supported by analyzing the time-domain response. Figure 4 illustrates the time-traces to a zero-input response, in which $2Re(v_i)$ is the initial condition. In here, v_i is the eigenmode-associated eigenvector, i.e., the Dutch roll eigenvector is used to excite the Dutch roll eigenmode.

These distortions can be compared to the distortions found by OMCT at the frequency of the Dutch roll eigenmode. The natural frequency of the Dutch roll is 3.2738 rad/s. The nearest OMCT test frequency is 3.9810 rad/s and gives as distortions; for sway specific force (test 8) $|f_y| = 0.75$ and $\angle f_y = 29.7°$ lead, for roll rate (test 3) $|p| = 0.68$ and $\angle p = 19.9°$ lead and for raw rate (test 5) $|r| = 0.68$ and $\angle r = 19.9°$ lead. Especially the coupled sway and roll channels show relatively large differences between EMD and OMCT results, underlining the value of using eigenmodes instead of isolated sinusoids.

Magnitude distortions for the other eigenmodes, using EMD, are shown in Table 1. As the aperiodic roll and spiral mode are both aperiodic modes, only a magnitude distortion and possibly a sign change can be obtained. Interesting to observe is the large magnitude distortion of the roll- and yaw rate for the spiral mode. The time-domain representation of the spiral mode (Figure 6) depicts these motion cues as essentially zero. Which is explained by the eigenvalue being close to the imaginary axis, e.g., $\lambda_{sm} = -0.0018$, and the high-pass rotation channels that strongly attenuate these cues.

Aircraft motions can be described in the time domain by a continuously varying combination of eigenmodes. The influence of a particular mode at a particular time can be expressed by the system's modal response. The modal coordinate transformation, which can be computed as $\boldsymbol{z}(t) = V_{\boldsymbol{x}}^{-1} \boldsymbol{x}^{EMD}(t)$, yields complex variables representing the system's modal response in the time domain. The Mode Participation Factor (MPF) is the absolute value of this complex variable $\boldsymbol{z}$ and reveals how each mode participates at each time point in a particular manoeuvre [12] and also depends on pilot inputs, e.g. if the pilot is exciting a particular mode, then the MPF yield a larger participation of that particular mode. Moreover, MPFs have been used to identify dominant modes in a particular manoeuvre or tasks [7].

MPFs are useful to identify important modes, e.g., identify which modes are excited in a particular manoeuvre. In the experiment performed by Stoev et al. [9], the short period eigenmode was excited by the pilot as illustrated by the dominant MPF. The short period is a desired mode necessary for performing manoeuvres, such as pitch captures, and is easily excited. On the other hand, the Dutch roll is an unpleasant mode and usually damped with a yaw damper. Therefore, this study differs in its use of the MPF from the earlier study performed by Stoev et al. [9].

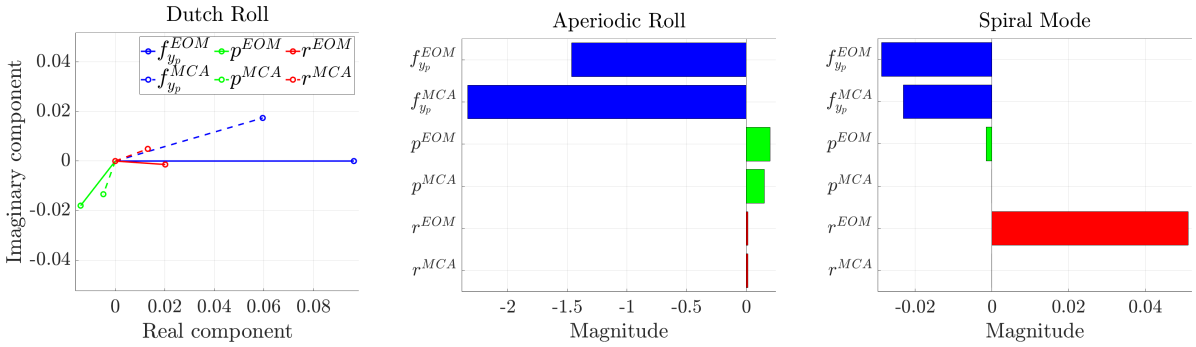

(a) Dutch Roll ($\lambda_{dr} = -0.2778 \pm 3.2616i$)

(b) Aperiodic Roll ($\lambda_{ar} = -4.0740$)

(c) Spiral Mode ($\lambda_{sm} = -0.0018$)

Fig. 3 Example of Eigenvector Distortion Plots

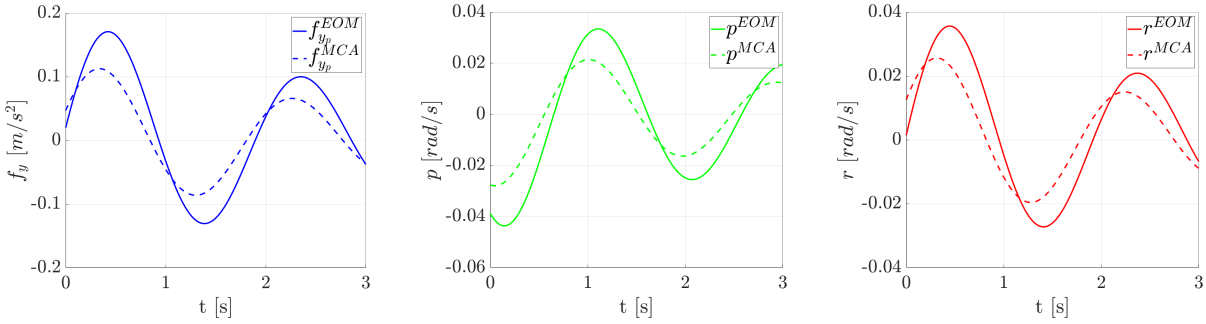

Fig. 4 Time Histories of Dutch Roll Eigenmode Excitation

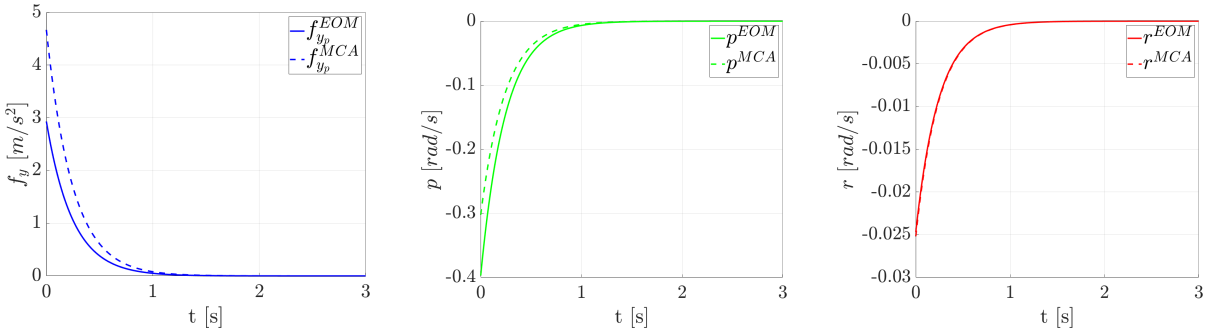

Fig. 5 Time Histories of Aperiodic Roll Eigenmode Excitation

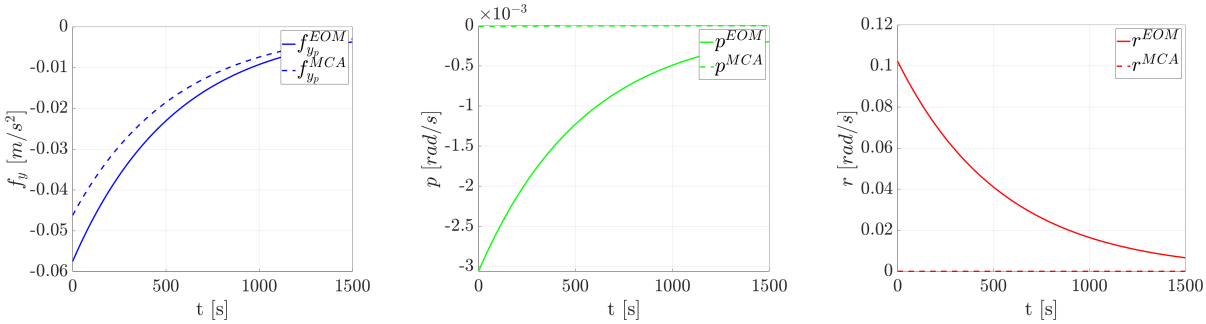

Fig. 6 Time Histories of Aperiodic Spiral Mode Excitation

Table 1 Example Magnitude- and Phase Distortions

Dutch Roll		Aperiodic Roll	Spiral Mode
$\lvert f_y \rvert = 0.64$	$\angle f_y = 16.3°$ lead	$\lvert f_y \rvert = 1.59$	$\lvert f_y \rvert = 0.80$
$\lvert p \rvert = 0.62$	$\angle p = 18.1°$ lead	$\lvert p \rvert = 0.76$	$\lvert p \rvert = 0.003$
$\lvert r \rvert = 0.69$	$\angle r = 24.5°$ lead	$\lvert r \rvert = 1.02$	$\lvert r \rvert = 0.00$

III. Perceptual Eigenmode Distortion

A. Methodology

The EMD method was introduced to overcome the shortcomings of the OMCT method. For this, a different method is used to perform the distortion analysis, in which motion cue distortions are investigated using eigenvectors. Yet this method has its limitations, the resulting components of the eigenvectors for specific forces and rotational rates cannot easily be compared to one-another because of their different units. Which implies that a dominant motion cue is not apparent by analyzing and comparing the component magnitudes.

The Perceptual Eigenmode Distortion (PEMD) introduced in this paper is an extension to the EMD analysis, in which the EMD is extended with a perception model. Initially, the PEMD had two additions. The derived eigenvectors assume a vestibular system that perceives motion cues one-to-one, whereas an actual vestibular system introduces an additional magnitude- and phase distortion. The first addition was to include a linear model of the vestibular system. However, as the EOM outputs, $\boldsymbol{y}^{EOM}$, and MCA outputs, $\boldsymbol{y}^{MCA}$, pass through the same vestibular system, their relative magnitude- and phase distortions remain the same.

In the derivation, this addition increased the complexity as the number of states almost doubled. A critical point is that the vestibular system model is an idealization and simplification of an actual vestibular system. As the limitation of the EMD can also be solved without this addition, the linear vestibular system addition is left out.

The second addition is to re-express the output vector in terms of motion perception thresholds instead of engineering units. The threshold for motion perception is the value that motion is not perceived by humans anymore [13]. After re-expressing the output vector, all motion cues have the same unit, which is called the *threshold unit* and is dimensionless. When motion cues in an eigenmode have the same magnitude, these cues have the same chance of exceeding its threshold when exciting that mode with a certain magnitude. As the output vector is re-expressed, the output matrix is also changed ($C^{EMD} \rightarrow C^{PEMD}$). The same eigenvector analysis is performed, using the new output matrix, which results in eigenvectors all expressed in threshold units. As the eigenvectors now have the same units the components of the eigenvectors can be compared to one-another and a dominant motion cue can be identified.

B. Perception Model Extension

The problem with using perception thresholds is that these vary per person and depend on factors such as workload and task [2]. Furthermore, these thresholds tend to vary per frequency [14] and are affected by motion in different directions. This paper attempts to incorporate perception thresholds in the eigenvector analysis. Developing a complete threshold model would be too ambitious as this stage. Therefore, the perception thresholds used are chosen as constants.

The threshold values used are obtained from a recent simulator study [13]. These values are, however, not constant with frequency and therefore, average values are used [14]. The used threshold values for sway specific force, roll- and yaw rate are, $\check{f}_y = 0.0743\ [m/s^2]$, $\check{p} = 0.00521\ [rad/s]$ and $\check{r} = 0.0166\ [rad/s]$, respectively.

The reformulated output vector, Equation 17, is obtained by dividing the elements of the C^{EMD} matrix by its associated threshold value, which is illustrated in Equation 16. In here, the symbol $\vee$ indicates that threshold units are used. As the outputs are scaled to the same unit, the different output states can be compared in magnitude.

$$C^{PEMD} = \begin{bmatrix} C^{EMD}(1)/\check{f}_y \\ C^{EMD}(2)/\check{p} \\ C^{EMD}(3)/\check{r} \\ C^{EMD}(4)/\check{f}_y \\ C^{EMD}(5)/\check{p} \\ C^{EMD}(6)/\check{r} \end{bmatrix} \tag{16}$$

$$\check{\boldsymbol{y}}^{PEMD} = \begin{bmatrix} \check{f}_{y_p}^{EOM} & \check{p}^{EOM} & \check{r}^{EOM} & \check{f}_{y_p}^{MCA} & \check{p}^{MCA} & \check{r}^{MCA} \end{bmatrix}^T \tag{17}$$

C. Eigenvector Distortion Analysis

Now, the eigenvector analysis is performed for PEMD in the same way as for EMD. First, the eigenvectors of the A^{EMD} matrix are determined, which are expressed in $\boldsymbol{x}^{EMD}$ states. To obtain the motion cue distortions expressed in threshold units, the eigenvectors are multiplied with the new output matrix, C^{PEMD}:

$$V_{\check{\boldsymbol{y}}} = C^{PEMD} V_{\boldsymbol{x}} \tag{18}$$

These new eigenvectors are used to determine the motion cue distortions. The individual magnitude- and phase distortions are identical to the EMD's, as each relative distortion remains unchanged. Figure 7 shows the new eigenvectors.

As all components of the eigenvectors are now expressed in the same unit, the magnitudes can be compared to one-another. Therefore the following observations can be made; for the Dutch roll, Figure 7a, roll rate is the dominant motion cue. Also, sway specific force and yaw rate are about equal. For the aperiodic roll, Figure 7b, roll rate is the dominant motion cue and yaw rate is least dominant. For the spiral mode, Figure 7c, yaw rate is the most dominant motion cue. Yet, this motion cue is not simulated as depicted by the zero magnitude of $\check{r}^{MCA}$. Furthermore, the simulated roll rate is negligible.

It must be noted that magnitudes of the eigenvectors in Figure 7 vary in time, e.g., the magnitudes gets smaller as the mode decays. Therefore, the axes contain no numbers. However, the relative magnitudes and phase remain always the same over time for a given mode and flight condition.

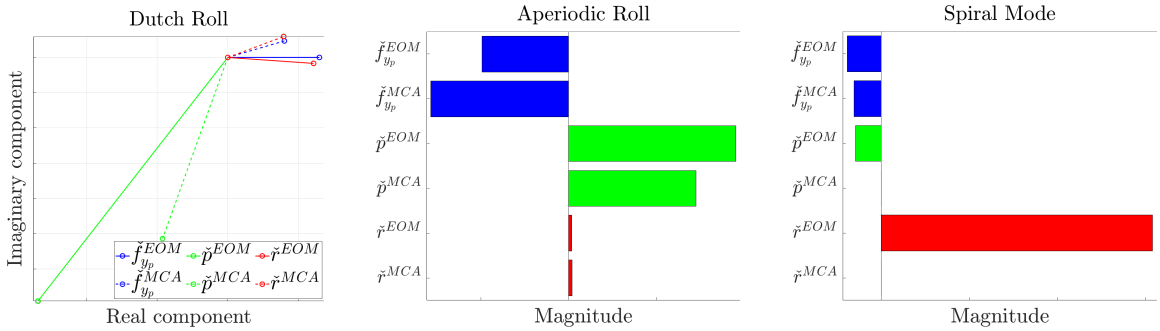

(a) Dutch Roll **(b) Aperiodic Roll** **(c) Spiral Mode**

Fig. 7 Example of Eigenvector Distortion Plots

It is hypothesized that a larger eigenvector component magnitude implies a larger contribution of a motion cue in an eigenmode. It must be stated that this contribution depends on the flight condition. In this paper, the Cessna Citation 500 in cruise condition is used, as defined in Table 3. The contribution of each motion cue per eigenmode for a given flight condition, which is defined as e.g., $W_{\square} = |\check{\square}^{EOM}| / \left(|\check{f}_{y_p}^{EOM}| + |\check{p}^{EOM}| + |\check{r}^{EOM}| \right)$ for a given eigenmode, is given in Table 2. This contribution can be used as a weighting factor for tuning, as described in next section.

Table 2 Eigenmode Motion Cue Contribution for Flight Condition Table 3

	f_y	p	r
Dutch Roll	$W_{f_y}^{DR} = 0.188$	$W_p^{DR} = 0.635$	$W_r^{DR} = 0.177$
Aperiodic Roll	$W_{f_y}^{AR} = 0.337$	$W_p^{AR} = 0.651$	$W_r^{AR} = 0.013$
Spiral Mode	$W_{f_y}^{SM} = 0.103$	$W_p^{SM} = 0.078$	$W_r^{SM} = 0.819$

IV. Tuning Algorithm

In the latest OMCT evaluation method, magnitude- and phase distortions are evaluated separately. The study done by De Ridder and Roza [15] uses OMCT for automatically tuning the MCA parameters. The work of Fu [16] gave another perspective on formulating this objective function.

In the study done by Fu [16] it was found that a change of dynamics in control loading is not perceived by humans when the change in eigenvalue that occurs fall within a threshold region in the complex plane. For control loading, this threshold region is a square. As a result, it does not matter whether it is a magnitude distortion and/or phase distortion As long as the distortion is within this threshold region, it is not perceived by the human operator. Only a change outside this region is detected by the human operator. Although Fu [16] considered the system's eigenvalue and PEMD is focused on the system's eigenvector, the similarity inspired a new way of defining an objective function for tuning.

For PEMD, rather than optimizing only the magnitude distortion or phase distortion, an objective function is formulated in which the Euclidean distance between the $\square^{EOM}$ and $\square^{MCA}$ components is minimized. Figure 8 illustrates this Euclidean distance, $D^{\square}_{\square}$ with the top index denoting the mode and the bottom index the cue. Equation 19 shows the Euclidean distance for sway specific force of the Dutch roll. The $\boldsymbol{p}$ indicates the MCA parameters that can be varied to change this distance. The other distances are formulated similarly.

$$D^{DR}_{f_y}(\boldsymbol{p}) = ||\check{f}^{EOM}_{y_p} - \check{f}^{MCA}_{y_p}(\boldsymbol{p})||_{DR} \tag{19}$$

Next, the contributions of each motion cue per eigenmode, from Table 2, is added. For example, in Figure 8a the magnitude of roll rate, $\check{p}^{EOM}$, is larger than that of the sway specific force, $\check{f}^{EOM}_{y_p}$, and yaw rate, $\check{r}^{EOM}$. Consequently, it is more important to minimize the Euclidean distance for roll rate than for sway specific force and yaw rate. By multiplying the individual contributions (weights), $W^{\square}_{\square}$, with its associated Euclidean distance, this effect is achieved. Equations 20 to 22 show the cost functions, $C^{\square}$, for Dutch roll, aperiodic roll and spiral mode, respectively.

$$C^{DR}(\boldsymbol{p}) = W^{DR}_{f_y} \cdot D^{DR}_{f_y}(\boldsymbol{p}) + W^{DR}_{p} \cdot D^{DR}_{p}(\boldsymbol{p}) + W^{DR}_{r} \cdot D^{DR}_{r}(\boldsymbol{p}) \tag{20}$$

$$C^{AR}(\boldsymbol{p}) = W^{AR}_{f_y} \cdot D^{AR}_{f_y}(\boldsymbol{p}) + W^{AR}_{p} \cdot D^{AR}_{p}(\boldsymbol{p}) + W^{AR}_{r} \cdot D^{AR}_{r}(\boldsymbol{p}) \tag{21}$$

$$C^{SM}(\boldsymbol{p}) = W^{SM}_{f_y} \cdot D^{SM}_{f_y}(\boldsymbol{p}) + W^{SM}_{p} \cdot D^{SM}_{p}(\boldsymbol{p}) + W^{SM}_{r} \cdot D^{SM}_{r}(\boldsymbol{p}) \tag{22}$$

Finally, an objective function can be formulated. The objective function, as in Equation 23, minimizes the Euclidean distance for the eigenvectors in the selected eigenmodes. Eigenmodes can be prioritized by changing the values of α, β and γ, where $\alpha + \beta + \gamma = 1$ and $0 \leq \alpha, \beta, \gamma \leq 1$.

$$min: \quad Z(\boldsymbol{p}) = \alpha \cdot C^{DR}(\boldsymbol{p}) + \beta \cdot C^{AR}(\boldsymbol{p}) + \gamma \cdot C^{SM}(\boldsymbol{p}) \tag{23}$$

Ideally, all Euclidean distances would be zero. However, most full flight simulators have motion limitations. The motion is limited by the actuators driving the motion platform. Apart from the actuator lengths, the maximum velocity and acceleration it can achieve is limited. Therefore, actuator constraints are added. Equations 24 to 26 show the actuator constraints in length, velocity and acceleration, respectively.

$$\boldsymbol{l}_{min} + B_l \leq \boldsymbol{l}_{response}(\boldsymbol{p}, \boldsymbol{m}) \leq \boldsymbol{l}_{max} - B_u \tag{24}$$

$$|\boldsymbol{v}_{response}(\boldsymbol{p}, \boldsymbol{m})|_{max} \leq \boldsymbol{v}_{max} \tag{25}$$

$$|\boldsymbol{a}_{response}(\boldsymbol{p}, \boldsymbol{m})|_{max} \leq \boldsymbol{a}_{max} \tag{26}$$

In here, $\boldsymbol{m}$ represents a representative manoeuvre, which can be used to ensure that the available motion space is not exceeded. Buffers can be introduced to further restrict the available motion space, i.e., the lower- and upper buffer distances (B_l and B_u, respectively) can be increased.

The formulation of the tuning algorithm allows for great flexibility. The user can specify which eigenmode is tuned. Furthermore, different representative manoeuvres can be used to optimize for different training tasks. Also, the actuator buffer distance in Equation 24 can be used to limit the motion space. A similar tuning algorithm can also be derived for a linear vehicle model in symmetric flight.

One approach is to use *genetic algorithms* to implement this automatic tuning algorithm. Genetic algorithms are stochastic global search and optimization methods which apply the principle of natural biological evolution through survival of the fittest [17]. In this study, the automatic tuning algorithm was implemented in Matlab/Simulink using the built-in genetic algorithm, i.e., the **ga** function.

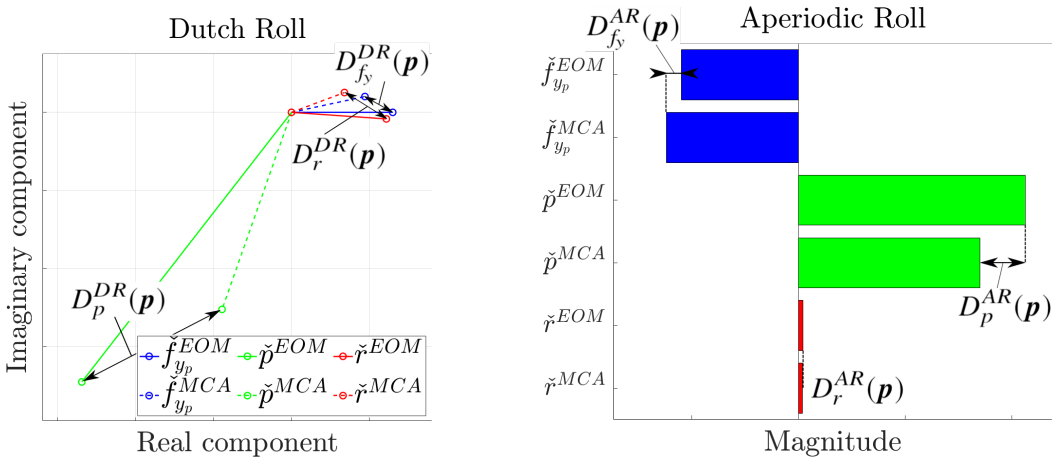

Fig. 8 Euclidean Distance

V. Pilot-in-the-Loop Experiment

To investigate the potential of the PEMD, the automatic tuning algorithm and validate the resulting motion cueing solution, a pilot-in-the-loop experiment was performed with the TU Delft's SIMONA Research Simulator [10]. The simulated aircraft was a nonlinear model of the Cessna Citation 500 business jet. Three different MCA configurations were used in the experiment, which were compared in a double-blind pairwise pattern and with an objective performance metric. In total seven pilots participated in the experiment. After a discussion of the three MCA configurations, some general information of the participants is given, which is followed by a review of the apparatus and experiment task. Finally, hypotheses and corresponding dependent measures are given.

A. Independent Variables: MCA Configurations

This study applied the tuning algorithm to a lateral model of the Cessna Citation 500 in cruise configuration, Table 3. The lateral model has three eigenmodes, namely: Dutch roll, aperiodic roll and spiral mode. Ideally, the MCA parameters are optimized for all eigenmodes concurrently. Yet, only the Dutch roll and aperiodic roll were selected for tuning the configurations. The spiral mode was left out as motion simulators have a limited motion space and are thus better in simulating high-frequency motions than low-frequency [1]. Furthermore, the Dutch roll and aperiodic roll can be excited with a small deviation from the trim conditions, whereas large deviations are required for the spiral mode.

This paper analyzed a total of three CWA configurations. The first configuration is the baseline configuration, B, which was separately tuned by an MCA tuning expert and was based on experience and rules of thumb. Additionally, this configuration satisfied the latest OMCT criteria, specified in *ICAO - Manual of Criteria for the Qualification of Flight Simulation Training Devices* [6]. The second configuration, O, was tuned to only satisfy the OMCT tests. The last configuration, P, was tuned according to the tuning algorithm of Section IV. For this, the spiral mode was excluded. Pilot feedback from previous experiments indicated that simultaneous tuning could improve the realism of motion cues [9], and therefore $\alpha = \beta = 0.5$ was chosen. For all configurations, a representative Dutch roll manoeuvre, in which the Dutch roll was excited by the pilot with a repeated rudder input, was simulated to ensure that the found MCA settings did not exceed the available motion space. It is important to note that $\boldsymbol{m}$, in Equations 24 to 26, represent the time history of this representative manoeuvre. Tables 4 and 5 present the resulting CWA parameter settings and distortions, respectively. As the yaw cue was the least dominant motion cue for both the Dutch roll and aperiodic roll, all configurations have identical MCA parameters for yaw. These yaw parameters were tuned to satisfy the OMCT *yaw due to yaw* test, i.e., test 5.

Table 3 Asymmetric Stability and Control Derivatives for Cessna Citation 500, condition: Cruise

C_{Y_β}	=	−0.0750	C_{l_β}	=	−0.1061	C_{n_β}	=	0.1305	V	=	160.3 $[m/s]$	C_L = 0.2239 $[-]$
C_{Y_p}	=	−0.0109	C_{l_p}	=	−0.5209	C_{n_p}	=	−0.0672	h	=	5000 $[m]$	ρ = 0.7361 $[kg/m^3]$
C_{Y_r}	=	0.8499	C_{l_r}	=	−0.1522	C_{n_r}	=	−0.2089	S	=	24.2 $[m^2]$	K^2_{XX} = 0.019 $[-]$
$C_{Y_{\delta_a}}$	=	−0.0400	$C_{l_{\delta_a}}$	=	−0.1848	$C_{n_{\delta_a}}$	=	−0.0140	m	=	5207 $[kg]$	K^2_{ZZ} = 0.042 $[-]$
$C_{Y_{\delta_r}}$	=	0.2300	$C_{l_{\delta_r}}$	=	0.0358	$C_{n_{\delta_r}}$	=	−0.0947	b	=	13.36 $[m]$	K_{XZ} = 0.002 $[-]$

For all configurations, the eigenvector distortions are depicted in Figures 9 to 11 and quantified in Table 5. From inspection, it can be observed that configurations B and O have rather similar distortions. For the Dutch roll, both configurations preserve a rather low phase distortion for f_y and p, e.g., a maximum of 14.8° for f_y. For aperiodic roll, both configurations exhibit reasonable magnitude distortions of no more than 17%. However, both contain a sign change for the roll cue, i.e., the roll cue is simulated in the opposite direction in this mode. Configuration P has the lowest phase distortion in f_y for the Dutch roll. The p has a larger phase distortion but almost no magnitude distortion, making the Euclidean distance smaller than for the B- and O configuration. From Figure 11b it can be observed that the f_y and p motion cues for the aperiodic roll exactly match the aircraft dynamics.

The eigenvalues for Dutch roll, aperiodic roll and spiral mode, shown in Equation 27, aid in the understanding of how the tuning algorithm behaves. These eigenvalues provide information about the nature, timing and decay of an eigenmode. As the Dutch roll eigenvalue is closer to the imaginary axis than the eigenvalue of the aperiodic roll, the decay is slower. To cue the Dutch roll more realistically, the motion platform would require more motion space. It must be stated that the motion space, in Equations 24 to 26 are configured such that the available motion space is comparable to the used motion space of configurations B and O. Otherwise, pilots can identify the P configuration by only focusing on the magnitude of the motion. Furthermore, would the pilot make a control error, the simulator would automatically run to its limits if the P configuration was tuned to use all available motion space.

$$\lambda_{dr} = -0.2778 \pm 3.2616i \qquad \lambda_{ar} = -4.0740 \qquad \lambda_{sm} = -0.0018 \tag{27}$$

Offline OMCT tests were applied to the three MCA configurations. In here, motion platform dynamics were excluded [18]. The results of these tests are depicted in Figure 12. The configurations B and O complied with the fidelity boundaries defined by ICAO 9625 [6]. As this is an offline test, it must be noted that for example, the outliers in Figure 12c will likely be within the boundaries due to an additional lag of the actuator dynamics [18].

The frequency response for the P configuration performed the worst on the OMCT test. As can be observed, the P configuration lies slightly outside the fidelity boundary for the second half and first half of the roll test 3 and 4, respectively. Furthermore, it partly lies outside the fidelity boundary of the sway test 8.

Table 4 Classical Washout Algorithm Filter Parameters for all Configurations used in the Experiment

	K_{f_y} $[-]$	$\omega_{n_{f_y}}$ $[rad/s]$	$\omega_{b_{f_y}}$ $[rad/s]$	ζ_{f_y} $[-]$	ω_{n_t} $[rad/s]$	ζ_t $[-]$	K_p $[-]$	ω_{n_p} $[rad/s]$	ζ_p $[-]$	K_r $[-]$	ω_{n_r} $[rad/s]$	ζ_r $[-]$
B	0.70	0.80	0.00	1.00	2.00	1.00	0.70	0.80	1.00	0.70	0.80	1.00
O	0.60	1.00	0.00	1.00	2.00	1.00	0.60	0.80	0.80	0.70	0.80	1.00
P	0.60	0.75	0.00	0.911	1.50	0.80	1.067	0.928	0.70	0.70	0.80	1.00

Table 5 Magnitude- and Phase Distortions for all CWA Configurations

	Dutch Roll						Aperiodic Roll		
	$\lvert f_y \rvert$	$\angle f_y$ [°]	$\lvert p \rvert$	$\angle p$ [°]	$\lvert r \rvert$	$\angle r$ [°]	$\lvert f_y \rvert$	$\lvert p \rvert$	$\lvert r \rvert$
B	0.535	13.077 lead	0.651	3.076 lead	0.687	27.929 lead	0.921	0.911	1.084
O	0.393	14.768 lead	0.599	0.976 lag	0.687	27.929 lead	0.836	0.882	1.084
P	0.472	5.089 lag	1.010	15.305 lead	0.687	27.929 lead	1.000	1.000	1.084

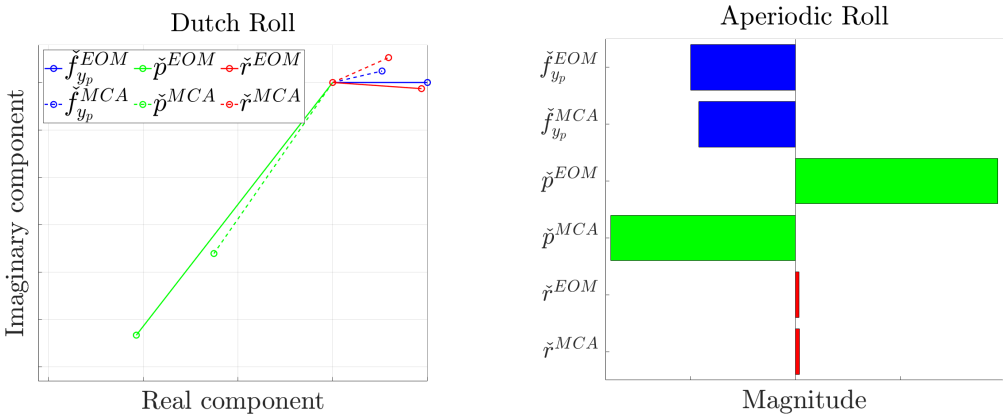

(a) **(b)**

Fig. 9 Configuration *B*

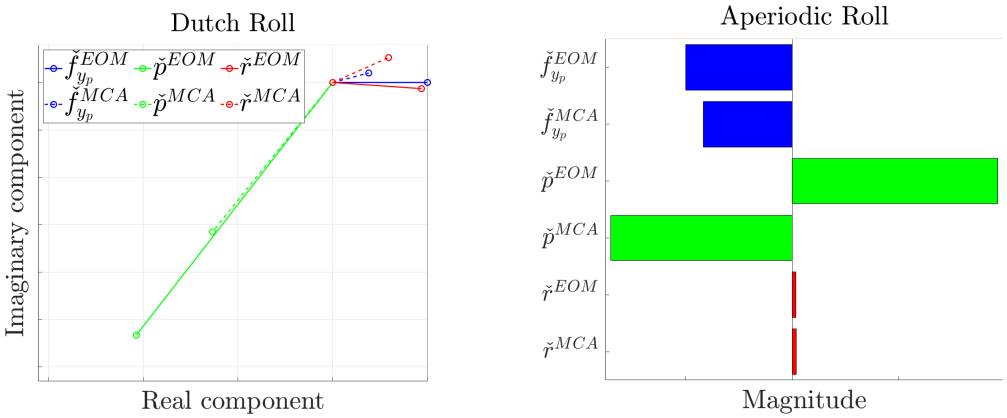

(a) **(b)**

Fig. 10 Configuration *O*

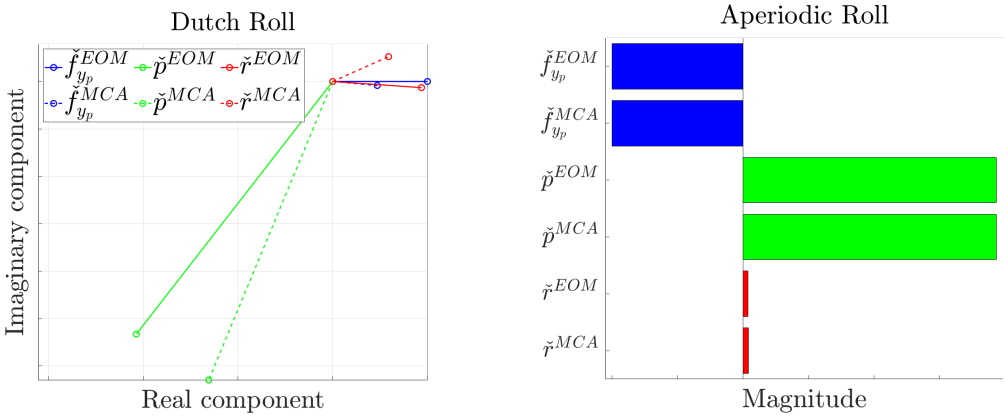

(a) **(b)**

Fig. 11 Configuration *P*

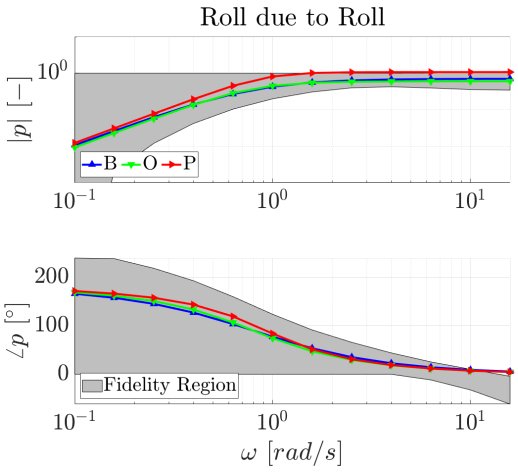

(a) Test 3

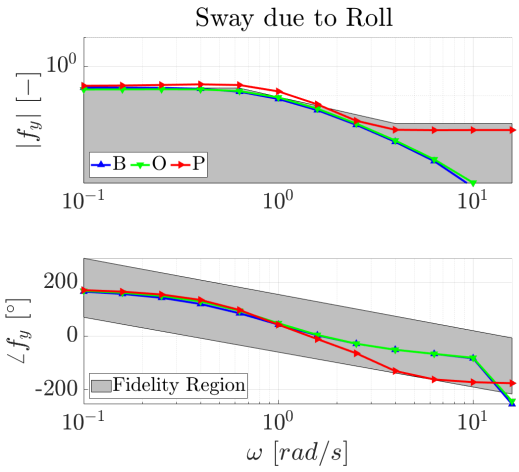

(b) Test 4

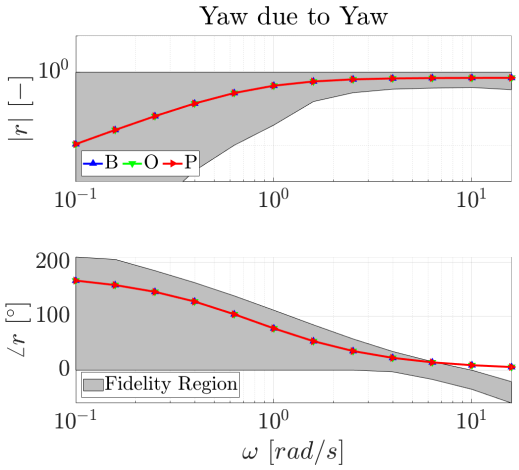

(c) Test 5

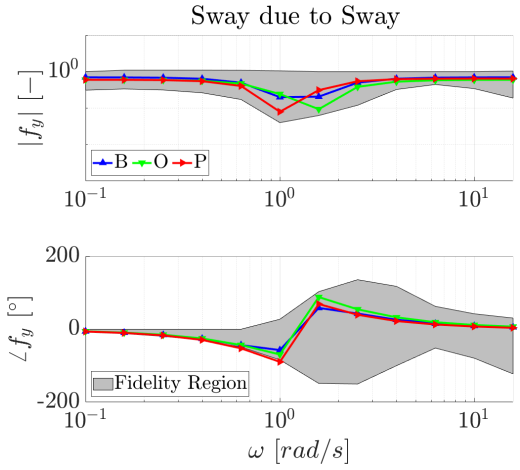

(d) Test 8

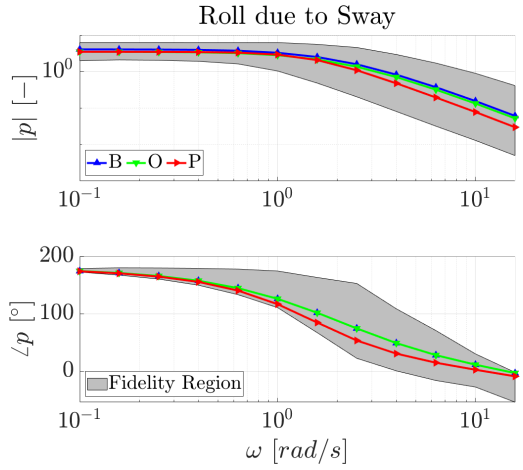

(e) Test 9

Fig. 12 Objective Motion Cueing Test Results for all Configurations

B. Participants

Seven pilots participated in the experiment and performed a series of pair-wise comparisons between the three MCA configurations. However, due to problems with the visual system the original Pilot 3 was removed and replaced in the analysis by Pilot 7. Therefore, from now on only six pilots are considered. The order, in which the different motion conditions were evaluated, was designed using a Latin Square distribution. All participating pilots, except Pilot 5, had flying experience with the Cessna Citation 550 aircraft. Pilots 1 to 6 had, at the time of participating, approximately 2,400, 1,300, 3,900, 5,800, 12,600 and 13,000 hours of flight experience, respectively. Also, Pilots 1 and 2 indicated to operate in general aviation, Pilots 3 and 4 indicated to operate in general- and civil aviation, and Pilots 5 and 6 indicated to operate in civil aviation. Furthermore, all pilots, except Pilot 1, deemed to have experience in performing motion simulation experiments. Lastly, all participating pilots were men. This experiment was approved by the Human Research Ethics Committee of the TU Delft, and informed consent was obtained from each pilot.

Table 6 Latin Square Matrix of the Experiment Conditions for all Pilots

Pilot	Conditions								
1	Training	*O - P*	*O - B*	*P - B*	No Motion	*B - P*	*B - O*	*P - O*	No Motion
2		*P - B*	*O - P*	*O - B*		*B - O*	*P - O*	*B - P*	
3*		*O - B*	*P - B*	*O - P*		*P - O*	*B - P*	*B - O*	
4		*B - P*	*B - O*	*P - O*		*O - P*	*O - B*	*P - B*	
5		*B - O*	*P - O*	*B - P*		*P - B*	*O - P*	*O - B*	
6		*P - O*	*B - P*	*B - O*		*O - B*	*P - B*	*O - P*	

*Pilot 3 has been replaced due to problems with the visual system.

C. Apparatus

The SIMONA Research Simulator (SRS) [10], features a hydraulic Steward motion platform of six degrees of freedom. An impression of the SRS is shown in Figure 13a. It has a collimated display system with a field-of-view of 180° and 40°, in horizontal- and vertical direction, respectively. Three projectors, mounted on top of the simulator, are used as visual system and have a refresh rate of 120 Hz. FlightGear Flight Simulator was used to render the outside visuals. The flight instruments presented to the pilot, Figure 13b, were rendered using OpenGL. To mask the noise coming from the motion platform, aircraft engine noise was played over the headset.

The simulated aircraft was a nonlinear model of the Cessna Citation 500 business jet. It was trimmed at an altitude of 5,000 m with a weight of 5,207 kg and velocities V_{TAS} = 160 m/s and V_{IAS} = 245 kts. The aircraft was in cruise configuration with flaps and gear UP and thrust at 94.8% Fan RPM. It was controlled with the control column and rudder pedals. Finally, the yaw damper and the longitudinal CWA were disabled, so lateral motion cues were clearly felt while longitudinal motion cues were not simulated.

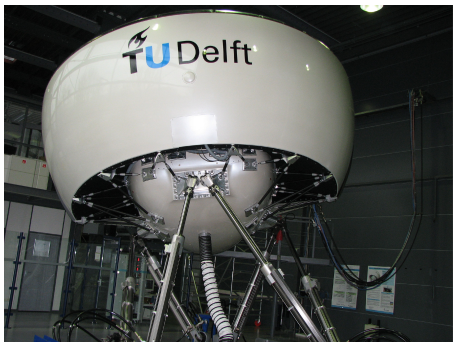

(a) SIMONA Research Simulator

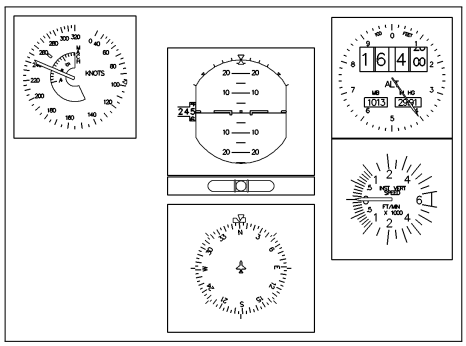

(b) Flight Instruments

Fig. 13 Flight Simulator

D. Experiment Task

In the experiment, a series of pair-wise comparisons between the three MCA configurations were performed on the SRS as a subjective evaluation. This format was based on the experiment by Stoev et al. [9], which received positive feedback. The pilot was instructed to compare pairs of different MCA configurations and select a *winner* for each pair, which corresponds to the configuration that resembles real flight most realistically. Due to the subtle differences between configurations and recommendations of Stoev et al. [9], the pilot was asked to give a confidence level ranging from 0 to 2, where; 0 is *no confidence*, 1 is *normal confidence* and 2 is *high confidence*. With a confidence level of 0, the pair-wise comparison is not taken into account.

Throughout each run, the Dutch roll eigenmode was excited externally with a specially-designed gust of semi-random amplitude and direction. The gust was a single sine-shaped pulse* with its frequency matching the Dutch roll eigenmode and was injected, every 10 seconds, as a side-slip angle. With this gust, the Dutch roll was excited. However, the aperiodic roll was also excited slightly. Within each evaluated pair, one run lasted for 130 seconds and consisted of a passive- and active part. After 10 seconds, the Dutch roll was excited every 10 seconds for 12 times.

The first 6 times constitute the passive part, in which the pilot was not allowed to touch the controls. Here the pilot gets acquainted with the motion signature and natural response of the aircraft. The last 6 times constitute the active part, in which the pilot was instructed to suppress the Dutch roll eigenmode at the moment the aircraft was excited. As the aircraft was specially trimmed for the flight condition, as in Table 3, the pilot was instructed to minimize all altitude and heading deviations with respect to the altitude and heading after the passive part. In here the pilot was allowed to use their preferred strategy, i.e., using rudder and/or aileron. As the aircraft was trimmed, the altitude and heading differences between before and after the passive part were negligible.

Besides the 6 pair-wise comparisons, two additional runs were performed and served as a baseline. The aircraft configuration was exactly the same but the MCA was disabled, so the motion platform remained at its neutral position. These runs contained only an active part, which lasted for 130 seconds instead of 60. One of these runs was after the third pair and one after the sixth. In here, no preferred configuration had to be stated, as this single run was only used to gather reference performance data.

Training was similar to the experiment performed by Stoev et al. [9] and lasted approximately 20 minutes for each pilot, during which the pilot flew all the MCA configurations twice in randomized order based on the Latin Square matrix. Each training run lasted 130 seconds, during which the pilot can practice to suppress the Dutch roll, as well as obtaining a feeling of the aircraft motion signature. Including briefing and training, the experiment lasted for approximately 1.5 hours.

E. Dependent Measures

The main recorded variables are the preferred MCA configurations in each evaluated pair, i.e., subjective choice, together with a confidence level ranging from 0 to 2. The preferred configuration is the configuration which represents the motion cues most realistically.

The influence of motion parameters on performance is tested by determining the Dutch roll suppression performances for each pilot. The Dutch roll MPF's are used for this purpose. Given an external Dutch roll excitation, the dashed line in Figure 14 illustrates the aircraft's natural response, i.e., without pilot input. In the active part, the pilot was instructed to suppress the Dutch roll, giving the actual aircraft response, illustrated by the solid line. Would the actual response lie below the natural response, then this is identified as positive performance (P^+), indicated in green, i.e., green area integrated over time. Contrarily, would the actual response lie above the natural response, then this is identified as negative performance (P^-), indicated in red, i.e., red area integrated over time.

For every 10 seconds, in the active part, the performance P_{10s} is calculated using Equation 28. In here, P^n is the natural response integrated over time. Would the performance be greater than 0, the pilot has a positive performance and has a better Dutch roll suppression than the natural response. Contrarily, would the performance be lower than 0, the pilot has

*Which looks like: $\beta_{gust} = \frac{A}{2}\cos(\omega_{DR} \cdot t - \pi) + \frac{A}{2}$, $\left[0, \frac{2\pi}{\omega_{DR}}\right]$, where: A and ω_{DR} are the amplitude and Dutch roll frequency, respectively.

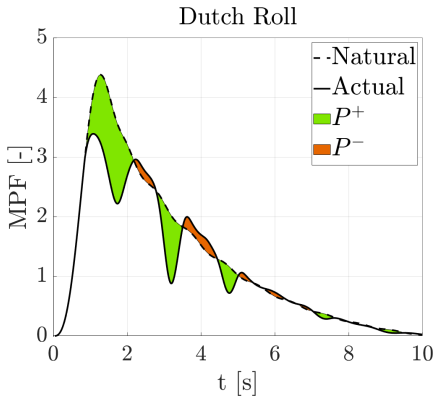

Fig. 14 Visualization of Dutch Roll Suppression Performance

negative performance and the natural response is better than the actual response. To calculate this performance, the aircraft states and pilot inputs are recorded.

$$P_{10s} = \frac{P^+ - P^-}{P^n} \cdot 100\% \tag{28}$$

F. Hypotheses

1) It was hypothesized that the PEMD tuned configuration was preferred over the OMCT and baseline tuned configurations, for an aircraft which was excited in the Dutch roll. This was hypothesized as the aircraft dynamics were taken into account during the PEMD tuning process. This hypothesis was rejected if the PEMD tuned configuration received a lower overall score than the OMCT and/or baseline tuned configuration.
2) It was hypothesized that the pilot had a better performance in suppressing the Dutch roll eigenmode with the PEMD tuned configuration than with the OMCT and baseline tuned configurations. This hypothesis was rejected if no significant difference was found, with $\alpha = 0.05$.

VI. Results

Pilot preference for the different motion configurations is analyzed through the results of all pair-wise comparisons. Figure 15 presents the results of all pair-wise comparisons evaluated by all pilots. In here, the bar height represents the number of times a configuration has been preferred, multiplied with the associated confidence level (0, 1 or 2). Furthermore, each pilot is visualized by a different color. Additionally, the raw data are presented in the appendix.

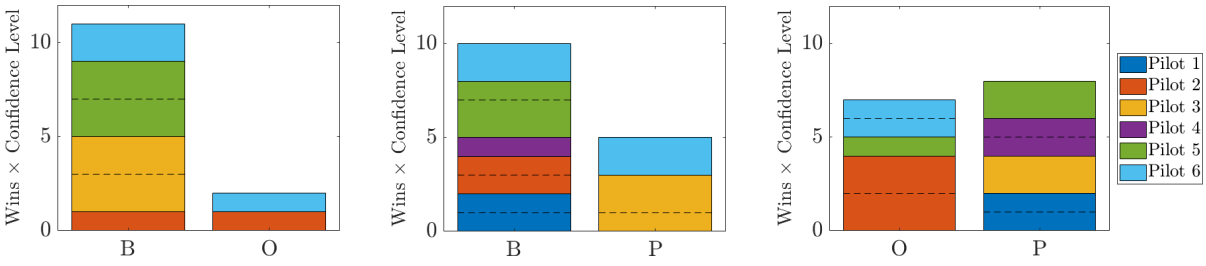

Fig. 15 Results of Pair-wise Comparisons for Evaluated Pairs (See Appendix for Raw Data)

As every pair is evaluated twice per pilot, e.g., *B-O* and *O-B*, *within-pair* consistency is present when a pilot prefers the same configuration in both evaluations. Analyzing Figure 15 reveals that Pilot 2 has a within-pair inconsistency in pair *B-O*, Pilot 5 in pair *O-P*, and Pilot 6 in pairs *B-O* and *B-P*. Not visible from the figure is the number of times that a confidence level of 0 is given. In total, pair *B-O* received four times a confidence level of 0, twice by Pilot 1 and 4. Additionally, pair *B-P* received once a confidence level of 0 by Pilot 4, and pair *O-P* once by Pilot 3.

Statistical modelling is used to make a data-based ranking between the three different configurations. For this, data are fit to a Bradley-Terry pattern model. The Bradley-Terry model is chosen as this model is popular for pair-wise comparisons

of highly dependent data [19]. A Matlab implementation*, which uses the Newton-Raphson method, is used to estimate the *worth parameters*, which provide the probability that configuration i is preferred over j, Equation 29.

$$P(i > j) = \frac{\pi_i}{\pi_i + \pi_j} \tag{29}$$

After normalizing, i.e., $\pi_B + \pi_O + \pi_P = 1$, the resulting worth parameters are $\{\pi_B, \pi_O, \pi_P\} = \{0.601, 0.165, 0.234\}$. From ranking based on these worth parameters, the B configuration is the winning configuration, with $\pi_B = 0.601$, followed by configuration P with $\pi_P = 0.234$. Finally, configuration O with $\pi_O = 0.165$. Using Equation 29, the probability that configuration P is preferred over configuration B and O is 0.280 and 0.586, respectively.

This leads to the conclusion that the first hypothesis is rejected, as the B configuration received a higher subjective rating than the P configuration. Yet, the P configuration received a marginally higher rating than the O configuration.

The influence of motion parameters on performance is tested by determining the Dutch roll suppression performance. This performance is calculated for each pilot for the active parts of each run, resulting in 96 data points per pilot. Which can be divided into 24 data points for each condition, e.g., the three configurations and the no-motion condition. To compare the different conditions, a *within-subjects* design is used. In a within-subject design, each subject tests all the conditions, yielding one data point for each condition. To fit in within-subject design, the average performance for each pilot and condition is used, i.e., calculating the average of the 24 data points for each pilot and condition. The raw results for all conditions are presented in Figure 16.

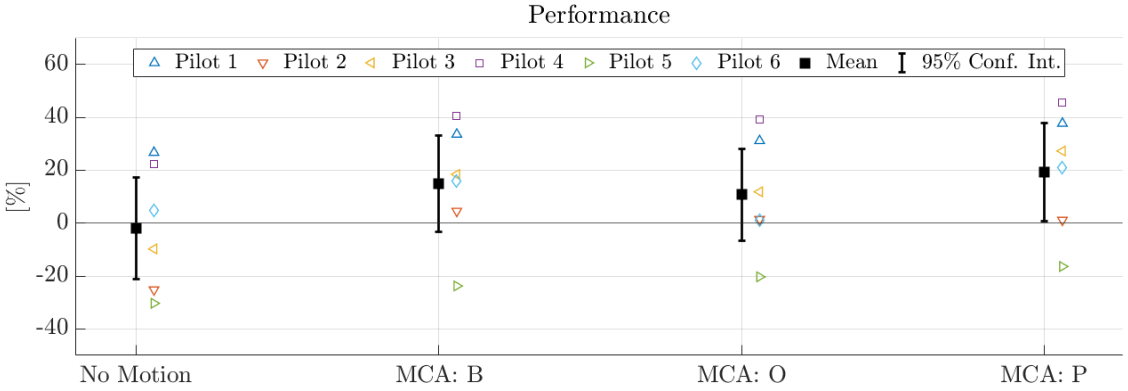

Fig. 16 Performance per Configuration - Not Corrected for Between-Subject Variability

From Figure 16, different observations can be made; Pilots 1 and 4 have the highest performance for all conditions. Pilots 2 and 5 have on average a negative performance, where Pilot 5 even has negative performance for all conditions, meaning that the Dutch roll is excited instead of suppressed. Also, all pilots, except Pilot 6, have lowest performance with the no-motion condition. However, these data are not corrected for *between-subject* variability, e.g., every pilot has on average a different performance. To better observe trends over the motion conditions, Figure 17 depicts the performance data corrected for between-subject variability.

Comparing Figures 16 and 17, it can be observed that the performances per condition are more concentrated after the between-subject variability correction. Data are concentrated the most for the B- and P configuration. It can be observed that pilots suppressed 19.3%, on average, of the Dutch roll with the P configuration. Furthermore, on average, pilots suppressed 14.9% and 10.7% of the Dutch roll with configurations B and O, respectively. When the motion was turned-off, pilots were exciting the Dutch roll by approximately 2.0% instead of suppressing it.

For statistical analysis, a Repeated-Measures ANOVA test is used, as the data were found to satisfy the sphericity- and normality assumption. The results are $F(3, 15) = 13.832$ and $p < 0.0005$, indicating that a significant difference can be identified. Post-hoc tests using the Bonferroni correction, with $\alpha = 0.05$, revealed that the pilot performance is significantly better with the P configuration than without motion ($p = 0.017$). However, the improvement in performance

*`http://personal.psu.edu/drh20/code/btmatlab/`, accessed on December 20, 2019

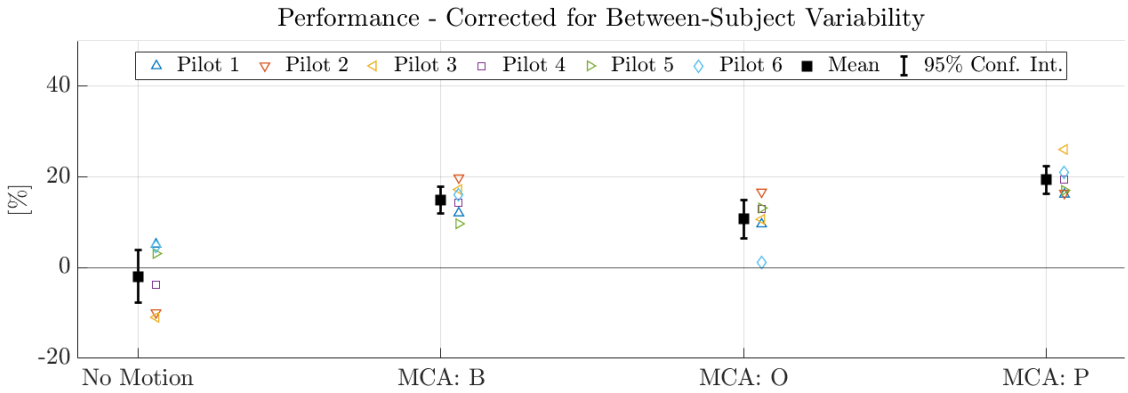

Fig. 17 Performance per Configuration - Corrected for Between-Subject Variability

between the B configuration and the no-motion condition is not significant ($p = 0.063$). Between the P configuration and B configuration no significant difference in performance is found ($p = 0.291$). Furthermore, between the P configuration and O configuration no significant difference is found ($p = 0.224$). The pilots have similar performance with the B and O configurations ($p = 0.966$).

The Repeated-Measures ANOVA results are used to test the performance. On average, pilots have the highest performance with the P configuration. A significant improvement is found for the P configuration in comparison to the no-motion configuration. Yet, as no significant differences are identified between the B, O and P configurations, the second hypothesis is rejected.

VII. Discussion

The purpose of this paper is to extend EMD with a pilot perception model, apply the EMD to the lateral model of the Cessna Citation 500, derive an automatic tuning algorithm and validate the resulting motion cueing solution with a pilot-in-the-loop experiment. Six pilots performed pair-wise comparisons of three MCA configurations in an experiment, in which they had to suppress the Dutch roll eigenmode which was externally excited.

After performing the experiment the majority of pilots indicated to have difficulties in picking a preferred configuration, as the three configurations felt similar. The pair-wise comparison format used (including confidence levels) received positive feedback. Also, the way each run was divided into a passive- and active part was deemed beneficial for picking a preferred configuration, as the passive part allowed for focus on the motion signature. Also, several pilots suggested to increase the number of pairs to allow for more comparisons as the differences between configurations are very subtle.

Additionally, most pilots indicated deficiencies in the slip indicator. The initial ball direction was correct, but the ball was under-damped. Some pilots even indicated that this influenced their Dutch roll suppression performance. Furthermore, some pilots indicated that the yoke was too sensitive and resulted in over-correction, which sometimes led to exciting the Dutch roll rather than suppressing it.

Different Dutch roll suppression techniques were used by the pilots. First, some pilots only used rudder, whereas others used ailerons, or a combination of both. Second, some pilots gave a single pulse as input, whereas others gave several inputs, e.g. a doublet input. Pilots 1 and 4, which had the highest performance for all conditions, gave mostly doublet inputs to the rudder.

The values for α and β in the tuning algorithm were chosen rather arbitrarily. When the Dutch roll is externally excited, the aperiodic roll is excited a little as well. Should this external eigenmode excitation be used in the future, an approach would be to choose values for α and β based on the relative MPFs given a certain external excitation.

The P configuration was configured such that the available motion space was similar to the used motion space in configurations B and O. Motion cue distortions, associated to the Dutch roll, could have been less if more motion space was available to the tuning algorithm.

Finally, the differences in results for both hypothesis are at first unexpected. The *B* configuration is the winner for the first hypothesis. Whereas, the *P* configuration is the winner in the second, however, not significant. It must be noted that the first hypothesis evaluates *perceptual fidelity* [11], while the second hypothesis evaluates *pilot performance*. These are two different evaluations and are not necessarily related, e.g., the pilot can perceive something as realistic, but this does not imply that its performance is good.

VIII. Recommendations

In general, EMD/PEMD has shown great potential but a possible drawback compared to OMCT is that OMCT evaluates fidelity over a range of frequencies, whereas EMD/PEMD only evaluates particular eigenmodes. EMD/PEMD tuning might be improved by evaluating eigenmodes corresponding to different flight conditions.

Clearly visible from the results of pair *B*-*O* is the need to further refine the OMCT fidelity boundaries. Both configurations satisfy the OMCT fidelity criteria. Among pairs, a confidence level of 0 was given the most to this pair (four times, whereas other pairs only once). Additionally, this pair has two within-pair inconsistencies. This indicates that both configurations are quite similar. Yet, the *B* configuration performed better on the subjective rating. Furthermore, pilots have a higher suppression performance with this configuration. Both indicate the need for further refinement of the OMCT fidelity boundaries.

Constant perception thresholds are used in the current PEMD. In reality, these vary per person and frequency but also depend on factors such as workload and task [2, 14]. The next step for PEMD could be to use perception thresholds which correspond to the frequency of different eigenmodes. Also, personalized motion cueing can be considered by obtaining someone's perception thresholds and use these to optimize for a motion configuration, which can be useful for training purposes.

In motion cueing, motion is often perceived as too intense if cued one-to-one [20]. This is confirmed by some pilots who indeed reported that perceived motion for the *P* configuration was too intense. A follow-up study could be to scale the aircraft model associated eigenvectors in the tuning algorithm, which has influence on the relative importance of magnitude- and phase distortion minimization. However, less motion space will be necessary.

IX. Conclusion

This paper presents the application of the *Perceptual Eigenmode Distortion* applied to a lateral fixed-wing aircraft model. It is shown that by re-expressing the output vector eigenvectors, different units can be compared and the contributions of different motion cues in an eigenmode can be identified. Furthermore, an automatic tuning algorithm was introduced in which an MCA parameter-set can be obtained that minimizes the eigenvector distortions for a given flight condition and representative manoeuvre.

A pilot-in-the-loop experiment was performed for testing the hypotheses. The first hypothesis, which evaluated the pilot preference using pair-wise comparisons, was rejected as the baseline configuration scored highest instead of the PEMD tuned configuration. However, subjective ratings were complicated by pilot inconsistencies and uncertainties. An assessment method that minimizes the pilot bias would be beneficial for future subjective evaluations. Even though pilots have highest performance with the PEMD tuned configuration; the second hypothesis, which evaluated the influence of motion parameters on Dutch roll suppression performance, was rejected as this difference was not significant.

In general, PEMD and associated tuning algorithm yield a method for evaluating and tuning motion cueing algorithms. The method has potential and can be used as a stepping stone to further improve objective evaluation methods. Furthermore, the methodology can be applied to any vehicle model and might be used to enhance objective motion cueing as a whole.

Appendix

Table 7 Pilot Selected Winner for each Pair, with Corresponding Confidence Level

Pilot	Conditions											
1	Training	***O*** - ***P***	1	*O* - ***B***	0	*P* - ***B***	1	No Motion	***B*** - *P*	1	*B* - ***O***	0	***P*** - *O*	1	No Motion
2		*P* - ***B***	1	***O*** - *P*	2	*O* - ***B***	1		*B* - ***O***	1	*P* - ***O***	2	***B*** - *P*	1	
3		*O* - ***B***	2	***P*** - *B*	1	*O* - ***P***	2		*P* - *O*	0	*B* - ***P***	2	***B*** - *O*	2	
4		***B*** - *P*	1	*B* - *O*	0	***P*** - *O*	1		*O* - ***P***	1	*O* - *B*	0	*P* - *B*	0	
5		***B*** - *O*	2	***P*** - *O*	2	***B*** - *P*	2		*P* - ***B***	1	***O*** - *P*	1	*O* - ***B***	2	
6		*P* - ***O***	1	*B* - ***P***	2	*B* - ***O***	1		*O* - ***B***	2	*P* - ***B***	2	***O*** - *P*	1	

References

[1] Reid, L. D., and Nahon, M. A., "Flight simulation motion-base drive algorithms: part 1. Developing and testing equations," *UTIAS Report*, 1985, pp. 5.1–5.24.

[2] Hosman, R. J. A. W., and Van der Vaart, J. C., "Vestibular models and thresholds of motion perception. Results of tests in a flight simulator," *Report LR-265*, Delft University of Technology, 1978, pp. 26–32.

[3] Sinacori, J. B., "The determination of some requirements for a helicopter flight research simulation facility," *NASA*, 1977, pp. 1–36.

[4] Schroeder, J. A., "Helicopter Flight Simulation Motion Platform Requirements," Ph.D. thesis, Stanford University, Jan. 1998.

[5] Gouverneur, B., Mulder, J. A., Van Paassen, M. M., Stroosma, O., and Field, E., "Optimisation of the SIMONA Research Simulator's Motion Filter Settings for Handling Qualities Experiments," *AIAA Modeling and Simulation Technologies Conference and Exhibit*, 2003, pp. 25–37. https://doi.org/10.2514/6.2003-5679.

[6] *Manual of Criteria for the Qualification of Flight Simulation Training Devices - Volume 1 - Aeroplanes*, International Civil Aviation Organization, 4th ed., 2015.

[7] Miletović, I., "Motion Cueing Fidelity in Rotorcraft Flight Simulation: A New Perspective using Modal Analysis," Ph.D. thesis, Delft University of Technology, Jan. 2020.

[8] Dalmeijer, W., Miletović, I., Stroosma, O., and Pavel, M. D., "Extending the Objective Motion Cueing Test to Measure Rotorcraft Simulator Motion Characteristics," *73rd Annual AHS International Forum and Technology Display*, 2017, pp. 1876–1891.

[9] Stoev, S., Van Paassen, M. M., Stroosma, O., Miletović, I., and Mulder, M., "Eigenmode Distortion Analysis for Motion Cueing Evaluation in Fixed-Wing Aircraft Simulators," *AIAA Modeling and Simulation Technologies Conference and Exhibit*, 2019, pp. 1–19. https://doi.org/10.2514/6.2019-0179.

[10] Stroosma, O., Van Paassen, M. M., and Mulder, M., "Using the SIMONA Research Simulator for Human-machine Interaction Research," *AIAA Modeling and Simulation Technologies Conference and Exhibit*, 2003, pp. 1–8. https://doi.org/10.2514/6.2003-5525.

[11] Pool, D. M., "Objective Evaluation of Flight Simulator Motion Cueing Fidelity Through a Cybernetic Approach," Ph.D. thesis, Delft University of Technology, Sep. 2012.

[12] Oppenheim, A. V., and Verghese, G. C., *Signals, Systems and Inference, Global Edition*, Pearson, 2017.

[13] Heerspink, H., Berkouwer, W. R., Stroosma, O., Van Paassen, M. M., Mulder, M., and Mulder, J. A., "Evaluation of Vestibular Thresholds for Motion Detection in the SIMONA Research Simulator," *AIAA Modeling and Simulation Technologies Conference and Exhibit*, 2005, pp. 15–17. https://doi.org/10.2514/6.2005-6502.

[14] Groen, E. L., Wentink, M., Valente Pais, A. R., Mulder, M., and Van Paassen, M. M., "Motion Perception Thresholds in Flight Simulation," *AIAA Modeling and Simulation Technologies Conference and Exhibit*, 2006, pp. 1–11. https://doi.org/10.2514/6.2006-6254.

[15] De Ridder, K., and Roza, Z. C., "Automatic Optimization of Motion Drive Algorithms using OMCT," *AIAA Modeling and Simulation Technologies Conference and Exhibit*, 2015, pp. 1–11. https://doi.org/10.2514/6.2015-1139.

[16] Fu, W., "Evidence-based development and evaluation of haptic interfaces for manual control," Ph.D. thesis, Delft University of Technology, Jun. 2019. https://doi.org/10.4233/uuid:b5953a17-322d-49e6-87ba-e299673e8b84.

[17] Holland, J. H., *Adaptation in Natural and Artificial Systems: An Introductory Analysis with Applications to Biology, Control, and Artificial Intelligence*, MIT Press, 1992.

[18] Stroosma, O., Van Paassen, M. M., Mulder, M., Hosman, R. J. A. W., and Advani, S. K., "Applying the Objective Motion Cueing Test to a Classical Washout Algorithm," *AIAA Modeling and Simulation Technologies Conference and Exhibit*, American Institute of Aeronautics and Astronautics, 2013, pp. 1–14. https://doi.org/10.2514/6.2013-4834.

[19] Cattelan, M., "Models for Paired Comparison Data: A Review with Emphasis on Dependent Data," *Statistical Science*, Vol. 27, No. 3, 2012, pp. 412–433.

[20] Valente Pais, A. R., Van Paassen, M. M., Mulder, M., and Wentink, M., "Perception Coherence Zones in Flight Simulation," *Journal of Aircraft*, Vol. 47, 2010, pp. 2039–2048. https://doi.org/10.2514/1.C000281.

This page is intentionally left blank.

II

AIAA Paper - Appendices

This page is intentionally left blank.

A

Decomposition of the Extended Aircraft State-Space System

This appendix defines every element of the aircraft state-space system. For clarity, the dimensional equations of motion are shown first (Equation A.1). The symbols appearing in Equations A.2 and A.3 are recapitulated in Tables A.1 and A.2, respectively.

$$
\begin{aligned}
W\cos\theta_0\Delta\phi + Y_v\Delta v + Y_{\dot{v}}\Delta\dot{v} + Y_p\Delta p + Y_r\Delta r + Y_{\delta_a}\Delta\delta_a + Y_{\delta_r}\Delta\delta_r &= m(\Delta\dot{v} + \Delta r V)\\
L_v\Delta v + L_p\Delta p + L_r\Delta r + L_{\delta_a}\Delta\delta_a + L_{\delta_r}\Delta\delta_r &= I_{xx}\Delta\dot{p} - I_{xz}\Delta\dot{r}\\
N_v\Delta v + N_{\dot{v}}\Delta\dot{v} + N_p\Delta p + N_r\Delta r + N_{\delta_a}\Delta\delta_a + N_{\delta_r}\Delta\delta_r &= I_{zz}\Delta\dot{r} - I_{xz}\Delta\dot{p}\\
\Delta\dot{\psi} &= \tfrac{\Delta r}{cos\theta_0}\\
\Delta\dot{\phi} &= \Delta p + \Delta r\tan\theta_0
\end{aligned}
\tag{A.1}
$$

$$
\begin{gathered}
\Delta\dot{\boldsymbol{x}}^{EOM} = A^{EOM}\Delta\boldsymbol{x}^{EOM} + B^{EOM}\Delta\boldsymbol{u}^{EOM}\\
\begin{bmatrix}\dot{v}\\ \dot{\phi}\\ \dot{p}\\ \dot{r}\end{bmatrix} = \begin{bmatrix} y_\beta & y_\phi V & y_p\frac{b}{2} & y_r\frac{b}{2}\\ 0 & 0 & 1 & 0\\ l_\beta\frac{2}{b} & 0 & l_p & l_r\\ n_\beta\frac{2}{b} & 0 & n_p & n_r\end{bmatrix}\begin{bmatrix}v\\ \phi\\ p\\ r\end{bmatrix} + \begin{bmatrix} y_{\delta_a}V & y_{\delta_r}V\\ 0 & 0\\ l_{\delta_a}\frac{2V}{b} & l_{\delta_r}\frac{2V}{b}\\ n_{\delta_a}\frac{2V}{b} & n_{\delta_r}\frac{2V}{b}\end{bmatrix}\begin{bmatrix}\delta_a\\ \delta_r\end{bmatrix}
\end{gathered}
\tag{A.2}
$$

$$
\begin{gathered}
\Delta\boldsymbol{y}^{EOM} = C^{EOM}\Delta\boldsymbol{x}^{EOM} + D^{EOM}\Delta\boldsymbol{u}^{EOM}\\
\begin{bmatrix} f_{y_p}^{EOM}\\ p^{EOM}\\ r^{EOM}\end{bmatrix} = \begin{bmatrix} C_{f_y v} & C_{f_y\phi} & C_{f_y p} & C_{f_y r}\\ 0 & 0 & 1 & 0\\ 0 & 0 & 0 & 1\end{bmatrix}\boldsymbol{x} + \begin{bmatrix} D_{f_y\delta_a} & D_{f_y\delta_r}\\ 0 & 0\\ 0 & 0\end{bmatrix}\boldsymbol{u}
\end{gathered}
\tag{A.3}
$$

Table A.1: Symbols Appearing in the General State-Space Representation of Equation A.2

	y_i	l_i	n_i
$i=\beta$	$\frac{V}{b}\frac{C_{Y_\beta}}{2\mu_b}$	$\frac{V}{b}\frac{C_{l_\beta}K_Z^2+C_{n_\beta}K_{XZ}}{4\mu_b(K_X^2K_Z^2-K_{XZ}^2)}$	$\frac{V}{b}\frac{C_{l_\beta}K_{XZ}+C_{n_\beta}K_X^2}{4\mu_b(K_X^2K_Z^2-K_{XZ}^2)}$
$i=\phi$	$\frac{V}{b}\frac{C_L}{2\mu_b}$	0	0
$i=p$	$\frac{V}{b}\frac{C_{Y_p}}{2\mu_b}$	$\frac{V}{b}\frac{C_{l_p}K_Z^2+C_{np}K_{XZ}}{4\mu_b(K_X^2K_Z^2-K_{XZ}^2)}$	$\frac{V}{b}\frac{C_{l_p}K_{XZ}+C_{np}K_X^2}{4\mu_b(K_X^2K_Z^2-K_{XZ}^2)}$
$i=r$	$\frac{V}{b}\frac{C_{Y_r}-4\mu_b}{2\mu_b}$	$\frac{V}{b}\frac{C_{l_r}K_Z^2+C_{n_r}K_{XZ}}{4\mu_b(K_X^2K_Z^2-K_{XZ}^2)}$	$\frac{V}{b}\frac{C_{l_r}K_{XZ}+C_{n_r}K_X^2}{4\mu_b(K_X^2K_Z^2-K_{XZ}^2)}$
$i=\delta_a$	$\frac{V}{b}\frac{C_{Y_{\delta a}}}{2\mu_b}$	$\frac{V}{b}\frac{C_{l_{\delta_a}}K_Z^2+C_{n_{\delta a}}K_{XZ}}{4\mu_b(K_X^2K_Z^2-K_{XZ}^2)}$	$\frac{V}{b}\frac{C_{l_{\delta_a}}K_{XZ}+C_{n_{\delta a}}K_X^2}{4\mu_b(K_X^2K_Z^2-K_{XZ}^2)}$
$i=\delta_r$	$\frac{V}{b}\frac{C_{Y_{\delta_r}}}{2\mu_b}$	$\frac{V}{b}\frac{C_{l_{\delta_r}}K_Z^2+C_{n_{\delta_r}}K_{XZ}}{4\mu_b(K_X^2K_Z^2-K_{XZ}^2)}$	$\frac{V}{b}\frac{C_{l_{\delta_r}}K_{XZ}+C_{n_{\delta_r}}K_X^2}{4\mu_b(K_X^2K_Z^2-K_{XZ}^2)}$

Table A.2: Symbols Appearing in the Output Vector State-Space Representation of Equation A.3

	C_{f_yi}	$C_{\dot{p}i}$	$C_{\dot{r}i}$
$i=v$	$y_\beta+l_\beta\frac{2}{b}l_z+n_\beta\frac{2}{b}l_x$	$l_\beta\frac{2}{b}$	$n_\beta\frac{2}{b}$
$i=\phi$	$y_\phi V-g$	0	0
$i=p$	$y_p\frac{b}{2}-u_{s_0}\alpha_0+l_pl_z+n_pl_x$	l_p	n_p
$i=r$	$y_r\frac{b}{2}+u_{s_0}+l_rl_z+n_rl_x$	l_r	n_r

	D_{f_yi}	$D_{\dot{p}i}$	$D_{\dot{r}i}$
$i=\delta_a$	$y_{\delta_a}+l_{\delta_a}\frac{2V}{b}l_z+n_{\delta_a}\frac{2V}{b}l_x$	$l_{\delta_a}\frac{2V}{b}$	$n_{\delta_a}\frac{2V}{b}$
$i=\delta_r$	$y_{\delta_r}+l_{\delta_r}\frac{2V}{b}l_z+n_{\delta_r}\frac{2V}{b}l_x$	$l_{\delta_r}\frac{2V}{b}$	$n_{\delta_r}\frac{2V}{b}$

B
Decomposition of the Modified CWA State-Space System

This appendix defines every element in the state-space system corresponding to the modified Classical Washout Algorithm. The symbols appearing in Equations B.2 to B.6 are recapitulated in Tables A.1 and A.2 or originate from the high- and low-pass filter parameters.

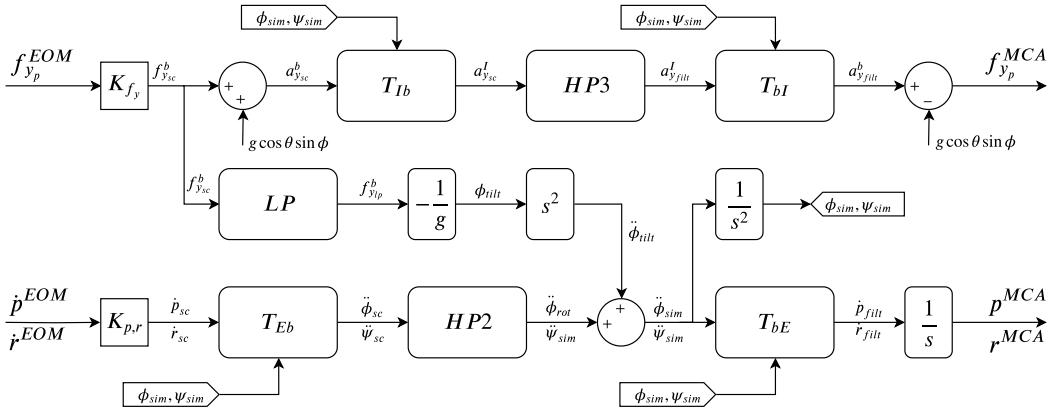

Figure B.1: Classical Washout Algorithm Adapted for Lateral EMD [16]

$$
\begin{aligned}
\Delta\dot{\boldsymbol{x}}^{MCA} &= A^{MCA}\Delta\boldsymbol{x}^{MCA} + B^{MCA}\Delta\boldsymbol{u}^{MCA} \\
\Delta\boldsymbol{u}^{MCA} &= \begin{bmatrix}\Delta f_{y_p}^{EOM} & \Delta\dot{p}^{EOM} & \Delta\dot{r}^{EOM}\end{bmatrix}^T \\
\Delta\boldsymbol{x}^{MCA} &= \begin{bmatrix}A_y^I & S_y^I & V_y^I & \phi_{rot} & \dot{\phi}_{rot} & \phi_{tilt} & \dot{\phi}_{tilt} & \phi_{sim} & \dot{\phi}_{sim} & \psi_{sim} & \dot{\psi}_{sim} & p_{filt}\end{bmatrix}^T
\end{aligned}
\tag{B.1}
$$

$$
A^{MCA} = \begin{bmatrix}
0 & 1 & 0 & 0 & 0 & 0 & 0 & 0 & 0 & 0 & 0 & 0 \\
0 & 0 & 1 & 0 & 0 & 0 & 0 & 0 & 0 & 0 & 0 & 0 \\
-C_{f_y} & -B_{f_y} & -A_{f_y} & 0 & 0 & 0 & 0 & g & 0 & 0 & 0 & 0 \\
0 & 0 & 0 & 0 & 1 & 0 & 0 & 0 & 0 & 0 & 0 & 0 \\
0 & 0 & 0 & -B_p & -A_p & 0 & 0 & 0 & 0 & 0 & 0 & 0 \\
0 & 0 & 0 & 0 & 0 & 0 & 1 & 0 & 0 & 0 & 0 & 0 \\
0 & 0 & 0 & 0 & 0 & -B_t & -A_t & 0 & 0 & 0 & 0 & 0 \\
0 & 0 & 0 & 0 & 0 & 0 & 0 & 0 & 1 & 0 & 0 & 0 \\
0 & 0 & 0 & -B_p & -A_p & -B_t^2 & -A_tB_t & 0 & 0 & 0 & 0 & 0 \\
0 & 0 & 0 & 0 & 0 & 0 & 0 & 0 & 0 & 0 & 1 & 0 \\
0 & 0 & 0 & 0 & 0 & 0 & 0 & 0 & 0 & -B_r & -A_r & 0 \\
0 & 0 & 0 & -B_p & -A_p & -B_t^2 & -A_tB_t & 0 & 0 & \theta_0 B_r & \theta_0 A_r & 0
\end{bmatrix}
\tag{B.2}
$$

$$B^{MCA} = \begin{bmatrix} 0 & 0 & 0 \\ 0 & 0 & 0 \\ K_{f_y} & 0 & 0 \\ 0 & 0 & 0 \\ 0 & K_p & \theta_0 K_r \\ 0 & 0 & 0 \\ -\frac{K_{f_y}}{g} & 0 & 0 \\ 0 & 0 & 0 \\ -\frac{K_{f_y} B_t}{g} & K_p & \theta_0 K_r \\ 0 & 0 & 0 \\ 0 & 0 & K_r \\ -\frac{K_{f_y} B_t}{g} & K_p & 0 \end{bmatrix} \tag{B.3}$$

$$\Delta \boldsymbol{y}^{MCA} = \begin{bmatrix} f_{y_p}^{MCA} \\ p^{MCA} \\ r^{MCA} \end{bmatrix} = C^{MCA} \Delta \boldsymbol{x}^{MCA} + D^{MCA} \Delta \boldsymbol{u}^{MCA} \tag{B.4}$$

$$C^{MCA} = \begin{bmatrix} -C_{f_y} & -B_{f_y} & -A_{f_y} & 0 & 0 & 0 & 0 & 0 & 0 & 0 & 0 & 0 \\ 0 & 0 & 0 & 0 & 0 & 0 & 0 & 0 & 0 & 0 & 0 & 1 \\ 0 & 0 & 0 & 0 & 0 & 0 & 0 & 0 & 0 & 0 & 1 & 0 \end{bmatrix} \tag{B.5}$$

$$D^{MCA} = \begin{bmatrix} K_{f_y} & 0 & 0 \\ 0 & 0 & 0 \\ 0 & 0 & 0 \end{bmatrix} \tag{B.6}$$

C
Decomposition of the State-Space System Coupling

This appendix defines every element of the coupling matrices necessary for combining the aircraft state-space and CWA state-space. The symbols appearing are recapitulated in Tables A.1 and A.2.

$$\begin{bmatrix} \Delta\dot{\boldsymbol{x}}^{EOM} \\ \Delta\dot{\boldsymbol{x}}^{MCA} \end{bmatrix} = \begin{bmatrix} A^{EOM} & 0 \\ A^{COUP} & A^{MCA} \end{bmatrix} \begin{bmatrix} \Delta\boldsymbol{x}^{EOM} \\ \Delta\boldsymbol{x}^{MCA} \end{bmatrix} + \begin{bmatrix} B^{EOM} \\ B^{COUP} \end{bmatrix} \Delta\boldsymbol{u}^{EOM} \tag{C.1}$$

$$B^{COUP} = \begin{bmatrix} 0 & 0 \\ 0 & 0 \\ K_{f_y} D_{f_y\delta_a} & K_{f_y} D_{f_y\delta_r} \\ 0 & 0 \\ K_p D_{\dot{p}\delta_a} + \theta_0 K_r D_{\dot{r}\delta_a} & K_p D_{\dot{p}\delta_r} + \theta_0 K_r D_{\dot{r}\delta_r} \\ 0 & 0 \\ -\frac{K_{f_y}}{g} D_{f_y\delta_a} & -\frac{K_{f_y}}{g} D_{f_y\delta_r} \\ 0 & 0 \\ -\frac{K_{f_y} B_t}{g} D_{f_y\delta_a} + K_p D_{\dot{p}\delta_a} + \theta_0 K_r D_{\dot{r}\delta_a} & -\frac{K_{f_y} B_t}{g} D_{f_y\delta_r} + K_p D_{\dot{p}\delta_r} + \theta_0 K_r D_{\dot{r}\delta_r} \\ 0 & 0 \\ K_r D_{\dot{r}\delta_a} & K_r D_{\dot{r}\delta_r} \\ -\frac{K_{f_y} B_t}{g} D_{f_y\delta_a} + K_p D_{\dot{p}\delta_a} & -\frac{K_{f_y} B_t}{g} D_{f_y\delta_r} + K_p D_{\dot{p}\delta_r} \end{bmatrix} \tag{C.2}$$

$$\begin{bmatrix} \Delta\boldsymbol{y}^{EOM} \\ \Delta\boldsymbol{y}^{MCA} \end{bmatrix} = \begin{bmatrix} C^{EOM} & 0 \\ C^{COUP} & C^{MCA} \end{bmatrix} \begin{bmatrix} \Delta\boldsymbol{x}^{EOM} \\ \Delta\boldsymbol{x}^{MCA} \end{bmatrix} + \begin{bmatrix} D^{EOM} \\ D^{COUP} \end{bmatrix} \Delta\boldsymbol{u}^{EOM} \tag{C.3}$$

$$C^{COUP} = \begin{bmatrix} K_{f_y} C_{f_y v} & K_{f_y} C_{f_y\phi} & K_{f_y} C_{f_y p} & K_{f_y} C_{f_y r} \\ 0 & 0 & 0 & 0 \\ 0 & 0 & 0 & 0 \end{bmatrix} \tag{C.4}$$

$$D^{COUP} = \begin{bmatrix} K_{f_x} D_{f_x\delta_a} & K_{f_x} D_{f_x\delta_r} \\ 0 & 0 \\ 0 & 0 \end{bmatrix} \tag{C.5}$$

$$
A^{COUP} = \begin{bmatrix}
0 & 0 & 0 & 0 \\
0 & 0 & 0 & 0 \\
K_{f_y} C_{f_y v} & K_{f_y} C_{f_y \phi} & K_{f_y} C_{f_y p} & K_{f_y} C_{f_y r} \\
0 & 0 & 0 & 0 \\
K_p C_{\dot{p}v} + \theta_0 K_r C_{\dot{r}v} & K_p C_{\dot{p}\phi} + \theta_0 K_r C_{\dot{r}\phi} & K_p C_{\dot{p}p} + \theta_0 K_r C_{\dot{r}p} & K_p C_{\dot{p}r} + \theta_0 K_r C_{\dot{r}r} \\
0 & 0 & 0 & 0 \\
-\frac{K_{fy}}{g} C_{f_y v} & -\frac{K_{fy}}{g} C_{f_y \phi} & -\frac{K_{fy}}{g} C_{f_y p} & -\frac{K_{fy}}{g} C_{f_y r} \\
0 & 0 & 0 & 0 \\
-\frac{K_{fy} B_t}{g} C_{f_y v} + K_p C_{\dot{p}v} + \theta_0 K_r C_{\dot{r}v} & -\frac{K_{fy} B_t}{g} C_{f_y \phi} + K_p C_{\dot{p}\phi} + \theta_0 K_r C_{\dot{r}\phi} & -\frac{K_{fy} B_t}{g} C_{f_y p} + K_p C_{\dot{p}p} + \theta_0 K_r C_{\dot{r}p} & -\frac{K_{fy} B_t}{g} C_{f_y r} + K_p C_{\dot{p}r} + \theta_0 K_r C_{\dot{r}r} \\
0 & 0 & 0 & 0 \\
K_r C_{\dot{r}v} & K_r C_{\dot{r}\phi} & K_r C_{\dot{r}p} & K_r C_{\dot{r}r} \\
-\frac{K_{fy} B_t}{g} C_{f_y v} + K_p C_{\dot{p}v} & -\frac{K_{fy} B_t}{g} C_{f_y \phi} + K_p C_{\dot{p}\phi} & -\frac{K_{fy} B_t}{g} C_{f_y p} + K_p C_{\dot{p}p} & -\frac{K_{fy} B_t}{g} C_{f_y r} + K_p C_{\dot{p}r}
\end{bmatrix} \tag{C.6}
$$

D
Pilot Briefing

D.1. Purpose

Flight simulators exist already for more than a century and are popular as they achieve a high behavioural fidelity (meaning that the pilot behaves similar in both aircraft and flight simulator), which is effective for training. In modern pilot training, flight simulator training is a major part of the learning curriculum. Several qualifications are performed on these simulators to ensure this high quality training. The current state-of-the-art objective evaluation method has, however, its limitations. To tackle these, a novel objective evaluation method is currently being developed in the Control & Simulation group at the Faculty of Aerospace Engineering in TU Delft. This method specifically targets the cueing of Dutch Roll eigenmode dynamics. This experiment uses several configurations and uses subjective pilot feedback to determine the potential of this alternative method.

D.2. Apparatus

The TU Delft's SIMONA Research Simulator (SRS), which is located at the Faculty of Aerospace Engineering, is used for this experiment (Figure D.1a). Inside the simulator, a full outside visual (e.g. out the window imagery) is provided. In the cockpit, a basic instrument panel is displayed in front of the pilot, as depicted in Figure D.1b. The simulator motion system will be used to simulate the aircraft responses. Also, you will wear noise cancelling headphones which play engine noise sound, this to mask the false auditory cues coming from the hydraulic motion actuators. The aircraft configuration used is the Cessna Citation 500 aircraft in cruise. The control column and rudder paddles can be used to control the aircraft.

(a) SIMONA Research Simulator

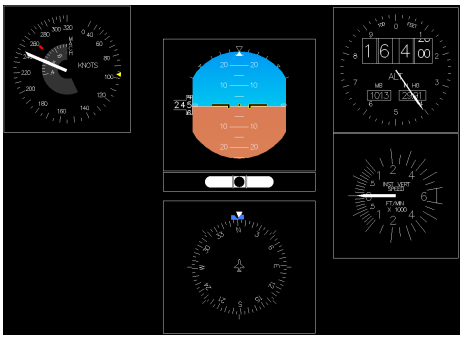

(b) Primary Flight Display

Figure D.1: Flight Simulator

D.3. Experiment Task

In the experiment taking place, you will perform a series of pair-wise comparisons (Table D.1) between a total of three configurations of the Classical Washout Algorithm (CWA)

in the SRS. Your goal during the experiment is to compare pairs of different CWA configurations and select a *winner* for each pair. The winner would be the configuration that resembles the real flight most realistically. Besides this you are asked to give a confidence level ranging from 0 to 2, where: 0 is *no confidence*, 1 is *normal confidence* and 2 is *high confidence*. Please note that when a confidence level of 0 is given, the pair-wise comparison is not taken into account, as no difference could be identified. Throughout the run the Dutch Roll eigenmode will be externally excited using a gust of random amplitude. Each run last for 2 minutes and consists of a passive and active part. The passive part last for 70 seconds, in which you just sit in the aircraft and do not respond to the external excitation of the Dutch Roll. The aim of this passive part is to get sufficiently acquainted with the lateral motion signature. The researcher then indicates when the passive part switches to the active part. During the active part, you aim to suppress the Dutch Roll eigenmode at the moment that the aircraft is excited. Furthermore, you try to minimize the altitude and heading deviations. This active part lasts for 60 seconds after which the run is stopped by the researcher. The aircraft is fully controllable, however, only the lateral motions will be felt. Also, the yaw damper will be disabled, to allow for a better determination of the lateral motion signature. During the experiment you must stick to the following experiment boundaries:

- No full deflections of the control column and rudder are allowed.
- The airspeed deviation must be minimized.
- No throttle changes.

Table D.1: Experiment Test Pairs

	Pair 1	Pair 2	Pair 3	Run	Pair 4	Pair 5	Pair 6	Run
Training	A - B	A - B	A - B	No motion	A - B	A - B	A - B	No motion

Please note, Table D.1 only indicates 2 configurations, e.g. A and B. The real experiment has more than two configurations in which the order will be randomized.

Besides the 6 pairs that will be evaluated in the pair-wise comparison, to additional runs will be performed. The aircraft configuration for these runs is exactly the same, but, the motion platform will be turned off. In these runs, there is only an active part, which lasts for 130 seconds instead of 60. One of the runs is after the third pair and one after the sixth pair (Table D.1). Furthermore, no preferred configuration has to be stated, as this is a single run.

D.4. Experiment Procedure

After meeting at the coffee area in the SIMONA building this briefing will be discussed. Any questions you have will be answered by the researcher. Also, you will be asked to sign a consent form. Before the experiment starts you will be given a safety briefing.

The complete experiment is conducted in one day, and will take approximately one and a half hour. During the experiment, you will receive approximately 20 minutes of training, during which you will fly all individual configurations twice in randomized order. Each training run will last two minutes. Once the training is completed the evaluation phase will start in which you will compare the different CWA configurations.

D.5. Experiment Execution

For each evaluated pair, the subsequent procedure will be followed:

1. The researcher applies the settings of the first configuration (A) of the evaluated pair.
2. The researcher checks whether the participant is ready to proceed and initiates the run after a countdown from 3 (3-2-1-go).
3. The participant gets acquainted with the motion signature and does not control the aircraft for 70 seconds (passive part).
4. The researcher informs the pilot that the active part starts.
5. The participant flies the aircraft for 60 seconds and tries to suppress the Dutch Roll eigenmode (active part).
6. The researcher applies the settings of the second configuration (B) of the evaluated pair.
7. The researcher checks whether the participant is ready to proceed and initiates the run after a countdown from 3.
8. The participant gets acquainted with the motion signature and does not control the aircraft for 70 seconds (passive part).
9. The researcher informs the pilot that the active part starts.
10. The participant flies the aircraft for 60 seconds and tries to suppress the Dutch Roll eigenmode (active part).
11. The participant indicate the preferred configuration, together with a confidence level (0 - 1 - 2).

D.6. Contact Information

Contact Information Researcher	**Contact Information Research Supervisor**
Guido Tillema	Ir. O. Stroosma
G.H.J.Tillema@student.tudelft.nl	O.Stroosma@tudelft.nl

This page is intentionally left blank.

E
Verification and Validation

E.1. Verification

The derivation of the complete EMD model is quite extensive and therefore prone to errors. To ensure a correct derivation, a verification environment is built. In Figure E.1 the Simulink verification environment is depicted. In here the outputs of **1** are from the nonlinear MCA, which is also illustrated in Figure E.2. During the EMD derivation this nonlinear MCA is linearized, in the verification environment this linearized MCA is represented with **2**. To check whether this linearization is performed correctly, the outputs of **1** and **2** must be identical. Another essential step in the derivation of the complete EMD system is the coupling between EOM and MCA. To verify that this system coupling is derived correctly, the responses of **2** and **3** must be identical.

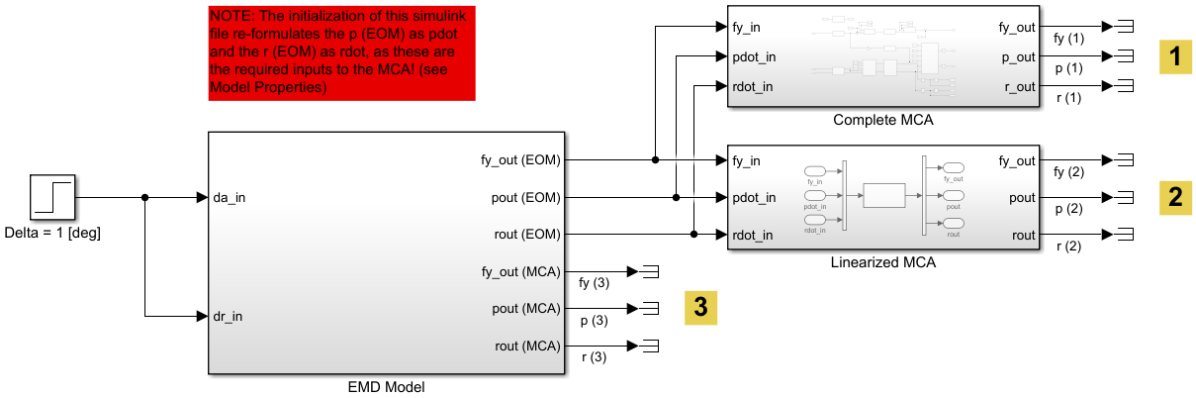

Figure E.1: Verification Environment in Simulink

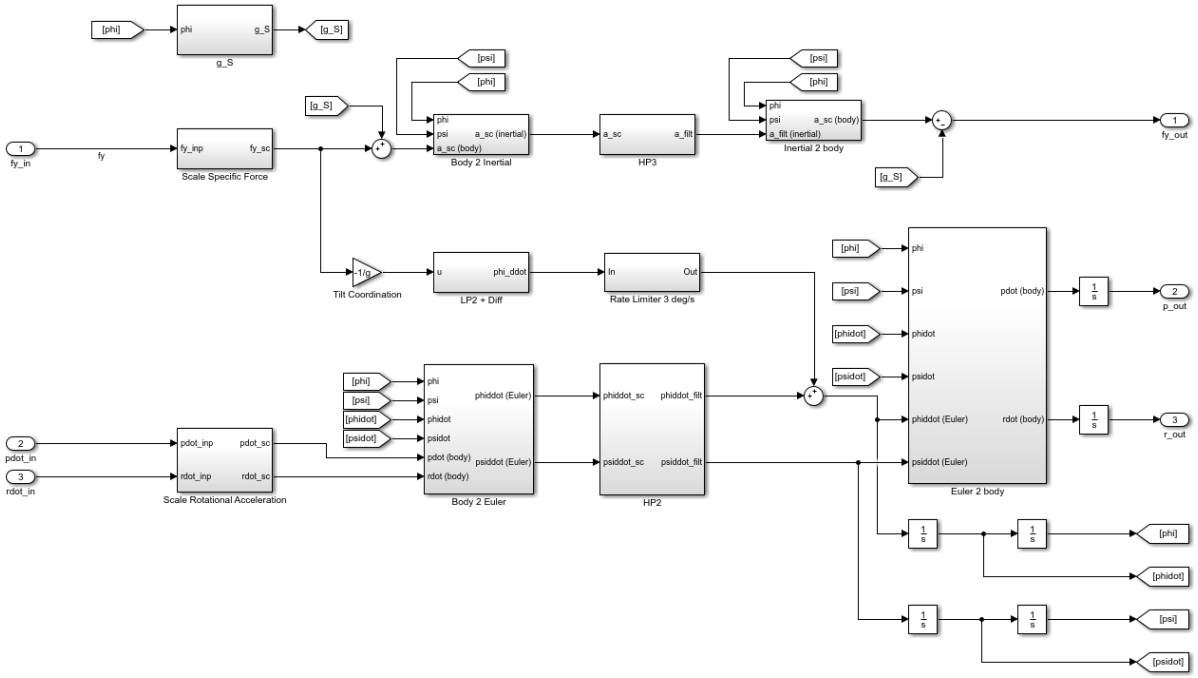

Figure E.2: Non-linear Simulink Model of the Classical Washout Algorithm
(sub-system 1 of Figure E.1)

Figure E.3 depicts the response to an aileron and rudder step input of 1 degree. As is clearly evident the response of **1**, **2** and **3** are identical. From here it can be verified that the derivation and implementation of the EMD system is performed correctly.

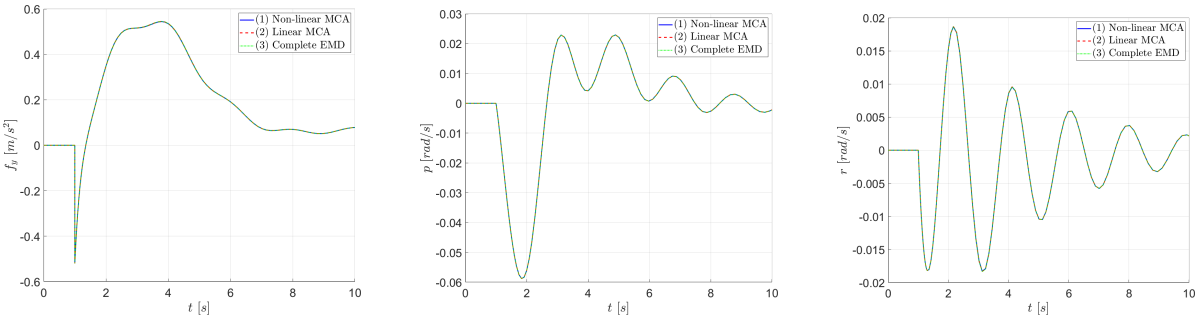

Figure E.3: Verification of the Motion Cues

E.2. Validation

In order to validate that the right model of the Cessna Citation 500 is implemented, a simulation is performed. In this simulation the response of the complete Cessna Citation 500 is compared to the response of the linear (simplified) model.

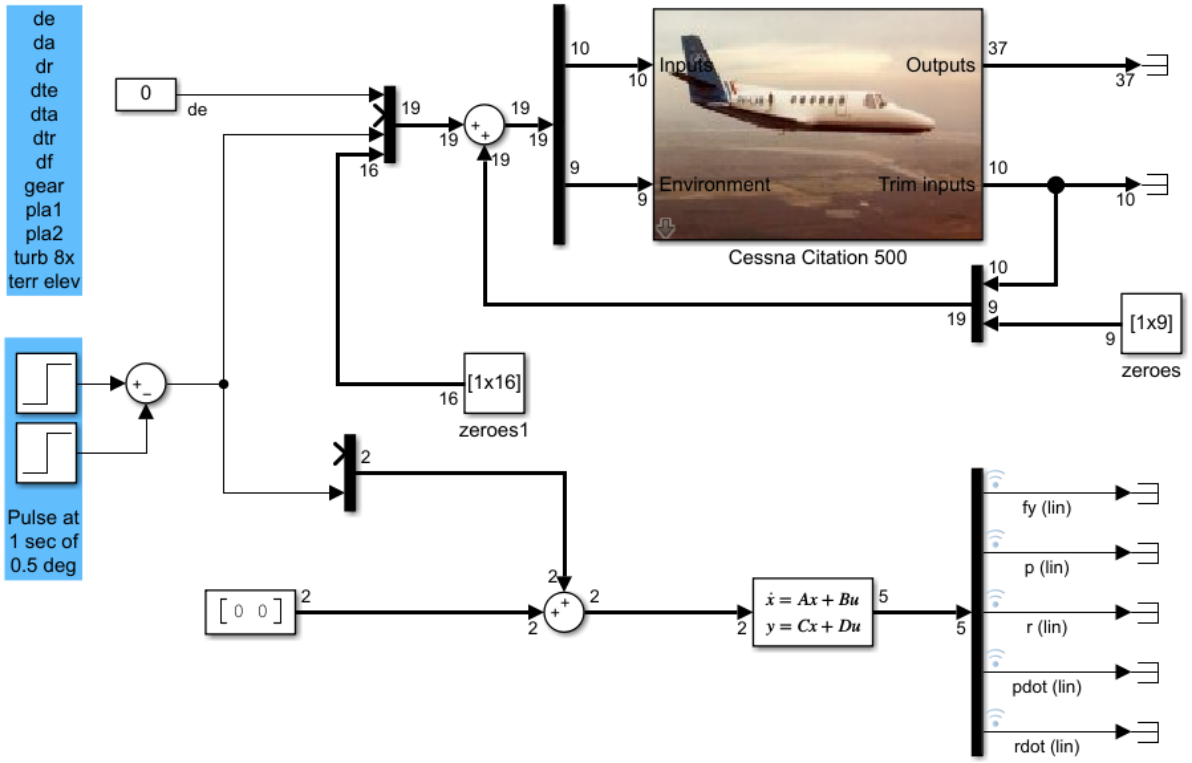

Figure E.4: Validation Model of Cessna Citation 500

Figure E.5 depicts the response to an rudder pulse input of 0.5 degrees. As depicted in this figure, the responses of the different motion cues of the linear EOM resemble the complete EOM to a high degree. Therefore, it is concluded that the correct model of the Cessna Citation 500 is implemented.

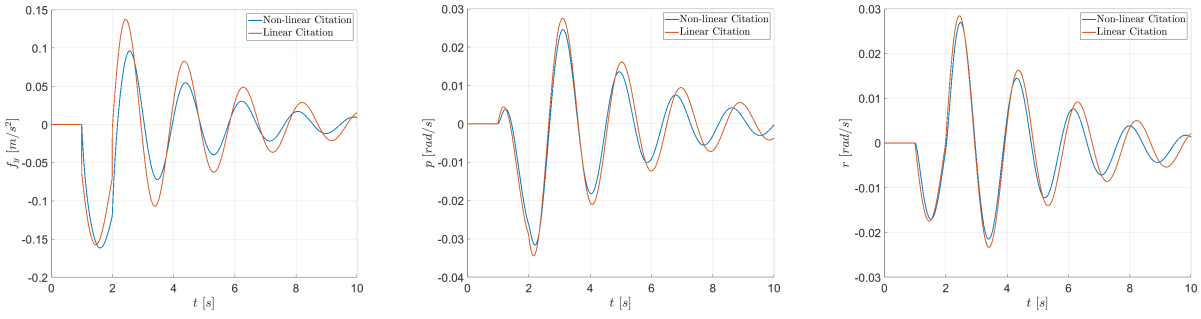

Figure E.5: Validation of the Motion Cues

This page is intentionally left blank.

F

Individual Pilot Results

This appendix contains an analysis for each pilot individually. This appendix is divided into 7 sections, each corresponding to a single pilot. Each section starts with a subjective evaluation, in here the pilot preferred configuration is indicated together with corresponding confidence level. Furthermore, the pilot comments are included. Hereafter, a general evaluation is given, in which pilot feedback towards the complete experiment is stated. Also, general observations are stated here. Finally, an objective evaluation which shows the objective performance for each run visually. Also, the means per configuration are calculated and a One-Way ANOVA is performed. Here, the winning configuration is marked in bold, also, the significance is marked if found significant.

F.1. Pilot 1

F.1.1. Subjective Evaluation

Table F.1: Pilot 1 - Subjective Rating

Pair	Confidence	Pilot Comment
MCA: O - **MCA: P**	1	There was barely a difference between the two motion configurations, however the second configuration felt slightly more intense and realistic.
MCA: O - MCA: B	0	The two configurations did not feel different.
MCA: P - **MCA: B**	1	The two configurations felt quite similar, however with the second configuration the Dutch Roll was easier to suppress and therefore this configuration is preferred.
No Motion (1)	N.A.	The visual system is very strong, making it feel that actual motion is perceived even if there isn't.
MCA: B - MCA: P	1	The seat is getting to feel a little hard. There are only slight differences between the two configurations. The first configuration felt slightly more intense and realistic.
MCA: B - MCA: O	0	Tried to focus on different things, listen to actuator noise, instrument response and magnitude of motions but no difference could be identified.
MCA: P- MCA: O	1	Both configurations quite similar, however, the first configuration had more roll motion cues which felt more realistic.
No Motion (2)	N.A.	-

F.1.2. General Evaluation

- It is very difficult to make a decision as you don't know on what exactly you have to focus, e.g. you don't know what the exact differences are between the different configurations.
- Sometimes the evaluation was based on the perceived noise coming from the actuators.
- The Dutch Roll was only suppressed with a rudder input. The ailerons were not used for this purpose.
- The length of the experiment was fine. The way of evaluating in pairs was experienced as pleasant.

F.1.3. Objective Evaluation

Table F.2: Pilot 1 - Mean Performance per Configuration

MCA	Mean	N	Std. Deviation
No Motion	.2665	24	.2240
MCA: B	.3354	24	.3244
MCA: O	.3111	24	.2865
MCA: P	.3766	24	.2001
Total	.3224	96	.2623

Table F.3: Pilot 1 - Multiple Comparison (Tukey HSD)

(I) MCA	(J) MCA	Mean Difference (I-J)	Std. Error	Sig.	95% Confidence Interval	
					Lower Bound	Upper Bound
No Motion	MCA: O	-.0445	.0760	.9362	-.2435	.1544
	MCA: P	-.1101	.0760	.4731	-.3091	.0889
	MCA: B	-.0688	.0760	.8022	-.2678	.1301
MCA: B	No Motion	.0688	.0760	.8022	-.1301	.2678
	MCA: O	.0243	.0760	.9886	-.1747	.2233
	MCA: P	-.0413	.0760	.9482	-.2402	.1577
MCA: O	No Motion	.0445	.0760	.9362	-.1544	.2435
	MCA: P	-.0656	.0760	.8242	-.2645	.1334
	MCA: B	-.0243	.0760	.9886	-.2233	.1747
MCA: P	No Motion	.1101	.0760	.4731	-.0889	.3091
	MCA: O	.0656	.0760	.8242	-.1334	.2645
	MCA: B	.0413	.0760	.9482	-.1577	.2402

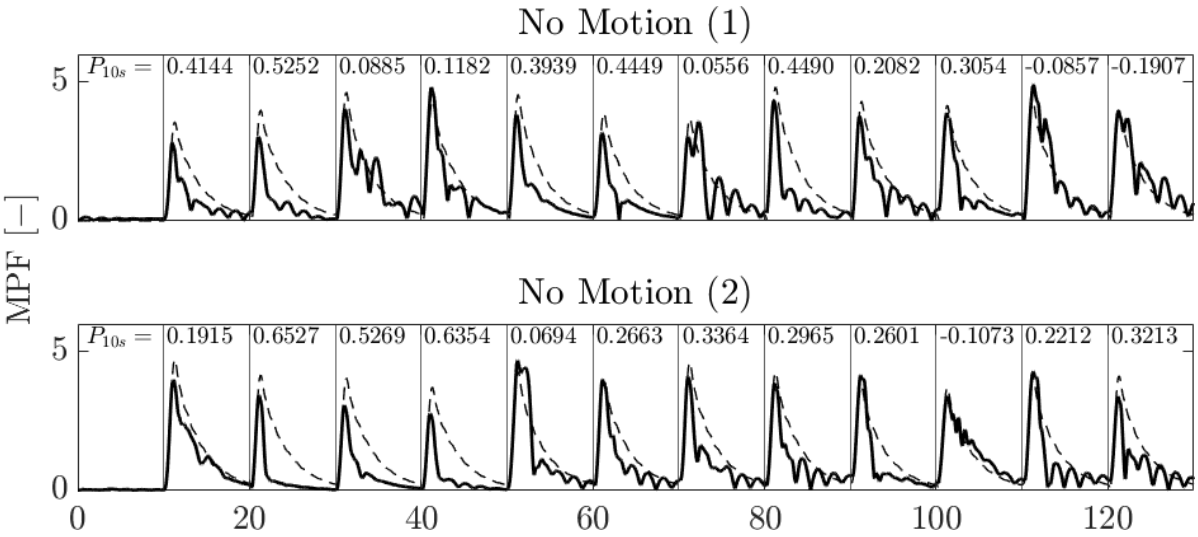

Figure F.1: Pilot 1 - No Motion

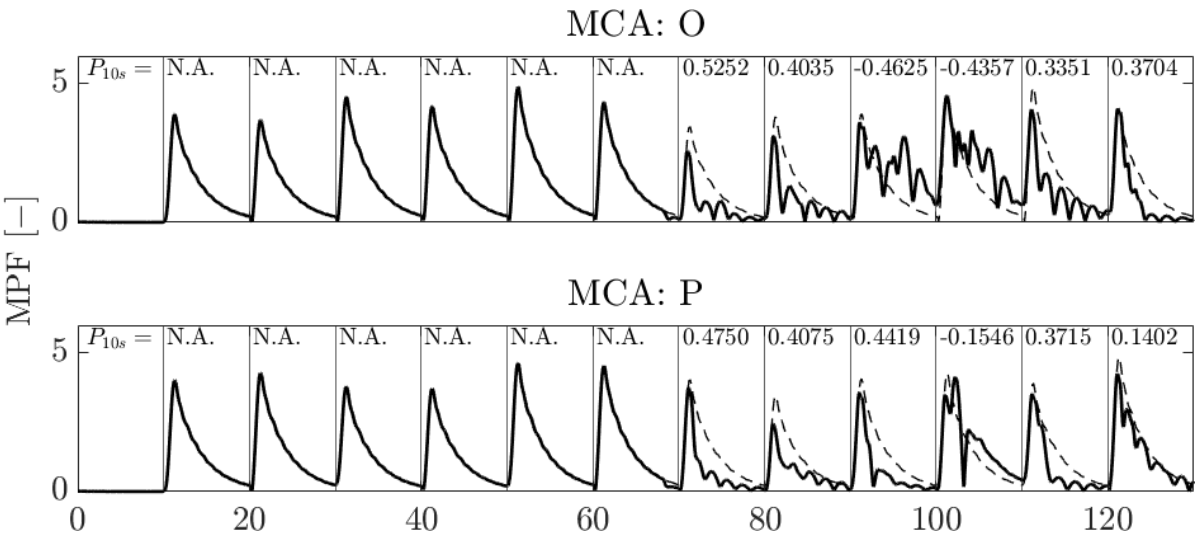

Figure F.2: Pilot 1 - Pair 1

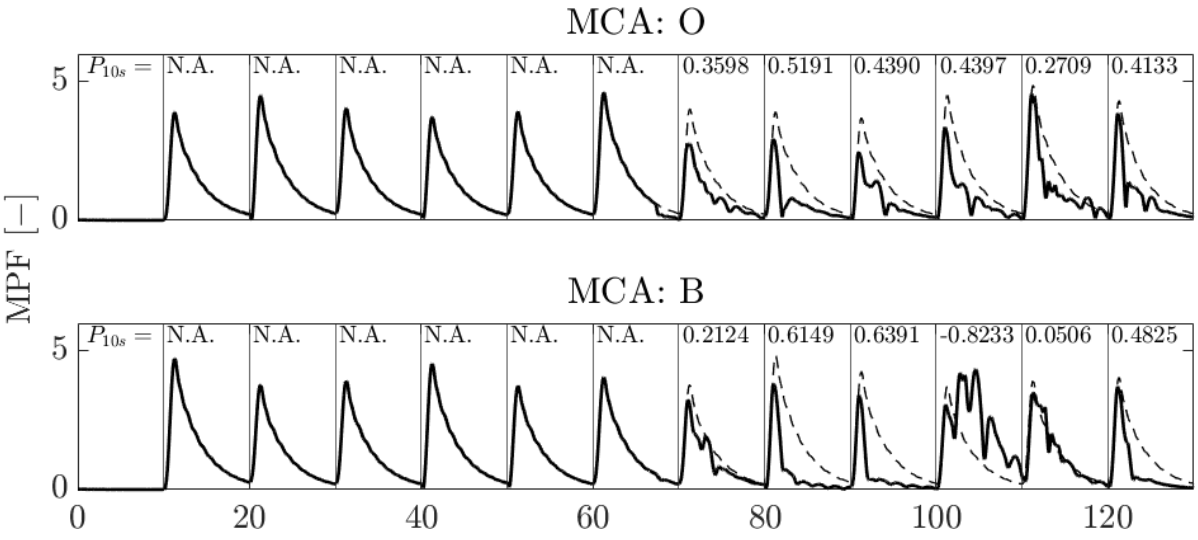

Figure F.3: Pilot 1 - Pair 2

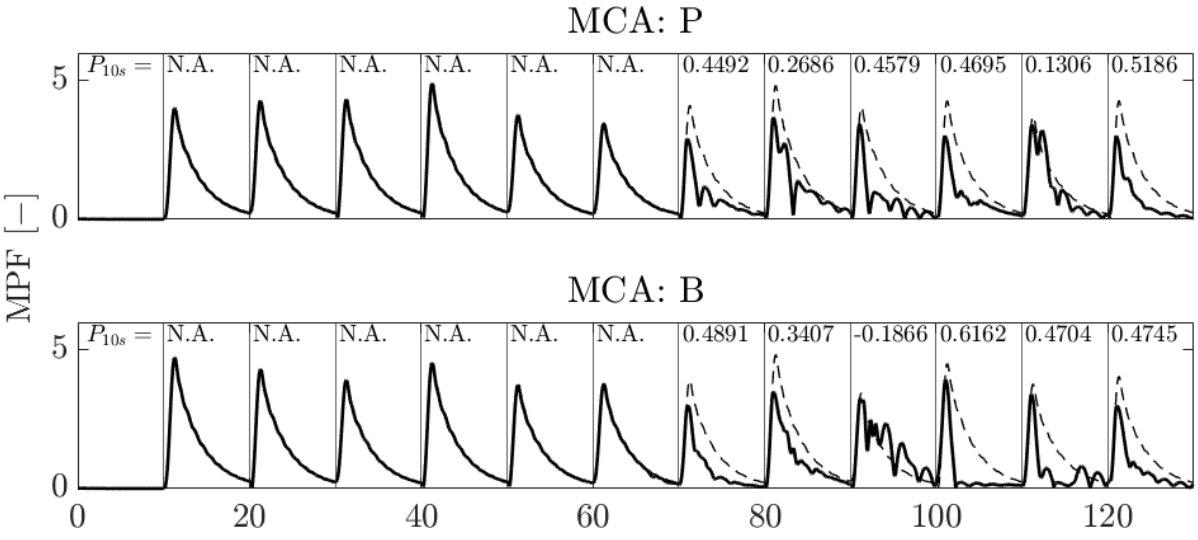

Figure F.4: Pilot 1 - Pair 3

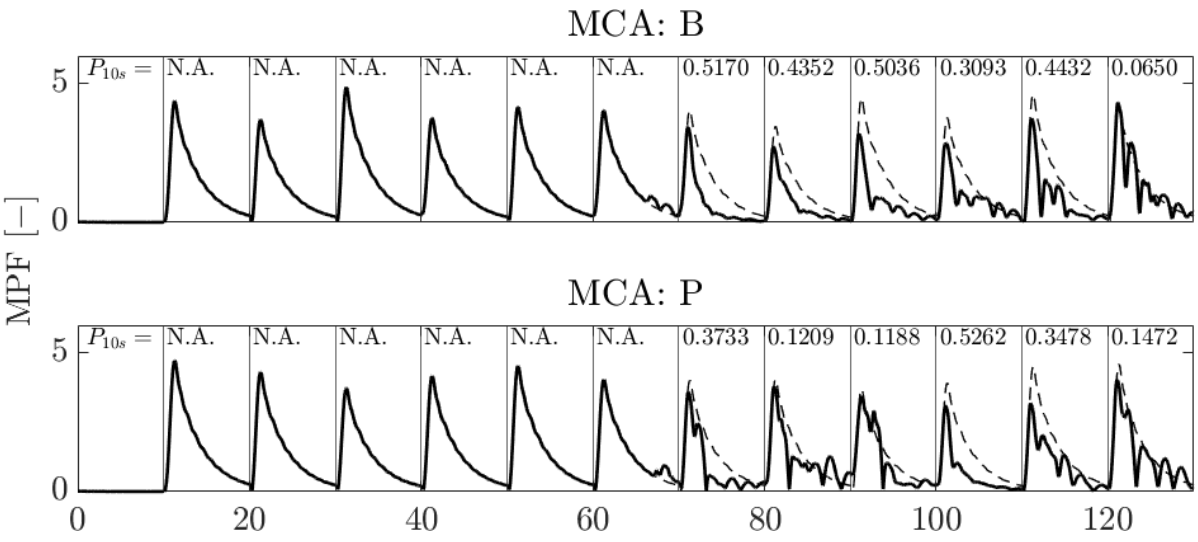

Figure F.5: Pilot 1 - Pair 4

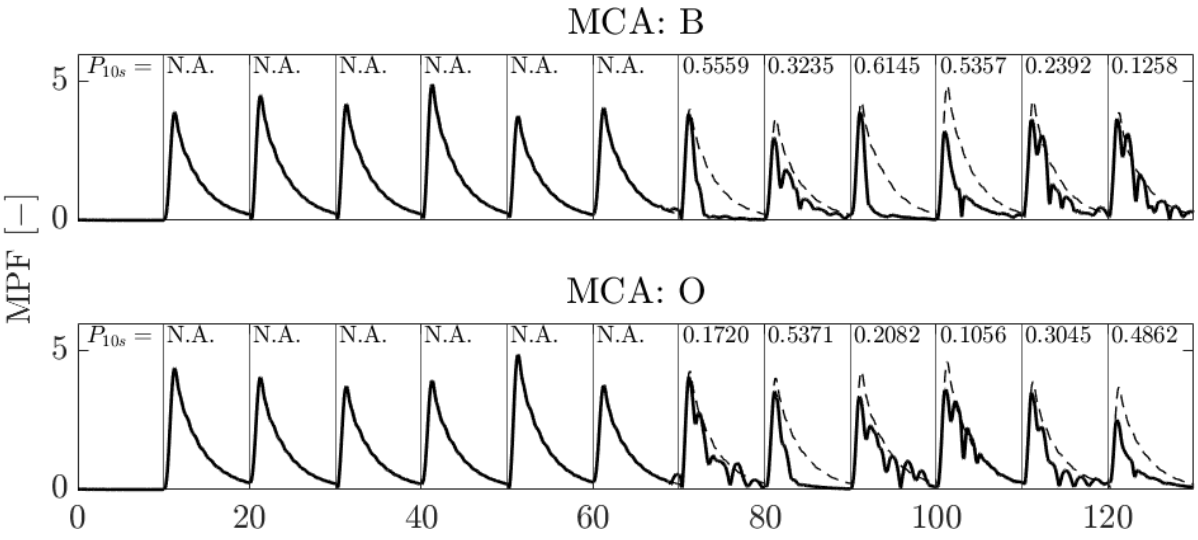

Figure F.6: Pilot 1 - Pair 5

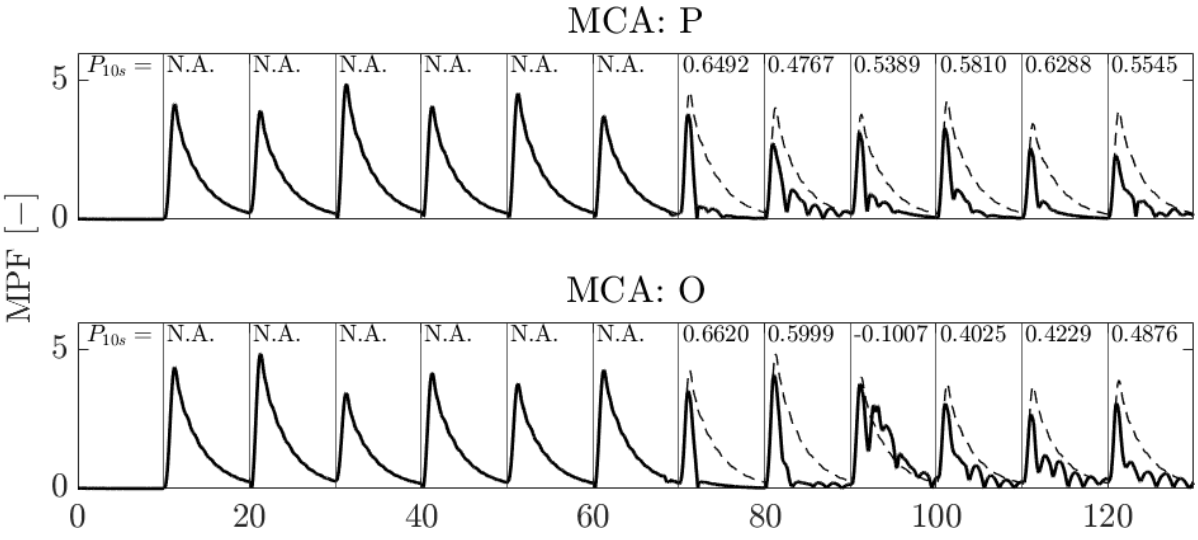

Figure F.7: Pilot 1 - Pair 6

F.2. Pilot 2

F.2.1. Subjective Evaluation

Table F.4: Pilot 2 - Subjective Rating

Pair	Confidence	Pilot Comment
MCA: P - **MCA: B**	1	There was not a lot of difference between the two motion configurations. The first configuration felt a little bit too intense. The second configuration was slightly more pleasant.
MCA: O - MCA: P	2	The second configuration felt too intense.
MCA: O - **MCA: B**	1	There was not a lot of difference between the two configurations, however, the second configuration felt a bit softer which was more pleasant.
No Motion (1)	N.A.	Focused on horizon during the run, as the visual is very strong it felt as if there was actual motion. This configuration can easily result in motion sickness.
MCA: B - **MCA: O**	1	There was not a lot of difference between the configurations. Felt that there was a larger effect to control errors in the second configuration.
MCA: P - **MCA: O**	2	The first configuration felt slightly too intense. The second configuration felt softer, also pulling the control column was easier.
MCA: B - MCA: P	1	When overcompensating the second configuration felt too intense, therefore the first configuration was chosen.
No Motion (2)	N.A.	Felt that with motion the performance was way better, because of the motion cue onsets.

F.2.2. General Evaluation

- The slip indicator felt under-damped.
- The controls were very sensitive and little control force was required, which easily resulted in over-correction.
- The breakout for the rudder was too large.
- The visual system was very strong making it feel that there are longitudinal motion cues even when the selective-gains were zero.
- The flight model felt correct.
- The are no remarks on the way of evaluating the motion pairs.

F.2.3. Objective Evaluation

Table F.5: Pilot 2 - Mean Performance per Configuration

MCA	Mean	N	Std. Deviation
No Motion	-.2519	24	.1889
MCA: B	.0453	24	.2641
MCA: O	.0142	24	.2335
MCA: P	.0114	24	.2921
Total	-.0452	96	.2720

Table F.6: Pilot 2 - Multiple Comparison (Tukey HSD)

(I) MCA	(J) MCA	Mean Difference (I-J)	Std. Error	Sig.	95% Confidence Interval	
					Lower Bound	Upper Bound
No Motion	MCA: O	-.2662	.0715	**.0019**	-.4532	-.0791
	MCA: P	-.2633	.0715	**.0022**	-.4504	-.0763
	MCA: B	-.2972	.0715	**.0004**	-.4843	-.1102
MCA: B	No Motion	.2972	.0715	**.0004**	.1102	.4843
	MCA: O	.0311	.0715	.9723	-.1560	.2182
	MCA: P	.0339	.0715	.9645	-.1531	.2210
MCA: O	No Motion	.2662	.0715	**.0019**	.0791	.4532
	MCA: P	.0028	.0715	1.0000	-.1842	.1899
	MCA: B	-.0311	.0715	.9723	-.2182	.1560
MCA: P	No Motion	.2633	.0715	**.0022**	.0763	.4504
	MCA: O	-.0028	.0715	1.0000	-.1899	.1842
	MCA: B	-.0339	.0715	.9645	-.2210	.1531

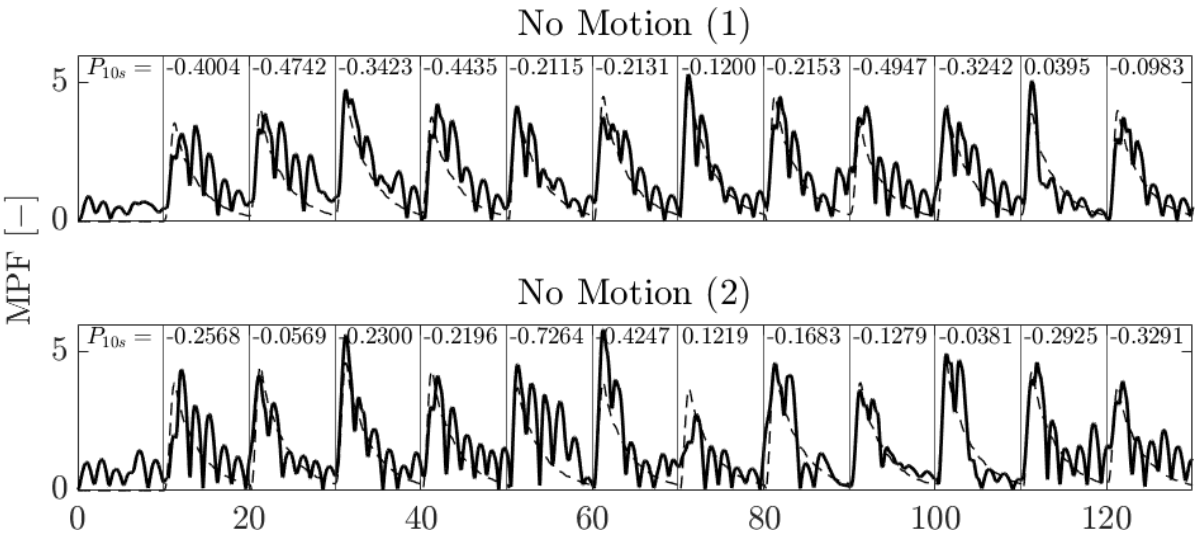

Figure F.8: Pilot 2 - No Motion

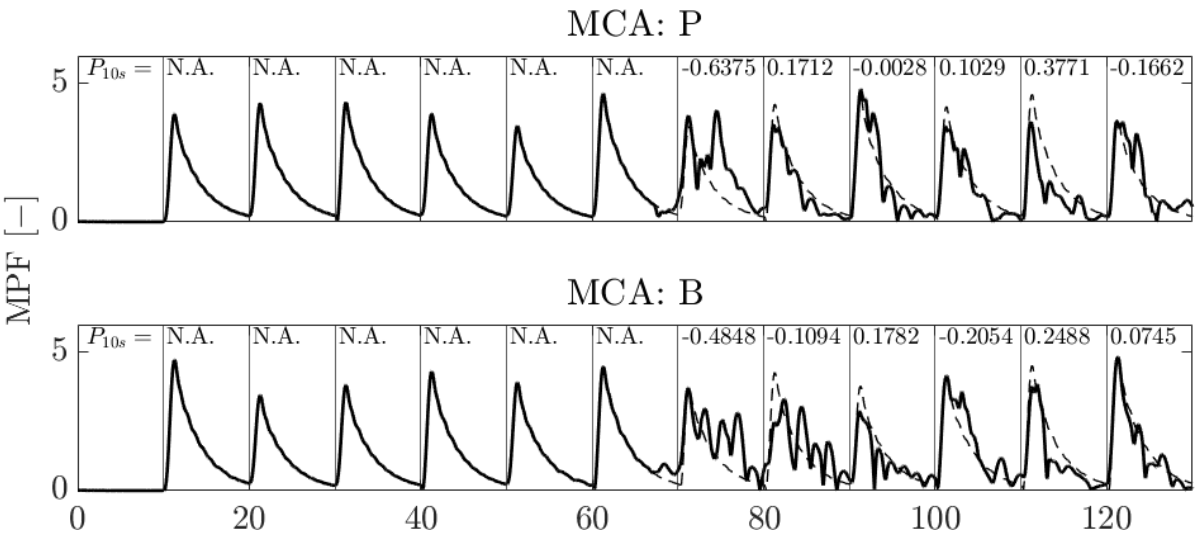

Figure F.9: Pilot 2 - Pair 1

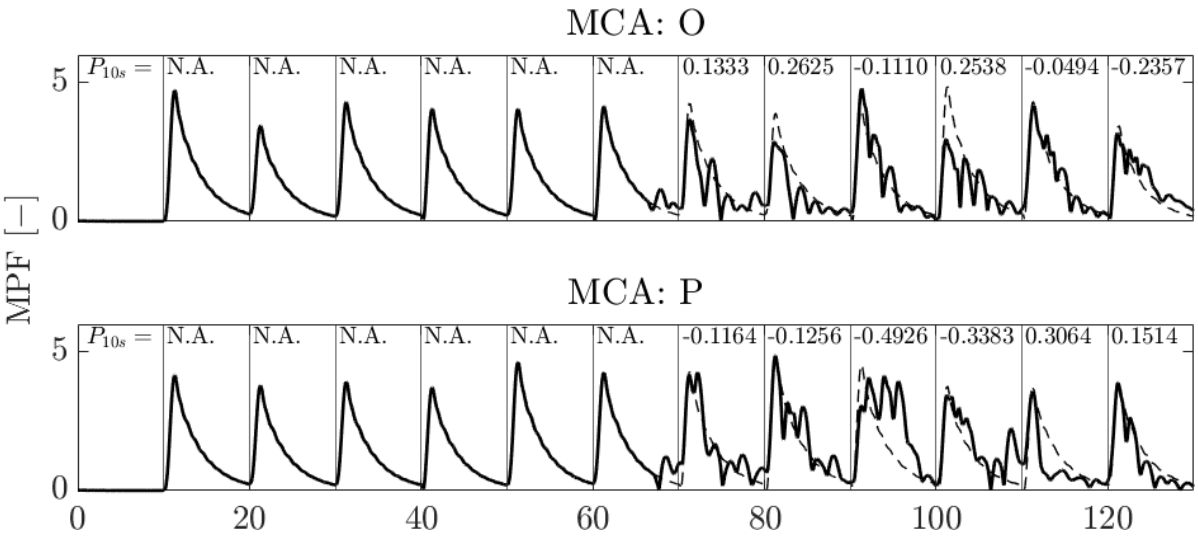

Figure F.10: Pilot 2 - Pair 2

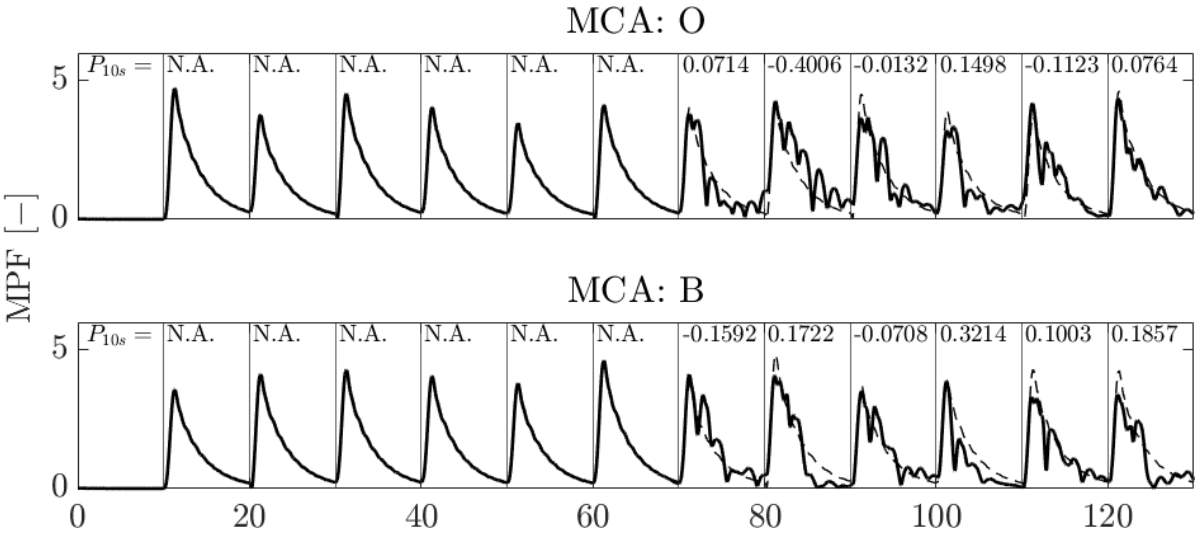

Figure F.11: Pilot 2 - Pair 3

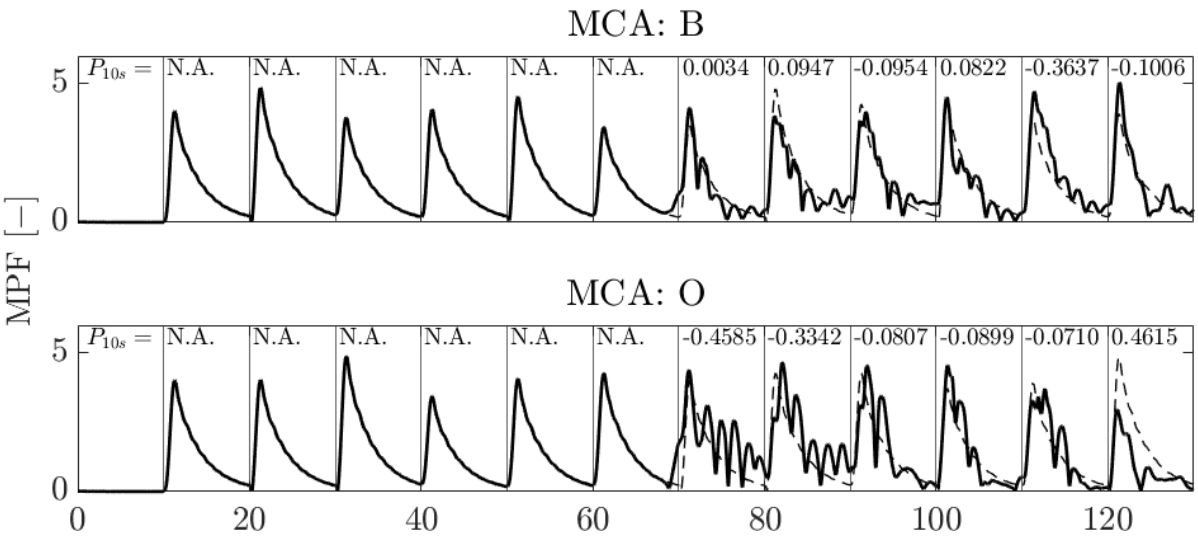

Figure F.12: Pilot 2 - Pair 4

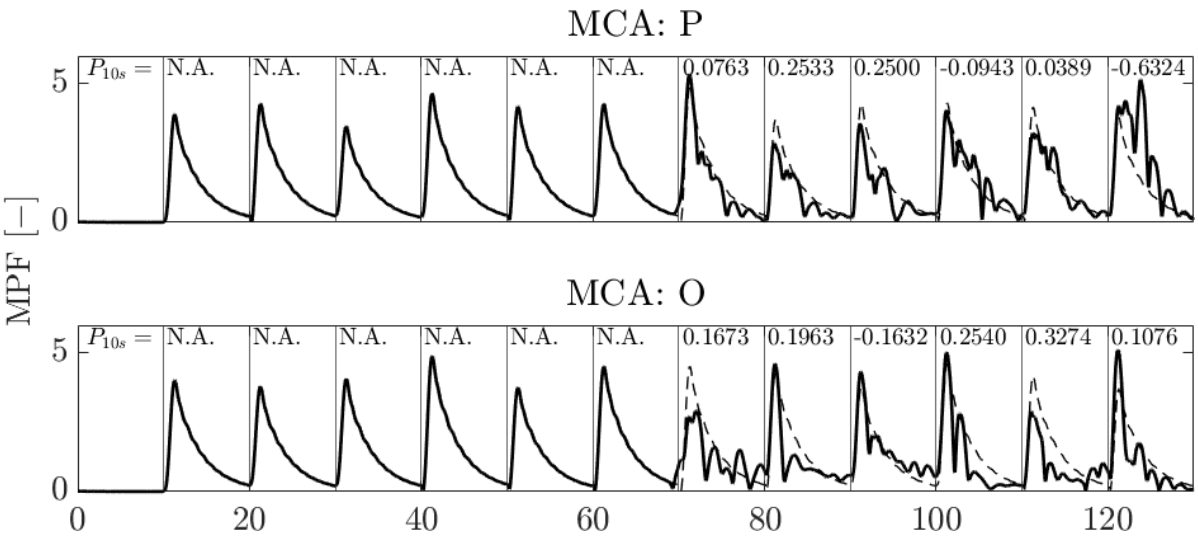

Figure F.13: Pilot 2 - Pair 5

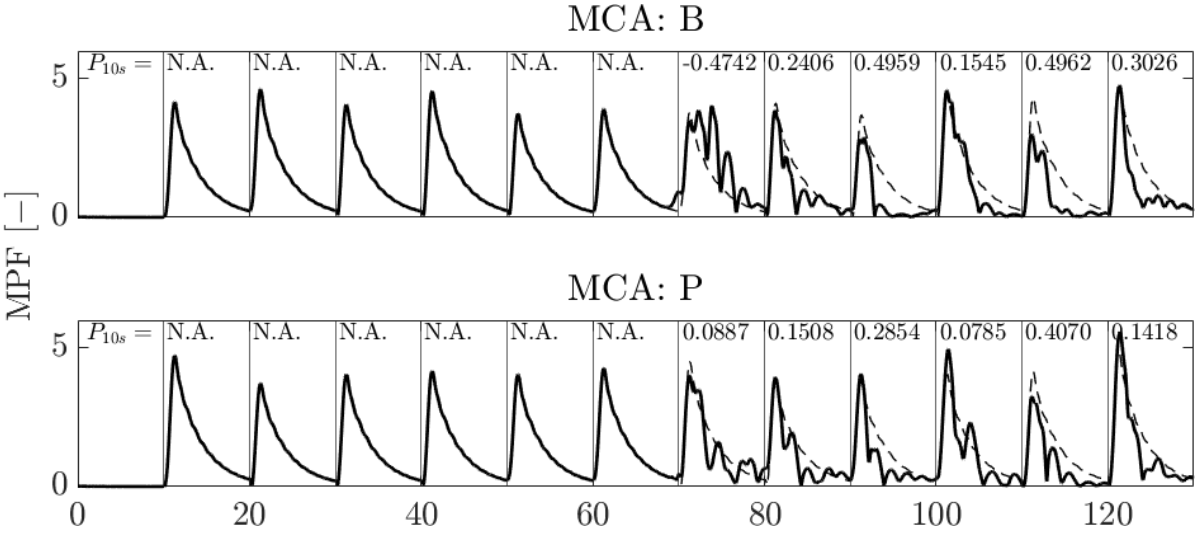

Figure F.14: Pilot 2 - Pair 6

F.3. Pilot 3a (replaced)

F.3.1. Subjective Evaluation

Table F.7: Pilot 3a - Subjective Rating

Pair	Confidence	Pilot Comment
MCA: O - **MCA: B**	2	The slip indicator is difficult to use as guidance. Initial onset is correct but then start to move under-damped.
MCA: P - MCA: B	2	-
MCA: O - MCA: P	0	Felt there was better control in the second configuration. However, no difference in the perceived motion.
No Motion (1)	N.A.	-
MCA: P - **MCA: O**	2	-
MCA: B - MCA: P	2	-
MCA: B - MCA: O	2	Getting the timing right to suppress the Dutch Roll is difficult as the ball is not always moving in the correct direction.
No Motion (2)	N.A.	The run without motion felt very doable.

F.3.2. General Evaluation

- The slip-indicator is not correct, therefore it is very difficult to control the lateral motion of the aircraft and a PIO easily occurs.
- No difference between the Dutch Roll period was experienced between the different configurations.
- The slip-indicator is usually the easiest indicator for lateral motion cues. Alternatively, the sky pointer could be used, however, this one was not very accurate.
- The outside visual felt too slow.

F.3.3. Objective Evaluation

Table F.8: Pilot 3a - Mean Performance per Configuration

MCA	Mean	N	Std. Deviation
No Motion	-.0243	24	.1452
MCA: B	-.1185	24	.2745
MCA: O	-.2386	24	.5209
MCA: P	-.1807	24	.2950
Total	-.1405	96	.3413

Table F.9: Pilot 3a - Multiple Comparison (Tukey HSD)

(I) MCA	(J) MCA	Mean Difference (I-J)	Std. Error	Sig.	95% Confidence Interval	
					Lower Bound	Upper Bound
No Motion	MCA: O	.2143	.0973	.1306	-.0404	.4690
	MCA: P	.1564	.0973	.3798	-.0983	.4111
	MCA: B	.0942	.0973	.7681	-.1605	.3489
MCA: B	No Motion	-.0942	.0973	.7681	-.3489	.1605
	MCA: O	.1201	.0973	.6073	-.1346	.3748
	MCA: P	.0622	.0973	.9190	-.1925	.3169
MCA: O	No Motion	-.2143	.0973	.1306	-.4690	.0404
	MCA: P	-.0578	.0973	.9336	-.3126	.1969
	MCA: B	-.1201	.0973	.6073	-.3748	.1346
MCA: P	No Motion	-.1564	.0973	.3798	-.4111	.0983
	MCA: O	.0578	.0973	.9336	-.1969	.3126
	MCA: B	-.0622	.0973	.9190	-.3169	.1925

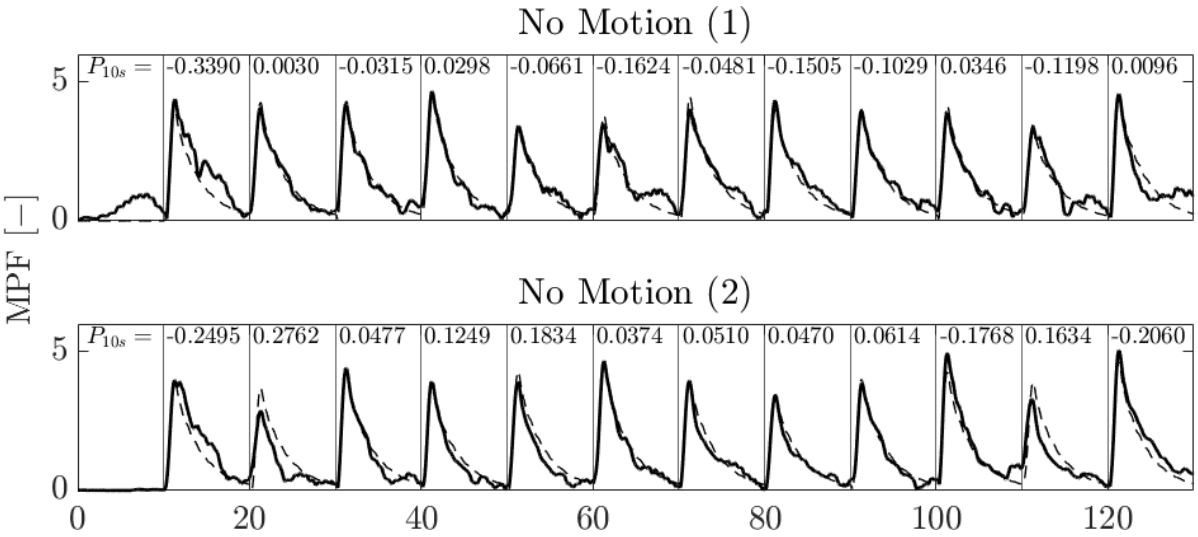

Figure F.15: Pilot 3a - No Motion

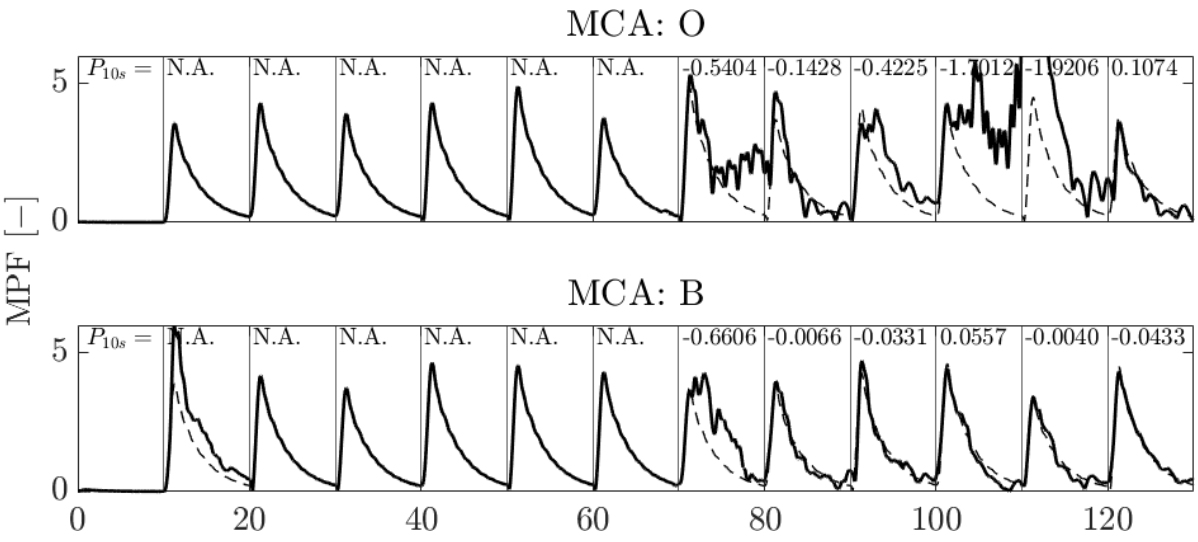

Figure F.16: Pilot 3a - Pair 1

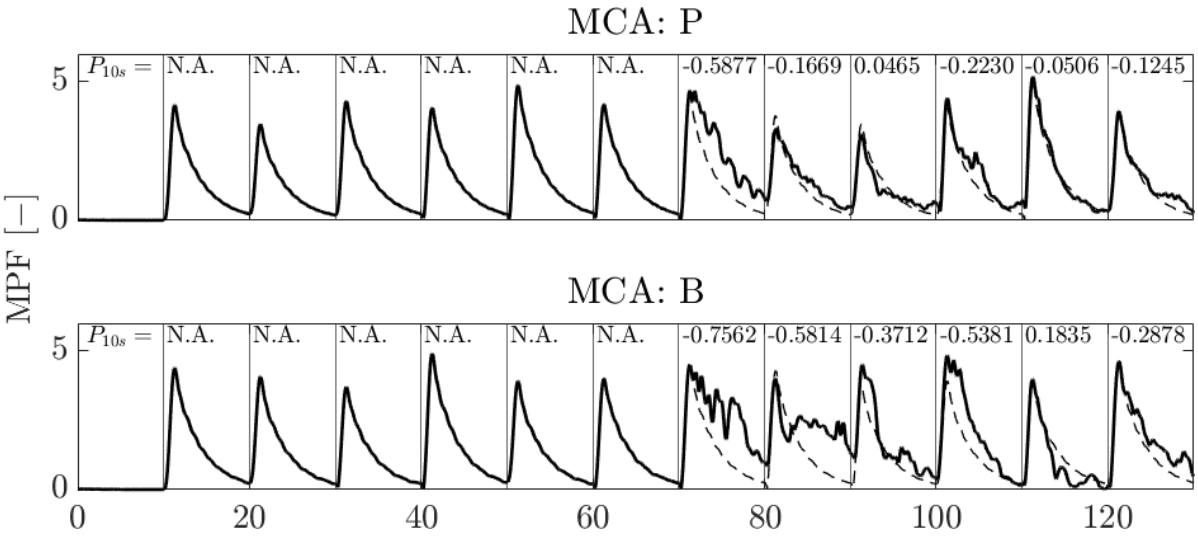

Figure F.17: Pilot 3a - Pair 2

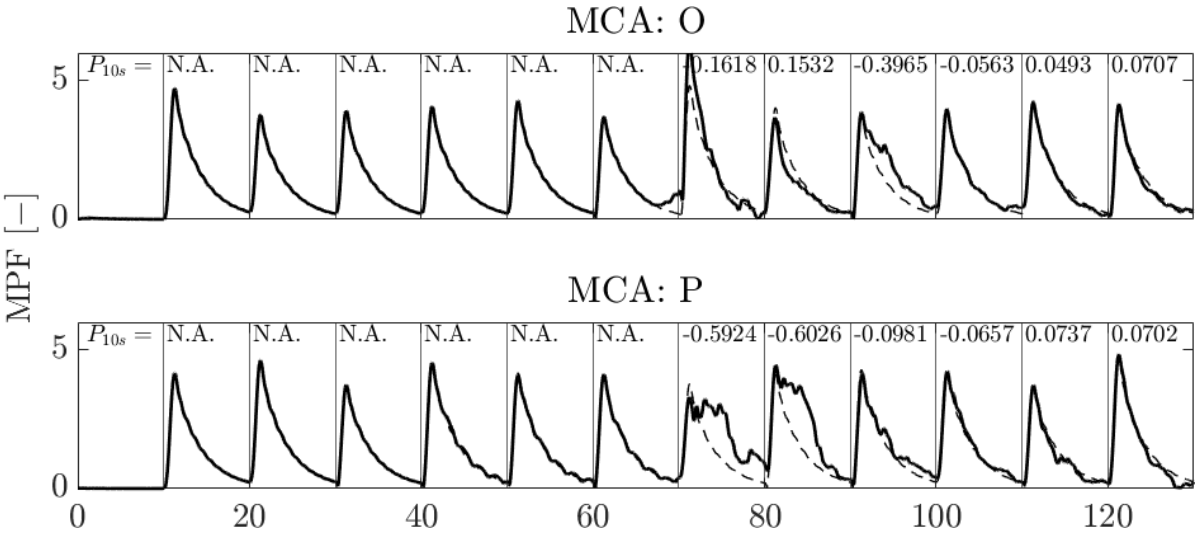

Figure F.18: Pilot 3a - Pair 3

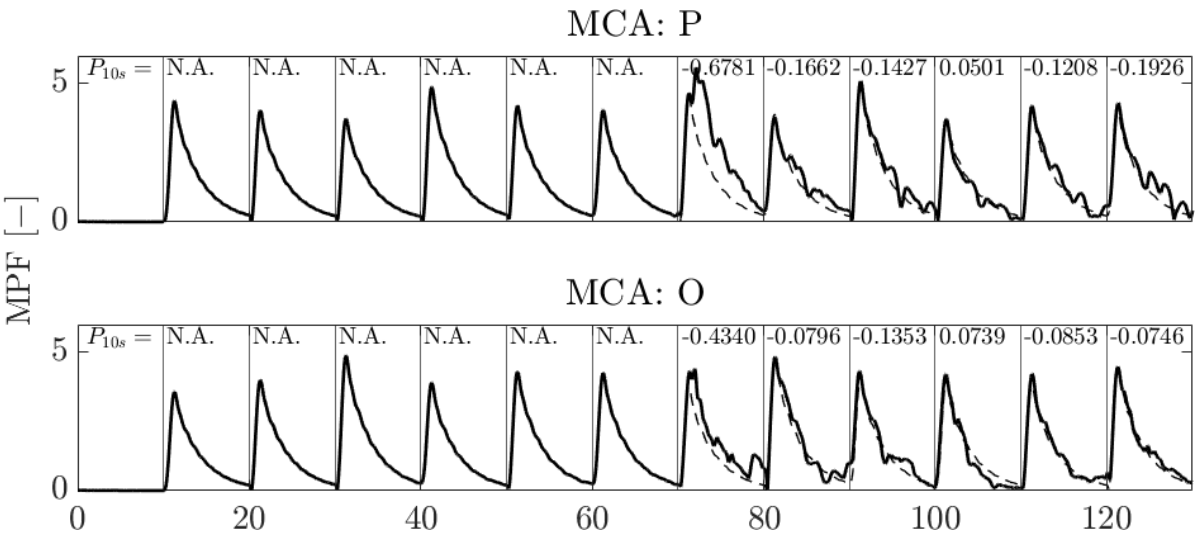

Figure F.19: Pilot 3a - Pair 4

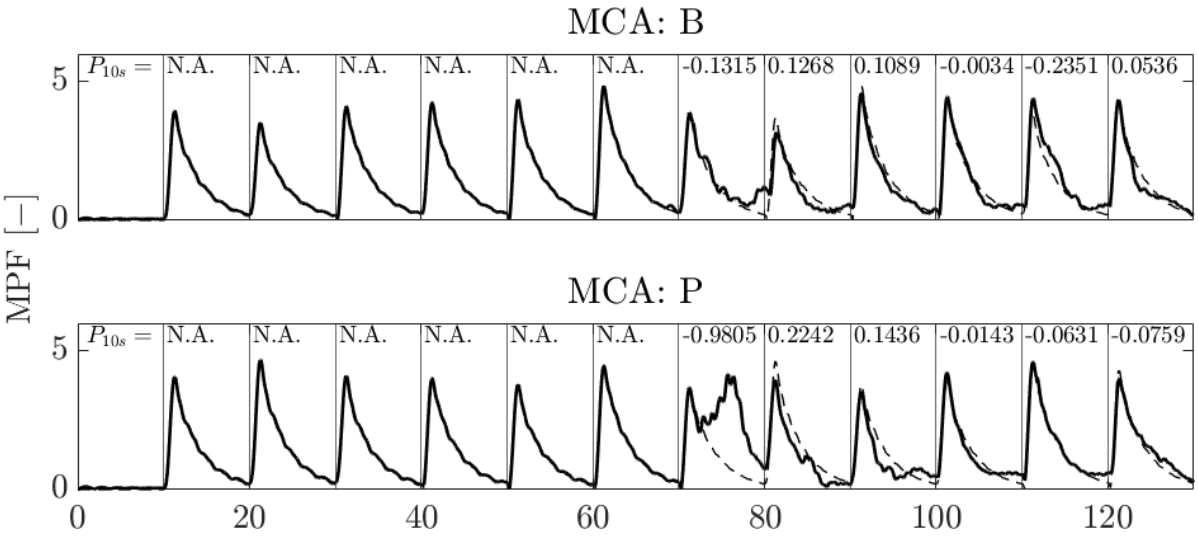

Figure F.20: Pilot 3a - Pair 5

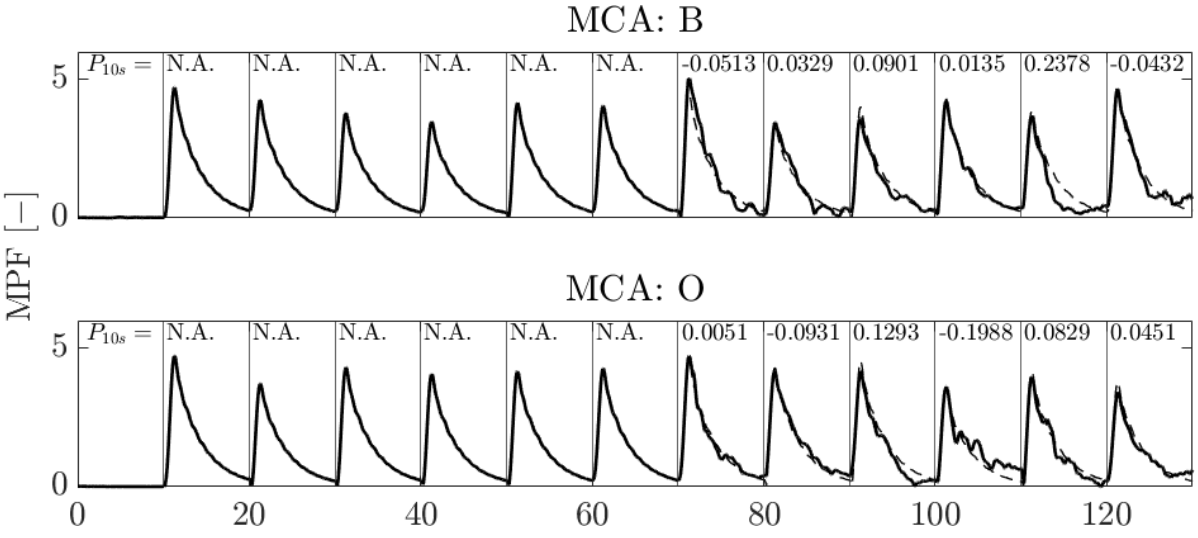

Figure F.21: Pilot 3a - Pair 6

F.4. Pilot 3

F.4.1. Subjective Evaluation

Table F.10: Pilot 3 - Subjective Rating

Pair	Confidence	Pilot Comment
MCA: O - **MCA: B**	2	The second configuration had more motion and was more pleasant to control.
MCA: P - MCA: B	1	The two configurations were extremely similar, however, the first configuration felt slightly more realistic.
MCA: O - **MCA: P**	2	In the first configuration the yaw was dominant, but there was only little sway. The second configuration was easier to control.
No Motion (1)	N.A.	Without motion cues, suppressing the Dutch Roll is tough. Also, it feels a bit unnatural.
MCA: P - MCA: O	0	The two configurations were extremely similar, the second had just slightly less sway. No difference was identified.
MCA: B - **MCA: P**	2	In the second configuration, the roll and sway were more present, which was easier to control and felt more realistic.
MCA: B - MCA: O	2	The first configuration felt more realistic than the second configuration. Also, there was more roll motion in the first. However, it felt that it was easier to control the second.
No Motion (2)	N.A.	Missing motion onset cue.

F.4.2. General Evaluation

- There was usually a clear difference between the configurations, which also translated to performance.
- Every configuration felt way better than the run without motion.
- The pilot sometimes closed its eyes during the passive part to identify the motion signature.
- The pairwise comparisons received a positive feedback.
- The passive part of the run was not necessary.
- The experiment could have been longer, e.g. evaluating more pairs.
- In general, no false cues were identified. Only, sometimes the amplitude felt a bit low.

F.4.3. Objective Evaluation

Table F.11: Pilot 3 - Mean Performance per Configuration

MCA	Mean	N	Std. Deviation
No Motion	-.0977	24	.2471
MCA: B	.1840	24	.1789
MCA: O	.1182	24	.1719
MCA: P	.2724	24	.1722
Total	.1192	96	.2361

Table F.12: Pilot 3 - Multiple Comparison (Tukey HSD)

(I) MCA	(J) MCA	Mean Difference (I-J)	Std. Error	Sig.	95% Confidence Interval	
					Lower Bound	Upper Bound
No Motion	MCA: O	-.2159	.0563	**.0013**	-.3633	-.0686
	MCA: P	-.3701	.0563	**.0000**	-.5175	-.2227
	MCA: B	-.2818	.0563	**.0000**	-.4291	-.1344
MCA: B	No Motion	.2818	.0563	**.0000**	.1344	.4291
	MCA: O	.0658	.0563	.6478	-.0815	.2132
	MCA: P	-.0883	.0563	.4017	-.2357	.0590
MCA: O	No Motion	.2159	.0563	**.0013**	.0686	.3633
	MCA: P	-.1542	.0563	**.0367**	-.3015	-.0068
	MCA: B	-.0658	.0563	.6478	-.2132	.0815
MCA: P	No Motion	.3701	.0563	**.0000**	.2227	.5175
	MCA: O	.1542	.0563	**.0367**	.0068	.3015
	MCA: B	.0883	.0563	.4017	-.0590	.2357

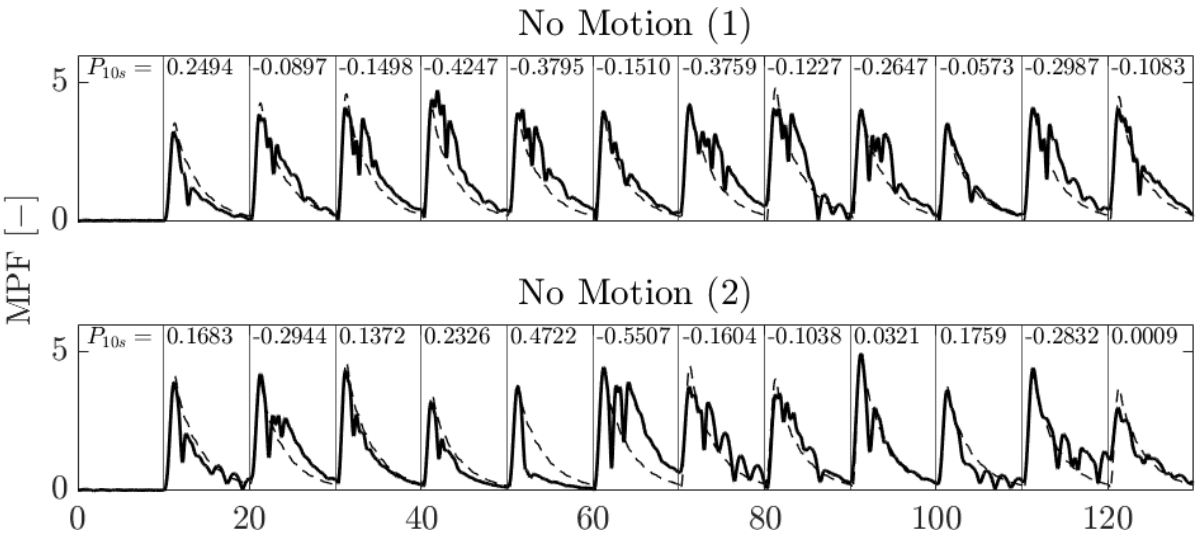

Figure F.22: Pilot 3 - No Motion

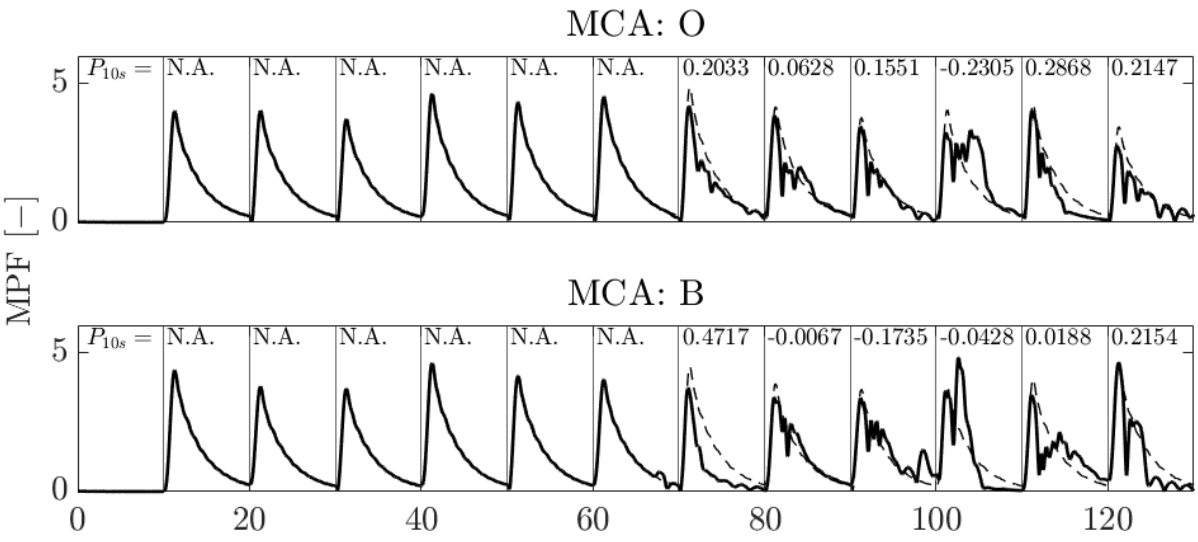

Figure F.23: Pilot 3 - Pair 1

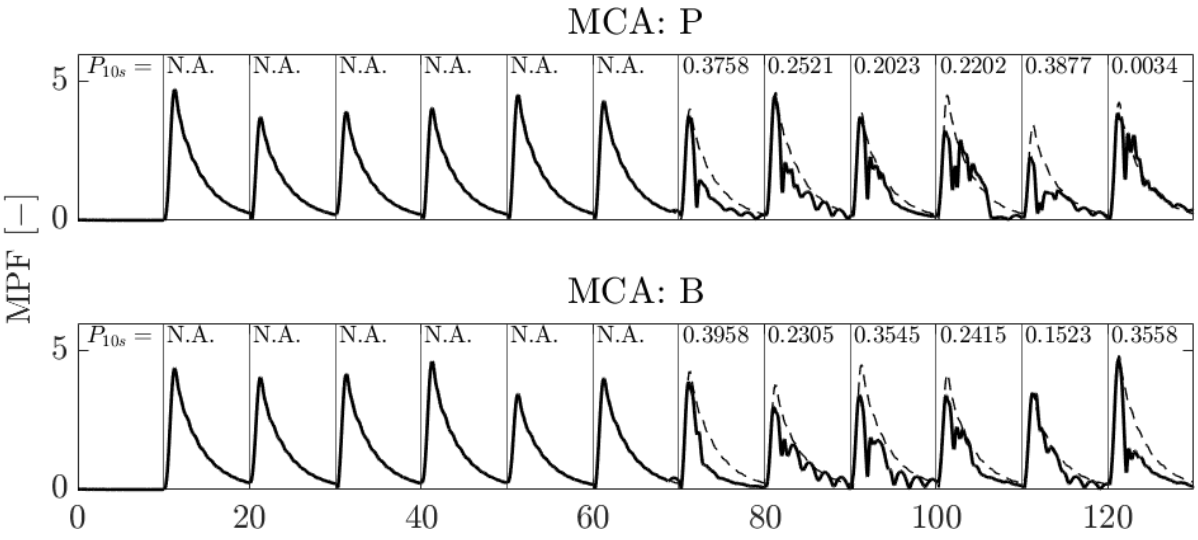

Figure F.24: Pilot 3 - Pair 2

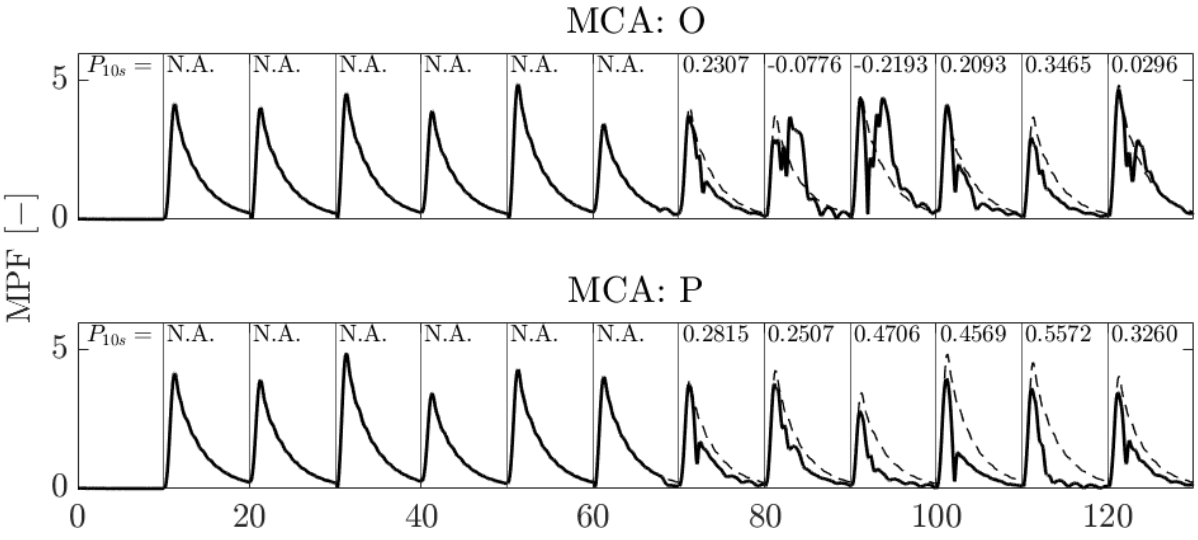

Figure F.25: Pilot 3 - Pair 3

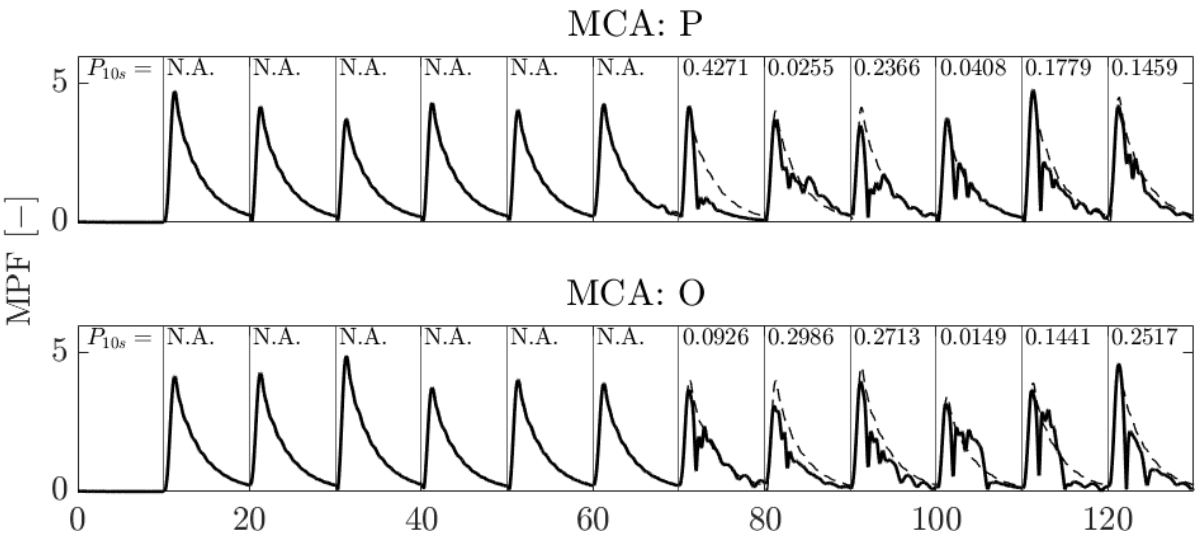

Figure F.26: Pilot 3 - Pair 4

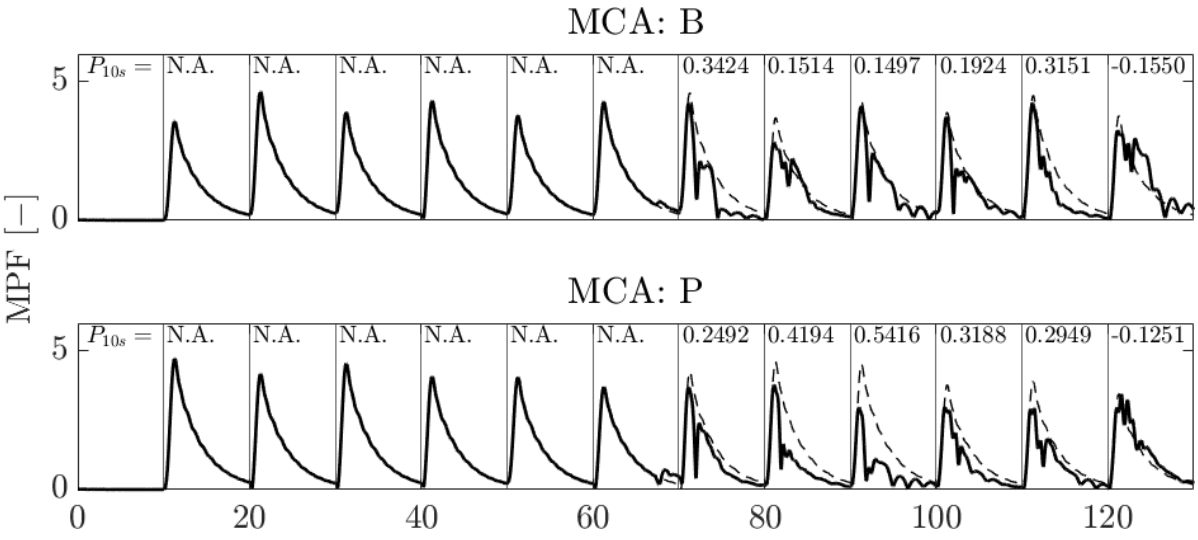

Figure F.27: Pilot 3 - Pair 5

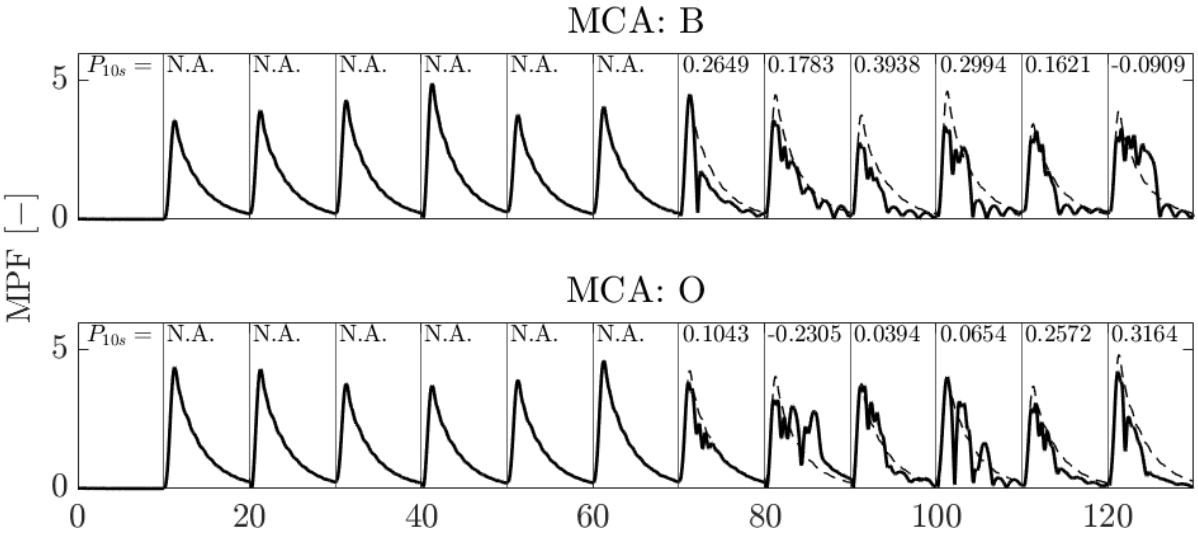

Figure F.28: Pilot 3 - Pair 6

F.5. Pilot 4

F.5.1. Subjective Evaluation

Table F.13: Pilot 4 - Subjective Rating

Pair	Confidence	Pilot Comment
MCA: B - MCA: P	1	-
MCA: B - MCA: O	0	No difference between the two configurations could be identified. The success of the Dutch Roll suppression depends on whether you have the onset right, otherwise you excite rather than suppress.
MCA: P - MCA: O	1	There was no clear difference between the two configurations, however there was a slight preference for the first configuration.
No Motion (1)	N.A.	As the visual is quite strong, the missing of motion was not perceived that much.
MCA: O - **MCA: P**	1	-
MCA: O - MCA: B	0	Experiment was getting a little bit long, coffee would have been nice.
MCA: P - MCA: B	0	No difference could be identified.
No Motion (2)	N.A.	As the motion onset was missing, the initial excitation was sometimes perceived slightly later.

F.5.2. General Evaluation

- In the beginning there was a rudder offset as the control were not centered.
- The success of the suppression depends on whether you have the initial direction right, if not, it is difficult to suppress.
- Sometimes only one pulse was enough to suppress the Dutch Roll, however sometimes an additional push was necessary.
- Even though he said confidence level of 1, it sometimes could also have been 0.
- Without motion you miss the motion onset.
- Did not use the slip indicator to suppress the Dutch Roll as the ball was not reliable. Used outside visual instead.
- The way of evaluating the different motion configurations was experienced pleasant.
- The passive part gave most information about the motion signature.

F.5.3. Objective Evaluation

Table F.14: Pilot 4 - Mean Performance per Configuration

MCA	Mean	N	Std. Deviation
No Motion	.2235	24	.2294
MCA: B	.4048	24	.2260
MCA: O	.3914	24	.1910
MCA: P	.4553	24	.2065
Total	.3687	96	.2279

Table F.15: Pilot 4 - Multiple Comparison (Tukey HSD)

(I) MCA	(J) MCA	Mean Difference (I-J)	Std. Error	Sig.	95% Confidence Interval	
					Lower Bound	Upper Bound
No Motion	MCA: O	-.1679	.0617	**.0384**	-.3294	-.0064
	MCA: P	-.2318	.0617	**.0017**	-.3933	-.0703
	MCA: B	-.1813	.0617	**.0214**	-.3428	-.0198
MCA: B	No Motion	.1813	.0617	**.0214**	.0198	.3428
	MCA: O	.0134	.0617	.9964	-.1481	.1749
	MCA: P	-.0505	.0617	.8455	-.2120	.1110
MCA: O	No Motion	.1679	.0617	**.0384**	.0064	.3294
	MCA: P	-.0639	.0617	.7289	-.2254	.0976
	MCA: B	-.0134	.0617	.9964	-.1749	.1481
MCA: P	No Motion	.2318	.0617	**.0017**	.0703	.3933
	MCA: O	.0639	.0617	.7289	-.0976	.2254
	MCA: B	.0505	.0617	.8455	-.1110	.2120

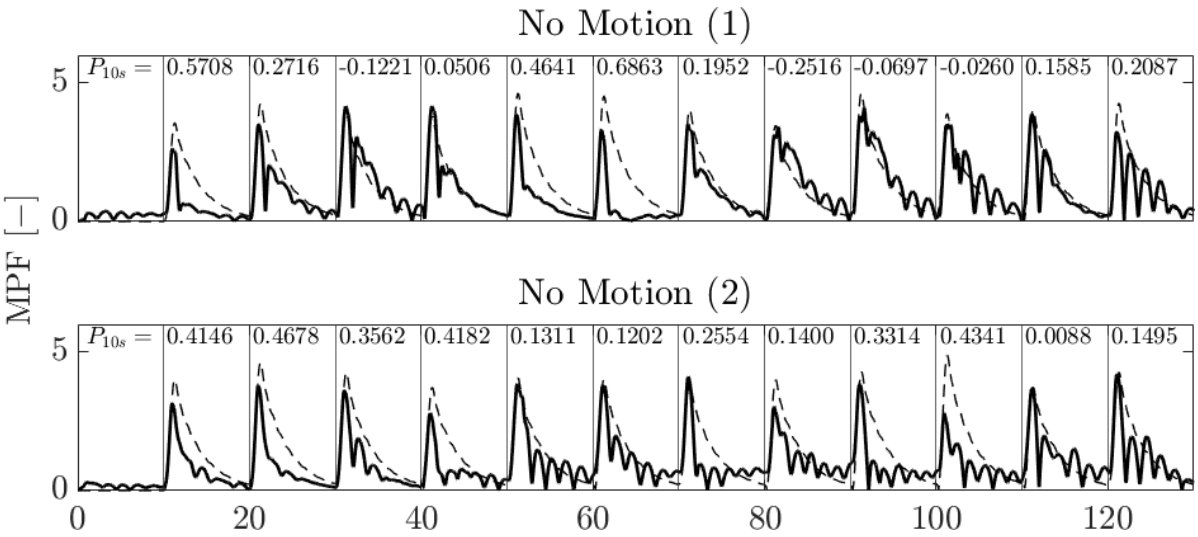

Figure F.29: Pilot 4 - No Motion

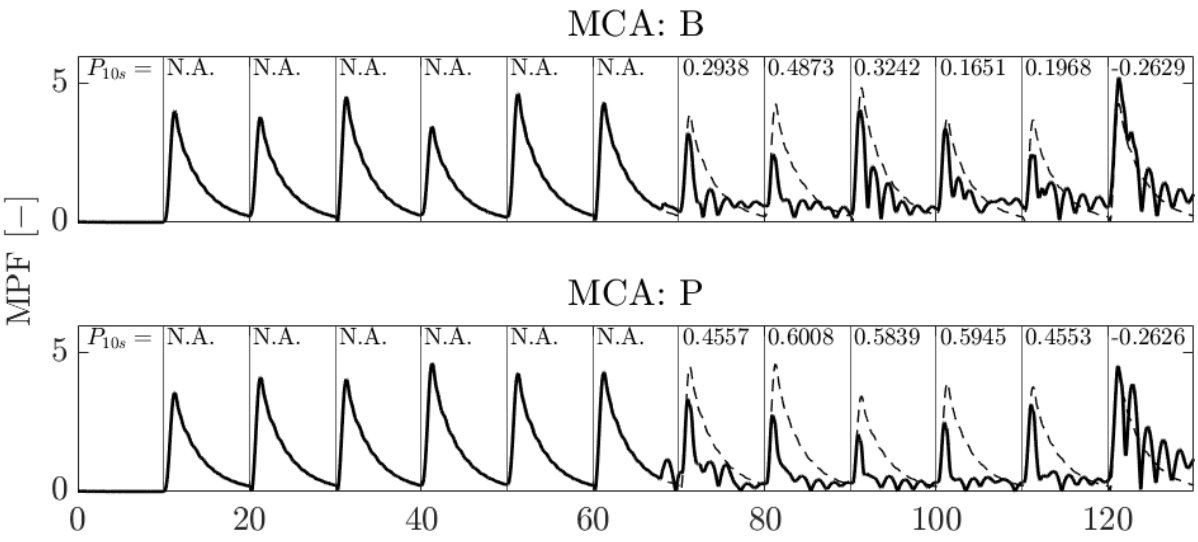

Figure F.30: Pilot 4 - Pair 1

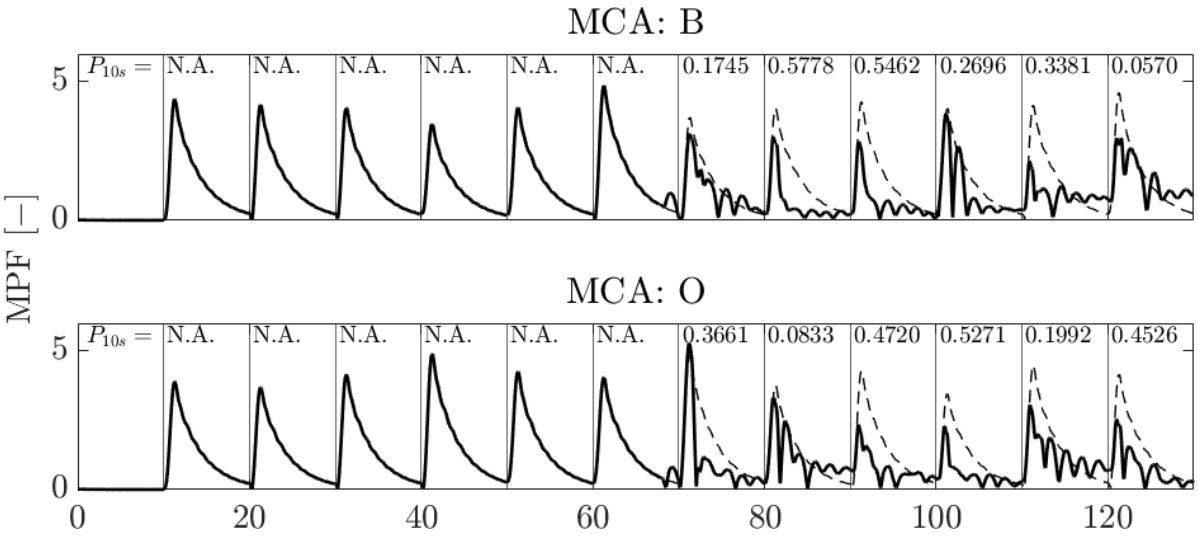

Figure F.31: Pilot 4 - Pair 2

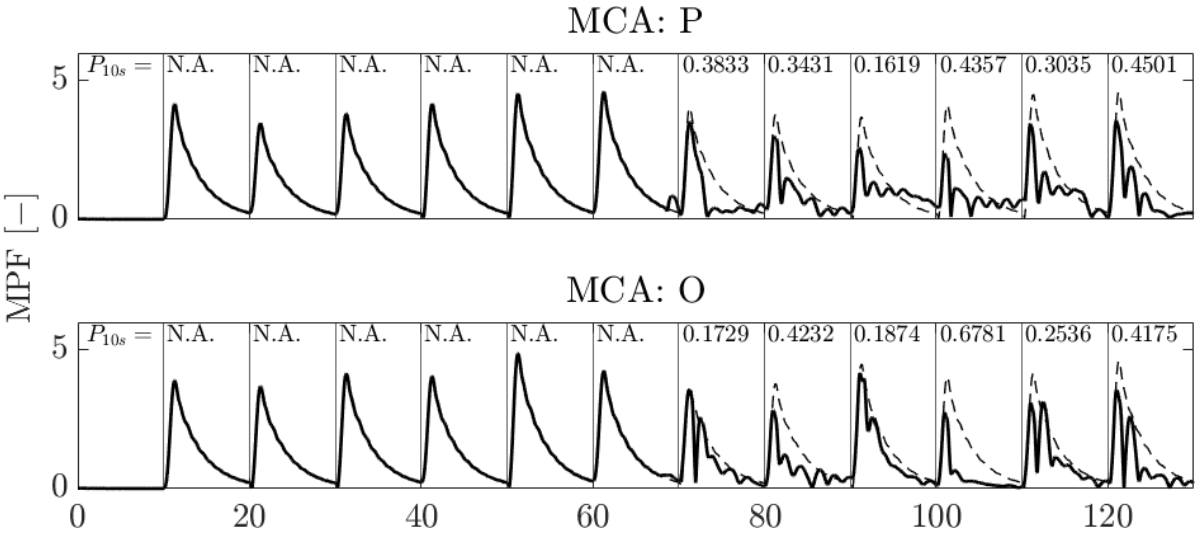

Figure F.32: Pilot 4 - Pair 3

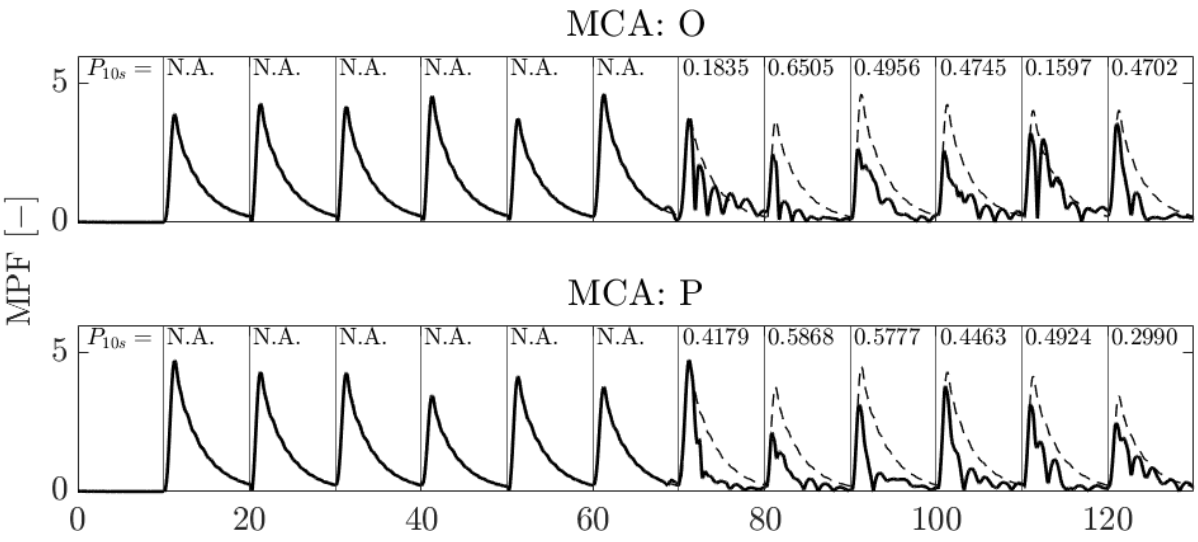

Figure F.33: Pilot 4 - Pair 4

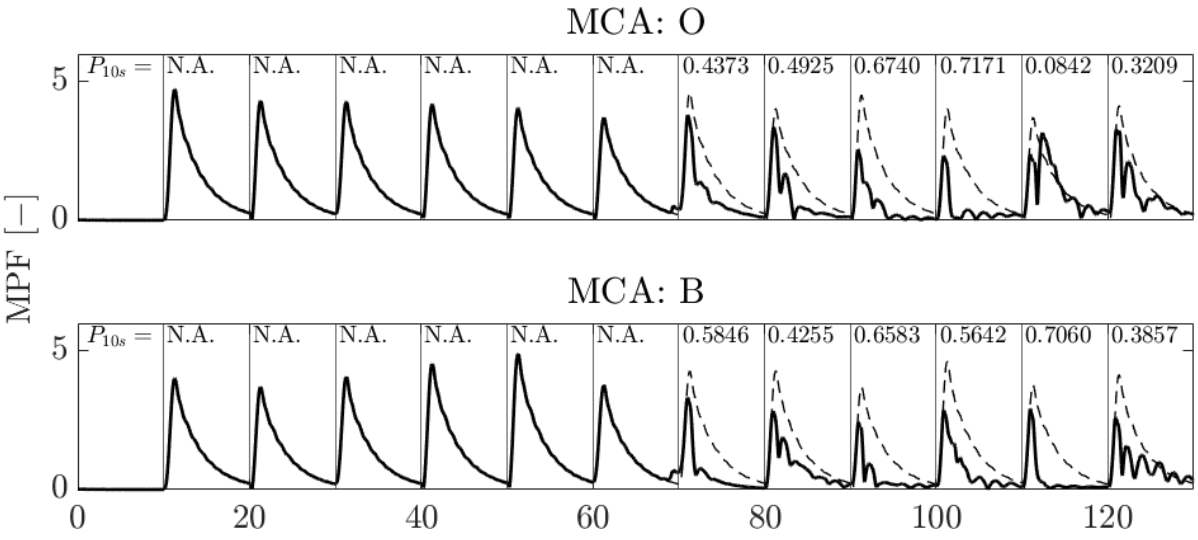

Figure F.34: Pilot 4 - Pair 5

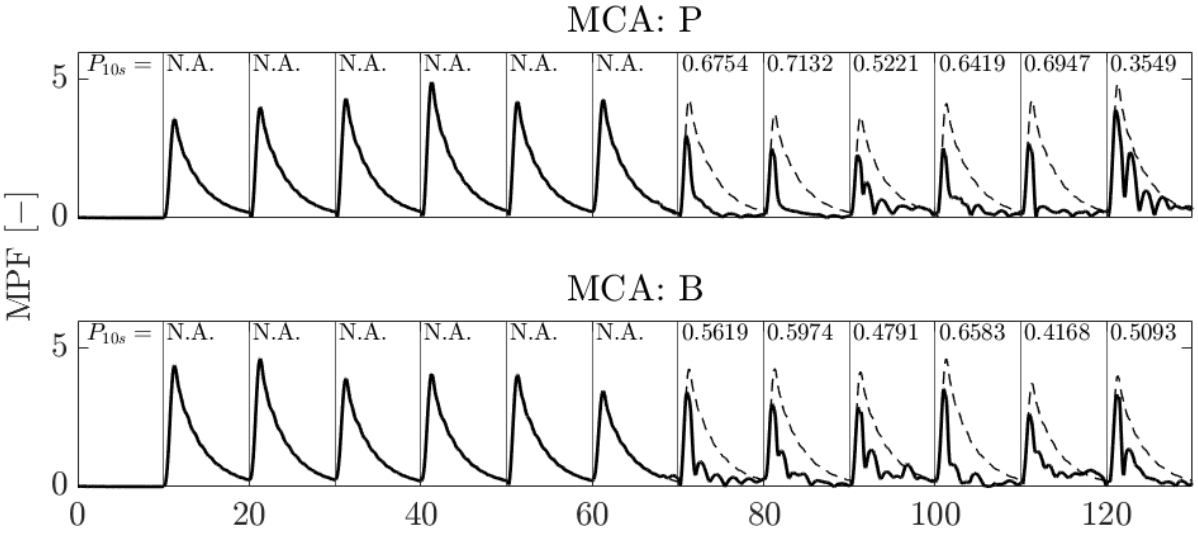

Figure F.35: Pilot 4 - Pair 6

F.6. Pilot 5

F.6.1. Subjective Evaluation

Table F.16: Pilot 5 - Subjective Rating

Pair	Confidence	Pilot Comment
MCA: B - MCA: O	2	Somehow the engine noise turned-off in the second run. The second configuration was bad as there was barely any bank information.
MCA: P - MCA: O	2	The first configuration was fairly okay. The second configuration did not cue any bank and yaw was only perceived slightly. Evaluation was performed with eyes closed.
MCA: B - MCA: P	2	The first configuration was the best till now. The second configuration missed sway motion cues, also had the feeling that the point of rotation was somewhat next to you. It is difficult to get the side-slip completely to zero.
No Motion (1)	N.A.	Had the feeling that motion cues are very beneficial for performing the task.
MCA: P - **MCA: B**	1	In the second configuration the bank was missing a little bit. However, this configuration was chosen as it was easier to correct.
MCA: O - MCA: P	1	The first configuration felt slightly more realistic, however no large differences between the two.
MCA: O - **MCA: B**	2	In the first configuration had the feeling that you were sitting in front of the centre-of-gravity. The second configuration had a better correlation between visual and motion. Also, sway and yaw were present and correcting was easier.
No Motion (2)	N.A.	-

F.6.2. General Evaluation

- The desired speed and altitude were quite confusing, e.g. 245 kts and 16,400 ft.
- Usually a pilot only has to give one rudder input and let the aircraft damp the Dutch Roll itself. However, during the experiment the pilot was asked to actively suppress the Dutch Roll.
- The slip-indicator was not correct, felt a little bit under-damped.
- The way the experiment evaluated the different pairs was good. The experiment could even have been longer as the difference between the configurations are so small.

F.6.3. Objective Evaluation

Table F.17: Pilot 5 - Mean Performance per Configuration

MCA	Mean	N	Std. Deviation
No Motion	-.3033	24	.2409
MCA: B	-.2377	24	.1485
MCA: O	-.2030	24	.2376
MCA: P	-.1640	24	.1502
Total	-.2270	96	.2029

Table F.18: Pilot 5 - Multiple Comparison (Tukey HSD)

(I) MCA	(J) MCA	Mean Difference (I-J)	Std. Error	Sig.	95% Confidence Interval	
					Lower Bound	Upper Bound
No Motion	MCA: O	-.1003	.0576	.3081	-.2510	.0503
	MCA: P	-.1393	.0576	.0805	-.2899	.0114
	MCA: B	-.0657	.0576	.6654	-.2163	.0850
MCA: B	No Motion	.0657	.0576	.6654	-.0850	.2163
	MCA: O	-.0346	.0576	.9313	-.1853	.1160
	MCA: P	-.0736	.0576	.5789	-.2243	.0770
MCA: O	No Motion	.1003	.0576	.3081	-.0503	.2510
	MCA: P	-.0390	.0576	.9056	-.1896	.1117
	MCA: B	.0346	.0576	.9313	-.1160	.1853
MCA: P	No Motion	.1393	.0576	.0805	-.0114	.2899
	MCA: O	.0390	.0576	.9056	-.1117	.1896
	MCA: B	.0736	.0576	.5789	-.0770	.2243

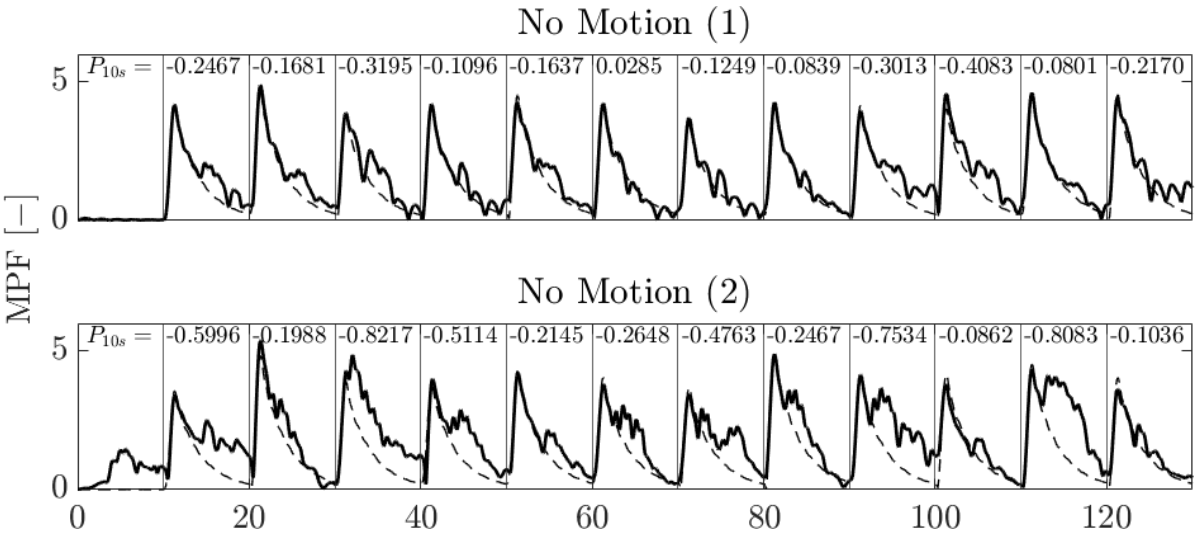

Figure F.36: Pilot 5 - No Motion

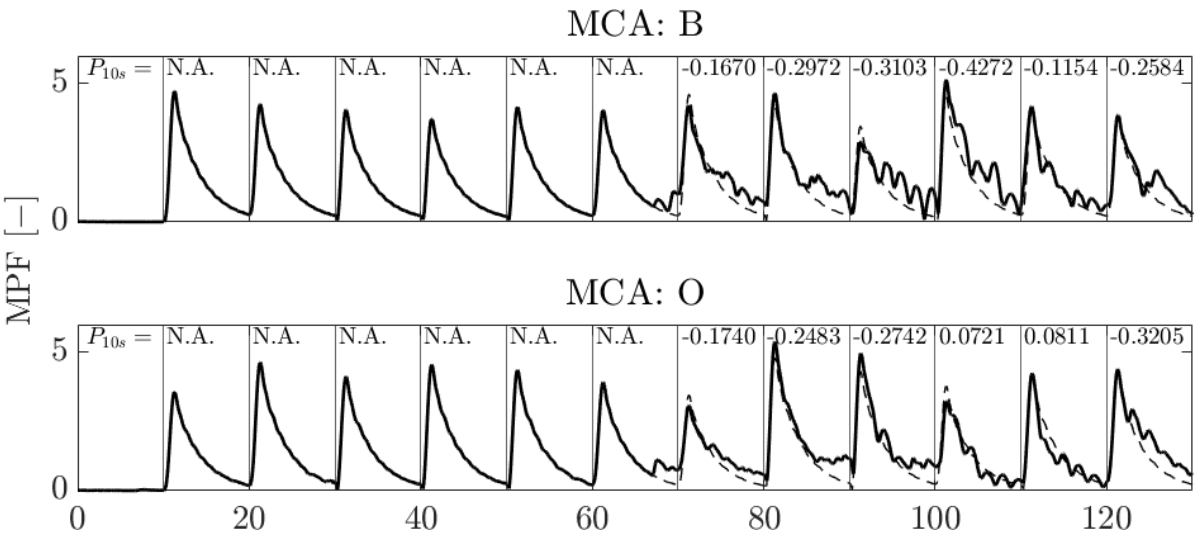

Figure F.37: Pilot 5 - Pair 1

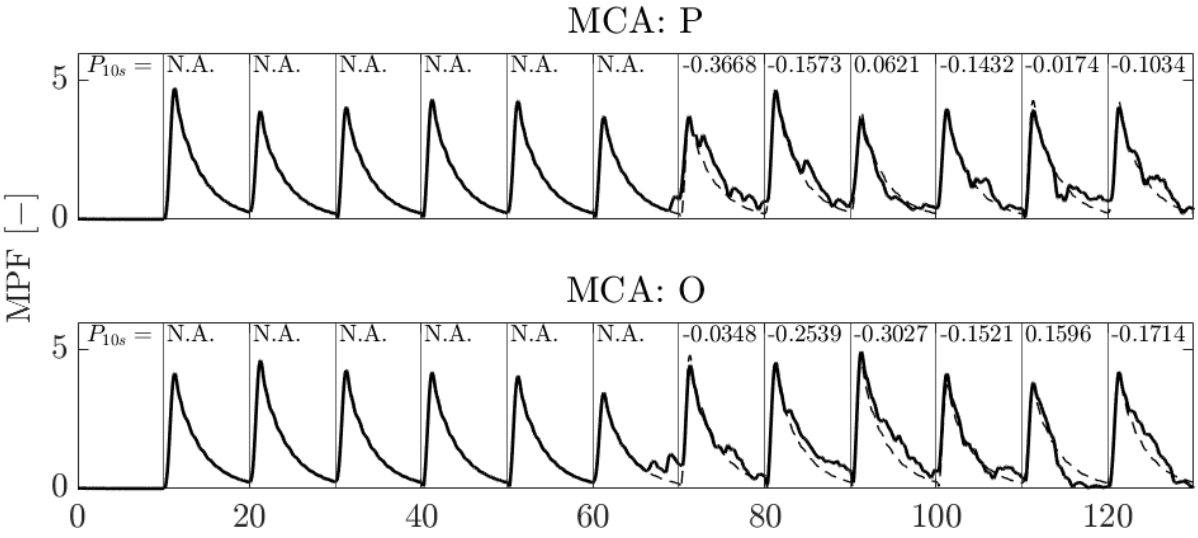

Figure F.38: Pilot 5 - Pair 2

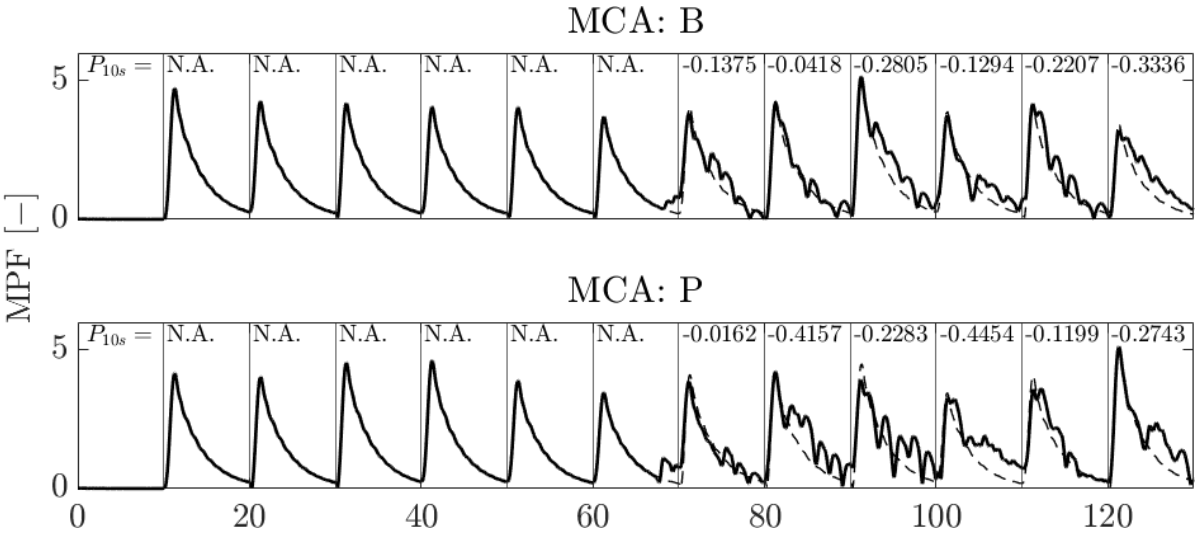

Figure F.39: Pilot 5 - Pair 3

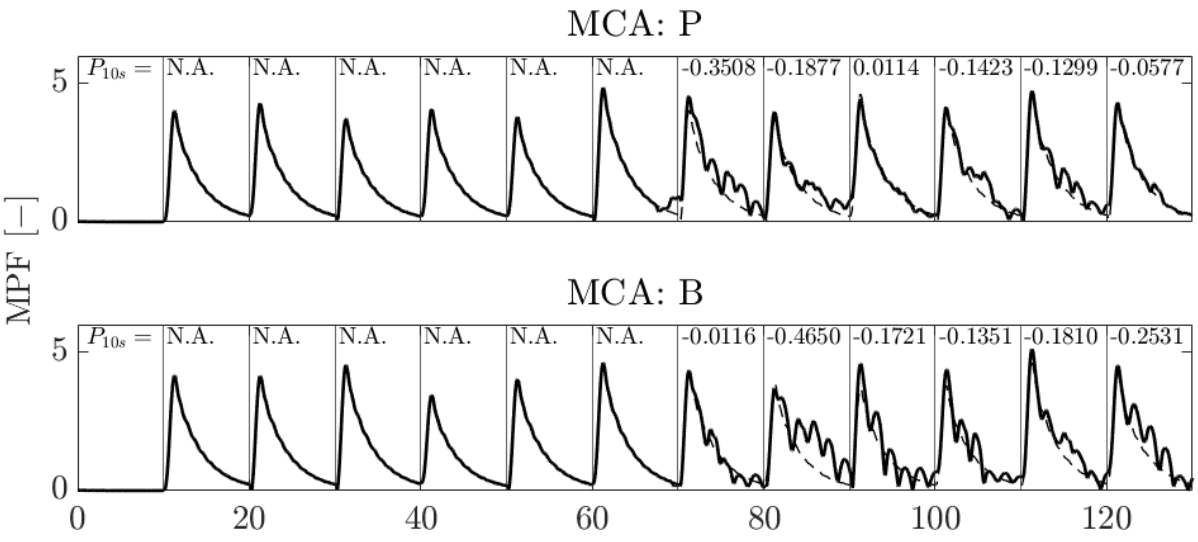

Figure F.40: Pilot 5 - Pair 4

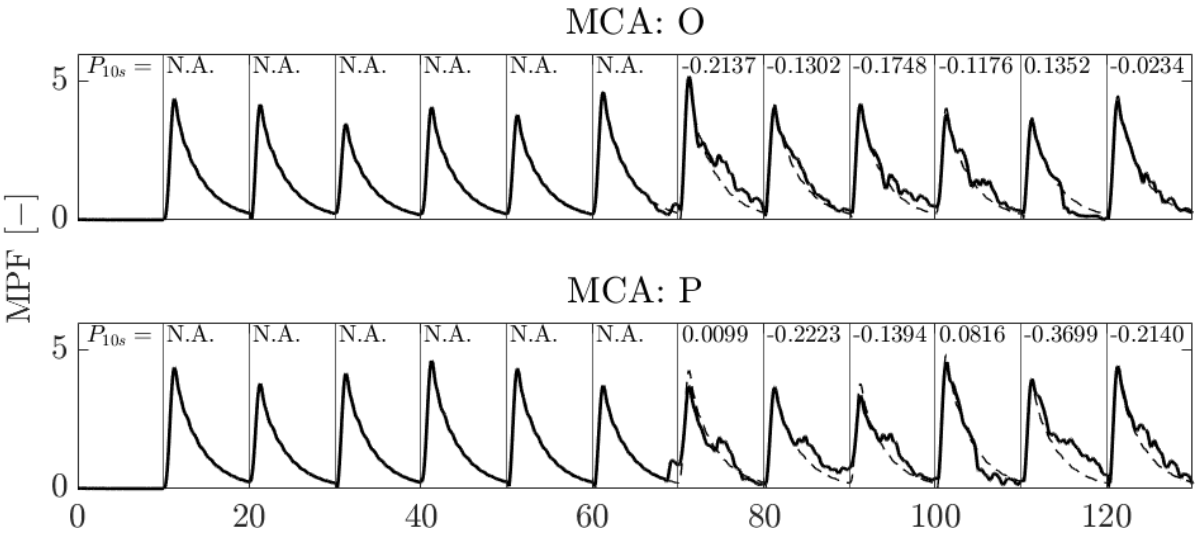

Figure F.41: Pilot 5 - Pair 5

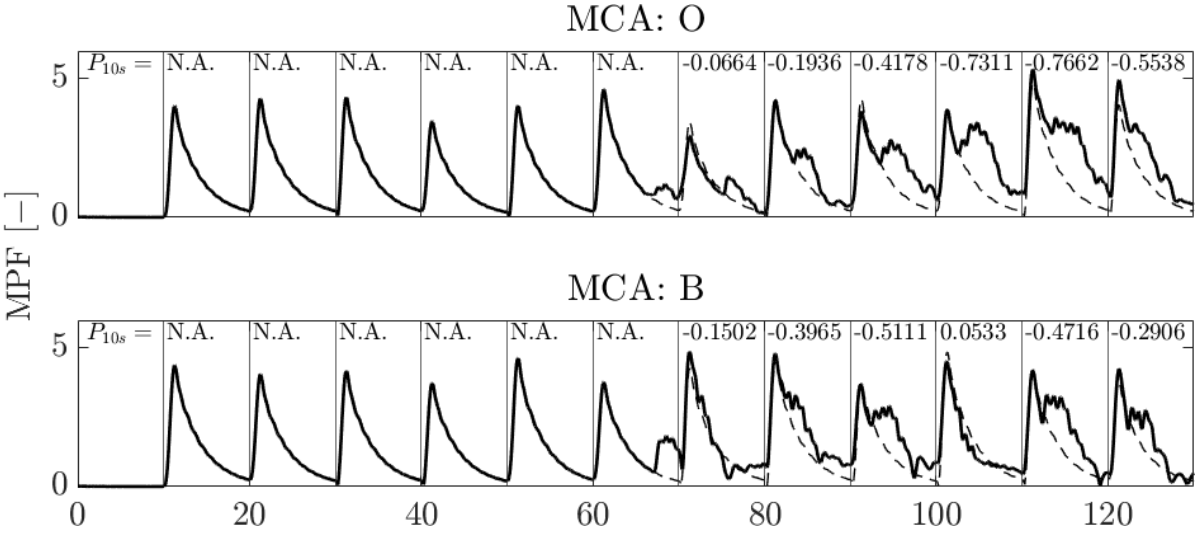

Figure F.42: Pilot 5 - Pair 6

F.7. Pilot 6

F.7.1. Subjective Evaluation

Table F.19: Pilot 6 - Subjective Rating

Pair	Confidence	Pilot Comment
MCA: P - **MCA: O**	1	For the first configuration it felt that the motion was lagging behind the visual. In the second configuration the yaw motion was better, but there was not a lot of roll response.
MCA: B - **MCA: P**	2	The first configuration felt somewhat soft. Also, sometimes you feel a response that you do not expect. The second configuration felt better and there was good correlation between visual and motion.
MCA: B - **MCA: O**	1	There was too little response in the first configuration. In the second configuration the yaw was more realistic. There was not a lot of difference in roll between the two configurations.
No Motion (1)	N.A.	This configuration feels weird as the motion (onset) is missing. Not a lot of difference in the control task was experienced.
MCA: O - **MCA: B**	2	There was only little roll in the first configuration, but the yaw was fine. The Dutch Roll was easy to suppress. The second configuration felt just slightly better.
MCA: P - **MCA: B**	2	The motion is lagging behind the visual in the first configuration. In the second configuration, the yaw was clearly present, but there was not a lot of roll. The correlation between visual and motion was good.
MCA: O - MCA: P	1	There was only little difference between the two configurations, however, the first felt slightly better as there was a larger roll amplitude.
No Motion (2)	N.A.	The motion onset cue is missing.

F.7.2. General Evaluation

- Pilot uses the outside visual for the Dutch Roll suppression and uses the clouds as reference. Therefore, the side-slip indicator was not perceived as incorrect or annoying.
- The pilot was active in giving a continuous opposite rudder input to suppress the Dutch Roll.
- The difference between the different configurations was sometimes very little, making evaluation difficult.
- Experiment could have been longer in which the pairs are evaluated even more times.
- The way the experiment was conducted was good.
- The way that a run was divided into a passive and active part was pleasant.

F.7.3. Objective Evaluation

Table F.20: Pilot 6 - Mean Performance per Configuration

MCA	Mean	N	Std. Deviation
No Motion	.0466	24	.2633
MCA: B	.1594	24	.3413
MCA: O	.0110	24	.2487
MCA: P	.2091	24	.2372
Total	.1065	96	.2831

Table F.21: Pilot 6 - Multiple Comparison (Tukey HSD)

(I) MCA	(J) MCA	Mean Difference (I-J)	Std. Error	Sig.	95% Confidence Interval	
					Lower Bound	Upper Bound
No Motion	MCA: O	.0356	.0796	.9700	-.1726	.2438
	MCA: P	-.1625	.0796	.1800	-.3707	.0457
	MCA: B	-.1128	.0796	.4914	-.3210	.0954
MCA: B	No Motion	.1128	.0796	.4914	-.0954	.3210
	MCA: O	.1484	.0796	.2502	-.0598	.3566
	MCA: P	-.0497	.0796	.9239	-.2579	.1585
MCA: O	No Motion	-.0356	.0796	.9700	-.2438	.1726
	MCA: P	-.1981	.0796	.0682	-.4063	.0101
	MCA: B	-.1484	.0796	.2502	-.3566	.0598
MCA: P	No Motion	.1625	.0796	.1800	-.0457	.3707
	MCA: O	.1981	.0796	.0682	-.0101	.4063
	MCA: B	.0497	.0796	.9239	-.1585	.2579

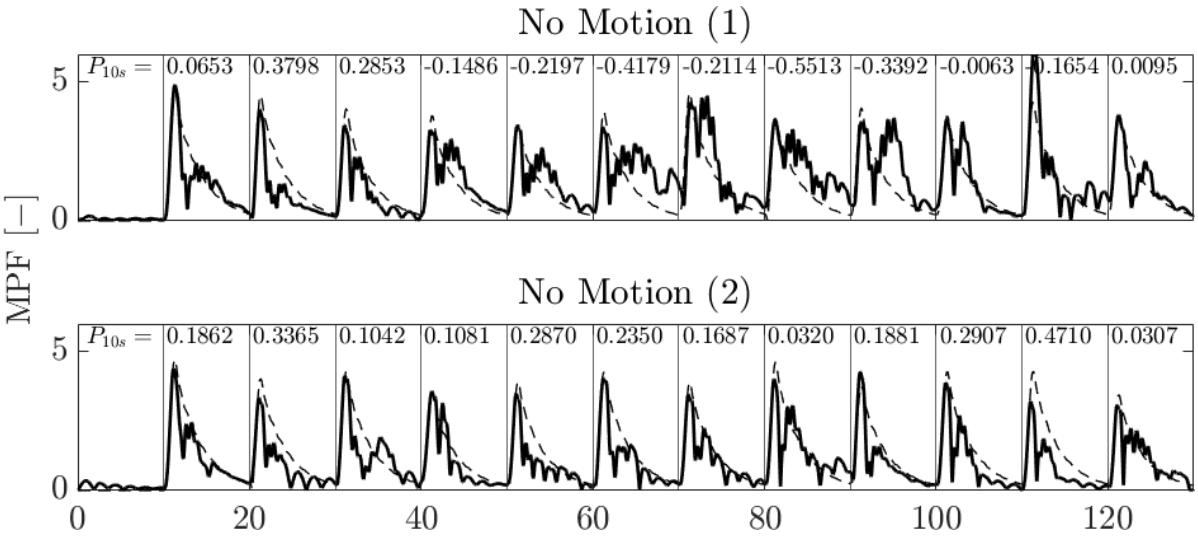

Figure F.43: Pilot 6 - No Motion

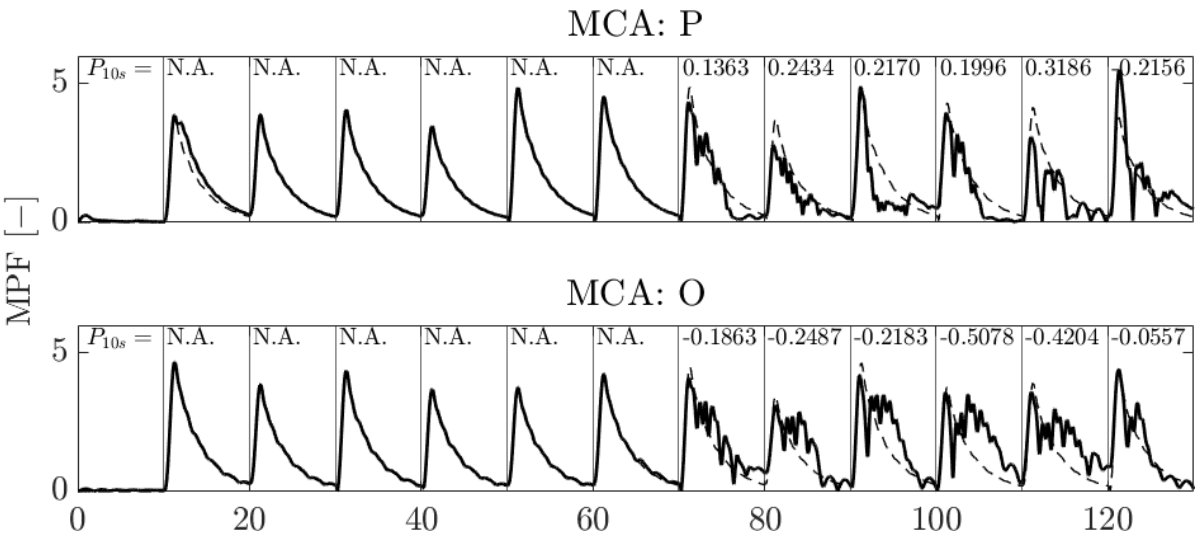

Figure F.44: Pilot 6 - Pair 1

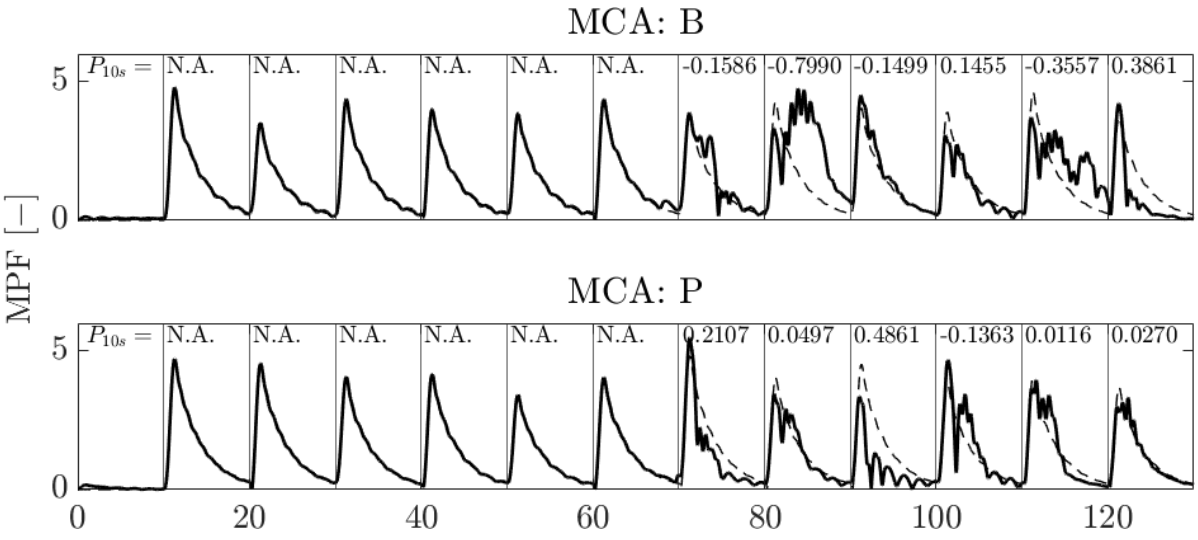

Figure F.45: Pilot 6 - Pair 2

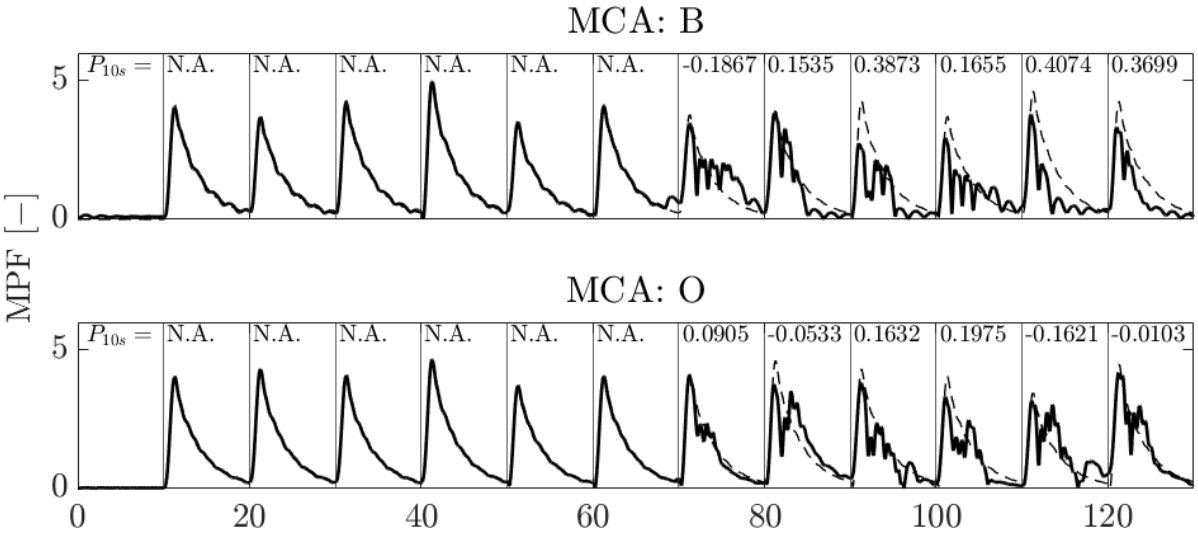

Figure F.46: Pilot 6 - Pair 3

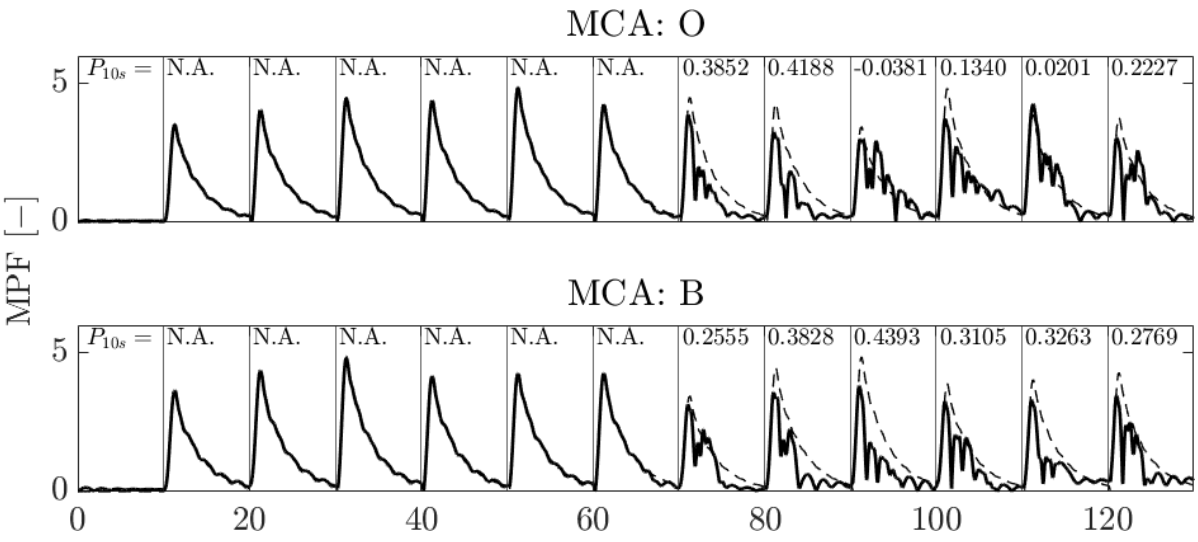

Figure F.47: Pilot 6 - Pair 4

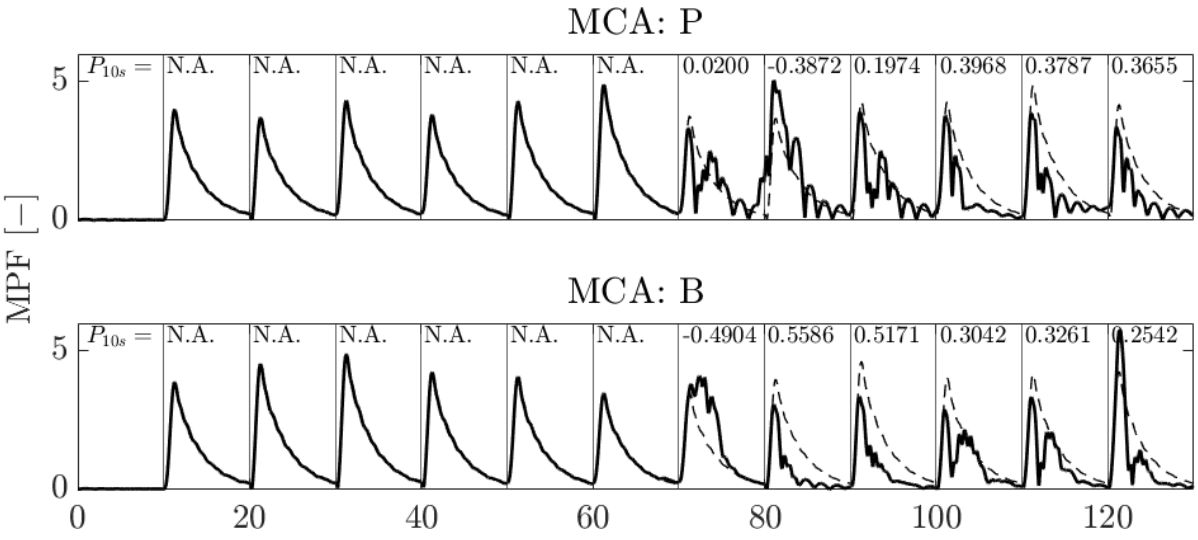

Figure F.48: Pilot 6 - Pair 5

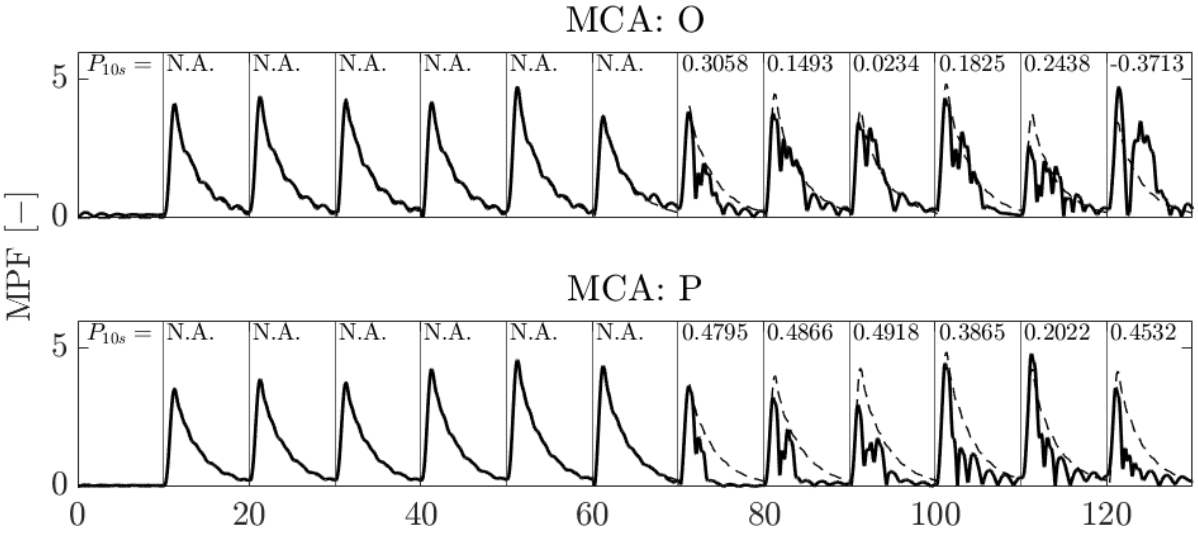

Figure F.49: Pilot 6 - Pair 6

This page is intentionally left blank.

G

Repeated Measures ANOVA Results

Table G.1: Descriptive Statistics and Test of Normality

	Mean	Std. Deviation	N	Shapiro-Wilk		
				Statistic	df	Sig.
No Motion	-.0194	.2391	6	.919	6	.498
MCA: B	.1485	.2288	6	.942	6	.679
MCA: O	.1071	.2175	6	.956	6	.789
MCA: P	.1935	.2322	6	.951	6	.749

Table G.2: Mauchly's Test of Sphericity

Within Subjects Effect	Mauchly's W	χ^2	df	Sig.	Epsilon		
					Greenhouse-Geisser	Huynh-Feldt	Lower-bound
Motion Condition	.318	4.268	5	.524	.637	1.000	.333

Table G.3: Tests of Within-Subject Effects

Source		Type III Sum of Squares	df	Mean Square	F	Sig.	Partial Eta Squared
Motion Condition	Sphericity Assumed	.151	3	.050	13.832	.000	.734
	Greenhouse-Geisser	.151	1.911	.079	13.832	.002	.734
	Huynh-Feldt	.151	3.000	.050	13.832	.000	.734
	Lower-bound	.151	1.000	.151	13.832	.014	.734
Error(Motion Condition)	Sphericity Assumed	.055	15	.004			
	Greenhouse-Geisser	.055	9.556	.006			
	Huynh-Feldt	.055	15.000	.004			
	Lower-bound	.055	5.000	.011			

Table G.4: Pairwise Comparisons

(I) MCA	(J) MCA	Mean Difference (I-J)	Std. Error	Sig.*	95% Confidence Interval	
					Lower Bound	Upper Bound
No Motion	MCA: B	-.168	.042	.063	-.346	.010
	MCA: O	-.127	.046	.238	-.320	.067
	MCA: P	-.213	.039	.017	-.378	-.047
MCA: B	No Motion	.168	.042	.063	-.010	.346
	MCA: O	.041	.025	.966	-.065	.148
	MCA: P	-.045	.017	.291	-.118	.028
MCA: O	No Motion	.127	.046	.238	-.067	.320
	MCA: B	-.041	.025	.966	-.148	.065
	MCA: P	-.086	.031	.224	-.216	.043
MCA: P	No Motion	.213	.039	.017	.047	.378
	MCA: B	.045	.017	.291	-.028	.118
	MCA: O	.086	.031	.224	-.043	.216

*Adjustment for multiple comparisons: Bonferroni

This page is intentionally left blank.

H

Two-Way ANOVA Results

The Dutch Roll suppression performance is calculated for each pilot for the active parts of each run, resulting in 96 data-points per pilot. Which can be divided into 24 data-points for each condition, e.g. the three configurations and the no-motion condition. To compare the different conditions, a *within-subjects* design is used. In a within-subject design, each subject tests all the conditions, yielding one data point for each condition. To fit in within-subject design, the average performance for each pilot and condition is used, i.e. calculating the average of the 24 data-points for each pilot and condition. As of this, a lot of variance data gets lost. Therefore, a Two-Way ANOVA is also performed, the results of this test is not included in the paper and serve as an extension of the analysis. This appendix presents the results for the Two-Way ANOVA test.

Table H.1: Descriptive Statistics

Pilot	MCA	Mean	Std. Deviation	N
1	No Motion	.2665	.2240	24
	MCA: O	.3111	.2865	24
	MCA: P	.3766	.2001	24
	MCA: B	.3354	.3244	24
	Total	.3224	.2623	96
2	No Motion	-.2519	.1889	24
	MCA: O	.0142	.2335	24
	MCA: P	.0114	.2921	24
	MCA: B	.0453	.2641	24
	Total	-.0452	.2720	96
3	No Motion	-.0977	.2471	24
	MCA: O	.1182	.1719	24
	MCA: P	.2724	.1722	24
	MCA: B	.1840	.1789	24
	Total	.1192	.2361	96
4	No Motion	.2235	.2294	24
	MCA: O	.3914	.1910	24
	MCA: P	.4553	.2065	24
	MCA: B	.4048	.2260	24
	Total	.3687	.2279	96
5	No Motion	-.3033	.2409	24
	MCA: O	-.2030	.2376	24
	MCA: P	-.1640	.1502	24
	MCA: B	-.2377	.1485	24
	Total	-.2270	.2029	96
6	No Motion	.0466	.2633	24
	MCA: O	.0110	.2487	24
	MCA: P	.2091	.2372	24
	MCA: B	.1594	.3413	24
	Total	.1065	.2831	96
Total	No Motion	-.0194	.3171	144
	MCA: O	.1071	.3022	144
	MCA: P	.1935	.2995	144
	MCA: B	.1485	.3282	144
	Total	.1074	.3211	576

Table H.2: Tests of Between-Subject Effects

Source	Type III Sum of Squares	df	Mean Square	F	Sig.	Partial Eta Squared
Corrected Model	28.917	23	1.257	22.843	.000	.488
Intercept	6.649	1	6.649	120.805	.000	.180
Pilot	23.981	5	4.796	87.141	.000	.441
MCA	3.626	3	1.209	21.958	.000	.107
Pilot * MCA	1.311	15	.087	1.587	.072	.041
Error	30.381	552	.055			
Total	65.947	576				
Corrected Total	59.298	575				

Table H.3: Pairwise Comparisons - Motion Condition

(I) MCA	(J) MCA	Mean Difference (I-J)	Std. Error	Sig.*	95% Confidence Interval	
					Lower Bound	Upper Bound
No Motion	MCA: O	-.127	.028	.000	-.200	-.053
	MCA: P	-.213	.028	.000	-.286	-.140
	MCA: B	-.168	.028	.000	-.241	-.095
MCA: B	No Motion	.168	.028	.000	.095	.241
	MCA: O	.041	.028	.809	-.032	.115
	MCA: P	-.045	.028	.629	-.118	.028
MCA: O	No Motion	.127	.028	.000	.053	.200
	MCA: P	-.086	.028	.011	-.160	-.013
	MCA: B	-.041	.028	.809	-.115	.032
MCA: P	No Motion	.213	.028	.000	.140	.286
	MCA: O	.086	.028	.011	.013	.160
	MCA: B	.045	.028	.629	-.028	.118

*Adjustment for multiple comparisons: Bonferroni

Table H.4: Pairwise Comparisons - Pilot

(I) Pilot	(J) Pilot	Mean Difference (I-J)	Std. Error	Sig.*	95% Confidence Interval	
					Lower Bound	Upper Bound
1	2	.368	.034	.000	.268	.467
	3	.203	.034	.000	.103	.303
	4	-.046	.034	1.000	-.146	.053
	5	.549	.034	.000	.450	.649
	6	.216	.034	.000	.116	.316
2	1	-.368	.034	.000	-.467	-.268
	3	-.164	.034	.000	-.264	-.065
	4	-.414	.034	.000	-.514	-.314
	5	.182	.034	.000	.082	.282
	6	-.152	.034	.000	-.252	-.052
3	1	-.203	.034	.000	-.303	-.103
	2	.164	.034	.000	.065	.264
	4	-.250	.034	.000	-.349	-.150
	5	.346	.034	.000	.246	.446
	6	.013	.034	1.000	-.087	.113
4	1	.046	.034	1.000	-.053	.146
	2	.414	.034	.000	.314	.514
	3	.250	.034	.000	.150	.349
	5	.596	.034	.000	.496	.696
	6	.262	.034	.000	.162	.362
5	1	-.549	.034	.000	-.649	-.450
	2	-.182	.034	.000	-.282	-.082
	3	-.346	.034	.000	-.446	-.246
	4	-.596	.034	.000	-.696	-.496
	6	-.334	.034	.000	-.433	-.234
6	1	-.216	.034	.000	-.316	-.116
	2	.152	.034	.000	.052	.252
	3	-.013	.034	1.000	-.113	.087
	4	-.262	.034	.000	-.362	-.162
	5	.334	.034	.000	.234	.433

*Adjustment for multiple comparisons: Bonferroni

Optimized *P* Configuration

In the discussion section it is claimed that the motion cue distortion could have been less for the *P* configuration if more motion space was available to the tuning algorithm. This appendix illustrates a CWA parameter set that could have been obtained from the automatic tuning algorithm if the complete motion space of the SIMONA Research Simulator was used.

K_{f_y} [−]	$\omega_{n_{f_y}}$ $[rad/s]$	$\omega_{b_{f_y}}$ $[rad/s]$	ζ_{f_y} [−]	ω_{n_t} $[rad/s]$	ζ_t [−]	K_p [−]	ω_{n_p} $[rad/s]$	ζ_p [−]
0.613	0.777	0.500	0.600	1.198	0.600	1.060	0.500	0.600

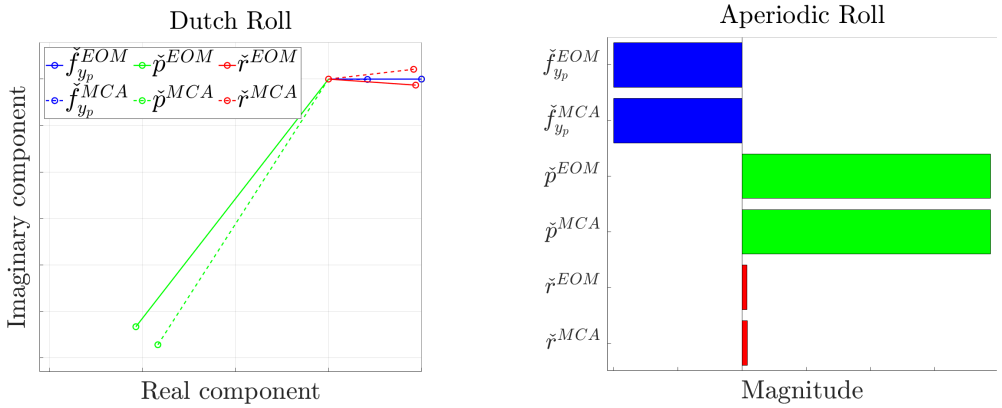

Figure I.1: Optimized *P* Configuration

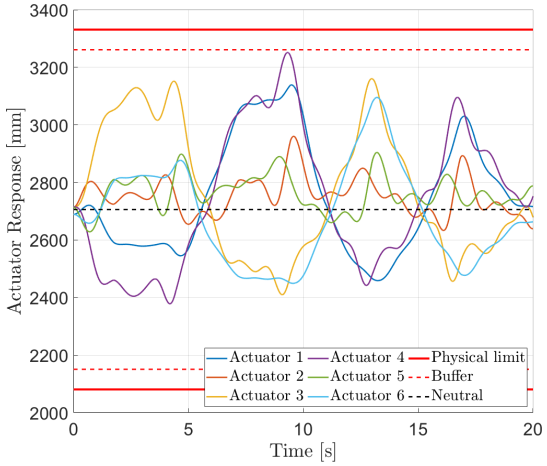

Figure I.2: Visualization of Actuator Responses

This page is intentionally left blank.

III

Preliminary Thesis Report

Preliminary thesis report has been graded already
Included for completeness

This page is intentionally left blank.

1 Introduction

Full flight simulators are standalone devices to replicate all motions and forces as would be perceived by the pilot in an aircraft. Ideally, the perceived motions and forces in the flight simulator are identical to the real aircraft, but where an aircraft has an (almost) infinite motion space, flight simulators have their physical limitations
The Motion Cueing Algorithm (MCA) has been developed to deal with these physical limits. Basically, the MCA is an algorithm between the flight model (Equations of Motion (EOM)) and motion platform (Figure 1.1). An MCA ensures that the motion platform is controlled in a safe way and ensures that the actuators, driving the motion platform, do not exceed their limits (e.g. actuator lengths).
In the past MCA-tuning experts tuned the variables of the algorithm until the pilot was satisfied. The resulting performance was generally expressed in terms of *high-fidelity* and *low-fidelity*, whereby high-fidelity means a high match between simulator and aircraft. As this fidelity-rating was subjective, the resulting tuning variables were different per pilot, but also dependent on the task and workload of the pilot.
The undesirability of only subjective evaluations was already recognized in the 70s and improved tuning procedures have been developed since, such as Sinacori [12], Schroeder [11] and Gouverneur [1].

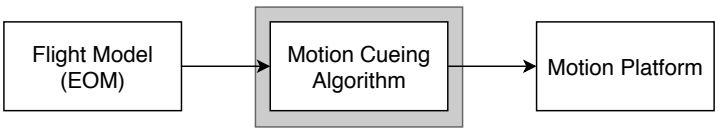

Figure 1.1: Flight Simulator: Motion Cueing Algorithm

These developments resulted in the current state-of-the-art method for objective evaluation of the flight simulator's fidelity: the Objective Motion Cueing Test (OMCT). This method has improved the tuning process and gives an objective and detailed picture on the performance of the MCA and motion platform combined (Figure 1.2). This analysis is performed in the frequency domain and uses the Fast Fourier Transform to obtain the frequency response function, which provides the magnitude- and phase distortions introduced by the MCA and motion platform.

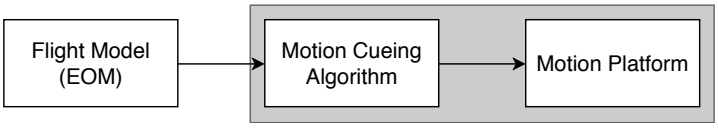

Figure 1.2: Flight Simulator Evaluation: Objective Motion Cueing Test

Despite the power of OMCT, this method has its shortcomings, such as its sine-wave input signals do not represent realistic motion experienced during flight and vehicle dynamics are not included in this test. Also, within OMCT each signal is studied in isolation, where aircraft motions are actually linked through dynamics.

To tackle these, the Control & Simulation section at the Faculty of Aerospace Engineering in TU Delft has developed a novel objective evaluation method, the Eigenmode Distortion (EMD). This EMD method uses a different approach to evaluate objective fidelity. Rather than analyzing in the frequency domain, this method investigates distortions of the motion cues imposed by the MCA in terms of eigenvectors, which represent the dynamic modes. To find these, the flight model is included in the test (Figure 1.3).

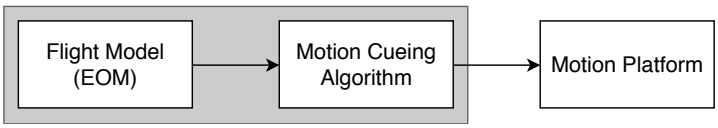

Figure 1.3: Flight Simulator Evaluation: Eigenmode Distortion Analysis

Despite the potential of this method, also this model has its complexity. The resulting eigenvectors are not comparable to one-another because the different eigenvectors have different units.
In this report, the extension of the EMD method with a so-called perception model, which is a mathematical representation of the human perception, is investigated to solve this limitation. In this report, this extension is referred to as the Perceptual Eigenmode Distortion (PEMD) (Figure 1.4).

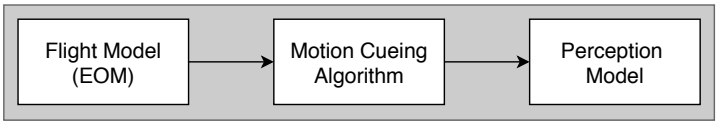

Figure 1.4: Flight Simulator Evaluation: Eigenmode Distortion Analysis with Perception Model Extension

The current implementation of the OMCT test, analyses the magnitude and phase distortions separately. Also, for the EMD method the resulting distortions are evaluated separately. Currently, there is no prioritizing in either optimizing magnitude- or phase distortions as these are considered equally important. This report, also, makes a step forward in the distortion minimization by considering simultaneous optimization. For this purpose, a new optimization function will be formulated.

The research objective of this thesis is to further evaluate the EMD method, particularly the influence of incorporating a so called pilot perception model (PEMD), by comparing the PEMD with a baseline and OMCT tuned configurations. A pilot-in-the-loop experiment with the SIMONA Research Simulator (SRS), which is the flight simulator at the Faculty of Aerospace Engineering, will be designed in order to evaluate the hypothesis (Chapter 8). This report, however, only focuses on the lateral model of the Cessna Citation 500 as previous work has been done already for the longitudinal model.

To realize this dissertation project the following central question and sub-questions are formulated:

To what extent is the Perceptual Eigenmode Distortion an improvement to the Eigenmode Distortion and Objective Motion Cueing Test (for the lateral model of the Cessna Citation 500)?

To answer this central question, the following sub-questions will be discussed and answered in the subsequent chapters of this report:

1. What are the fundamental differences between the EMD and OMCT methods for objective evaluation of simulator motion cueing fidelity?
   (a) Why is objective evaluation preferred over subjective evaluation of the simulator motion cueing fidelity?
   (b) Which other objective evaluation methods are available in practice?
   (c) What are the main principles of EMD?
   (d) What are the main principles of PEMD?
   (e) What are the main principles of OMCT?
2. How is the MCA currently implemented on the SIMONA Research Simulator?
3. How to apply the EMD method to the lateral model of the Cessna Citation 500 aircraft?
   (a) How was the EMD method previously applied on the linear symmetric model?
   (b) How to implement the lateral model of the Cessna Citation 500 aircraft?
4. How to incorporate a suitable pilot model?
   (a) What type of pilot models exist?
   (b) How to best model perceived specific forces and rotational rates?
   (c) What are the human vestibular thresholds and how to model these?
5. What is a suitable experiment set-up to evaluate and compare the PEMD configuration with the Baseline and OMCT tuned configuration?

This report is divided into different chapters where each of the earlier introduced concepts is elaborated in detail and the individual sub-questions are answered. The report is structured as follows:

- *Chapter 2*; describes the terminology used in this report. Furthermore, the Motion Cueing Algorithm is explained, which is the algorithm used to control the motion platform of the flight simulator. Lastly, an in-depth look into a hexapod 6 Degree of Freedom is given;
- *Chapter 3*; describes how motion cues are perceived by a human. It focuses on the vestibular system, which can be divided into the otolith and semi-circular canals. A mathematical representation of these is given as well. Lastly, not every motion cue is perceived, only motion cues above the perception thresholds are perceived, these perception thresholds are explained here;
- *Chapter 4*; describes the current state-of-the-art objective evaluation method, the Objective Motion Cueing Test. Rather than in the time domain, this method evaluates the Flight Simulator Training Device fidelity in the frequency domain by analyzing the response to sine-wave inputs;
- *Chapter 5*; contains a detailed derivation of the Eigenmode Distortion method. This method tries to tackle the shortcomings of the OMCT. Rather than using the frequency domain, this method evaluates the motion cue distortions by taking the vehicle dynamics into account and represents the distortions in terms of eigenvectors representing the dynamic modes of the aircraft;

- *Chapter 6*; contains a further development of the Eigenmode Distortion method. The problem with the resulting eigenvectors was that the magnitudes could not be compared. Therefore, two extensions of this EMD method will be analyzed. These extensions are refered to as the Perceptual Eigenmode Distortion as basically a perception model is added;
- *Chapter 7*; contains an optimization algorithm that can be used to find optimal Motion Cueing Algorithm settings to achieve highest performance in the previously designed Perceptual Eigenmode Distortion;
- *Chapter 8*; describes the experiment that is designed to answer the complete research question. An experiment is designed that evaluates the performance of an OMCT and PEMD tuned MCA;
- *Chapter 9*; establishes a conclusion of this report and answers the research questions.

2
Design of a Flight Simulator

Modern (high-fidelity) flight simulators consist of many hard- and software systems (Figure 2.1), all these systems work together to give the pilot the feeling of the actual aircraft. In general two types of simulators exist, ones with and without a moving motion platform. This report is about optimizing the settings of the algorithm that drives this motion platform. This algorithm is often referred to as Motion Cueing Algorithm (MCA) or Motion Drive Algorithm (MDA). The TU Delft's SIMONA Research Simulator (SRS) uses a MCA that is called the Classical Washout Algorithm (CWA). This algorithm is popular as of its simplicity, a detailed description of this algorithm is given in Section 2.2.
As depicted in Figure 2.1 the MCA is driven by the Equations of Motion (EOM). These EOM contain replicating equations that govern the physical behaviour of the actual aircraft. As can be seen in the figure, these EOM are based on many modules, such as the aerodynamic model and weather model. For this report, the linearized set of EOM are of relevance and therefore a detailed description of the connecting modules is left out.
The signals that leave the MCA are inputs to the motion platform, which moves the flight simulator with actuators. This movement is in such a way that the motion perception in the flight simulator is similar to that in the actual aircraft. A more detailed explanation of this motion platform is given Section 2.3. Before going into detail, some terminology needs to be emphasised, which is done in Section 2.1.

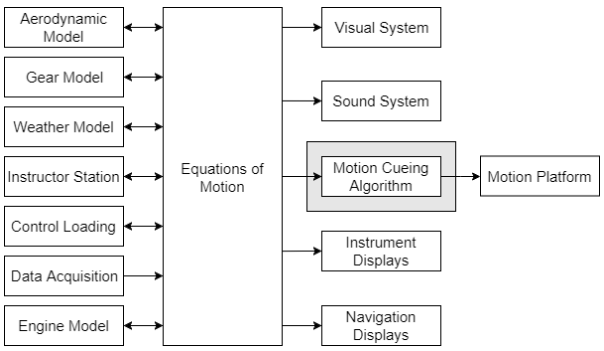

Figure 2.1: Principle of a Flight Simulator

2.1. Flight Simulator Terminology

2.1.1. Fidelity

Generally speaking the performance of a flight simulator is expressed in terms of *high-fidelity* and *low-fidelity*. In the modelling and simulation industry the term fidelity is lacking an absolute definition. Actually, it is used in a contradicting and a confusing manner. The definition used for now is according to Z.C. Roza [29]: *"Fidelity measurement is somehow based on the comparison between reality, or some abstraction of reality, and the simulated representation of this reality"*. For the sake of clarity, when a flight simulator has a high-fidelity it matches the actual aircraft to a very high degree. Different types of fidelity exist, i.e.:

1. Model fidelity: Match of the mathematical model input/output, this fidelity is assessed with a proof-of-match and is purely software based.

2. Objective fidelity: Match of measured motion cues, such as measuring the motion cues with an IMU and comparing it to the aircraft IMU data.

3. Perceptual fidelity: Match of the perceived cues in the simulator with the perceived cues in the actual vehicle, with this fidelity the human limits, such as perception thresholds, are taken into account.

4. Behavioural fidelity: Match of pilot behaviour.

2.1.2. Motion Cues

The term *motion cues* is commonly used in the simulator industry. Therefore, a well understanding about *motion cues* is required. Looking up the internet revealed several definitions. Each slightly different from one another. This section provides three definitions for the term *cue*, to see it from different perspectives. In the Webster's Encyclopedic Dictionary the word *cue* is defined as follow [28]:

> "*... a hint meant to guide behaviour.*"

R.H. Forgus and L.E. Melamed define *cue* in a slightly different way [22]:

> "*... stimuli which have* cue *value, i.e., which trigger some kind of reactive or adaptive action.*"

M. Baarspul defines a *cue* more related to an aircraft or flight simulator [18]:

> "*A cue is a cluster of sensory stimuly[i] - acting on the pilot via any of his sensory channels - closely correlated with a characteristic of the aeroplane and its behaviour, which is relevant to the pilot when flying the aeroplane.*"

When mentioning *motion cue*, the sensory stimuli required for motion perception is referred to.

2.1.3. Motion Cue Errors

The cueing of motions is a complicated process in which errors are not excluded. Grant [21] categorizes motion cue errors into four groups:

1. *False Cues;* either a motion cue that is in opposite direction to that experienced in an aircraft, a motion cue that occurs in the simulator which normally would not be experienced in the aircraft or a relatively high frequency distortion.

2. *Missing Cues;* a motion cue that is normally expected in an aircraft but missing in the flight simulator.

3. *Phase Errors;* for returning the motion platform to its neutral position a so called washout filter is used. This washout filter is n-order high-pass filter in which phase leads may be generated. Near the break frequency of the high-pass filter these phase errors may be noticed by the pilot.

4. *Scaling Errors;* in order to simulate an aircraft movement and also stay within the physical limits of the flight simulator, the movements are scaled down. Sometimes the motion is scaled too much resulting in scaling errors.

2.2. Motion Cueing Algorithm

Whenever a flight simulator is equipped with a moving motion platform, this platform needs to be connected to the EOM. This connection between motion platform and EOM is usually by means of a so called Motion Cueing Algorithm (MCA). This MCA takes the signals that leave the EOM and transforms these into positions and orientations of the Motion Reference Point (MRP). The parameters in this MCA are tuned in such a way that maximum cueing is achieved while keeping the simulator within the available motion space. In modern simulators different cueing algorithms can be implemented, these can become extremely advanced by including predictive control. However, most of these algorithms originate from the same, and known, Classical Washout Algorithm (CWA). This CWA was already developed in 1985 [16]. The CWA is, due its simplicity, the common used MCA for flight simulation, see Figure 2.2. The SRS also uses this CWA for motion cueing, therefore, this algorithm will be explained in detail in this section. The CWA basically consists of three channels, namely the specific force channel, tilt coordination channel and rotational channel. These channels are explained in detail next.

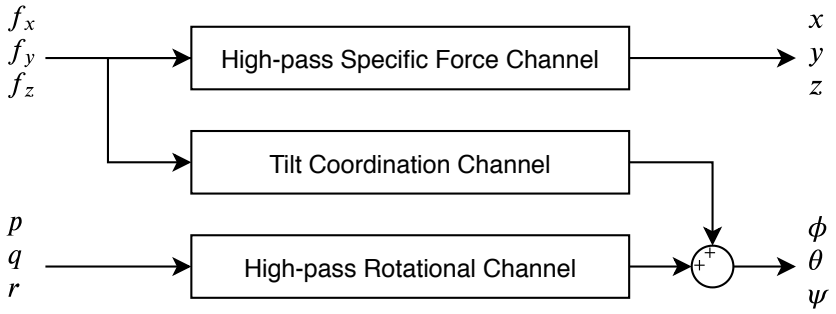

Figure 2.2: Classical Washout Algorithm

High-Pass Specific Force Channel

Usually the high-pass specific force channel handles 3 DOF, namely surge, sway and heave, see Figure 2.3. As surge, sway and heave are all translations, this channel is often also referred to as the high-pass translational channel. The signals entering this channel are the specific forces, which originate from the EOM. After these signals enter, the first step is to scale these. The scaling is used to decrease the overall amplitude of the input signals for mainly two reasons. Firstly, if the input is not scaled, the motion space limits are easily reached. However, over-scaling may result in no-motion. Secondly, people would perceive the motions as too intense if this input is not scaled. The actual high-pass filter filters accelerations, whereas the inputs of the channel are the specific forces. Specific force is the non-gravitational force per unit mass, so to make these into accelerations the gravitational components need to be added. This is done with the summation block after the scaling (Figure 2.3). Here g_S represent the different gravitational components, where:

$$g_S = \begin{bmatrix} -g\sin\theta \\ g\cos\theta\sin\phi \\ g\cos\theta\cos\phi \end{bmatrix} \tag{2.1}$$

After this summation, the signals are acceleration in x, y and z directions, however, these accelerations are in body reference frame. As filtering is only effective in the inertial frame,

these acceleration components need to be transformed from the body- to the inertial-frame. This transformation is done with the T_{Ib} block. Now the signals are finally ready to be filtered. The filter used is a third order high-pass filter. A high-pass filter is used so that only the fast motions are cued, as the slow motions will require too much motion space to be simulated. As the name already implies, only high frequency signals are passed through, whereas the low frequency signals are blocked. The reason for using a 3^{rd} order filter is that this filter is able to washout a step on specific force, this occurs for example during takeoff. This washout ensures that the motion platform always returns to its neutral position. This can be proven by the Final Value Theorem:

$$\begin{aligned}\lim_{t\to\infty} x(t) &= \lim_{s\to 0} sX(s) \\ &= \lim_{s\to 0} s(HP3(s)\frac{1}{s})\frac{1}{s^2} \\ &= \lim_{s\to 0} s(\frac{K\cdot s^2}{s^2+2\zeta\omega_n s+\omega_n^2}\frac{s}{s+\omega_b}\frac{1}{s})\frac{1}{s^2} \\ &= 0\end{aligned} \tag{2.2}$$

In this proof the $1/s$ indicates that a step signal is used and the $1/s^2$ integrates the signal twice to get position instead of acceleration. With this it is proven that a 3^{rd} order high-pass filter ensures that the motion platform returns back to its neutral position after a step input. The last step of the specific force channel is to integrate the signal leaving the high-pass filter twice in order to get positions. These positions are the x, y and z positions of the flight simulator platform.

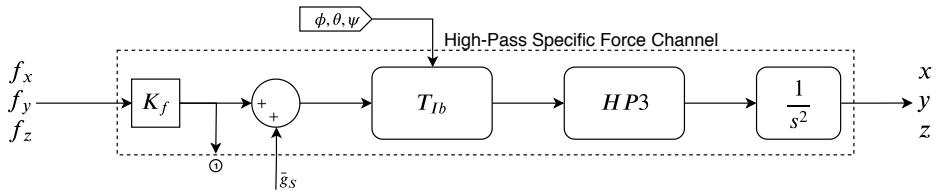

Figure 2.3: CWA - Specific Force Channel

Tilt Coordination Channel

Sustained specific forces are sensed by the pilot as a long-term change in magnitude and direction of the specific force in the absence of rotational motion [16]. Unfortunately, just a standard hexapod is not able to simulate these sustained specific forces, as of the limitations in motion space. However, on Earth there exists a continuous acceleration, which is the gravity. The gravitational force is used in the tilt coordination channel, by tilting the motion platform in such a way that the pilot experiences a continuous specific force. For example, when performing a take-off, the airplane experiences a sustained acceleration, to mimic this the motion platform is slowly tilted upwards such that the gravitational component pulls the pilot back in its seat (Figure 2.4).

As mentioned, this tilt coordination channel only simulates the sustained specific forces, to do so, a low-pass filter is used to filter out the high-frequency content of the signal. This low-pass filter is also the first block in the tilt coordination channel, see Figure 2.5. Hereafter, the filtered signal is transformed into simulator tilt angles that represent these specific forces. Basically this tilt coordination channel rotates the simulator, however, it is important that these rotations are not experienced by the pilot as this would result in false cues.

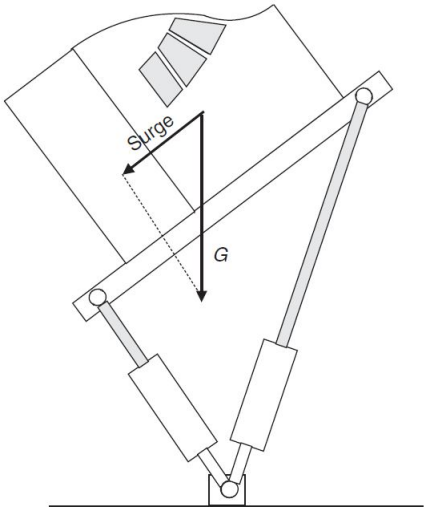

Figure 2.4: Tilting the motion platform upwards to provide surge acceleration [3]

In order to ensure that this tilting stays below the vestibular thresholds (Section 3.3) a rate limiter can be introduced. This rate limiter is also the last block of the tilt coordination channel, the resulting angles are added to the angles of the rotational channel, which will be explained next.

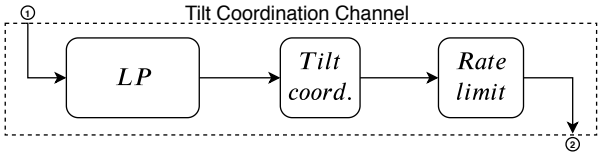

Figure 2.5: CWA - Tilt Coordination Channel

High-Pass Rotational Channel

The high-pass rotational channel deals with the aircraft rotational rates. These rates come from the EOM and are the roll-, pitch- and yaw rate. The rotational channel discussed here is based on the CWA developed initially by Reid and Nahon [16]. Instead of using rotational rates, rotational accelerations could be used as well as input to the channel. The SRS for example also uses rotational accelerations, however, this itself has some implications, which will be discussed. For similar reasons as with the specific force channel, the first step is to scale the rotational rates from the EOM. The resulting signals, however, are in body reference frame. Therefore, a transformation from body to Euler frame is performed. This transformation is indicated in Figure 2.6 as T_{Eb}. If rotational accelerations were used the partial derivative of this transformation would have been used, namely $T_{Eb}\dot{\omega} + \dot{T}_{Eb}\omega$. After this transformation the signals can be filtered, also here only the high-frequency content of the signal is simulated. Now a second-order high-pass filter is used in order to even washout steps on rotational rates.
The next step is to integrate the filtered signals to get simulator angles. If rotational accelerations were the inputs to this channel, a double integration would have been necessary. The resulting angles are summed with the angles from the tilt coordination channel, which together gives the simulator tilting angles.

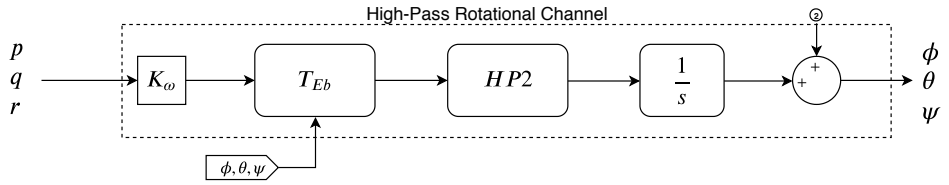

Figure 2.6: CWA - Rotational Channel

The resulting position coordinates and angles are send to the motion platform, which is responsible for actually moving the simulator through space. The motion platform kinematics is, therefore, elaborated in next section.

2.3. Motion Platform

2.3.1. History of Motion Platforms

In approximately 100 years the flight simulation industry experienced an enormous evolution. In these years many inventors have been busy with flight simulation technology. The first approach on building a flight simulator was by anchoring a real aircraft to the ground, this approach was already in 1910 by Sanders Teacher [5]. He used a modified aircraft that was positioned somewhere in an exposed field, such that it faced the wind. With this approach the trainee was able to practice control responses from the wind. In the same year two other approaches were developed as well. The first one was The Walters machine, which did not rely on wind, instead it used disturbances that were created by the instructor. The student tried to maintain equilibrium by using the controls that were connected by wires and pulleys to the frame [14]. Antoinette used a similar approach but used two half sections of a barrel that were moved by the instructor [20]. These movements represented the pitch and roll of the aircraft. None of these three approaches were successful that time, the wind was not reliable and the phase between the instructor and student was too big and created a mismatch.

Since 1920 experiments using compressed air actuators and/or electric motors started. These motion systems had the intention to mimic the feel of a real aircraft. However, all these experiments failed due to the lack of realistic dynamic responses. Nine years later the first effective ground based pilot training device was created. This device, which was designed by Ed Link, is nowadays known as the Link Trainer [17]. Several developments took place in the years after.

In the early 1950's the modern flight simulator started taking its form [20]. Yet, these simulators did not yet include motion systems. These motion systems started coming back in the late 1950's, with the production of 2 Degree of Freedom (DOF), 3 DOF and 4 DOF systems. In the early 1960's Link developed a 3 DOF system, this became a standard in the flight simulation industry for quite some years.

In 1965 Steward developed a 6 DOF motion platform that was able to effectively combine linear and angular motions [4]. This platform is often referred to as hexapod. Hexapod indicates the six independent hydraulic or electric legs of the motion platform. There have been major improvements in the performance of actuator systems, as well as the geometry of these platforms. However, the basic configuration of this hexapod remained unchanged to today.

In modern flight simulators, the cabin is usually placed on top of the payload platform. For high fidelity flight simulators it can happen that these exceed a mass of 18,000 kg [3].

Furthermore, the centre of gravity of the cabin is usually above the mounting points of the actuators, which illustrates the extreme demands for these mechanical systems.
A pilot in an aircraft experiences both linear and angular motions along the three body axes of the aircraft. A hexapod motion platform is able to simulate linear motions, namely: surge, sway and heave, as well as angular motions: roll, pitch and yaw. Together these six different motion cues make up for 6 DOF. These motion cues are simulated using the actuators attached to the motion platform. One of the requirements of these actuators is having enough power to smoothly create these motion cues. Nowadays, motion platforms are usually equipped with electrical actuators, however, in the past hydraulic actuators were used instead. These hydraulic actuators had several disadvantages such as the amount of maintenance and use of dangerous hydraulic fluids.
As the motion platform is moved by the actuators, these actuators also define the limitations of the motion platform. These limitations are in motion space, defined by the actuator lengths, as well as the maximum actuator velocities and accelerations. These actuators are controlled usually by a motion computer that uses the output from the MCA, which contains position coordinates (x, y and z) and angles (ϕ, θ and ψ). These position coordinates and angles altogether describe the orientation of the motion platform.

2.3.2. Actuator Space

The MCA parameters are usually tuned such that the motion platform stays within its physical limits. This tuning can be done to some extend offline by looking at the actuator responses of a particular test signal. In order to do so, the MCA outputs must be expressed in actuator space. This transformation is derived next.
One way of transforming the DOF-space into the actuator space is by expressing the actuators as vectors. Figure 2.7 illustrates the hexapod actuators as vectors. In the next derivation the payload platform centroid is the Motion Reference Point (MRP).

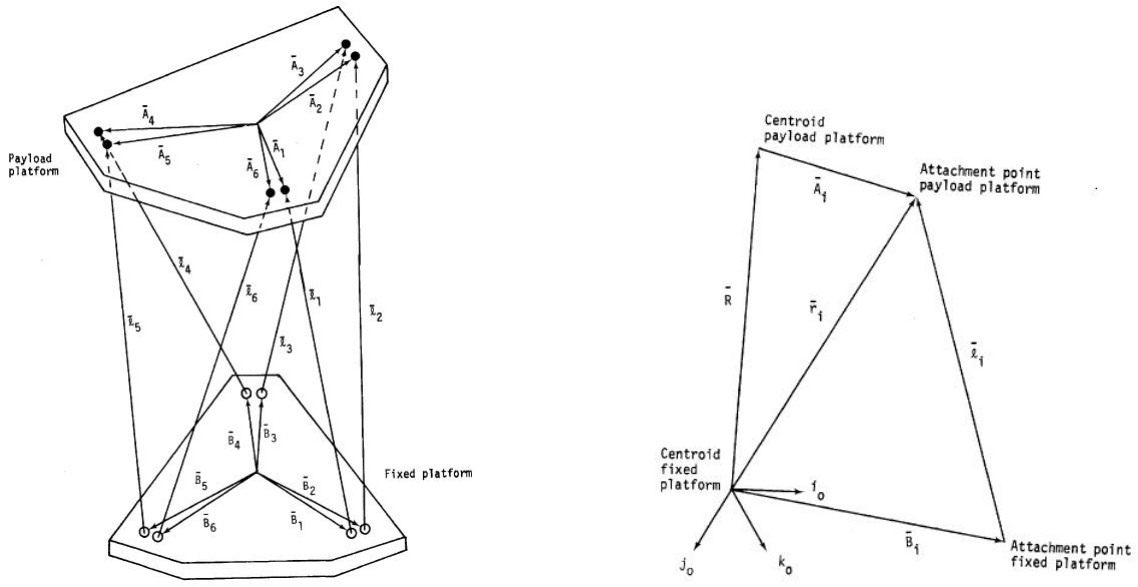

(a) Motion Platform Orientation (b) Vector relationship for actuator i

Figure 2.7: Vector relationships between the origins of each coordinate system and the actuator attachment points of a hexapod motion platform [13]

From Figure 2.7b an expression for each actuator with respect to the centroid of the payload

platform and fixed platform can be derived. From there the following two vector relations are derived:

$$\boldsymbol{r}_i = \boldsymbol{A}_i + \boldsymbol{R} \tag{2.3}$$

$$\boldsymbol{r}_i = \boldsymbol{B}_i + \boldsymbol{l}_i \tag{2.4}$$

Combining these equations gives the following relationship:

$$\boldsymbol{l}_i = \boldsymbol{A}_i + \boldsymbol{R} - \boldsymbol{B}_i \tag{2.5}$$

This equation, however, is derived with respect to the fixed reference frame. Whereas, the known $\boldsymbol{A_{i,S}}$ are defined with respect to the moving simulator frame. Therefore, an Euler transformation is required to determine the vectors $\boldsymbol{A}_i$. The following Euler transformation is used:

$$\boldsymbol{A}_i = T_{Ib}\boldsymbol{A}_{i,S} \tag{2.6}$$

where:

$$T_{Ib} = \begin{bmatrix} \cos\psi\cos\theta & \cos\psi\sin\theta\sin\phi - \sin\psi\cos\phi & \cos\psi\sin\theta\cos\phi + \sin\psi\sin\phi \\ \sin\psi\cos\theta & \sin\psi\sin\theta\sin\phi + \cos\psi\cos\phi & \sin\psi\sin\theta\cos\phi - \cos\psi\sin\phi \\ -\sin\theta & \cos\theta\sin\phi & \cos\theta\cos\phi \end{bmatrix} \tag{2.7}$$

Substituting Equation 2.6 into 2.5 yields:

$$\boldsymbol{l}_i = T_{Ib}\boldsymbol{A}_{i,S} + \boldsymbol{R} - \boldsymbol{B}_i \tag{2.8}$$

Now the actuator lengths can easily be determined by determining the magnitudes of the $\boldsymbol{l}_i$ vectors.

$$|\,\boldsymbol{l}_i\,| = \sqrt{l_{i,x}^2 + l_{i,y}^2 + l_{i,z}^2} \tag{2.9}$$

This concludes the derivation for determining the actuator lengths. These lengths can now be compared with the maximum and minimum lengths to determine whether the flight simulator stays within the available motion space. Another limitation might be the maximum actuator speed and acceleration, these can be determined simply by taking the derivative of the actuator lengths.

3
Motion Perception

Motions acting on the human body result in some kind of signals in the central nervous system inside the brain. Motion can be perceived with different organs, such as the vestibular system, eyes or by touch. This chapter focuses on the motion perception with the vestibular system, which is described in Section 3.1. To employ the PEMD this vestibular system needs to be modelled (Section 3.2). Lastly, the perception thresholds are elaborated in Section 3.3.

3.1. Vestibular System

Inside the human brain the central nervous system is the part where the sense of motion, perceived by a human, is processed. The signals entering are emanated from visual (eyes), haptic (touch) and/or vestibular sensors. This chapter only covers the vestibular system and its representative model. The vestibular system is responsible for the perception of specific forces and angular accelerations. This particular system is extremely important for the perception of motion in the absence of vision. This vestibular organ can generally be divided into two parts; the Otoliths for perceiving the translational specific forces and the Semi-Circular Canals for perceiving the angular accelerations.

3.1.1. Otolith

Specific force is defined as the non-gravitational force per unit mass and is perceived by the otolith. The otolith, which is located in the inner ear, consists of two parts. Firstly, the utricle, which share common base with the Semi-Circular Canals, is for vertical heave sensitivity. Secondly, the downward extension of the utricle, called the saccule. This saccule is for horizontal sensitivity, thus surge and sway specific forces. Both the utricle and saccule have vestibular hair cells, which are called the macula [15].
Each macula is covered with an otolithic membrane. On top of this membrane are otoconia, which are calcium carbonate crystals. The purpose of these crystals is to make the otolithic membrane heavier than the structures and fluids that surrounding it. So when a specific force is applied to the body the crystals will shear the otolithic membrane, which causes the stereocilia (vestibular hairs) to bend. Bending of these vestibular hair cell will alter the neuron firing rate to the central nervous system in the brain.
The otolith itself is, however, not capable to make a distinction between head tilt and sustained acceleration. In flight simulators this imperfection of the vestibular organ is used to simulate linear accelerations. Which is also the reason for the tilt coordination channel in the MCA. To pursue this perception of acceleration, the motion platform is slowly tilted, such that the gravitational vector enforces the stereocilia in a certain direction, creating the illusion of constant acceleration. This is also the reason for the rate limiter that is present in the tilt coordination channel, this enforces the rotational rate to stay below the rotational perception threshold so that this rotation is not experienced.

3.1.2. Semi-Circular Canals

Angular accelerations are perceived by the Semi-Circular Canals (SCC), which consists of three circular canals in approximately three orthogonal planes. These canals are filled with a liquid that is called endolymph. Each canal has an enlargement called the ampulla. In this enlargement there is a gelatinous membrane, which is called the cupula. This cupula covers the crista ampullaris which itself contain hair cells [15].
When a rotational acceleration is applied to the body and thus outside the SCC, the fluid lags behind and moves relative to the cupula. This moving fluid causes the cupula to deflect in opposite direction to the direction of rotation. This deflection of the cupula alters the neural firing rate in the ampullary nerve fibers toward the central nervous system inside the brain. This change in neural firing rate indicates an angular acceleration. However, when the rotational acceleration is sustained and constant, the fluid flow velocity becomes equal to the rotational rate of the body. When this happens, the cupula will not be deflected anymore and no rotational rate is detected.
The mass of the cupula is equal to that of the endolymph, which makes the Semi-Circular Canals almost completely insensitive to linear accelerations.

3.2. Perception Model

The brain is a complicated system, in which some parts, such as the vestibular system, can be modelled by transfer functions. The reason for deriving these linear transfer functions for the vestibular system is that these models will be used in Chapter 6 to extend the EMD method with a perception model. The representative models of the vestibular system that will be presented next have been derived from experiments of large groups of participants. Apart from humans, numerous experiments with squirrel monkeys have been performed as well [2]. Next the resulting transfer functions of the vestibular system are presented.

3.2.1. Otolith Model

The representative model for the Otolith (OTO) is based on an accelerometer with over-damped mass-spring-dashpot characteristics.

$$H_{OTO}(s) = \frac{K(\tau_1 s+1)}{(\tau_2 s+1)(\tau_3 s+1)} \tag{3.1}$$

The parameters of this otolith model have been found by means of experiments. However, as several institutions have performed these experiments, some of which even with slightly different setups, the resulting parameters tend to vary. The parameters used in this report are based on Reid and Nahon [16], and are: K = 0.4, τ_1 = 13.2 s, τ_2 = 5.33 s and τ_3 = 0.66 s. It is maybe not the most up-to-date model, however, it provides an accurate enough representation to illustrate the ultimate goal of this report, which is the development of the PEMD analysis.

3.2.2. Semi-Circular Canal Model

The representative model for the Semi-Circular Canals (SCC) is based on an overdamped torsion-pendulum model.

$$H_{SCC}(s) = \frac{\tau_1 \tau_2 s^2}{(\tau_1 s+1)(\tau_2 s+1)(\tau_3 s+1)} \tag{3.2}$$

Also here different formulations exists, however, again the model from Reid and Nahon is used. The parameters associated to this transfer function are: τ_1 = 30.0 s, τ_2 = 10.2 s and τ_3 = 0.1 s.

3.3. Perception Thresholds

Apart from motion perception dynamics, perception thresholds are also to be taken into account. The threshold for motion perception is the value that motion is not perceived anymore by humans. Two different thresholds exist; the upper and lower thresholds. The upper threshold is the value at which the stimulus switches from not perceived to perceived, the lower threshold is when the opposite occurs. As will become clear later in the report, these perception thresholds play a crucial part in the development of the PEMD.
The inclusion of these perception thresholds becomes apparent when analyzing test signals. So is it possible that a non-zero input into the model gives a non-zero output signal, however, this does not guarantee that this motion cue is actually perceived. For example, this motion cue could have been below the perceivable threshold and remain unnoticed. Unfortunately the problem with these thresholds is that these are not just a constant value. In reality many factors, such as workload, are involved. Furthermore, these thresholds tend to vary per frequency.
As it would be too ambitious to incorporate all these effects and because the PEMD requires linear models, these thresholds are chosen as constants somewhere in the normal operational range [6, 7]. The perception thresholds as given in Table 3.1 will be the ones used for the remainder of this report.

Table 3.1: Absolute Thresholds for Six Motion Axes [6]

Sensor	Motion	Threshold
OTO	Surge	$7.42 \cdot 10^{-2}\ m/s^2$
	Sway	$7.43 \cdot 10^{-2}\ m/s^2$
	Heave	$1.23 \cdot 10^{-1}\ m/s^2$
SCC	Roll	$5.21 \cdot 10^{-3}\ rad/s$
	Pitch	$7.34 \cdot 10^{-3}\ rad/s$
	Yaw	$1.66 \cdot 10^{-2}\ rad/s$

This page is intentionally left blank.

4
Objective Motion Cueing Test

Chapter 2 discussed the general design of a flight simulator and how a MCA can control the motion platform. The performance of this MCA can be expressed in terms of fidelity. In the past this was by means of subjective tuning. However, modern simulators use objective tests, such as the Objective Motion Cueing Test, which is explained in Section 4.1. Hereafter, the actual test procedure is explained in Section 4.2. Lastly, the fidelity boundaries, which are necessary to rate the objective fidelity, are explained in Section 4.3.

4.1. OMCT Background

In the past, MDAs filter settings were tuned by means of subjective test. Herein, pilots had to fly certain missions after which they gave feedback to the tuning experts. These experts then changed some tuning parameters of the MDA, the pilot then had to fly again a certain manoeuvre. This process was repeated until the pilots were satisfied with the perceived motions. However, the problem is that every person perceives motion in a slightly different way. For example, perception thresholds may vary per person, furthermore, these thresholds can also depend on the pilot's task and workload [6]. This resulted in big differences in tuning values of similar flight simulators. The undesirability of purely subjective evaluation was already recognized in the 70s and different tuning procedures have been proposed since, such as; Sinacori [12], Schroeder [11] and Gouverneur [1].
All these developments resulted in the current state-of-the-art method for objective evaluation of the flight simulator's fidelity: the Objective Motion Cueing Test (OMCT). As of its successes the OMCT is now part of the *ICAO - Manual of Criteria for the Qualification of Flight Simulation Training Devices* [9]. This method increases the transparency of the tuning process. Rather than the time domain, each OMCT test is performed in the frequency domain by analyzing the response to 12 different sine-wave input signals. These sine-wave input signals are generated by a signal generator, see Figure 4.1, and are directly inserted to the MCA.

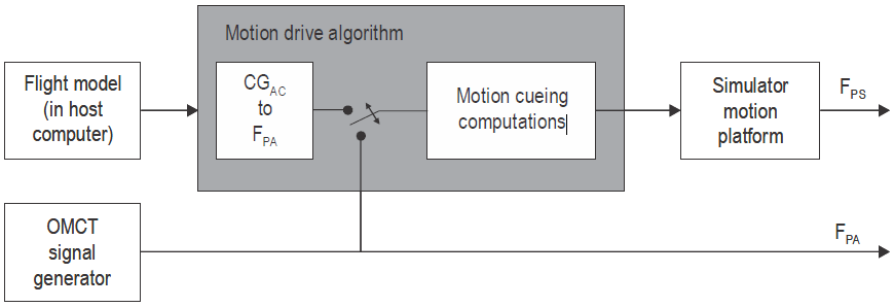

Figure 4.1: Objective Motion Cueing Test [9]

The OMCT then analyses the difference between the input signal (F_{PA}) and the resulting output measured at the pilot station on the motion platform (F_{PS}). These differences give a magnitude and phase distortion, which are then plotted onto Bode plots. ICAO's OMCT

Manual also provides desired boundaries, with these the objective fidelity can be assessed. In total OMCT consists of 10 separate tests which measures either direct outputs, such as *roll due to roll*, or cross-coupling outputs, such as *roll due to sway*. Altogether, this method gives a detailed picture of the combined performance of the MCA and motion platform dynamics [23].

4.2. OMCT Test Procedure

As mentioned, OMCT consists of 10 individual test, where each test injects and measures 12 separate frequencies. The 10 OMCT test defined by ICAO are:

- OMCT test 1: *Pitch response due to pitch input*;
- OMCT test 2: *Surge response due to pitch input*;
- OMCT test 3: *Roll response due to roll input*;
- OMCT test 4: *Sway response due to roll input*;
- OMCT test 5: *Yaw response due to yaw input*;
- OMCT test 6: *Surge response due to surge input*;
- OMCT test 7: *Pitch response due to surge input*;
- OMCT test 8: *Sway response due to sway input*;
- OMCT test 9: *Roll response due to sway input*; and
- OMCT test 10: *Heave response due to heave input.*

Each of these tests contain 12 test frequencies, which are inserted either to the specific force channel or the rotational channel. For the specific force channel, the following specific force equation is defined to model the sine-wave input signals.

$$f_{PA}^{x,y,z} = A\sin(\omega t) \tag{4.1}$$

For the rotational channel, the following angular acceleration equations are defined to model the sine-wave input signals.

$$\dot{p}_{PA} = -A\omega^2 \sin(\omega t) \tag{4.2}$$

$$\dot{q}_{PA} = -A\omega^2 \sin(\omega t) \tag{4.3}$$

$$\dot{r}_{PA} = -A\omega^2 \sin(\omega t) \tag{4.4}$$

The associated input frequencies and amplitudes for each test are shown in Table 4.1. The test frequencies are the same for each of the OMCT test.
Figure 4.1 visualizes where the signals from the OMCT signal generator are inserted to the MDA. These input sine-wave signals are processed trough the MCA and, hereafter, simulated by the motion platform. The response to each of these input signals is measured with accelerometers at the OMCT reference point, which is 35 cm below the DERP. Research has shown that offline tuning can also be performed, which avoid the complexity to some extent [19]. Frequency response functions are used to relate the output response to the input. A complete overview of these functions for each test is shown in Appendix F. These transfer functions, H, are computed in the frequency domain. A fast fourier transform is used to compute these frequency response functions, which results in complex numbers. With this complex number a magnitude distortion, $|H|$, and phase distortion, $\angle H$, between F_{PA} and F_{PS} can be determined. These distortions can then be plotted onto Bode plots and checked whether these are between the provided fidelity boundaries.

Table 4.1: Specific force and rotational input amplitudes [9]

Frequency signal number	Frequency ω $[rad/s]$	Specific force amplitude A $[m/s^2]$	Angular acceleration amplitude $A\omega^2$ $[°/s^2]$
1	0.100	1.00	0.060
2	0.158	1.00	0.150
3	0.251	1.00	0.251
4	0.398	1.00	0.398
5	0.631	1.00	0.631
6	1.000	1.00	1.000
7	1.585	1.00	1.585
8	2.512	1.00	2.512
9	3.981	1.00	3.981
10	6.310	1.00	6.310
11	10.000	1.00	10.000
12	15.849	1.00	10.000

4.3. OMCT Boundaries

The fidelity boundaries for magnitude and phase distortion have been defined by ICAO. These boundaries have been determined by simulating a limited number of FSTD with either electric of hydraulic driven motion platforms. As there are still some concerns about the current boundaries, future changes of these boundaries are not ruled out. The boundaries used in this report boundaries defined by ICAO [9], which was last updated in 2015. The so-called fidelity boundaries indicate for each OMCT test frequency if the FSTD response can be classified as *high-fidelity* or *low-fidelity*. Lies the response between the boundaries, then it can be classified as high-fidelity, if not, as low-fidelity. Figure 4.2 visualizes the fidelity boundaries for the roll response due to a roll input.

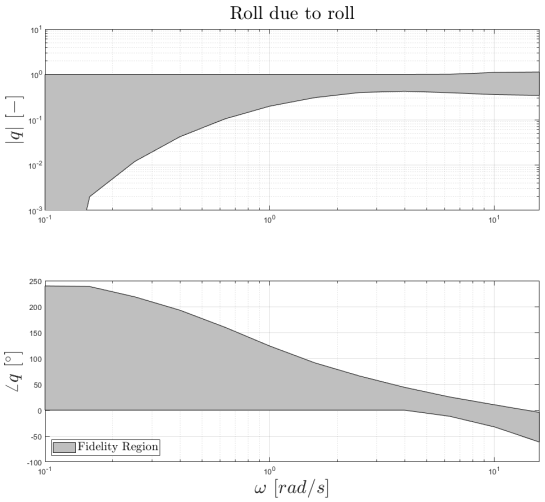

Figure 4.2: OMCT Fidelity Boundaries for Test 3

This page is intentionally left blank.

5
Eigenmode Distortion

The previous chapter discussed the Objective Motion Cueing Test. Here an alternative to this evaluation method is presented, the Eigenmode Distortion (EMD) analysis. Firstly, the EMD methodology is elaborated in Section 5.1. Hereafter, an eigenvector analysis is performed for the symmetric model of the Cessna Citation 500, Section 5.2. This section illustrates the reasons for linearizing both EOM and MCA. Then the actual linearization is performed for the asymmetric EOM (Section 5.3.1) and MCA (Section 5.3.2). The aircraft model and MCA model need to be combined into a single system, this is done in Section 5.3.3. Finally, Section 5.3.4 contains an eigenvector analysis performed on the asymmetrical system.

5.1. Eigenmode Distortion Methodology

Despite the power of OMCT, this method has its shortcomings. First of all, the sine-wave input signal does not represent realistic motion experienced during flight. Secondly, the simulated vehicle dynamics are not included in this test. However, research revealed that this might have an influence on the OMCT results [26], and finally, the response to each signal is studied in isolation, while aircraft motions are actually linked through dynamics. The EMD method, developed by Miletović et al [8], is an objective evaluation method to address these shortcomings. EMD investigates the distortion of the motion cues imposed by the MCA in terms of eigenvectors, which represent the dynamic modes, such as phugoid and short-period. Figure 5.1 illustrates how the EMD method differs from the OMCT method.

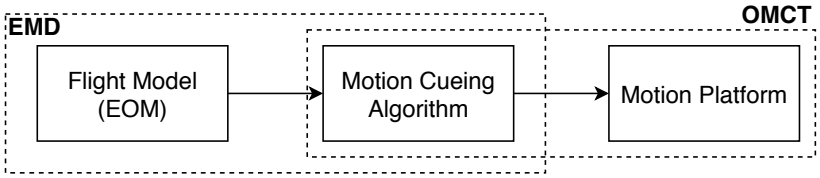

Figure 5.1: Domain of Evaluation Method

EMD investigates the motion cue distortions in term of eigenvectors. However, to get these eigenvectors a linear model of the complete system is required. For this, the EMD uses linear models for both EOM and MCA. The linear model structure for the EOM in asymmetric flight is given in Equations 5.1 to 5.3. These EOM describe the dynamic behaviour of the aircraft and represent the motion as experienced by the pilot in the aircraft. In these equations, the Δ indicates that these motions are actually perturbations relative to a trimmed and linearized initial condition. The $\Delta \boldsymbol{x}^{EOM}$ state vector is exactly known from flight dynamics and is further elaborated in Section 5.3.1.

$$\Delta \dot{\boldsymbol{x}}^{EOM} = A^{EOM} \Delta \boldsymbol{x}^{EOM} + B^{EOM} \Delta \boldsymbol{u}^{EOM} \tag{5.1}$$

$$\Delta \boldsymbol{x}^{EOM} = \begin{bmatrix} \Delta v_s & \Delta \phi & \Delta p_b & \Delta r_b \end{bmatrix}^T \tag{5.2}$$

$$\Delta \boldsymbol{u}^{EOM} = \begin{bmatrix} \Delta \delta_a & \Delta \delta_r \end{bmatrix}^T \tag{5.3}$$

With a flight simulator motions resulting from the EOM are cued by a MCA. This MCA is for the EMD analysis also linearized. However, the exact formulation of the $\Delta \boldsymbol{x}^{MCA}$ state vector depends on the MCA used. In Section 5.3.2 the state space for the CWA is derived.

$$\Delta \dot{\boldsymbol{x}}^{MCA} = A^{MCA} \Delta \boldsymbol{x}^{MCA} + B^{MCA} \Delta \boldsymbol{u}^{MCA} \tag{5.4}$$

$$\Delta \boldsymbol{u}^{MCA} = \begin{bmatrix} \Delta f_{y_p}^{EOM} & \Delta \dot{p}^{EOM} & \Delta \dot{r}^{EOM} \end{bmatrix}^T \tag{5.5}$$

In order to make EMD possible the two linear systems need to be coupled into one single system. This single system is then only exited by means of pilot inputs $\Delta \boldsymbol{u}^{EOM}$ which are the control surface deflections. In order to effectively combine the two systems a coupling between the two is designed in Section 5.3.3, which will have the form as in Equations 5.6 to 5.8

$$\Delta \dot{\boldsymbol{x}}^{EMD} = A^{EMD} \Delta \boldsymbol{x}^{EMD} + B^{EMD} \Delta \boldsymbol{u}^{EMD} \rightarrow \begin{bmatrix} \Delta \dot{\boldsymbol{x}}^{EOM} \\ \Delta \dot{\boldsymbol{x}}^{MCA} \end{bmatrix} = \begin{bmatrix} A^{EOM} & 0 \\ A^{COUP} & A^{MCA} \end{bmatrix} \begin{bmatrix} \Delta \boldsymbol{x}^{EOM} \\ \Delta \boldsymbol{x}^{MCA} \end{bmatrix} + \begin{bmatrix} B^{EOM} \\ B^{COUP} \end{bmatrix} \Delta \boldsymbol{u}^{EOM} \tag{5.6}$$

$$\Delta \boldsymbol{y}^{EMD} = C^{EMD} \Delta \boldsymbol{x}^{EMD} + D^{EMD} \Delta \boldsymbol{u}^{EMD} \rightarrow \Delta \boldsymbol{y}^{EMD} = \begin{bmatrix} C^{EOM} & 0 \\ C^{COUP} & C^{MCA} \end{bmatrix} \begin{bmatrix} \Delta \boldsymbol{x}^{EOM} \\ \Delta \boldsymbol{x}^{MCA} \end{bmatrix} + \begin{bmatrix} D^{EOM} \\ D^{COUP} \end{bmatrix} \Delta \boldsymbol{u}^{EOM} \tag{5.7}$$

$$\Delta \boldsymbol{y}^{EMD} = \begin{bmatrix} \Delta f_{y_p}^{EOM} & \Delta p^{EOM} & \Delta r^{EOM} & \Delta f_{y_p}^{MCA} & \Delta p^{MCA} & \Delta r^{MCA} \end{bmatrix}^T \tag{5.8}$$

This combined linear system result is used for the EMD analysis. After determining the eigenvectors of the A^{EMD} a transformation is performed. This transformation allows to relate the eigenvectors of the aircraft model and MCA to one another. By analyzing these resulting eigenvectors, the magnitude and phase distortion between aircraft and simulator can be visualized. These distortions are caused by the MCA and depend on the chosen settings of this MCA.
This report focuses mainly on the lateral aircraft model, however, to illustrate the actual eigenvector analysis the analysis is first performed for the eigenvectors of the symmetric aircraft model in next section. This section aims to illustrate the reasons for linearizing the EOM and MCA to perform the eigenvector analysis. The complete derivation of this linear model for the symmetric aircraft model is not included in this chapter, but can be found in Appendix C. As becomes evident from Appendix C, the formulas become quite elaborate and, therefore, the Δ notation is dropped for the remaining of this chapter, but in fact represent perturbations from their trimmed and linearized conditions.

5.2. Eigenvector Analysis for Symmetric Model

Usually when analyzing aircraft eigenmodes, eigenvalues are used. These eigenvalues give information about the nature of the mode. For example, a Dutch Roll has two complex poles, meaning that it is a periodic mode or the Spiral mode has one real pole on close to the imaginary axis, meaning that it is an aperiodic mode of slow nature.

$$A^{EMD} V = \lambda^{EMD} V \tag{5.9}$$

Additionally eigenmodes can be analyzed in terms of eigenvectors, Equation 5.9. These eigenvectors provide information on how different states interact in each eigenmode. These can also be used to determine the distortions. In order to do so, first the eigenvectors of the A^{EMD} matrix need to be determined. These eigenvectors are expressed in the $\boldsymbol{x}^{EMD}$ states. However, the distortion analysis is between the specific forces and rotational rates from

the EOM and MCA. To get these, the eigenvectors can simply be multiplied with the C^{EMD} matrix.

$$V_y = C^{EMD} \cdot V \tag{5.10}$$

$$y = \begin{bmatrix} f_{x_p}^{EOM} & f_{z_p}^{EOM} & q^{EOM} & f_{x_p}^{MCA} & f_{z_p}^{MCA} & q^{MCA} \end{bmatrix}^T \tag{5.11}$$

Figure 5.2 is a visualization of this eigenvector analysis applied to the Cessna Citation 500 using the settings as described in [24], given in Tables A.1 and B.1. In here the solid lines represent the motion cue eigenvectors as experienced in the actual aircraft, furthermore, the dashed lines represent the motion cue eigenvectors as experienced in the flight simulator. Any phase and magnitude difference between these solid and dashed lines is, consequently, caused by the MCA. These plots can for example be used as tuning strategy to minimize the phase and magnitude distortion between the eigenvectors from the EOM and MCA.

One must realize that a comparison in magnitudes between specific forces and rotational rates is not possible as of their different dimensions. For example, the x specific force eigenvector has a much larger magnitude than the pitch rate eigenvector. However, it would be completely wrong to conclude from this that the specific force is therefore a more dominant motion cue. This is also part of the motivation of continuing the research into the EMD analysis and incorporating a pilot model (Chapter 6). Applying this pilot model reveals that actually the pitch rate is more dominant than the x specific force, which supports the statement that a comparison between magnitudes cannot be made at this stage between specific forces and rotational rates.

The magnitude distortion of an eigenvector can be defined by the ratio between EMD and MCA magnitudes, namely: $|\Delta| = \frac{|\Delta^{MCA}|}{|\Delta^{EOM}|}$. Furthermore, the phase distortions are defined by the angle between the eigenvector. If the eigenvector corresponding to the positive conjugate eigenvalues are visualised, counter-clockwise and clockwise phase distortion indicate phase lead and lag, respectively. From Figure 5.2a, which illustrates the short period eigenvectors, the following can be concluded; $f_{x_p}^{MCA}$ has a phase distortion of 24.3° lead (counter-clockwise) and magnitude distortion $|f_{x_p}| = \frac{|f_{x_p}^{MCA}|}{|f_{x_p}^{EOM}|} = 0.81$. Furthermore, $f_{z_p}^{MCA}$ has a phase distortion of 92.93° lead and magnitude distortion $|f_{z_p}| = 0.70$. Lastly, q^{MCA} has a phase distortion of 23.3° lead and magnitude distortion $|q| = 0.70$. These observation are supported by analyzing the time domain plots in Figure 5.3. These time traces are the result of a zero-input response, where the system has an initial condition of $2Re(v_i)$. In here v_i is the eigenvector associated to the eigenmode, so for the short period eigenvector is used to excite the short period eigenmode.

Previously the results for the short period were elaborated, however, the symmetric EOM also contain a so called phugoid eigenmode. The eigenvectors associated to this phugoid motion are illustrated in Figure 5.2b. Here the following can be concluded: $f_{x_p}^{MCA}$ has a phase distortion of 23.1° lag (clockwise) and magnitude distortion $|f_{x_p}| = 0.79$. Furthermore, $f_{z_p}^{MCA}$ has a phase distortion of 108° lag and magnitude distortion $|f_{z_p}| = 0.0006$. Lastly, q^{MCA} has a phase distortion of 94.2° lag and magnitude distortion $|q| = 0.11$. Interesting are these significant differences in magnitudes for both the z specific force and pitch rate, which in time domain (Figure 5.4) give an almost zero output. The reason for this is that a flight simulator has not enough motion space to simulate these components of the phugoid motion.

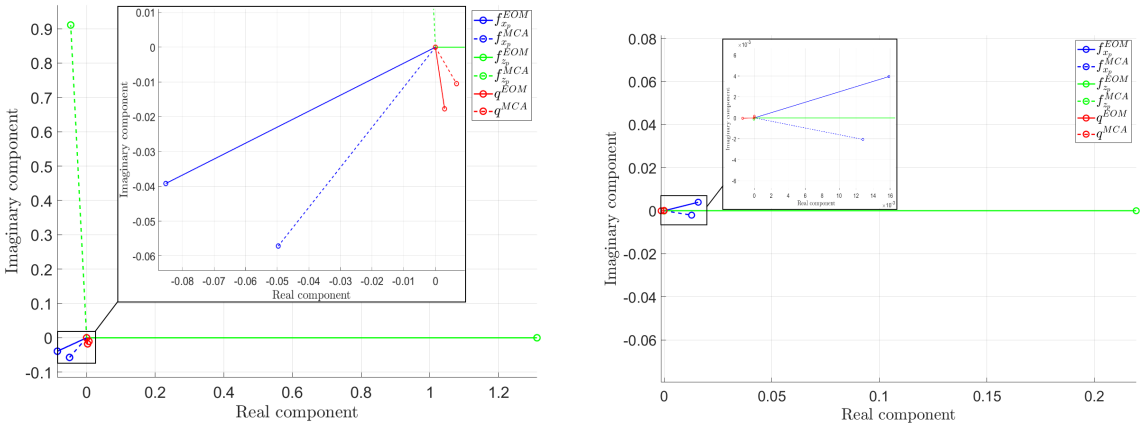

(a) Short Period (b) Phugoid

Figure 5.2: Example of Eigenvector Distortion Plots

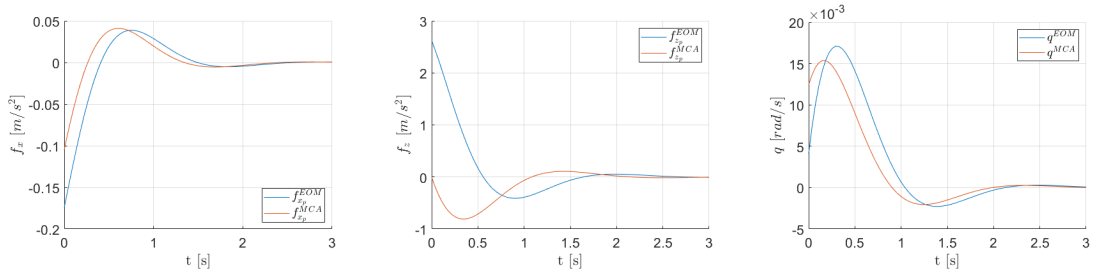

(a) (b) (c)

Figure 5.3: Time Histories of Short Period Eigenmode Excitation

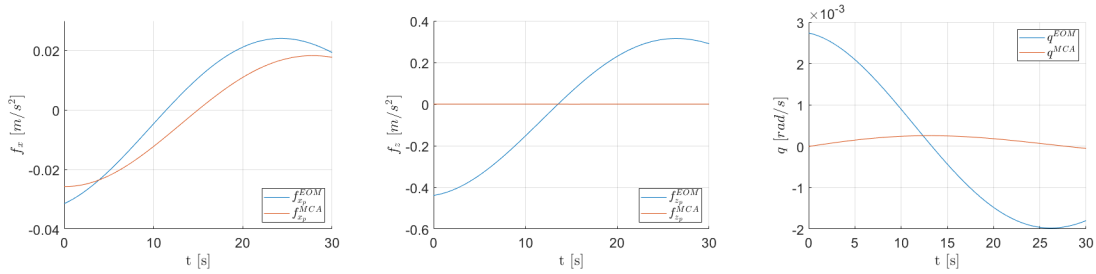

(a) (b) (c)

Figure 5.4: Time Histories of Phugoid Eigenmode Excitation

5.3. Asymmetric Model

Whereas previous section only illustrated the actual eigenvector analysis, this section will performs all steps involved for the asymmetrical model which are necessary to perform this analysis. Furthermore, it must be mentioned again that for all presented formulas the Δ notation is dropped but in fact represent perturbations from their trimmed and linearized conditions.

5.3.1. Aircraft Model

The dimensional asymmetric EOM, given in Equations 5.12 to 5.16, are the linearized equations that replicate the asymmetrical behaviour of the aircraft. These equations are derived

in the stability reference frame and assume a steady, straight, symmetric flight conditions with a flat and non-rotating Earth.

$$W\cos\theta_0\phi + Y_v v + Y_{\dot{v}}\dot{v} + Y_p p + Y_r r + Y_{\delta_a}\delta_a + Y_{\delta_r}\delta_r = m(\dot{v} + rV) \tag{5.12}$$

$$L_v v + L_p p + L_r r + L_{\delta_a}\delta_a + L_{\delta_r}\delta_r = I_{xx}\dot{p} - I_{xz}\dot{r} \tag{5.13}$$

$$N_v v + N_{\dot{v}}\dot{v} + N_p p + N_r r + N_{\delta_a}\delta_a + N_{\delta_r}\delta_r = I_{zz}\dot{r} - I_{xz}\dot{p} \tag{5.14}$$

$$\dot{\psi} = \frac{r}{cos\theta_0} \tag{5.15}$$

$$\dot{\phi} = p + r\tan\theta_0 \tag{5.16}$$

These dimensional EOM are transformed into a dimensionless state-space representation using the steps as in classical flight dynamics [10], yielding:

$$\begin{bmatrix} \dot{\beta} \\ \dot{\phi} \\ \frac{\dot{p}b}{2V} \\ \frac{\dot{r}b}{2V} \end{bmatrix} = \begin{bmatrix} y_\beta & y_\phi & y_p & y_r \\ 0 & 0 & 2\frac{V}{b} & 0 \\ l_\beta & 0 & l_p & l_r \\ n_\beta & 0 & n_p & n_r \end{bmatrix} \begin{bmatrix} \beta \\ \phi \\ \frac{pb}{2V} \\ \frac{rb}{2V} \end{bmatrix} + \begin{bmatrix} y_{\delta_a} & y_{\delta_r} \\ 0 & 0 \\ l_{\delta_a} & l_{\delta_r} \\ n_{\delta_a} & n_{\delta_r} \end{bmatrix} \begin{bmatrix} \delta_a \\ \delta_r \end{bmatrix} \tag{5.17}$$

The definition of the newly introduced symbols are recapitulated in Table 5.1.

Table 5.1: Symbols Appearing in the General State-Space Representation of Equation 5.17

	y_i	l_i	n_i
$i=\beta$	$\frac{V}{b}\frac{C_{Y_\beta}}{2\mu_b}$	$\frac{V}{b}\frac{C_{l_\beta}K_Z^2+C_{n_\beta}K_{XZ}}{4\mu_b(K_X^2K_Z^2-K_{XZ}^2)}$	$\frac{V}{b}\frac{C_{l_\beta}K_{XZ}+C_{n_\beta}K_X^2}{4\mu_b(K_X^2K_Z^2-K_{XZ}^2)}$
$i=\phi$	$\frac{V}{b}\frac{C_L}{2\mu_b}$	0	0
$i=p$	$\frac{V}{b}\frac{C_{Y_p}}{2\mu_b}$	$\frac{V}{b}\frac{C_{l_p}K_Z^2+C_{n_p}K_{XZ}}{4\mu_b(K_X^2K_Z^2-K_{XZ}^2)}$	$\frac{V}{b}\frac{C_{l_p}K_{XZ}+C_{n_p}K_X^2}{4\mu_b(K_X^2K_Z^2-K_{XZ}^2)}$
$i=r$	$\frac{V}{b}\frac{C_{Y_r}-4\mu_b}{2\mu_b}$	$\frac{V}{b}\frac{C_{l_r}K_Z^2+C_{n_r}K_{XZ}}{4\mu_b(K_X^2K_Z^2-K_{XZ}^2)}$	$\frac{V}{b}\frac{C_{l_r}K_{XZ}+C_{n_r}K_X^2}{4\mu_b(K_X^2K_Z^2-K_{XZ}^2)}$
$i=\delta_a$	$\frac{V}{b}\frac{C_{Y_{\delta_a}}}{2\mu_b}$	$\frac{V}{b}\frac{C_{l_{\delta_a}}K_Z^2+C_{n_{\delta_a}}K_{XZ}}{4\mu_b(K_X^2K_Z^2-K_{XZ}^2)}$	$\frac{V}{b}\frac{C_{l_{\delta_a}}K_{XZ}+C_{n_{\delta_a}}K_X^2}{4\mu_b(K_X^2K_Z^2-K_{XZ}^2)}$
$i=\delta_r$	$\frac{V}{b}\frac{C_{Y_{\delta_r}}}{2\mu_b}$	$\frac{V}{b}\frac{C_{l_{\delta_r}}K_Z^2+C_{n_{\delta_r}}K_{XZ}}{4\mu_b(K_X^2K_Z^2-K_{XZ}^2)}$	$\frac{V}{b}\frac{C_{l_{\delta_r}}K_{XZ}+C_{n_{\delta_r}}K_X^2}{4\mu_b(K_X^2K_Z^2-K_{XZ}^2)}$

The state-space system in Equation 5.17 uses dimensionless states, these are made dimensional by realizing the following relationships:

$$v = \beta V \qquad \dot{v} = \dot{\beta} V$$

Applying these relationships to the state-space of Equation 5.17 results in a state-space system that has dimensional states:

$$\begin{bmatrix} \dot{v} \\ \dot{\phi} \\ \dot{p} \\ \dot{r} \end{bmatrix} = \begin{bmatrix} y_\beta & y_\phi V & y_p\frac{b}{2} & y_r\frac{b}{2} \\ 0 & 0 & 1 & 0 \\ l_\beta\frac{2}{b} & 0 & l_p & l_r \\ n_\beta\frac{2}{b} & 0 & n_p & n_r \end{bmatrix} \begin{bmatrix} v \\ \phi \\ p \\ r \end{bmatrix} + \begin{bmatrix} y_{\delta_a}V & y_{\delta_r}V \\ 0 & 0 \\ l_{\delta_a}\frac{2V}{b} & l_{\delta_r}\frac{2V}{b} \\ n_{\delta_a}\frac{2V}{b} & n_{\delta_r}\frac{2V}{b} \end{bmatrix} \begin{bmatrix} \delta_a \\ \delta_r \end{bmatrix} \tag{5.18}$$

Next the output vector with the C- and D matrices must be formulated. As this is the asymmetrical EOM the specific force in sway direction and rotational roll and yaw rates are of interest. The rotational rates are directly available from the state-space representation of

Equation 5.17. The sway specific force, however, must be derived. Following the same steps as in previous section and including the transformation from stability to body frame (as the EOM are derived in stability frame) results in the following formulation:

$$\begin{aligned} f_{y_p} = \quad & \dot{u}_s \sin\beta + \dot{v}_s \cos\beta + r_b u_s \cos\beta \cos\alpha - r_b v_s \sin\beta \cos\alpha - r_b w_s \sin\alpha - p_b u_s \cos\beta \sin\alpha + \\ & p_b v_s \sin\beta \sin\alpha - p_b w_s \cos\alpha - g \cos\theta \sin\phi + \dot{p}_b l_z + \dot{r}_b l_x \end{aligned} \tag{5.19}$$

This sway specific force formulation represent the sway specific forces as perceived at pilot position in the aircraft simply by filling in the moment arms l_x and l_z, however, this formulation is not in the correct form. In order to write this equation as output vector, it must be linearized. Linearizing and imposing the trim conditions results in the following formulation:

$$f_{y_p} = \dot{v}_s - g\phi - u_{s_0}\alpha_0 p + u_{s_0} r + l_z \dot{p} + l_x \dot{r} \tag{5.20}$$

Now the output vector can be formulated, yielding:

$$\boldsymbol{y}^{EOM} = \begin{pmatrix} f_{y_p}^{EOM} \\ p^{EOM} \\ r^{EOM} \end{pmatrix} = \begin{bmatrix} C_{f_y v} & C_{f_y \phi} & C_{f_y p} & C_{f_y r} \\ 0 & 0 & 1 & 0 \\ 0 & 0 & 0 & 1 \end{bmatrix} \boldsymbol{x} + \begin{bmatrix} D_{f_y \delta_a} & D_{f_y \delta_r} \\ 0 & 0 \\ 0 & 0 \end{bmatrix} \boldsymbol{u} \tag{5.21}$$

This concludes the derivation of the sway specific force, roll- and yaw-rotational rate formulation experienced at pilot position. The definition of the newly introduced symbols of Equation 5.21 are recapitulated in Table 5.2.

Table 5.2: Symbols Appearing in the Output Vector State-Space Representation of Equation 5.21

	$C_{f_y i}$	$C_{\dot{p} i}$	$C_{\dot{r} i}$
$i = v$	$y_\beta + l_\beta \frac{2}{b} l_z + n_\beta \frac{2}{b} l_x$	$l_\beta \frac{2}{b}$	$n_\beta \frac{2}{b}$
$i = \phi$	$y_\phi V - g$	0	0
$i = p$	$y_p \frac{b}{2} - u_{s_0}\alpha_0 + l_p l_z + n_p l_x$	l_p	n_p
$i = r$	$y_r \frac{b}{2} + u_{s_0} + l_r l_z + n_r l_x$	l_r	n_r

	$D_{f_y i}$	$D_{\dot{p} i}$	$D_{\dot{r} i}$
$i = \delta_a$	$y_{\delta_a} + l_{\delta_a} \frac{2V}{b} l_z + n_{\delta_a} \frac{2V}{b} l_x$	$l_{\delta_a} \frac{2V}{b}$	$n_{\delta_a} \frac{2V}{b}$
$i = \delta_r$	$y_{\delta_r} + l_{\delta_r} \frac{2V}{b} l_z + n_{\delta_r} \frac{2V}{b} l_x$	$l_{\delta_r} \frac{2V}{b}$	$n_{\delta_r} \frac{2V}{b}$

5.3.2. Linearization of the Motion Cueing Algorithm

This section contains the linearization of the adapted CWA. This CWA was adapted to output sway specific force as well as roll- and yaw rates. This adaption is visualized in Figure 5.5 for the asymmetrical formulation of the CWA. The CWA as explained in Chapter 2 is highly non-linear, and is therefore linearized to allow for the EMD analysis. Previous section linearized the EOM, which are the inputs to the CWA, as of this, these inputs now represent deviation from the initial condition.

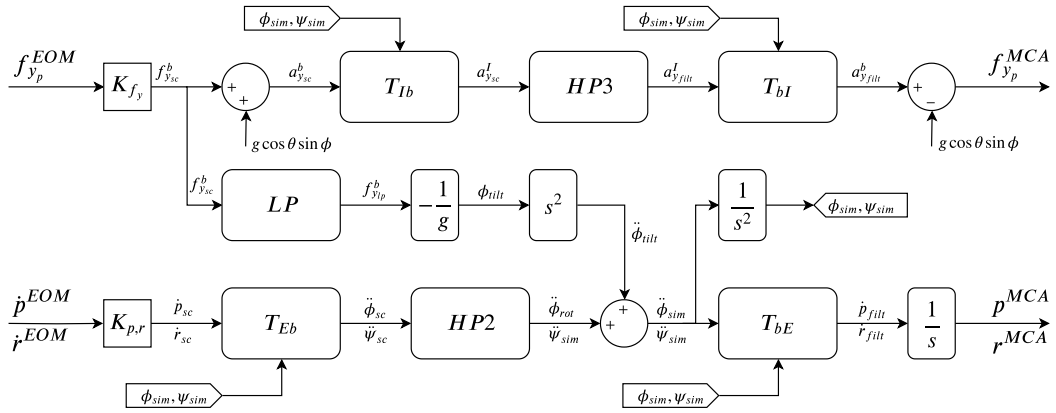

Figure 5.5: Classical Washout Algorithm Adapted for Lateral EMD [16]

The different components of this CWA (Figure 5.5) are presented in Equations 5.22 to 5.26.

$$T_{Ib} = \left[\sin\phi_{sim}\sin\theta_{sim}\sin\psi_{sim} + \cos\phi_{sim}\cos\psi_{sim}\right] \quad T_{bI} = T_{Ib}^T \tag{5.22}$$

$$T_{Eb} = \begin{bmatrix} 1 & \cos\phi_{sim}\tan\theta_{sim} \\ 0 & \frac{\cos\phi_{sim}}{\cos\theta_{sim}} \end{bmatrix} \qquad T_{bE} = \begin{bmatrix} 1 & -\sin\theta_{sim} \\ 0 & \cos\theta_{sim}\cos\phi_{sim} \end{bmatrix} \tag{5.23}$$

$$HP3_{f_y} = \frac{s^2}{s^2 + 2\zeta_{f_y}\omega_{n_{f_y}}s + \omega_{n_{f_y}}^2}\frac{s}{s+\omega_{b_{f_y}}} \rightarrow \frac{s^3}{s^3 + A_{f_y}s^2 + B_{f_y}s + C_{f_y}} \tag{5.24}$$

$$HP2_i = \frac{s^2}{s^2 + 2\zeta_i\omega_{n_i}s + \omega_{n_i}^2} \rightarrow \frac{s^2}{s^2 + A_i s + B_i} \tag{5.25}$$

where: $i = p$ and $i = r$ for the roll- and yaw- rotational channel, respectively.

$$LP = \frac{\omega_{n_t}^2}{s^2 + 2\zeta_t\omega_{n_t}s + \omega_{n_t}^2} \rightarrow \frac{B_t}{s^2 + A_t s + B_t} \tag{5.26}$$

Appendix C.2 contained an illustration of the linearization of the surge specific force channel. The exact same principles are applied to all channels of the asymmetric formulation of the CWA. These steps are not again visualized in this section as assumed general knowledge for control theory. The resulting linearized state-space formulation of the CWA can be written in the form:

$$\dot{\boldsymbol{x}}^{MCA} = A^{MCA}\boldsymbol{x}^{MCA} + B^{MCA}\boldsymbol{u}^{MCA} \tag{5.27}$$

where the state- and input-vector are:

$$\boldsymbol{x}^{MCA} = \left[A_y^I \quad S_y^I \quad V_y^I \quad \phi_{rot} \quad \dot{\phi}_{rot} \quad \phi_{tilt} \quad \dot{\phi}_{tilt} \quad \phi_{sim} \quad \dot{\phi}_{sim} \quad \psi_{sim} \quad \dot{\psi}_{sim} \quad p_{filt}\right]^T \tag{5.28}$$

$$\boldsymbol{u}^{MCA} = \left[f_y^{EOM} \quad \dot{p}^{EOM} \quad \dot{r}^{EOM}\right]^T \tag{5.29}$$

in there the system- and input matrices are:

$$A^{MCA} = \begin{bmatrix} 0 & 1 & 0 & 0 & 0 & 0 & 0 & 0 & 0 & 0 & 0 & 0 \\ 0 & 0 & 1 & 0 & 0 & 0 & 0 & 0 & 0 & 0 & 0 & 0 \\ -C_{f_y} & -B_{f_y} & -A_{f_y} & 0 & 0 & 0 & 0 & g & 0 & 0 & 0 & 0 \\ 0 & 0 & 0 & 0 & 1 & 0 & 0 & 0 & 0 & 0 & 0 & 0 \\ 0 & 0 & 0 & -B_p & -A_p & 0 & 0 & 0 & 0 & 0 & 0 & 0 \\ 0 & 0 & 0 & 0 & 0 & 0 & 1 & 0 & 0 & 0 & 0 & 0 \\ 0 & 0 & 0 & 0 & 0 & -B_t & -A_t & 0 & 0 & 0 & 0 & 0 \\ 0 & 0 & 0 & 0 & 0 & 0 & 0 & 0 & 1 & 0 & 0 & 0 \\ 0 & 0 & 0 & -B_p & -A_p & -B_t^2 & -A_t B_t & 0 & 0 & 0 & 0 & 0 \\ 0 & 0 & 0 & 0 & 0 & 0 & 0 & 0 & 0 & 0 & 1 & 0 \\ 0 & 0 & 0 & 0 & 0 & 0 & 0 & 0 & 0 & -B_r & -A_r & 0 \\ 0 & 0 & 0 & -B_p & -A_p & -B_t^2 & -A_t B_t & 0 & 0 & \theta_0 B_r & \theta_0 A_r & 0 \end{bmatrix} \tag{5.30}$$

$$B^{MCA} = \begin{bmatrix} 0 & 0 & 0 \\ 0 & 0 & 0 \\ K_{f_y} & 0 & 0 \\ 0 & 0 & 0 \\ 0 & K_p & \theta_0 K_r \\ 0 & 0 & 0 \\ -\frac{K_{f_y}}{g} & 0 & 0 \\ 0 & 0 & 0 \\ -\frac{K_{f_y} B_t}{g} & K_p & \theta_0 K_r \\ 0 & 0 & 0 \\ 0 & 0 & K_r \\ -\frac{K_{f_y} B_t}{g} & K_p & 0 \end{bmatrix} \tag{5.31}$$

As illustrated in Figure 5.5, the sway specific force, roll- and yaw-rate are the MCA outputs, this results in the following formulation of the output vector:

$$\boldsymbol{y}^{MCA} = \begin{pmatrix} f_{y_p}^{MCA} \\ p^{MCA} \\ r^{MCA} \end{pmatrix} = C^{MCA}\boldsymbol{x}^{MCA} + D^{MCA}\boldsymbol{u}^{MCA} \tag{5.32}$$

$$C^{MCA} = \begin{bmatrix} -C_{f_y} & -B_{f_y} & -A_{f_y} & 0 & 0 & 0 & 0 & 0 & 0 & 0 & 0 & 0 \\ 0 & 0 & 0 & 0 & 0 & 0 & 0 & 0 & 0 & 0 & 0 & 1 \\ 0 & 0 & 0 & 0 & 0 & 0 & 0 & 0 & 0 & 0 & 1 & 0 \end{bmatrix} \tag{5.33}$$

$$D^{MCA} = \begin{bmatrix} K_{f_y} & 0 & 0 \\ 0 & 0 & 0 \\ 0 & 0 & 0 \end{bmatrix} \tag{5.34}$$

This concludes the derivation of the sway specific forces, roll- and yaw rates filtered by the MCA experienced by the pilot in the flight simulator.

5.3.3. System Coupling

Now that the EOM and CWA are both formulated as separate state-space formulations, these must now be combined in one state-space formulation. As the MCA uses the EOM

outputs as inputs, these must be reformulated. This reformulation results in so-called coupling matrices that couples both individual state-space representations into one system. Figure 5.6 illustrates how the EOM and MCA are related to one-another.

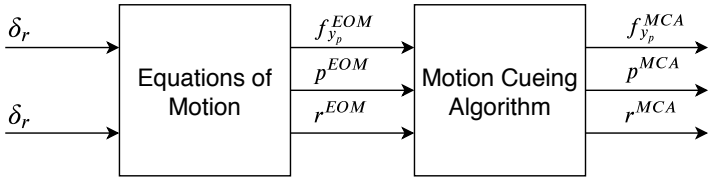

Figure 5.6: EOM and MCA Relation

For the EMD analysis to be possible, these two separate systems must be combined into one. This eventually results in a state-space of the form:

$$\dot{\boldsymbol{x}}^{EMD} = A^{EMD}\,\boldsymbol{x}^{EMD} + B^{EMD}\,\boldsymbol{u}^{EMD} \tag{5.35}$$

where the state- and input-vector are:

$$\boldsymbol{x}^{EMD} = \begin{bmatrix} v_s & \phi & p_b & r_b & A_y^I & S_y^I & V_y^I & \phi_{rot} & \dot{\phi}_{rot} & \phi_{tilt} & \dot{\phi}_{tilt} & \phi_{sim} & \dot{\phi}_{sim} & \psi_{sim} & \dot{\psi}_{sim} & p_{filt} \end{bmatrix}^T \tag{5.36}$$

$$\boldsymbol{u}^{EMD} = \begin{bmatrix} \delta_a & \delta_r \end{bmatrix}^T \tag{5.37}$$

Equations 5.31 and 5.34 use the EOM outputs as inputs. These must thus be transformed to allow the system coupling, which eventually can be written in the form:

$$A^{EMD} = \begin{bmatrix} A^{EOM} & 0 \\ A^{COUP} & A^{MCA} \end{bmatrix} \tag{5.38}$$

$$B^{EMD} = \begin{bmatrix} B^{EOM} \\ B^{COUP} \end{bmatrix} \tag{5.39}$$

$$\boldsymbol{y}^{EMD} = \begin{pmatrix} f_{y_p}^{EOM} \\ p^{EOM} \\ r^{EOM} \\ f_{y_p}^{MCA} \\ p^{MCA} \\ r^{MCA} \end{pmatrix} = \begin{bmatrix} C^{EOM} & 0 \\ C^{COUP} & C^{MCA} \end{bmatrix} \boldsymbol{x}^{EMD} + \begin{bmatrix} D^{EOM} \\ D^{COUP} \end{bmatrix} \boldsymbol{u}^{EMD} \tag{5.40}$$

In here Equation 5.31, B^{MCA}, which uses the EOM outputs as input, is rewritten as A^{COUP} and B^{COUP}, which expresses these EOM outputs using the EOM states and pilot inputs. The same is done for Equation 5.34, D^{MCA}, which is in its turn transformed into C^{COUP} and D^{COUP} for the same reason. The resulting coupling matrices are:

$$A^{COUP} = \begin{bmatrix} 0 & 0 & 0 & 0 \\ 0 & 0 & 0 & 0 \\ K_{f_y} C_{f_y v} & K_{f_y} C_{f_y \phi} & K_{f_y} C_{f_y p} & K_{f_y} C_{f_y r} \\ 0 & 0 & 0 & 0 \\ K_p C_{\dot{p} v} + \theta_0 K_r C_{\dot{r} v} & K_p C_{\dot{p}\phi} + \theta_0 K_r C_{\dot{r}\phi} & K_p C_{\dot{p}p} + \theta_0 K_r C_{\dot{r}p} & K_p C_{\dot{p}r} + \theta_0 K_r C_{\dot{r}r} \\ 0 & 0 & 0 & 0 \\ -\frac{K_{f_y}}{g} C_{f_y v} & -\frac{K_{f_y}}{g} C_{f_y \phi} & -\frac{K_{f_y}}{g} C_{f_y p} & -\frac{K_{f_y}}{g} C_{f_y r} \\ 0 & 0 & 0 & 0 \\ -\frac{K_{f_y} B_t}{g} C_{f_y v} + K_p C_{\dot{p} v} + \theta_0 K_r C_{\dot{r} v} & -\frac{K_{f_y} B_t}{g} C_{f_y \phi} + K_p C_{\dot{p}\phi} + \theta_0 K_r C_{\dot{r}\phi} & -\frac{K_{f_y} B_t}{g} C_{f_y p} + K_p C_{\dot{p}p} + \theta_0 K_r C_{\dot{r}p} & -\frac{K_{f_y} B_t}{g} C_{f_y r} + K_p C_{\dot{p}r} + \theta_0 K_r C_{\dot{r}r} \\ 0 & 0 & 0 & 0 \\ K_r C_{\dot{r} v} & K_r C_{\dot{r}\phi} & K_r C_{\dot{r}p} & K_r C_{\dot{r}r} \\ -\frac{K_{f_y} B_t}{g} C_{f_y v} + K_p C_{\dot{p} v} & -\frac{K_{f_y} B_t}{g} C_{f_y \phi} + K_p C_{\dot{p}\phi} & -\frac{K_{f_y} B_t}{g} C_{f_y p} + K_p C_{\dot{p}p} & -\frac{K_{f_y} B_t}{g} C_{f_y r} + K_p C_{\dot{p}r} \end{bmatrix} \tag{5.41}$$

$$B^{COUP} = \begin{bmatrix} 0 & 0 \\ 0 & 0 \\ K_{f_y} D_{f_y \delta_a} & K_{f_y} D_{f_y \delta_r} \\ 0 & 0 \\ K_p D_{\dot{p}\delta_a} + \theta_0 K_r D_{\dot{r}\delta_a} & K_p D_{\dot{p}\delta_r} + \theta_0 K_r D_{\dot{r}\delta_r} \\ 0 & 0 \\ -\frac{K_{f_y}}{g} D_{f_y \delta_a} & -\frac{K_{f_y}}{g} D_{f_y \delta_r} \\ 0 & 0 \\ -\frac{K_{f_y} B_t}{g} D_{f_y \delta_a} + K_p D_{\dot{p}\delta_a} + \theta_0 K_r D_{\dot{r}\delta_a} & -\frac{K_{f_y} B_t}{g} D_{f_y \delta_r} + K_p D_{\dot{p}\delta_r} + \theta_0 K_r D_{\dot{r}\delta_r} \\ 0 & 0 \\ K_r D_{\dot{r}\delta_a} & K_r D_{\dot{r}\delta_r} \\ -\frac{K_{f_y} B_t}{g} D_{f_y \delta_a} + K_p D_{\dot{p}\delta_a} & -\frac{K_{f_y} B_t}{g} D_{f_y \delta_r} + K_p D_{\dot{p}\delta_r} \end{bmatrix} \tag{5.42}$$

$$C^{COUP} = \begin{bmatrix} K_{f_y} C_{f_y v} & K_{f_y} C_{f_y \phi} & K_{f_y} C_{f_y p} & K_{f_y} C_{f_y r} \\ 0 & 0 & 0 & 0 \\ 0 & 0 & 0 & 0 \end{bmatrix} \tag{5.43}$$

$$D^{COUP} = \begin{bmatrix} K_{f_x} D_{f_x \delta_a} & K_{f_x} D_{f_x \delta_r} \\ 0 & 0 \\ 0 & 0 \end{bmatrix} \tag{5.44}$$

This concludes the derivation of the complete state-space system, which is now ready for the EMD analysis performed in next section.

5.3.4. Eigenvector Analysis

Now that the complete state-space for the asymmetrical EMD analysis has been derived, the actual eigenvector analysis can be performed. For this the eigenvectors of the A^{EMD} matrix are determined.

$$V_y = C^{EMD} \cdot V \tag{5.45}$$

$$y = \begin{bmatrix} f_{y_p}^{EOM} & p^{EOM} & r^{EOM} & f_{y_p}^{MCA} & p^{MCA} & r^{MCA} \end{bmatrix}^T \tag{5.46}$$

The resulting eigenvectors are then multiplied with the C^{EMD} matrix to express the eigenvectors in the desired states, namely the sway specific force, roll- and yaw rate experienced in the actual aircraft and in the flight simulator. The derived eigenvectors are visualized in Figure 5.7, which use the Cessna Citation 500 parameters from Table A.1 and example MCA parameters of Table B.2. As the aperiodic roll and spiral mode only have real eigenvalues, these only give a magnitude distortion, Figures 5.7b and 5.7c, respectively. The Dutch roll eigenmode has a complex pair of eigenvalues, which gives a distortion in both magnitude and phase, Figure 5.7a. The associated distortions are given in Table 5.3.

From the distortions of Table 5.3 it can be seen that the MCA is not capable to simulate the roll and yaw rates of the spiral mode. This has to do with the fact that this eigenmode is extremely slow and therefore require a lot of motion space to effectively simulate this with a flight simulator. However, a flight simulator motion space is limited by its actuator length making it impossible to cue this eigenmode with a standard hexapod motion platform.

Besides the eigenvectors the time traces of the individual eigenmodes are given in Figures 5.8 to 5.10. These figures support the distortions as given in Table 5.3, and are the result of a zero-input response where the system has an initial condition of $2Re(v_i)$.

Table 5.3: Distortion in Magnitude and Phase

Dutch Roll		Aperiodic Roll	Spiral Mode
$\lvert f_y \rvert = 0.64$	$\angle f_y = 16.3°$ lead	$\lvert f_y \rvert = 1.59$	$\lvert f_y \rvert = 0.80$
$\lvert p \rvert = 0.62$	$\angle p = 18.1°$ lead	$\lvert p \rvert = 0.76$	$\lvert p \rvert = 0.003$
$\lvert r \rvert = 0.69$	$\angle r = 24.5°$ lead	$\lvert r \rvert = 1.02$	$\lvert r \rvert = 0$

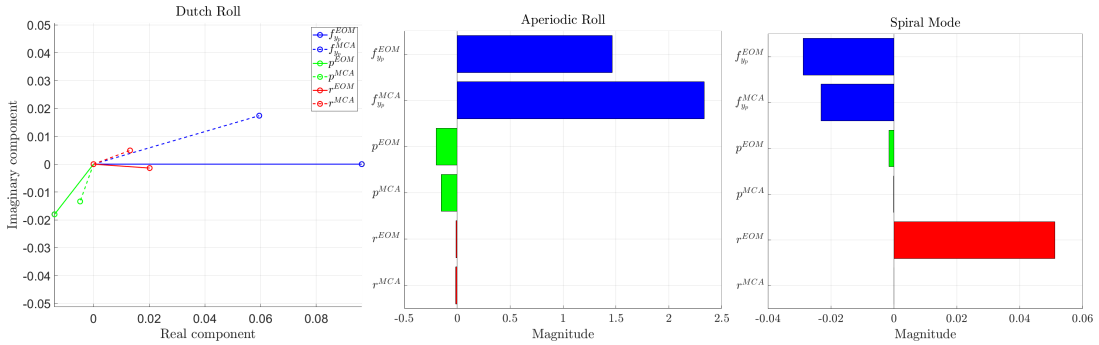

(a) Dutch Roll (b) Aperiodic Roll (c) Spiral Mode

Figure 5.7: Example of Eigenvector Distortion Plots

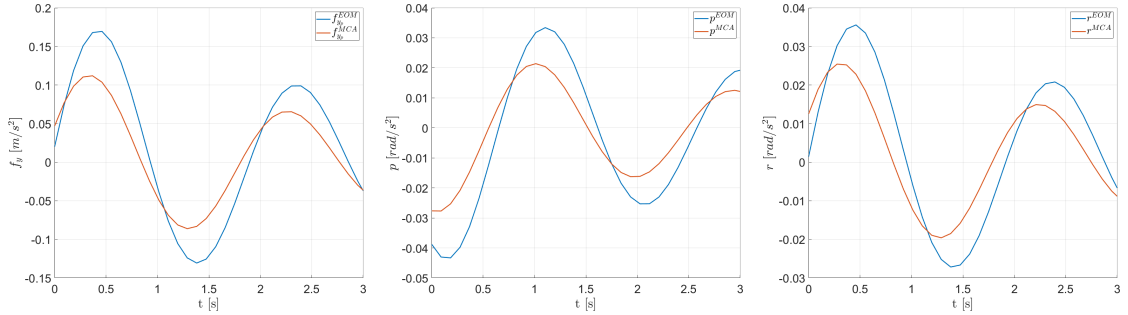

(a) (b) (c)

Figure 5.8: Time Histories of Dutch Roll Eigenmode Excitation

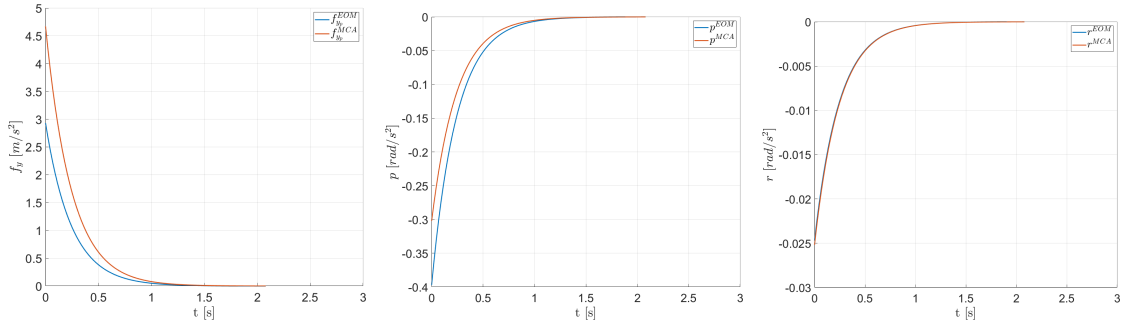

(a) (b) (c)

Figure 5.9: Time Histories of Aperiodic Roll Eigenmode Excitation

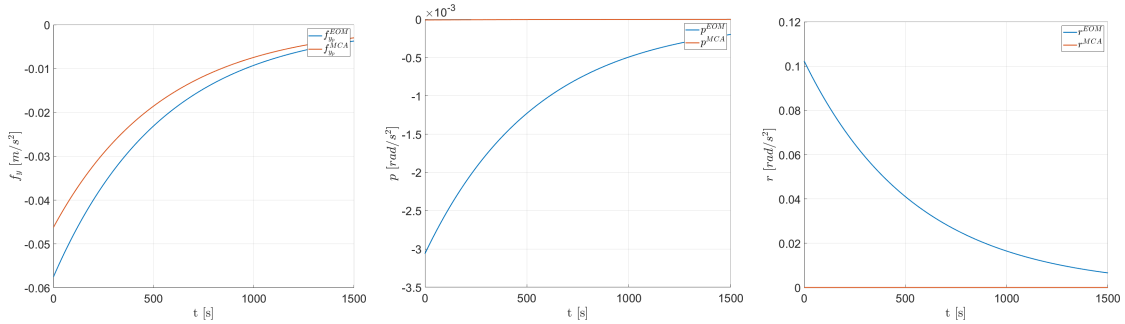

(a) (b) (c)

Figure 5.10: Time Histories of Aperiodic Spiral Mode Excitation

6
Perceptual Eigenmode Distortion

Previous chapter contained the Eigenmode Distortion analysis, however, the resulting plots in the complex plane showed limitations in the determination of dominant motion cues. Therefore, this chapter expands this EMD analysis by incorporating a so called perception model, namely the Perceptual Eigenmode Distortion (PEMD). This PEMD method is elaborated in Section 6.1, and has basically two extensions. The first extension is incorporating a model of the vestibular system, Section 6.2. The second extension is the use of motion perception thresholds, Section 6.3. Hereafter, an eigenvector analysis is performed for the symmetrical model (Section 6.4). Then, the effects of the two extensions are evaluated in Section 6.5. Finally, the results, of this evaluation, are used for the eigenvector analysis performed on the asymmetrical model (Section 6.6).

6.1. Perceptual Eigenmode Distortion Methodology

Previously it was elaborated that despite the potential of OMCT, this method has its shortcomings, such as the unrealistic test signals, exclusion of vehicle dynamics and the isolation of each test signal. To overcome these shortcomings the EMD analysis was introduced in previous chapter, this method used a different approach to investigate the distortions of the motion cues imposed by the MCA in terms of eigenvectors. These eigenvectors are visualized in the complex plane, from which the magnitude and phase distortions can be determined. Yet, this method has its disadvantages such as; the resulting eigenvectors for specific forces and rotational rates cannot be compared with one-another due to their different units. Thus, the dominant motion cue cannot be determined simply by looking at the magnitudes. Furthermore, the current eigenvectors assume a vestibular system that perceives the motion cues 1-to-1, whereas in real life this vestibular system introduces an additional magnitude and phase distortion. However, as the EOM outputs and MCA outputs pass through the vestibular system, their relative magnitude and phase distortions remain the same.

In this chapter two extensions of the EMD methods will be analysed. Firstly, the effects of including the vestibular system into the analysis. Secondly, the effect of including motion perception thresholds into the analysis. These extensions to the EMD method are referred to as the Perceptual Eigenmode Distortion (PEMD), as this new method incorporates a pilot perception model. Figure 6.1 illustrates how the PEMD method differs from the EMD method.

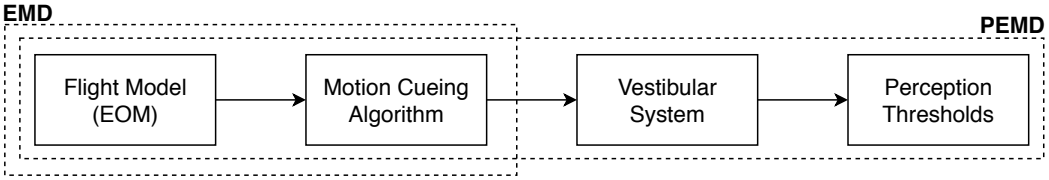

Figure 6.1: Domain of EMD and PEMD Methods

The PEMD method makes use of the resulting state-space system of the EMD method. Hereafter, the Otolith (OTO) and Semi-Circular Canals (SCC) of the human vestibular system are transformed into a state-space representation. Then, a state-space system is formulated that has as inputs the outputs of the EMD method and outputs how these are perceived, thus:

$$\boldsymbol{u}^{PER} = \begin{bmatrix} f_{x_p}^{EOM} & f_{z_p}^{EOM} & q^{EOM} & f_{x_p}^{MCA} & f_{z_p}^{MCA} & q^{MCA} \end{bmatrix}^T \tag{6.1}$$

$$\boldsymbol{y}^{PER} = \begin{bmatrix} \tilde{f}_{x_p}^{EOM} & \tilde{f}_{z_p}^{EOM} & \tilde{q}^{EOM} & \tilde{f}_{x_p}^{MCA} & \tilde{f}_{z_p}^{MCA} & \tilde{q}^{MCA} \end{bmatrix}^T \tag{6.2}$$

Like with the EMD method, the vestibular system must also be coupled to formulate one single system that has as input the control surface deflections given by the pilot. Therefore, a system coupling is formulated. The next step is to extend the system with the perception thresholds, this is done by dividing the output $\boldsymbol{y}^{PER}$ equation by the associated perception thresholds.

$$\check{\boldsymbol{y}}^{PER} = \begin{bmatrix} \check{\tilde{f}}_{x_p}^{EOM} & \check{\tilde{f}}_{z_p}^{EOM} & \check{\tilde{q}}^{EOM} & \check{\tilde{f}}_{x_p}^{MCA} & \check{\tilde{f}}_{z_p}^{MCA} & \check{\tilde{q}}^{MCA} \end{bmatrix}^T \tag{6.3}$$

If the eigenvectors are then multiplied with the C matrix, the resulting eigenvectors can be compared by magnitude as the units represent perception thresholds. This also allows for detecting the dominant motion cues in each mode. The two extensions of the PEMD method are first analysed for the symmetrical aircraft model of the Cessna Citation 500. This resulting system is then used for an eigenvector analysis. Hereafter, an evaluation of the two extensions is performed. Furthermore, in this evaluation the used tuning criteria for the symmetrical EMD model are revisited. The conclusions of the different extensions in the evaluation will be used for the eigenvector analysis of the asymmetric model of the Cessna Citation 500.

6.2. Vestibular System Extension to Symmetric Model

6.2.1. Vestibular System

Chapter 3 elaborates the working principles of the vestibular system, involving how translational and rotational motion are perceived with the OTO and SCC, respectively. The symmetric model, however, only includes specific forces in x and z direction and pitch rotational rate. This means that the vestibular system can modelled as illustrated in Figure 6.2. In the remainder of this chapter the tilde (~) represents the perceived motion by the vestibular system.

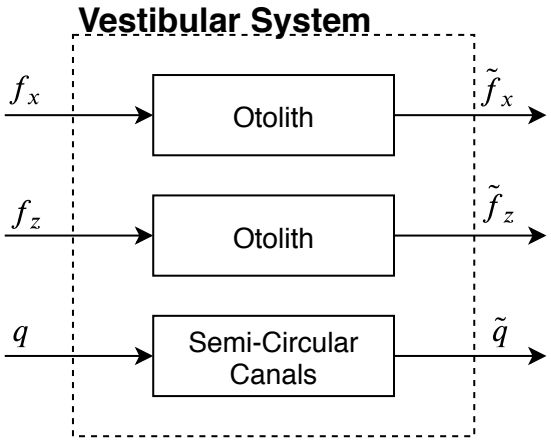

Figure 6.2: Systematic Representation of Vestibular System

Otolith

The OTO is responsible for the perception of specific forces and can be modelled as a transfer function [16]:

$$\frac{\tilde{f}_i}{f_i} = \frac{K_{\tilde{f}_i}\left(\tau_{\tilde{f}_{i_1}} s+1\right)}{\left(\tau_{\tilde{f}_{i_2}} s+1\right)\left(\tau_{\tilde{f}_{i_3}} s+1\right)} \rightarrow \frac{K_{\tilde{f}_i}\tau_{\tilde{f}_{i_1}} B_{\tilde{f}_i} s + K_{\tilde{f}_i} B_{\tilde{f}_i}}{s^2 + A_{\tilde{f}_i} s + B_{\tilde{f}_i}} \tag{6.4}$$

where: $i = x$ and $i = z$ for the specific force in x- and z-direction, respectively.

In order to make the PEMD analysis possible, this transfer function must be written as state-space. In state-space representation this transfer function can be written as:

$$\begin{bmatrix} \dot{x}_{f_{i_1}} \\ \dot{x}_{f_{i_2}} \end{bmatrix} = \begin{bmatrix} 0 & 1 \\ -B_{\tilde{f}_i} & -A_{\tilde{f}_i} \end{bmatrix} \begin{bmatrix} x_{f_{i_1}} \\ x_{f_{i_2}} \end{bmatrix} + \begin{bmatrix} 0 \\ 1 \end{bmatrix} f_i \tag{6.5}$$

$$\tilde{f}_i = \begin{bmatrix} K_{\tilde{f}_i} B_{\tilde{f}_i} & K_{\tilde{f}_i}\tau_{\tilde{f}_{i_1}} B_{\tilde{f}_i} \end{bmatrix} \begin{bmatrix} x_{f_{i_1}} \\ x_{f_{i_2}} \end{bmatrix} + \begin{bmatrix} 0 \end{bmatrix} f_i \tag{6.6}$$

Typical OTO parameter values are given in Table 6.1, and will be used in this chapter.

Semi-Circular Canals

The SCC is responsible for the perception of rotational rates, which means that for the symmetrical model the SCC perceives the pitch rates. The SCC is modelled with the transfer function [16]:

$$\frac{\tilde{q}}{q} = \frac{\tau_{\tilde{q}_1}\tau_{\tilde{q}_2} s^2}{(\tau_{\tilde{q}_1} s+1)(\tau_{\tilde{q}_2} s+1)(\tau_{\tilde{q}_3} s+1)} \rightarrow \frac{\tau_{\tilde{q}_1}\tau_{\tilde{q}_2} C_{\tilde{q}} s^2}{s^3 + A_{\tilde{q}} s^2 + B_{\tilde{q}} s + C_{\tilde{q}}} \tag{6.7}$$

Again for the PEMD analysis this transfer function was transferred to state-space representation, which yields:

$$\begin{bmatrix} \dot{x}_{q_1} \\ \dot{x}_{q_2} \\ \dot{x}_{q_3} \end{bmatrix} = \begin{bmatrix} 0 & 1 & 0 \\ 0 & 0 & 1 \\ -C_{\tilde{q}} & -B_{\tilde{q}} & -A_{\tilde{q}} \end{bmatrix} \begin{bmatrix} x_{q_1} \\ x_{q_2} \\ x_{q_3} \end{bmatrix} + \begin{bmatrix} 0 \\ 0 \\ 1 \end{bmatrix} q \tag{6.8}$$

$$\tilde{q} = \begin{bmatrix} 0 & 0 & \tau_{\tilde{q}_1}\tau_{\tilde{q}_2} C_{\tilde{q}} \end{bmatrix} \begin{bmatrix} x_{q_1} \\ x_{q_2} \\ x_{q_3} \end{bmatrix} + \begin{bmatrix} 0 \end{bmatrix} q \tag{6.9}$$

Typical SCC parameter values are given in Table 6.1, and will be used in this chapter.

Table 6.1: Vestibular Parameter Values from Reid & Nahon [16]

	K_i [−]	τ_{i_1} [s]	τ_{i_2} [s]	τ_{i_3} [s]
$i = f_x$	0.4	13.2	5.33	0.66
$i = f_z$	0.4	13.2	5.33	0.66
$i = q$	-	30.0	10.2	0.1

6.2.2. Vestibular State-Space

Now that the state-space representation of OTO and SCC is complete these can be combined into one single system that contains the whole vestibular system of the pilot. For this analysis it is essential to visualize how the pilot would perceive the motion in the aircraft, e.g. output of EOM. Furthermore, to compare these the pilot perception in the simulator

must be included as well, e.g. output of MCA. This means that two separate vestibular systems must be designed. Figure 6.3 visualizes these vestibular systems in combination with the earlier derived EMD model.

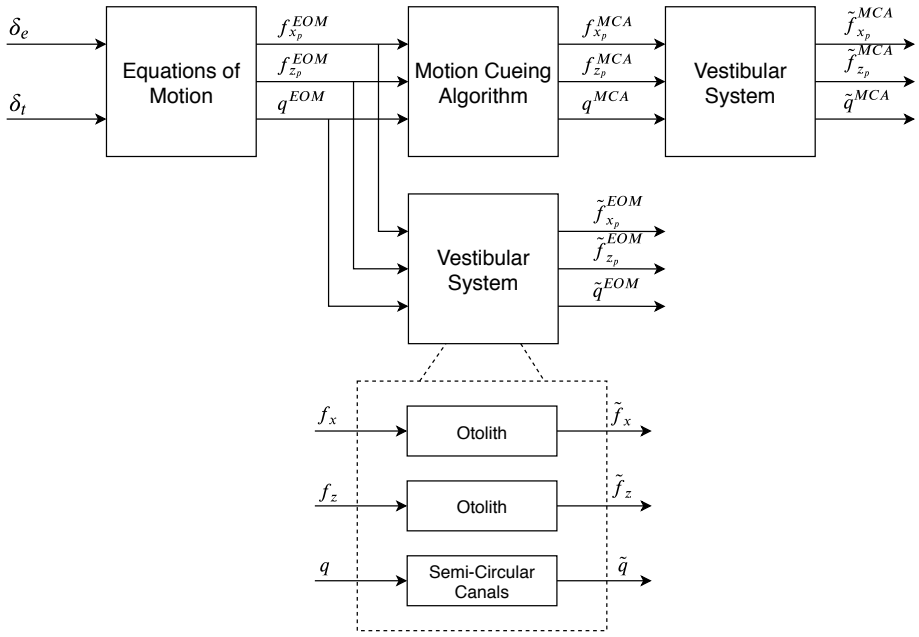

Figure 6.3: Incorporation of Vestibular System

The goal of this section is to formulate a state-space system that contains the two vestibular systems with its components. This state-space system must have the EMD outputs as input. Combining the state-space representations of the OTO and SCC this perception model is eventually modelled as:

$$\dot{\boldsymbol{x}}^{PER} = A^{PER}\,\boldsymbol{x}^{PER} + B^{PER}\,\boldsymbol{u}^{PER} \tag{6.10}$$

Where the state-vector and input-vector are:

$$\boldsymbol{x}^{PER} = \begin{bmatrix} x_{f_{x_1}}^{EOM} & x_{f_{x_2}}^{EOM} & x_{f_{x_1}}^{EOM} & x_{f_{x_2}}^{EOM} & x_{q_1}^{EOM} & x_{q_2}^{EOM} & x_{q_3}^{EOM} & x_{f_{x_1}}^{MCA} & x_{f_{x_2}}^{MCA} & x_{f_{x_1}}^{MCA} & x_{f_{x_2}}^{MCA} & x_{q_1}^{MCA} & x_{q_2}^{MCA} & x_{q_3}^{MCA} \end{bmatrix}^T \tag{6.11}$$

$$\boldsymbol{u}^{PER} = \begin{bmatrix} f_{x_p}^{EOM} & f_{z_p}^{EOM} & q^{EOM} & f_{x_p}^{MCA} & f_{z_p}^{MCA} & q^{MCA} \end{bmatrix}^T \tag{6.12}$$

$$A^{PER} = \begin{bmatrix} 0 & 1 & 0 & 0 & 0 & 0 & 0 & 0 & 0 & 0 & 0 & 0 & 0 & 0 \\ -B_{\tilde{f}_x} & -A_{\tilde{f}_x} & 0 & 0 & 0 & 0 & 0 & 0 & 0 & 0 & 0 & 0 & 0 & 0 \\ 0 & 0 & 0 & 1 & 0 & 0 & 0 & 0 & 0 & 0 & 0 & 0 & 0 & 0 \\ 0 & 0 & -B_{\tilde{f}_z} & -A_{\tilde{f}_z} & 0 & 0 & 0 & 0 & 0 & 0 & 0 & 0 & 0 & 0 \\ 0 & 0 & 0 & 0 & 0 & 1 & 0 & 0 & 0 & 0 & 0 & 0 & 0 & 0 \\ 0 & 0 & 0 & 0 & 0 & 0 & 1 & 0 & 0 & 0 & 0 & 0 & 0 & 0 \\ 0 & 0 & 0 & 0 & -C_{\tilde{q}} & -B_{\tilde{q}} & -A_{\tilde{q}} & 0 & 0 & 0 & 0 & 0 & 0 & 0 \\ 0 & 0 & 0 & 0 & 0 & 0 & 0 & 0 & 1 & 0 & 0 & 0 & 0 & 0 \\ 0 & 0 & 0 & 0 & 0 & 0 & 0 & -B_{\tilde{f}_x} & -A_{\tilde{f}_x} & 0 & 0 & 0 & 0 & 0 \\ 0 & 0 & 0 & 0 & 0 & 0 & 0 & 0 & 0 & 0 & 1 & 0 & 0 & 0 \\ 0 & 0 & 0 & 0 & 0 & 0 & 0 & 0 & 0 & -B_{\tilde{f}_z} & -A_{\tilde{f}_z} & 0 & 0 & 0 \\ 0 & 0 & 0 & 0 & 0 & 0 & 0 & 0 & 0 & 0 & 0 & 0 & 1 & 0 \\ 0 & 0 & 0 & 0 & 0 & 0 & 0 & 0 & 0 & 0 & 0 & 0 & 0 & 1 \\ 0 & 0 & 0 & 0 & 0 & 0 & 0 & 0 & 0 & 0 & 0 & -C_{\tilde{q}} & -B_{\tilde{q}} & -A_{\tilde{q}} \end{bmatrix} \tag{6.13}$$

$$B^{PER} = \begin{bmatrix} 0 & 0 & 0 & 0 & 0 & 0 \\ 1 & 0 & 0 & 0 & 0 & 0 \\ 0 & 0 & 0 & 0 & 0 & 0 \\ 0 & 1 & 0 & 0 & 0 & 0 \\ 0 & 0 & 0 & 0 & 0 & 0 \\ 0 & 0 & 0 & 0 & 0 & 0 \\ 0 & 0 & 1 & 0 & 0 & 0 \\ 0 & 0 & 0 & 0 & 0 & 0 \\ 0 & 0 & 0 & 1 & 0 & 0 \\ 0 & 0 & 0 & 0 & 0 & 0 \\ 0 & 0 & 0 & 0 & 1 & 0 \\ 0 & 0 & 0 & 0 & 0 & 0 \\ 0 & 0 & 0 & 0 & 0 & 0 \\ 0 & 0 & 0 & 0 & 0 & 1 \end{bmatrix} \tag{6.14}$$

As output the perceived specific forces and rotational rates in both aircraft and simulator are given by:

$$\begin{aligned} \boldsymbol{y}^{PER} &= \begin{bmatrix} \tilde{f}_{x_p}^{EOM} & \tilde{f}_{z_p}^{EOM} & \tilde{q}^{EOM} & \tilde{f}_{x_p}^{MCA} & \tilde{f}_{z_p}^{MCA} & \tilde{q}^{MCA} \end{bmatrix}^T \\ &= C^{PER}\,\boldsymbol{x}^{PER} + D^{PER}\,\boldsymbol{u}^{PER} \end{aligned} \tag{6.15}$$

$$C^{PER} = \begin{bmatrix} K_{\tilde{f}_x} B_{\tilde{f}_x} & K_{\tilde{f}_x} \tau_{\tilde{f}_{x_1}} B_{\tilde{f}_x} & 0 & 0 & 0 & 0 & 0 & 0 & 0 & 0 & 0 & 0 & 0 & 0 \\ 0 & 0 & K_{\tilde{f}_z} B_{\tilde{f}_z} & K_{\tilde{f}_z} \tau_{\tilde{f}_{z_1}} B_{\tilde{f}_z} & 0 & 0 & 0 & 0 & 0 & 0 & 0 & 0 & 0 & 0 \\ 0 & 0 & 0 & 0 & 0 & 0 & \tau_{\tilde{q}_1} \tau_{\tilde{q}_2} C_{\tilde{q}} & 0 & 0 & 0 & 0 & 0 & 0 & 0 \\ 0 & 0 & 0 & 0 & 0 & 0 & 0 & K_{\tilde{f}_x} B_{\tilde{f}_x} & K_{\tilde{f}_x} \tau_{\tilde{f}_{x_1}} B_{\tilde{f}_x} & 0 & 0 & 0 & 0 & 0 \\ 0 & 0 & 0 & 0 & 0 & 0 & 0 & 0 & 0 & K_{\tilde{f}_z} B_{\tilde{f}_z} & K_{\tilde{f}_z} \tau_{\tilde{f}_{z_1}} B_{\tilde{f}_z} & 0 & 0 & 0 \\ 0 & 0 & 0 & 0 & 0 & 0 & 0 & 0 & 0 & 0 & 0 & 0 & 0 & \tau_{\tilde{q}_1} \tau_{\tilde{q}_2} C_{\tilde{q}} \end{bmatrix} \tag{6.16}$$

$$D^{PER} = \begin{bmatrix} 0 & 0 & 0 & 0 & 0 & 0 \\ 0 & 0 & 0 & 0 & 0 & 0 \\ 0 & 0 & 0 & 0 & 0 & 0 \\ 0 & 0 & 0 & 0 & 0 & 0 \\ 0 & 0 & 0 & 0 & 0 & 0 \\ 0 & 0 & 0 & 0 & 0 & 0 \end{bmatrix} \tag{6.17}$$

This concludes the derivation of the vestibular perception state-space representation. Next, this perception model is connected to the EMD model into a single state-space representation.

6.2.3. System Coupling

In order to make the PEMD analysis possible the EMD and perception model must be connected combined into one state-space representation. Essentially this means that the inputs of the perception model must be written as states that form the EMD model. This resulting model will only have control surface deflections as inputs. This system coupling is visualized in Figure 6.4.

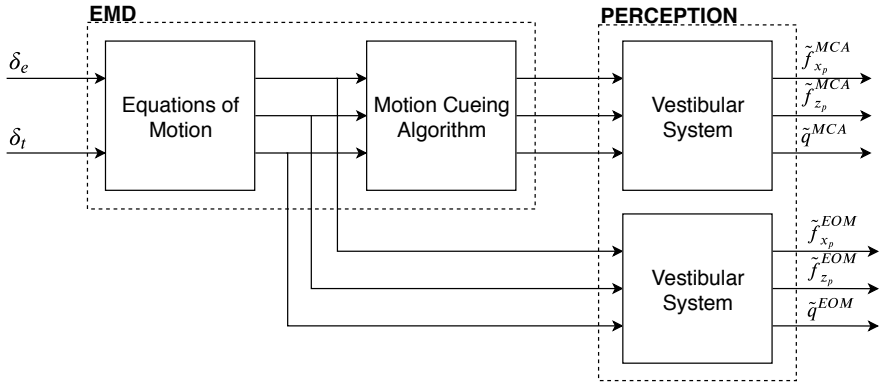

Figure 6.4: Coupling EMD with Vestibular System

This figure basically illustrates that the EMD and perception models are two separate models, which must be combined into one single system. In order to do so, again a system coupling matrix must be designed. The resulting PEMD system can be written as:

$$\dot{\boldsymbol{x}}^{PEMD} = A^{PEMD}\,\boldsymbol{x}^{PEMD} + B^{PEMD}\,\boldsymbol{u}^{PEMD} \tag{6.18}$$

Where the state-vector and input-vector are given by:

$$\boldsymbol{x}^{PEMD} = \begin{bmatrix} \boldsymbol{x}^{EMD} & \boldsymbol{x}^{PER} \end{bmatrix}^T \tag{6.19}$$

$$\boldsymbol{u}^{PEMD} = \begin{bmatrix} \delta_e & \delta_t \end{bmatrix}^T \tag{6.20}$$

In here $\boldsymbol{x}^{EMD}$ represents the state-vector of the EMD system given in Equation C.57 and $\boldsymbol{x}^{PER}$ represents the state-vector of the perception model given in Equation 6.11. Note that this results in a total system state-vector that contains 30 states. The PEMD state-space representation including the coupling matrices can be written as:

$$A^{PEMD} = \begin{bmatrix} A^{EMD} & 0 \\ A^{COUP} & A^{PER} \end{bmatrix} \tag{6.21}$$

$$B^{PEMD} = \begin{bmatrix} B^{EMD} \\ B^{COUP} \end{bmatrix} \tag{6.22}$$

$$\boldsymbol{y}^{PEMD} = \begin{pmatrix} \tilde{f}_{x_p}^{EOM} \\ \tilde{f}_{z_p}^{EOM} \\ \tilde{q}^{EOM} \\ \tilde{f}_{x_p}^{MCA} \\ \tilde{f}_{z_p}^{MCA} \\ \tilde{q}^{MCA} \end{pmatrix} = \begin{bmatrix} C^{EMD} & 0 \\ C^{COUP} & C^{PER} \end{bmatrix} \boldsymbol{x}^{PEMD} + \begin{bmatrix} D^{EMD} \\ D^{COUP} \end{bmatrix} \boldsymbol{u}^{PEMD} \tag{6.23}$$

In here Equation 6.14, B^{PER}, which uses the EMD outputs as input, is rewritten as A^{COUP} and B^{COUP}, which expresses these EMD outputs using the EMD states and pilot inputs. The same is done for Equation 6.17, D^{PER}, however as this is a zero matrix, the resulting C^{COUP} and D^{COUP} matrices are zero matrices as well. The resulting coupling matrices are:

$$A^{COUP} = \begin{bmatrix}
0 & 0 & 0 & 0 & 0 & 0 & 0 & 0 & 0 & 0 & 0 & 0 & 0 & 0 & 0 & 0 \\
C_{f_x u} & C_{f_x w} & C_{f_x \theta} & C_{f_x q} & 0 & 0 & 0 & 0 & 0 & 0 & 0 & 0 & 0 & 0 & 0 & 0 \\
0 & 0 & 0 & 0 & 0 & 0 & 0 & 0 & 0 & 0 & 0 & 0 & 0 & 0 & 0 & 0 \\
C_{f_z u} & C_{f_z w} & C_{f_z \theta} & C_{f_z q} & 0 & 0 & 0 & 0 & 0 & 0 & 0 & 0 & 0 & 0 & 0 & 0 \\
0 & 0 & 0 & 0 & 0 & 0 & 0 & 0 & 0 & 0 & 0 & 0 & 0 & 0 & 0 & 0 \\
0 & 0 & 0 & 0 & 0 & 0 & 0 & 0 & 0 & 0 & 0 & 0 & 0 & 0 & 0 & 0 \\
0 & 0 & 0 & 1 & 0 & 0 & 0 & 0 & 0 & 0 & 0 & 0 & 0 & 0 & 0 & 0 \\
0 & 0 & 0 & 0 & 0 & 0 & 0 & 0 & 0 & 0 & 0 & 0 & 0 & 0 & 0 & 0 \\
K_{f_x} C_{f_x u} & K_{f_x} C_{f_x w} & K_{f_x} C_{f_x \theta} & K_{f_x} C_{f_x q} & -C_{f_x} & -B_{f_x} & -A_{f_x} & 0 & 0 & 0 & 0 & 0 & 0 & 0 & 0 & 0 \\
0 & 0 & 0 & 0 & 0 & 0 & 0 & 0 & 0 & 0 & 0 & 0 & 0 & 0 & 0 & 0 \\
K_{f_z} C_{f_z u} & K_{f_z} C_{f_z w} & K_{f_z} C_{f_z \theta} & K_{f_z} C_{f_z q} & 0 & 0 & 0 & -C_{f_z} & -B_{f_z} & -A_{f_z} & 0 & 0 & 0 & 0 & 0 & 0 \\
0 & 0 & 0 & 0 & 0 & 0 & 0 & 0 & 0 & 0 & 0 & 0 & 0 & 0 & 0 & 0 \\
0 & 0 & 0 & 0 & 0 & 0 & 0 & 0 & 0 & 0 & 0 & 0 & 0 & 0 & 0 & 0 \\
0 & 0 & 0 & 0 & 0 & 0 & 0 & 0 & 0 & 0 & 0 & 0 & 0 & 0 & 0 & 1
\end{bmatrix} \tag{6.24}$$

$$B^{COUP} = \begin{bmatrix}
0 & 0 \\
D_{f_x \delta_e} & D_{f_x \delta_t} \\
0 & 0 \\
D_{f_z \delta_e} & D_{f_z \delta_t} \\
0 & 0 \\
0 & 0 \\
0 & 0 \\
0 & 0 \\
K_{f_x} D_{f_x \delta_e} & K_{f_x} D_{f_x \delta_t} \\
0 & 0 \\
K_{f_z} D_{f_z \delta_e} & K_{f_z} D_{f_z \delta_t} \\
0 & 0 \\
0 & 0 \\
0 & 0
\end{bmatrix} \tag{6.25}$$

$$C^{COUP} = zeros(6,16) \tag{6.26}$$

$$D^{COUP} = zeros(6,2) \tag{6.27}$$

This concludes the derivation of the complete state-space system, the next step would be to adapt the output equations to incorporate the perception thresholds, after which the actual PEMD analysis is possible.

6.3. Perception Thresholds Extension to Symmetric Model

The EMD eigenvector analysis revealed that the magnitude of the specific force and rotational rate eigenvectors could not be compared with one another, because of the difference in dimensions. A way to solve this is to express all eigenvectors in the same units allowing for a magnitude comparison. For this the threshold unit is chosen, basically the output vector of the PEMD is divided by the associated threshold value. This results in dimensionless eigenvectors that can be compared in magnitude, by comparing this magnitude the dominant motion cues can be identified. Basically all that needs to be done is dividing the

C^{PEMD} and D^{PEMD} matrices by their associated threshold values, yielding:

$$\check{C}^{PEMD} = \begin{bmatrix} C^{PEMD}(1)/\check{TH}_{f_x} \\ C^{PEMD}(2)/\check{TH}_{f_z} \\ C^{PEMD}(3)/\check{TH}_{q} \\ C^{PEMD}(4)/\check{TH}_{f_x} \\ C^{PEMD}(5)/\check{TH}_{f_z} \\ C^{PEMD}(6)/\check{TH}_{q} \end{bmatrix} \qquad \check{D}^{PEMD} = \begin{bmatrix} D^{PEMD}(1)/\check{TH}_{f_x} \\ D^{PEMD}(2)/\check{TH}_{f_z} \\ D^{PEMD}(3)/\check{TH}_{q} \\ D^{PEMD}(4)/\check{TH}_{f_x} \\ D^{PEMD}(5)/\check{TH}_{f_z} \\ D^{PEMD}(6)/\check{TH}_{q} \end{bmatrix} \tag{6.28}$$

This gives the dimensionless output vector as:

$$\check{\mathbf{y}}^{PER} = \begin{bmatrix} \check{\bar{f}}^{EOM}_{x_p} & \check{\bar{f}}^{EOM}_{z_p} & \check{\bar{q}}^{EOM} & \check{\bar{f}}^{MCA}_{x_p} & \check{\bar{f}}^{MCA}_{z_p} & \check{\bar{q}}^{MCA} \end{bmatrix}^T \tag{6.29}$$

In here the check mark ($\vee$), indicates that threshold units are used. For this stage the following threshold values are $\check{TH}_{f_x} = 0.0742$ $[m/s^2]$, $\check{TH}_{f_z} = 0.123$ $[m/s^2]$ and $\check{TH}_{q} = 0.00734$ $[rad/s]$, based on [6, 7]. This stage is mainly for illustration purpose, a later stage will require a better substantiated determination of these thresholds.

6.4. Eigenvector Analysis on Symmetric Model

Now that the entire PEMD state-space has been derived the eigenvector analysis can be performed. This eigenvector analysis is again performed using the same steps as described in Section 5.2.

$$y = \begin{bmatrix} \check{\bar{f}}^{EOM}_{x_p} & \check{\bar{f}}^{EOM}_{z_p} & \check{\bar{q}}^{EOM} & \check{\bar{f}}^{MCA}_{x_p} & \check{\bar{f}}^{MCA}_{z_p} & \check{\bar{q}}^{MCA} \end{bmatrix}^T \tag{6.30}$$

This results in eigenvectors expressed in the desired terms, namely the perceived specific forces and pitch rate. These eigenvectors are again plotted in the complex plane. This plot reveals the magnitude and phase distortions between the EOM and MCA.

Unlike with the EMD the magnitudes of all eigenvectors can now be compared with one another. As example the same parameters and settings for the Cessna Citation 500 aircraft as in Section 5.2 are used for illustration. The magnitude and phase distortions between EOM and MCA still remain the same as is evident in Table 6.2. However, looking at Figure 6.5 the magnitudes of the individual motion cues can now be compared. The resulting complex plane plots can be analyzed in the following way; consider Figure 6.5a, if someone can barely feel the pitch rotational rate, that person can certainly not feel the surge specific force as the magnitude is much smaller, but that person will most certainly be able to feel the heave specific force as the magnitude is larger. As can be seen, the heave specific force is the dominant motion cue and for the short period the surge specific force is the least present motion cue. This observation was not possible with the standard EMD as evident in Figure 5.2. This observation is quite useful, imagine that someone is tuning the MCA parameters for the short period mode and has to make a trade-off between pitch rate and surge specific force, then it is better to tune for pitch rate.

Table 6.2: Distortion in Magnitude and Phase

Short Period		Phugoid	
$\lvert f_x \rvert = 0.81$	$\angle f_x = 24.3°$ (lag)	$\lvert f_x \rvert = 0.79$	$\angle f_x = 23.1°$ (lead)
$\lvert f_z \rvert = 0.70$	$\angle f_z = 92.9°$ (lag)	$\lvert f_z \rvert = 0.0006$	$\angle f_z = 108°$ (lead)
$\lvert q \rvert = 0.70$	$\angle q = 23.3°$ (lag)	$\lvert q \rvert = 0.11$	$\angle q = 94.2°$ (lead)

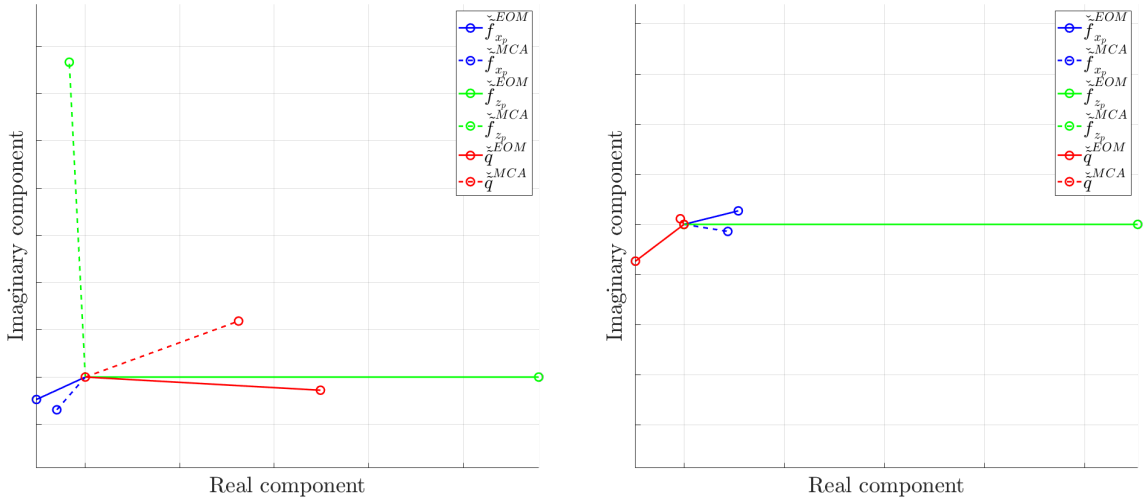

(a) Short Period (b) Phugoid

Figure 6.5: Example of Eigenvector Distortion Plots for PEMD

6.5. Evaluation of the Perception Model Extension of Symmetric Model

Incorporating the complete vestibular system increases the complexity of this eigenvector analysis significantly. For example, the number of states increased from 16 to 30 simply by including the vestibular system. As of this, the change of making a small error in the derivation increases as well. In order to determine whether this vestibular system incorporation is worth it, the thresholds are included in the EMD analysis as well. This was possible simply by adapting the C^{EMD} matrix. This resulted in:

$$\check{C}^{EMD} = \begin{bmatrix} C^{EMD}(1)/\check{TH}_{f_x} \\ C^{EMD}(2)/\check{TH}_{f_z} \\ C^{EMD}(3)/\check{TH}_{q} \\ C^{EMD}(4)/\check{TH}_{f_x} \\ C^{EMD}(5)/\check{TH}_{f_z} \\ C^{EMD}(6)/\check{TH}_{q} \end{bmatrix} \tag{6.31}$$

This adjusted $\check{C}^{EMD}$ is then used in the eigenvector analysis. The resulting eigenvectors together with the eigenvectors from the PEMD analysis are together visualized in Figures 6.6 and 6.7. In here the effect of incorporating only the vestibular system can be seen. As is evident from here, the relative magnitude and phase distortions remain the same, the only difference is that the overall magnitude is adjusted, as well as the system is rotated. In here, Figures 6.6a and 6.7a illustrate the same but have the $f_{z_p}^{EOM}$ aligned. As is evident from these figures, the same conclusion of dominant motion cues can be made. Another critical point is that the vestibular model derived in Section 6.2.2 is also an idealization and simplification of the actual vestibular system. For example the vestibular parameter values given in Table 6.1 vary per person. Also, the transfer functions used are just a simplification of the actual human vestibular system. For these reasons, the vestibular system is left-out in the remaining of the PEMD analysis, however, the incorporation of the perception thresholds will still be included as these allow the determination of dominant motion cues. With keeping this knowledge about the dominant cues in mind, the proposed criteria used to determine the MCA settings can be revisited. These settings are given in Table B.1 and

originate from [24]. According to this paper, the following tuning criteria were used, shown in their order of importance:

1. Minimize the phase distortion of all motion cues;
2. Maintain the relative phase between motion cues;
3. Minimize the magnitude distortion of all motion cues; and
4. Maintain a similar magnitude distortion level of all motion cues.

The resulting MCA settings were optimized for the short period eigenmode. Now with the new knowledge of dominant motion cues all motion cues do not have to be treated equally. For example, the PEMD revealed that the heave specific force is the dominant motion cue in the short period eigenmode, whereas the surge specific force is the least important motion cue. It makes therefore sense to optimize the magnitude and phase distortion for the heave specific force, rather than for all motion cues simultaneously.

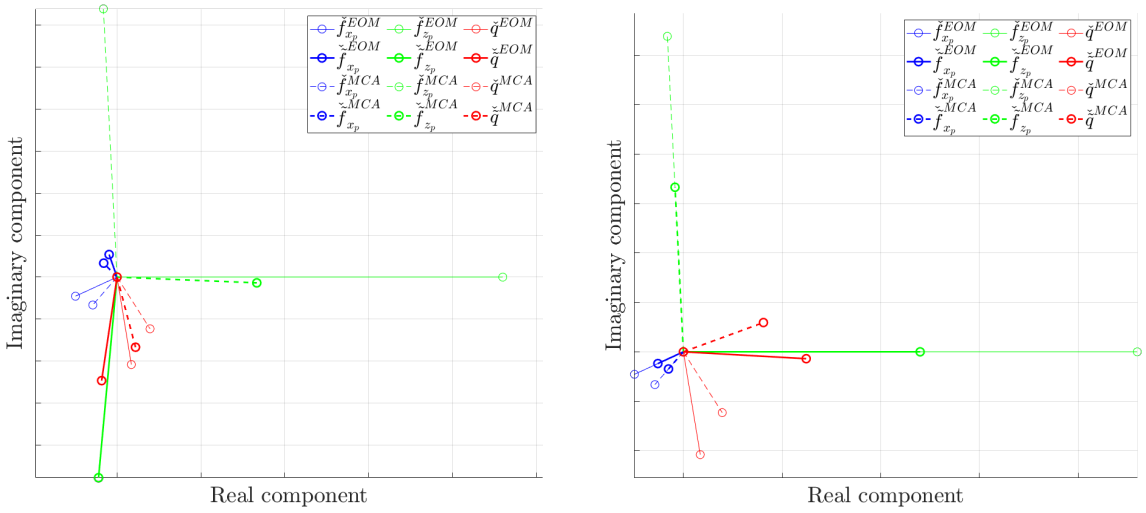

(a) Actual (b) Aligned

Figure 6.6: Short Period - Comparison between EMD and PEMD

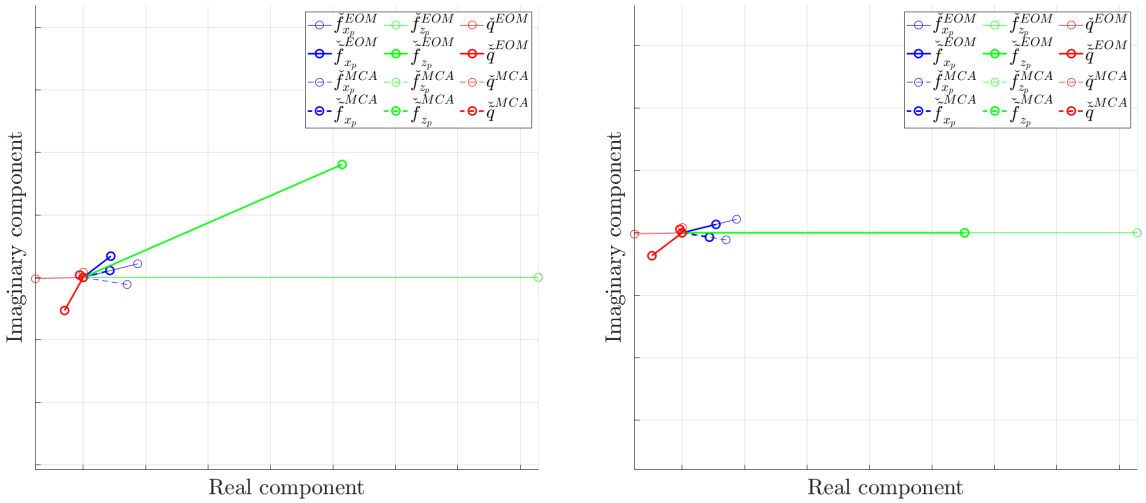

(a) Actual (b) Aligned

Figure 6.7: Phugoid - Comparison between EMD and PEMD

6.6. Eigenvector Analysis on Asymmetric Model

Previously the vestibular system that was connected to the EMD model, however, this addition seemed not worth the effort and increases the complexity significantly, e.g. 16 EMD states increased to 30 PEMD states. Therefore, for the lateral EMD model, which was derived in Section 5.3.3, the addition of vestibular system is left-out. However, the second step of the PEMD that includes the perception thresholds is still done, as this will reveal the dominant motion cues for each eigenmode.

The EMD analysis from Section 5.3.4 resulted in magnitude and phase distortions that could not be compared to one another, because of the differences in dimensions. To solve this problem again, the eigenvectors are all expressed in the same unit, namely thresholds. In order to do so, the rows in the C^{EMD} matrix must be divided by their associated threshold value, yielding:

$$\check{C}^{PEMD} = \begin{bmatrix} C^{EMD}(1)/\check{TH}_{f_y} \\ C^{EMD}(2)/\check{TH}_p \\ C^{EMD}(3)/\check{TH}_r \\ C^{EMD}(4)/\check{TH}_{f_y} \\ C^{EMD}(5)/\check{TH}_p \\ C^{EMD}(6)/\check{TH}_r \end{bmatrix} \tag{6.32}$$

In here the check mark ($\vee$), indicates that threshold units are used. For this stage these threshold values are $\check{TH}_{f_y} = 0.0743\ [m/s^2]$, $\check{TH}_p = 0.00521\ [rad/s]$ and $\check{TH}_r = 0.0166\ [rad/s]$, based on [6, 7]. This stage is mainly for illustration purpose, a later stage will require a better substantiated determination of these thresholds.

After again performing the eigenvector analysis, now with the $\check{C}^{PEMD}$, the resulting eigenvectors are expressed in the desired terms, namely:

$$y = \begin{bmatrix} \check{f}_{y_p}^{EOM} & \check{p}^{EOM} & \check{r}^{EOM} & \check{f}_{y_p}^{MCA} & \check{p}^{MCA} & \check{r}^{MCA} \end{bmatrix}^T \tag{6.33}$$

This matrix contains the same eigenvectors as in Section 5.3.4, however, now all expressed in threshold units. After plotting the resulting magnitude and phase distortions for each eigenmode the distortions can be compared to one another. The resulting distortion plots are illustrated in Figure 6.8 and uses the same parameters as in Section 5.3.4.

Looking at the resulting figures, the following observations can be made. For the Dutch Roll, the roll rate is the dominant motion cue, furthermore, the sway specific force and yaw rate are almost equally important. For the aperiodic roll also the roll rate is the dominant motion cue. The yaw rate is the least important motion cue for the aperiodic roll. For the spiral mode the yaw rate is the most important motion cue, however, this motion cue is not simulated by the flight simulator as can be seen by the zero magnitude. Furthermore, the magnitude of the roll rate that is simulated by the flight simulator is negligible. As the spiral mode is a very slow eigenmode, the conventional hexapod flight simulator is not capable to correctly simulate this as of the limitations in motion space.

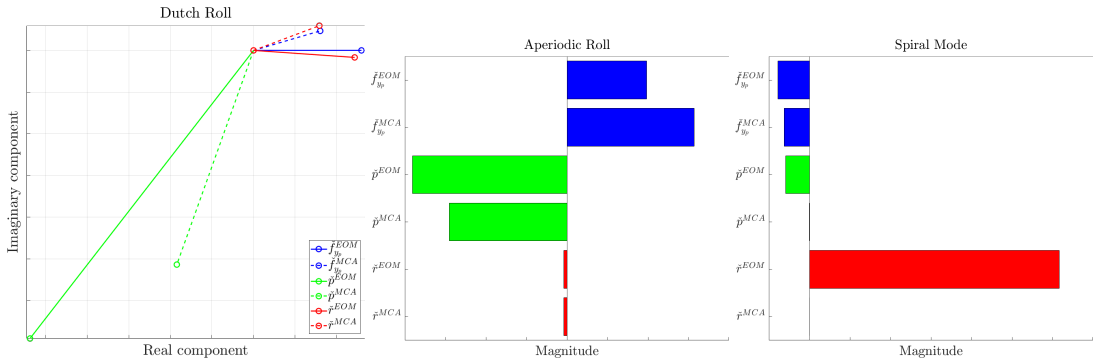

(a) Dutch Roll (b) Aperiodic Roll (c) Spiral Mode

Figure 6.8: Example of Eigenvector Distortion Plots

It was shown that for the EMD analysis of the symmetrical model, all the motion cues were treated equally important. However, by using the perception threshold extension dominant motion cues can be identified for a given flight condition. This information can be used in a smart way to find better MCA settings for minimizing the motion cue distortions. For the experiment of the symmetrical model, the MCA settings were selected manually. Next chapter uses the results of the PEMD eigenvector analysis to formulate a optimization function that automatically finds the most optimal MCA settings.

7
Tuning Algorithm

Previous chapter revealed some interesting insight on how human perception thresholds could be used to improve the EMD method. This chapter used this insight to construct an objective function that could be used to optimize the MCA tuning parameters for a given eigenmode. Section 7.1 constructs this objective function. Apart from the objective function, some constraints must be imposed as well, this is done in Section 7.2. Finally, an overview of the different parameter of this tuning algorithm is given in Section 7.3

7.1. Objective Function

The OMCT evaluation method, which is currently used to objectively evaluate the flight simulator's fidelity, evaluates the magnitude- and phase distortion separately. Initially an objective function was designed where the magnitude- and phase distortion could be optimized separately. The work of Wei Fu [27] gave, however, some interesting insight for an alternative formulation of this objective function. Figure 7.1 depicts the dynamics of an arbitrary system at a single frequency, this will be used to explain his findings. He found that a change of dynamics, in the control loading, is not perceived by humans when the change that occurred fall within the threshold region (the grey square). So it does not matter whether it is a magnitude distortion and/or phase distortion, as long as the distortion is within the threshold region it will not be perceived by the human operator. Only a change is detected by the human operator if the dynamics change exceeds this threshold region.

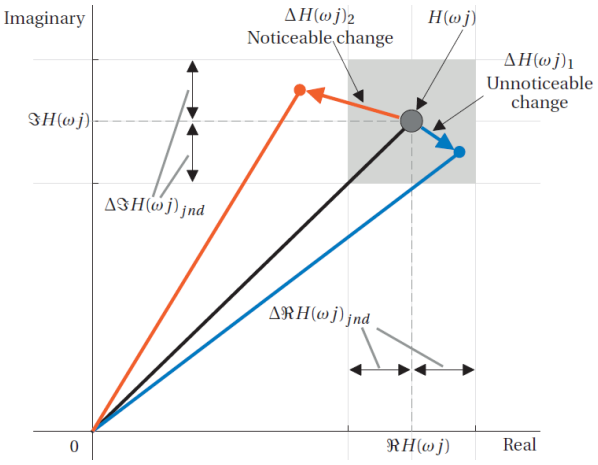

Figure 7.1: Threshold for Altered Perception of the System Dynamics [27]

Rather than just optimizing only the magnitude distortion or phase distortion, an alternative approach is chosen. The objective function formulated in this chapter aims to minimize the Euclidean distance between the eigenvectors from the EOM and the eigenvectors of the MCA. This Euclidean distance is illustrated for the Dutch Roll and Aperiodic Roll in Figures 7.2a and 7.2b, respectively.

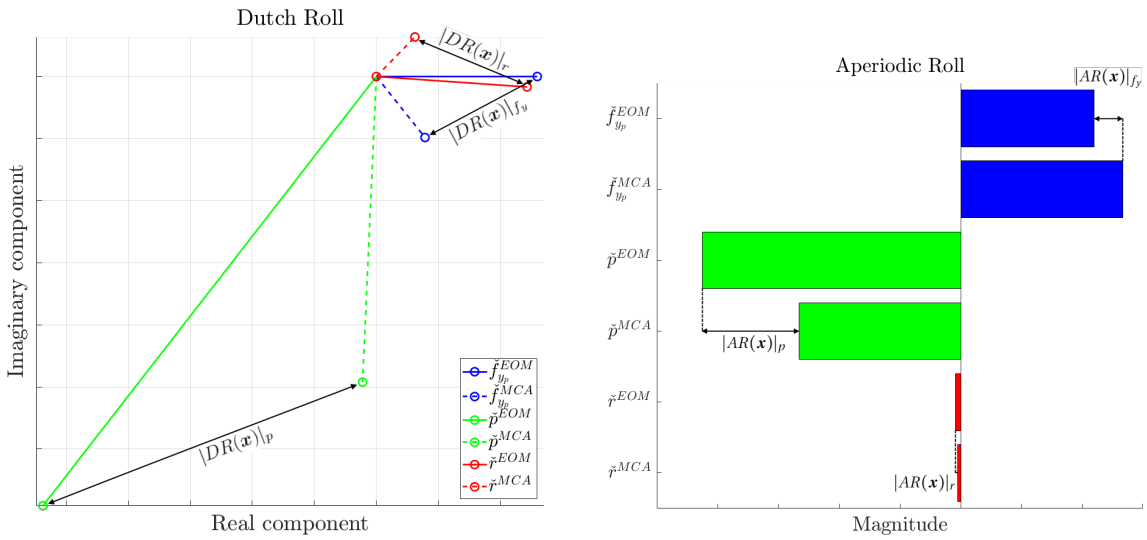

Figure 7.2: Euclidean Distance

Next it is important to determine the relative importance of the individual motion cues per eigenmode. For example, in Figure 7.2a the magnitude of the roll rate, $\check{p}^{EOM}$, is larger than that of the sway specific force, $\check{f}_{y_p}^{EOM}$, and yaw rate, $\check{r}^{EOM}$. This observation became possible, since the eigenvectors are now expressed in threshold units. Using this insight the magnitudes can be used as indication for dominance of a certain motion cue per eigenmode. In this report, this is referred to as the dominance of a motion cue. It must be mentioned that these dominance's depend also on the flight condition. Table 7.1 shows the dominance of the motion cues for the flight condition as stated in Appendix A.

Table 7.1: The Dominance of Motion Cues per Eigenmode

	f_y	p	r
Dutch Roll	$\%DR_{f_y} = 0.188$	$\%DR_p = 0.635$	$\%DR_r = 0.177$
Aperiodic Roll	$\%AR_{f_y} = 0.337$	$\%AR_p = 0.651$	$\%AR_r = 0.013$
Spiral Mode	$\%SM_{f_y} = 0.103$	$\%SM_p = 0.078$	$\%SM_r = 0.819$

Finally an objective function can be formulated, the objective function aims to minimize the Euclidean distances between the eigenvectors of the selected eigenmode. In the formulated objective function, an individual or several eigenmodes can be selected by changing the values of α, β and γ. For example, if it is desired to only optimize the Dutch Roll then α can be set to 1 and the β and γ can be set to 0. This option is added as every flight simulator has different characteristics. For example, the motion space of the SRS is limited in such a way that it cannot mimic the Aperiodic Spiral Mode, due to its slow nature. In this case γ can, for example, be set to 0. Equation 7.1 shows the resulting objective function. This objective function is minimized by varying the MCA parameters, which is indicated by $\boldsymbol{x}$.

$$min: \quad Z(\boldsymbol{x}) = \alpha \cdot DR(\boldsymbol{x}) + \beta \cdot AR(\boldsymbol{x}) + \gamma \cdot SM(\boldsymbol{x}) \tag{7.1}$$

where

$$\boldsymbol{x} = \begin{bmatrix} K_{f_y} & \omega_{n_{f_y}} & \omega_{b_{f_y}} & \omega_{n_t} & \zeta_{f_y} & \zeta_t & K_p & \omega_{n_p} & \zeta_p & K_r & \omega_{n_r} & \zeta_r \end{bmatrix}^T \tag{7.2}$$

$$\alpha + \beta + \gamma = 1 \tag{7.3}$$

$$0 \leq \alpha, \beta, \gamma \leq 1 \tag{7.4}$$

The eigenmodes appearing in the objective function, Equation 7.1, can each be written in terms of motion cue dominance's and Euclidean distances. This formulation is given in Equations 7.5 to 7.7. What is nice about incorporating these dominance terms is that when a motion cue has a high dominance then it is more important to minimize the Euclidean distance than for a motion cue with low dominance. Exactly this behaviour is achieved with the current formulation of the objective function.

$$DR(\boldsymbol{x}) = \%DR_{f_y} \cdot |DR(\boldsymbol{x})|_{f_y} + \%DR_p \cdot |DR(\boldsymbol{x})|_p + \%DR_r \cdot |DR(\boldsymbol{x})|_r \tag{7.5}$$

$$AR(\boldsymbol{x}) = \%AR_{f_y} \cdot |AR(\boldsymbol{x})|_{f_y} + \%AR_p \cdot |AR(\boldsymbol{x})|_p + \%AR_r \cdot |AR(\boldsymbol{x})|_r \tag{7.6}$$

$$SM(\boldsymbol{x}) = \%SM_{f_y} \cdot |SM(\boldsymbol{x})|_{f_y} + \%SM_p \cdot |SM(\boldsymbol{x})|_p + \%SM_r \cdot |SM(\boldsymbol{x})|_r \tag{7.7}$$

with, e.g.:

$$|DR(\boldsymbol{x})|_{f_y} = ||\check{f}_{y_p}^{EOM} - \check{f}_{y_p}^{MCA}(\boldsymbol{x})||_{DR} \tag{7.8}$$

The $\boldsymbol{x}$ indicate the MCA tuning parameters, as given in Equation 7.2, that can be changed in such a way that the objective function is minimized.

7.2. Constraints

Ideally the Euclidean distances between all the eigenvectors would be zero, this would imply that the flight simulator mimics the actual aircraft perfectly. However, as of reasons explained in Sections 2.2 and 2.3 this would require a huge motion space for the motion platform. This is usually not available as the motion space is limited by actuator lengths. Apart from the lengths, the actuators also have limitations in the maximum velocity and acceleration it can achieve.

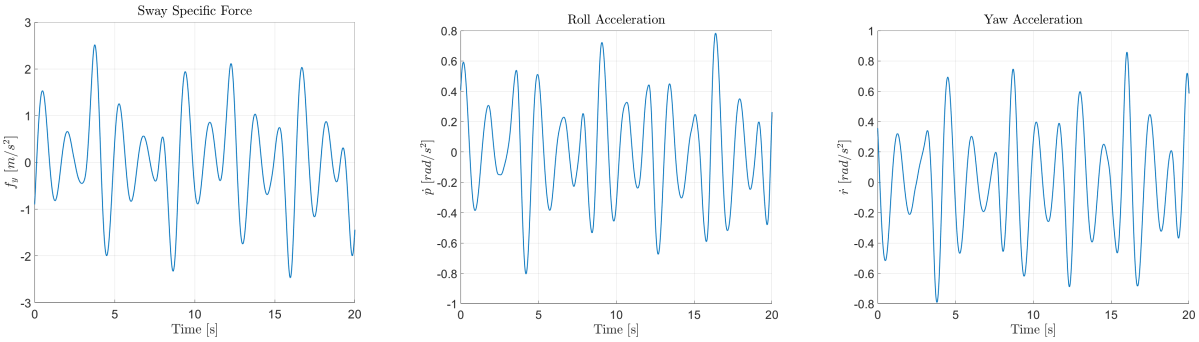

Figure 7.3: Time Traces of Representative Dutch Roll Excitation

Therefore, the objective function is extended with some constraints. For every parameter combination, the time traces of Figure 7.3 are simulated, $\boldsymbol{u} = f(f_y(t), \dot{p}(t), \dot{r}(t))$. The resulting actuator responses of this simulation are checked whether these stay within the limitations. The actuator constraints are formulated as follows:

$$l_{min} + B_l \leq l_{response}(\boldsymbol{x}, \boldsymbol{u}) \leq l_{max} - B_u \tag{7.9}$$

$$|v_{response}(\boldsymbol{x}, \boldsymbol{u})|_{max} \leq v_{max} \tag{7.10}$$

$$|a_{response}(\boldsymbol{x}, \boldsymbol{u})|_{max} \leq a_{max} \tag{7.11}$$

7.3. Tuning Algorithm Overview

Now the complete tuning algorithm has been derived, it is good to have a look at the different steps involved. This tuning algorithm was basically a continuation on the PEMD results, therefore a quick summary will be given. Where the OMCT test gave a detailed picture on the performance over a given frequency domain, the EMD and PEMD methods give distortion information for a given flight condition. Before using the tuning algorithm, the flight condition needs to be chosen which is used to linearize the EOM. These linearized EOM are then coupled to the linearized MCA using the steps described in Chapter 5. Hereafter, the output matrix must be divided by the vestibular thresholds to give all motion cues the same unit (threshold unit). After obtaining the eigenvectors of the system matrix and multiplying those with the output matrix (in threshold unit), the eigenvector distortions can be determined. These distortions indicate the amount of distortions caused by the MCA.

When taking the magnitude of the eigenvectors corresponding to the EOM, the dominance of each motion cue per eigenmode can be determined. The resulting dominance is constant for the earlier flight condition. In the tuning algorithm, these dominance are used to optimize the MCA settings for the given flight condition.

The formulation of the cost function allows for great flexibility. For example, the user can decide for which eigenmode is optimized, which is useful as different flight simulators have different performances. Also, when training a pilot how to operate an aircraft with a broken yaw damper, the settings can be optimized for simulating the Dutch Roll and aperiodic roll rather than the spiral mode.
Besides the cost function, the constrains also allow for flexibility. For example, different time histories, corresponding to different tasks, can be used. Also, a buffer distance is included in the actuator length constraint. So, by increasing this distance, the cost function will optimize the MCA parameters for a smaller motion space.

On paper this tuning approach seems to have great potential, however, to confirm this a pilot-in-the-loop experiment will have to be performed. When the EMD analysis was designed for linear model of the Cessna Citation 500, also a pilot-in-the-loop experiment was performed. For this experiment the MCA settings were selected manually and optimized for the short period eigenmode. During the experiment, the pilot was instructed to excite the short period eigenmode of the aircraft and was asked to give feedback on the realism of the motion signature.
The experiment corresponding to this report will differ from the experiment with the linear model of the Cessna Citation 500. Rather than selecting the MCA settings manually, the derived tuning algorithm will be used to optimize the MCA settings. Also, instead of exciting the short period mode, for this experiment the Dutch Roll will be excited. The Dutch Roll is chosen for this experiment, as it is more interesting to analyze than the aperiodic modes. The last difference is that the aircraft will be excited externally while the pilot is instructed to minimize the altitude and heading deviations. There are mainly two reasons for this. Firstly, there is more control over the amount of motion that the pilot is subjected to. Secondly, the task becomes an active flight task where the pilot has to control the aircraft. A more detailed explanation of this pilot-in-the-loop experiment will be given in the next chapter.

8

Pilot-in-the-Loop Experiment

A part from the main research question has been answered in last chapters, however, to answer the complete research question an experiment needs to be performed. This chapter designs this experiment which will be performed with the SRS.

In order to investigate the predictive capabilities of the PEMD methodology and validate its inherent assumptions, a pilot-in-the-loop experiment will be performed in the SRS. In total three different MCA configurations will be used.

8.1. Hypothesis

- It is hypothesized that the PEMD tuned configuration is preferred over the OMCT and baseline tuned configurations, for an aircraft which is externally excited by Dutch Roll. This is hypothesized because the aircraft dynamics are taken into account during the PEMD tuning process. This hypothesis is rejected if the PEMD tuned configuration receives a lower overall fidelity rating than the OMCT tuned configuration.
- It is hypothesized that the pilot has a better performance to suppress the Dutch Roll eigenmode with the PEMD tuned configuration than with the OMCT and baseline tuned configurations.

In order to test these hypothesis, different MCA configurations will be used. Table 8.1 shows these configurations, in here the Greek symbols refer to the optimization function in Equation 8.1.

$$min: \quad Z(\boldsymbol{x}) = \alpha \cdot DR(\boldsymbol{x}) + \beta \cdot AR(\boldsymbol{x}) + \gamma \cdot SM(\boldsymbol{x}) \tag{8.1}$$

Table 8.1: Labels and Description of the five used Configurations of the CWA

Label	Description
B	Baseline configuration (Appendix G)
O	OMCT tuned configuration with bad performance in PEMD (Appendix H)
P	PEMD tuned configuration with $\alpha = \beta = 0.5$ and $\gamma = 0.0$ (Appendix I)

Even though the experimental task will be to control the aircraft in which the Dutch Roll is externally excited, the *P* configuration is tuned for both Dutch Roll and Aperiodic Roll. The reason for this is that pilot feedback from a previous experiment with the longitudinal EMD indicated that tuning could be improved by considering simultaneous tuning, as all eigenmodes are always excited together, see Figure 8.1. The Aperiodic Spiral Mode, however, is not taken into account during tuning. This is because the SRS motion space is limited, and is therefore not able to cue this mode.

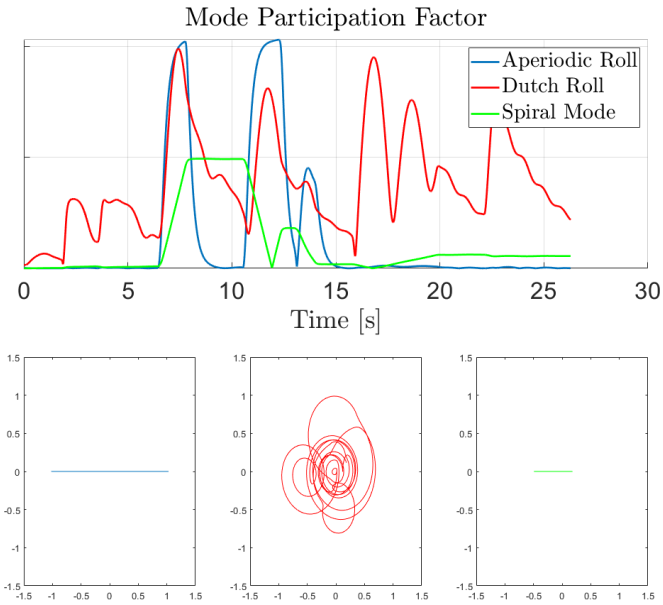

Figure 8.1: Mode Participation Factor of Flight on November 27, 2019

8.2. Experimental Task

The experimental task is to fly the Cessna Citation 500 aircraft and minimize the altitude and heading deviations. During the experiment, the Dutch Roll will externally be excited with a gust that introduces a side slip, see Figure 8.2. The yaw damper of the configured aircraft is disabled, so lateral motion cues will be clearly present. The surge, heave and pitch motions will be disabled, so the pilot can still control the aircraft in pitch, although these cues are not felt. Furthermore, the yaw motion settings are kept the same for all MCA configurations. After each evaluated pair, the pilot has to indicate a preferred MCA configuration. This judgement will be based on the sway and roll perceived motion cues. As the motion filters are tuned for a specific flight condition, it is important that the aircraft does not deviate too much from this trimmed condition, therefore, the following conditions have to be satisfied at all times:

- No full deflections of the control column and rudder are allowed.
- The airspeed deviation must be minimized.
- No throttle changes are allowed.

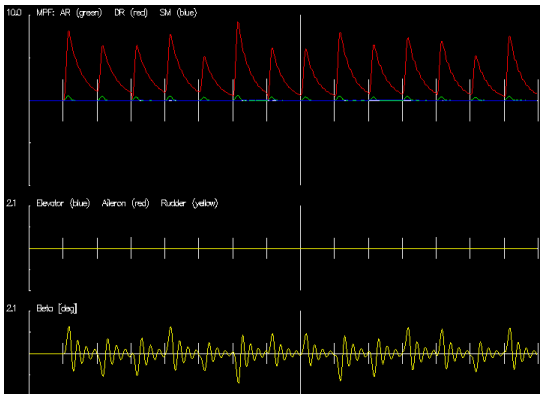

Figure 8.2: Motion Participation Factors of Dutch Roll Excited Aircraft

8.3. Experiment Structure

8.3.1. Simulator Setup

The simulated aircraft is a non-linear high fidelity model of the Cessna Citation 500 business jet. The initial trim condition is at an altitude of 5000m and Mach number of 0.5 with corresponding velocities $V_{TAS} = 160\ m/s$ and $V_{IAS} = 245\ kts$.

- Visuals: A full outside visual is provided at all times.
- Sound: Engine noise is played while the pilots are performing the task in order to mask any noise coming from the motion actuators.
- Control devices: Control column and rudder paddles are used for controlling the aircraft.
- Aircraft configuration: The aircraft is in cruise configuration:
  - Flaps: UP
  - Gear: UP
  - Thrust: 94.8% Fan RPM
  - $\delta_{e_0} = 0.3$ deg
  - Yaw damper: DISABLED

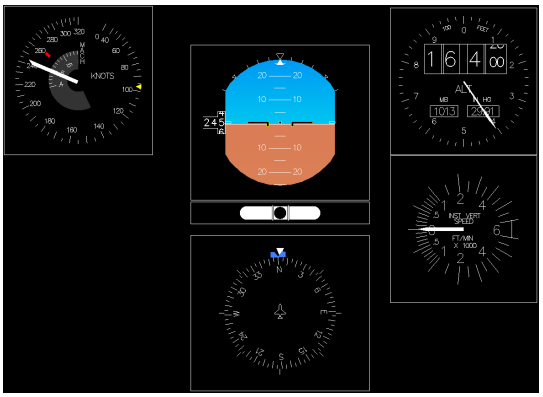

Figure 8.3: Instrument Panel used during Experiment

8.3.2. Dependent Measures

The main recorded variables are the preferred MCA configuration from each paired comparison together with a confidence level ranging from 0 to 2, where: 0 is *no confidence*, 1 is *normal confidence* and 2 is *high confidence*. Pilots are briefed to select the 'winner' as the configuration which presents the most realistic motion cues. For validation purpose, the following time histories are recorded:

- Pilot inputs;
- Aircraft states;
- Specific forces;
- Simulation motion cues; and
- Pilot's preference and confidence level.

8.3.3. Independent Variables

The independent variables are three different MCA configurations which will be tuned using the offline test environment in Matlab. The resulting MCA parameters will be used in the online experiment with the SRS.

8.3.4. Control Variables

For isolating the hypotheses, which is based on subjective rating from pilots, it is extremely important that all other factors that affect the pilot's behaviour do not vary over the different experimental conditions, and therefore the following control variables are defined:

- The display/instrument panel is kept constant.
- The controlled dynamics are kept constant, namely: same flight condition and same accurate high fidelity Citation model.
- Manipulator and its settings are kept constant
- Procedural variables: every pilot receives the same instructions and amount of training.

8.3.5. Training

Each pilot receives approximately 15 minutes of training, during which the pilot flies all the MCA configurations twice in randomized order. Every training run is one minute, during which the pilot can get a feeling of the aircraft control behaviour.

8.3.6. Subjects

In total 12 experienced pilots will be required. Experienced pilots are necessary as a subjective judgement (preferred MCA configuration) has to be made about the realism of the perceived motion cues. Table 8.2 contains a proposed Latin Square Matrix that visualizes the configurations to be flown by the different subjects.

Table 8.2: Latin Square Matrix of the Experiment Conditions for all Pilots

Subject	Conditions						
1	Training	*B - O*	*B - P*	*O - P*	*P - O*	*P - B*	*O - B*
2		*O - P*	*B - O*	*B - P*	*P - B*	*O - B*	*P - O*
3		*B - P*	*O - P*	*B - O*	*O - B*	*P - O*	*P - B*
4		*P - O*	*P - B*	*O - B*	*B - O*	*B - P*	*O - P*
5		*P - B*	*O - B*	*P - O*	*O - P*	*B - O*	*B - P*
6		*O - B*	*P - O*	*P - B*	*B - P*	*O - P*	*B - O*
7		*B - O*	*B - P*	*O - P*	*P - O*	*P - B*	*O - B*
8		*O - P*	*B - O*	*B - P*	*P - B*	*O - B*	*P - O*
9		*B - P*	*O - P*	*B - O*	*O - B*	*P - O*	*P - B*
10		*P - O*	*P - B*	*O - B*	*B - O*	*B - P*	*O - P*
11		*P - B*	*O - B*	*P - O*	*O - P*	*B - O*	*B - P*
12		*O - B*	*P - O*	*P - B*	*B - P*	*O - P*	*B - O*

9
Conclusions

Throughout the report the different sub-questions have been answered. The answers to these individual questions help to answer the the central research questions, which was:

To what extent is the Perception Eigenmode Distortion an improvement to the Eigenmode Distortion and Objective Motion Cueing Test (for the lateral model of the Cessna Citation 500)?

The first part of this research question has, however, already been answered. By including the perception thresholds in the derivation of the EMD, all the eigenvectors have the same unit. As of this, the magnitudes of the different motion cues can now be compared to one another in each eigenmode. Furthermore, a dominant motion cue can be identified for each eigenmode. So, for the flight condition used in Chapter 6 the dominant motion cues are roll rate for the Dutch Roll and aperiodic roll, and yaw rate for the spiral mode. Besides the use of vestibular threshold values, a model which included the vestibular system was formulated. This vestibular extension increased the complexity significantly, e.g. the system of 16 states became a system of 30 states. This extension is, however, removed as it was prone to errors without adding extra value.
The second part of this research question, the performance of the PEMD with respect to the OMCT will be evaluated using the proposed pilot-in-the-loop experiment.

This page is intentionally left blank.

Reference List

[1] Gouverneur B., Mulder J.A., van Paassen M.M., Stroosma O., and Field E. Optimisation of the simona research simulator's motion filter settings for handling qualities experiments. In *AIAA Modeling and Simulation Technologies Conference and Exhibit*, 08 2003. doi: 10.2514/6.2003-5679.

[2] Fernández C. and Goldberg J. Physiology of peripheral neurons innervating semicircular canals of the squirrel monkey. ii. response to sinusoidal stimulation and dynamics of peripheral vestibular system. *Journal of neurophysiology*, 34 4:661–75, 1971.

[3] Allerton D. *Principles of Flight Simulation*. Amer Inst of Aeronautics, 2009. ISBN 978-0-470-75436-8.

[4] Stewart D. A platform with six degrees of freedom. *Proceedings of the Institution of Mechanical Engineers*, 180(1):371–386, 1965.

[5] Haward D.M. The sanders teacher. Technical report, Flight, December 1910.

[6] Groen E., Wentink M., Valente Pais A., Mulder M., and van Paassen M.M. Motion perception thresholds in flight simulation. In *AIAA Modeling and Simulation Technologies Conference and Exhibit*, 2012. doi: 10.2514/6.2006-6254.

[7] Heerspink H., Berkouwerr W., Stroosma O., van Paassen M.M., Mulder M., and B. Mulder. Evaluation of vestibular thresholds for motion detection in the simona research simulator. In *AIAA Modeling and Simulation Technologies Conference and Exhibit*, 08 2005. ISBN 978-1-62410-057-4. doi: 10.2514/6.2005-6502.

[8] Miletović I., Pavel M.D., Stroosma O., Pool D.M., Van Paassen M.M., Wentink M., and Mulder M. Motion cueing fidelity in flight simulation: A novel perspective. *TBD*, 2014. To be submitted.

[9] *Manual of Criteria for the Qualification of Flight Simulation Training Devices - Volume 1 - Aeroplanes*. International Civil Aviation Organization, 4th edition, 2015.

[10] Mulder J.A., van Staveren W.H.J.J., van der Vaart J.C., de Weerdt E., de Visser C.C., in 't Veld A.C., and Mooij E. Lecture notes: Flight dynamics, March 2013.

[11] Schroeder J.A. *Helicopter Flight Simulation Motion Platform Requirements*. PhD thesis, Stanford University, 01 1999.

[12] Sinacori J.B. The determination of some requirements for a helicopter flight research simulation facility. In *NASA*, 1977.

[13] Dieudonne J.E., Parrish R.V., and Bardusch R.E. An actuator extension transformation for a motion simulator and an inverse transformation applying newton-raphson's method. Technical report, NASA, November 1972.

[14] Rolfe J.M. and Staples K.J. *Flight Simulation*. Cambridge University Press, 1986.

[15] Davis J.R., Johnson R., Stepanek J., and Fogarty J.A. *Fundamentals of aerospace medicine: Fourth edition*. Wolters Kluwer Health Adis (ESP), 11 2011. ISBN 9780781774666.

[16] Reid L.D. and Nahon M.A. Flight simulation motion-base drive algorithms: part 1. developing and testing equations. In *UTIAS Report*, 1985.

[17] Kelly L.L. and Parke R.B. *The Pilot Maker*. Grosset & Dunlap, 1970.

[18] Baarspul M. *Flight Simulation Techniques with Emphasis on the Generation of High Fidelity 6 DOF Motion Cues*. Number Memorandum M-553 in Memorandum Delft University of Technology, Department of Aerospace Engineering. Delft University of Technology, June 1986.

[19] Stroosma O., van Paassen M.M., Mulder M., Hosman R.J.A.W., and Advani S.K. Applying the objective motion cueing test to a classical washout algorithm. In *AIAA Model-*

ing and Simulation Technologies Conference and Exhibit. American Institute of Aeronautics and Astronautics, 2010.

[20] Adorian P., Staynes W., and Bolton M. *The Evolution of the Flight Simulator*. Royal Aeronautical Society, 1979.

[21] Grant P.R. *The Development of a Tuning Paradigm for Flight Simulator Motion Drive Algorithms*. Canadian theses. University of Toronto, 1996. ISBN 9780612117327.

[22] Forgus R.H. and Melamed L.E. *Perception: A Cognitive-Stage Approach*. McGraw Hill Book Co., second edition edition, 1966.

[23] Carsten S., Umut D., and Holger D. Objective motion cueing test – experiences of a new user. In *AIAA Modeling and Simulation Technologies Conference and Exhibit*, 06 2014. doi: 10.2514/6.2014-2205.

[24] Stoev S., Stroosma O., van Paassen M.M., Miletović I., and Mulder M. Eigenmode distortion analysis for motion cueing evaluation in fixed-wing aircraft simulators. In *AIAA Modeling and Simulation Technologies Conference and Exhibit*, 01 2019. doi: 10.2514/6.2019-0179.

[25] Advani S.K. *The Kinematic Design of Flight Simulator Motion-bases*. Control and Stimulation Series. Delft University Press, 1998. ISBN 9789040716713.

[26] Dalmeijer W., Miletović I., Stroosma O., and Pavel M. Extending the objective motion cueing test to measure rotorcraft simulator motion characteristics. In *73rd Annual AHS International Forum and Technology Display*, pages 1876–1891, 05 2017.

[27] Fu W. *Evidence-based development and evaluation of haptic interfaces for manual control*. PhD thesis, Delft University of Technology, 6 2019.

[28] Webster. *The New Lexicon Webster's Encyclopedic Dictionary of the English Language*. Lexicon Publications Inc., 1991.

[29] Roza Z.C. *Simulation fidelity Theory and Practice*. Delft University Press, 01 2005.

A

Cessna Citation I Stability and Control Derivatives

Table A.1: Symmetric and Asymmetric Stability and Control Derivatives for Cessna Citation 500, condition: Cruise

$V = 160.3\ [m/s]$	$h = 5000\ [m]$	$K^2_{XX} = 0.019\ [-]$
$S = 24.2\ [m^2]$	$m = 5207\ [kg]$	$K^2_{YY} = 1.114\ [-]$
$\bar{c} = 2.022\ [m]$	$\rho = 0.7361\ [kg/m^3]$	$K^2_{ZZ} = 0.042\ [-]$
$b = 13.36\ [m]$	$C_L = 0.2239\ [-]$	$K_{XZ} = 0.002\ [-]$
$C_{X_0} = -0.0277$	$C_{Z_0} = -0.2160$	$C_{m_0} = 0.2130$
$C_{X_u} = -0.0698$	$C_{Z_u} = -0.4702$	$C_{m_u} = 0.0561$
$C_{X_\alpha} = 0.0744$	$C_{Z_\alpha} = -5.6149$	$C_{m_\alpha} = -0.4982$
$C_{X_{\dot{\alpha}}} = 0.0259$	$C_{Z_{\dot{\alpha}}} = -0.2039$	$C_{m_{\dot{\alpha}}} = 0.1689$
$C_{X_q} = -0.4179$	$C_{Z_q} = -5.8339$	$C_{m_q} = 10.152$
$C_{X_{\delta_e}} = -0.0131$	$C_{Z_{\delta_e}} = -0.5814$	$C_{m_{\delta_e}} = -1.2269$
$C_{X_{\delta_t}} = 0.0000$	$C_{Z_{\delta_t}} = 0.0000$	$C_{m_{\delta_t}} = 0.0000$
$C_{Y_\beta} = -0.0750$	$C_{l_\beta} = -0.1061$	$C_{n_\beta} = 0.1305$
$C_{Y_p} = -0.0109$	$C_{l_p} = -0.5209$	$C_{n_p} = -0.0672$
$C_{Y_r} = 0.8499$	$C_{l_r} = -0.1522$	$C_{n_r} = -0.2089$
$C_{Y_{\delta_a}} = -0.0400$	$C_{l_{\delta_a}} = -0.1848$	$C_{n_{\delta_a}} = -0.0140$
$C_{Y_{\delta_r}} = 0.2300$	$C_{l_{\delta_r}} = 0.0358$	$C_{n_{\delta_r}} = -0.0947$

This page is intentionally left blank.

B
Motion Cueing Algorithm Settings for Examples

Table B.1: CWA Filter Parameters used for Symmetric EMD and PEMD Examples

K_{f_x}	0.8	[−]
$\omega_{n_{f_x}}$	1.0	$[rad/s]$
$\omega_{b_{f_x}}$	0.0	$[rad/s]$
ζ_{f_x}	1.0	[−]
ω_{n_t}	1.0	$[rad/s]$
ζ_t	1.0	[−]
K_{f_z}	0.5	[−]
$\omega_{n_{f_z}}$	2.5	$[rad/s]$
$\omega_{b_{f_z}}$	0.2	$[rad/s]$
ζ_{f_z}	1.0	[−]
K_q	0.7	[−]
ω_{n_q}	0.7	$[rad/s]$
ζ_q	1.0	[−]

Table B.2: CWA Filter Parameters used for Asymmetric EMD and PEMD Examples

K_{f_y}	0.8	[−]
$\omega_{n_{f_y}}$	1.0	$[rad/s]$
$\omega_{b_{f_y}}$	0.0	$[rad/s]$
ζ_{f_y}	1.0	[−]
ω_{n_t}	1.0	$[rad/s]$
ζ_t	1.0	[−]
K_p	0.7	[−]
ω_{n_p}	0.7	$[rad/s]$
ζ_p	1.0	[−]
K_r	0.7	[−]
ω_{n_r}	0.7	$[rad/s]$
ζ_r	1.0	[−]

This page is intentionally left blank.

C
Eigenmode Distortion on Symmetric Aircraft Model

C.1. Aircraft Model

This appendix derives the EMD applied for the symmetrical motion of the Cessna Citation 500 aircraft. In order to do so, the longitudinal Equations of Motion (EOM) must be defined. The dimensional symmetric EOM, given in Equations C.1 to C.4, are a set of linearized equations that replicate the physical behaviour of the actual aircraft. These derived linearized equations assume a steady, straight, symmetric flight condition with a flat and non-rotating Earth.

$$-W\cos\theta_0\Delta\theta + X_u\Delta u + X_w\Delta w + X_q\Delta q + X_{\delta_e}\Delta\delta_e + X_{\delta_t}\Delta\delta_t = m\Delta\dot{u} \tag{C.1}$$

$$-W\sin\theta_0\Delta\theta + Z_u\Delta u + Z_w\Delta w + Z_{\dot{w}}\Delta\dot{w} + Z_q\Delta q + Z_{\delta_e}\Delta\delta_e + Z_{\delta_t}\Delta\delta_t = m(\Delta\dot{w} - \Delta qV) \tag{C.2}$$

$$M_u\Delta u + M_w\Delta w + M_{\dot{w}}\Delta\dot{w} + M_q\Delta q + M_{\delta_e}\Delta\delta_e + M_{\delta_t}\Delta\delta_t = I_{yy}\Delta\dot{q} \tag{C.3}$$

$$\Delta\dot{\theta} = \Delta q \tag{C.4}$$

The above equations are a linearized set of EOM, however not yet in state-space representative form. Following the steps as in classical flight dynamics, these equations can we written as a non-dimensional linear time invariant state-space form [10]:

$$\begin{bmatrix} \Delta\dot{\hat{u}} \\ \Delta\dot{\alpha} \\ \Delta\dot{\theta} \\ \frac{\Delta\dot{q}\bar{c}}{V} \end{bmatrix} = \begin{bmatrix} x_u & x_\alpha & x_\theta & x_q \\ z_u & z_\alpha & z_\theta & z_q \\ 0 & 0 & 0 & \frac{V}{\bar{c}} \\ m_u & m_\alpha & m_\theta & m_q \end{bmatrix} \begin{bmatrix} \Delta\hat{u} \\ \Delta\alpha \\ \Delta\theta \\ \frac{\Delta q\bar{c}}{V} \end{bmatrix} + \begin{bmatrix} x_{\delta_e} & x_{\delta_t} \\ z_{\delta_e} & z_{\delta_t} \\ 0 & 0 \\ m_{\delta_e} & m_{\delta_t} \end{bmatrix} \begin{bmatrix} \Delta\delta_e \\ \Delta\delta_t \end{bmatrix} \tag{C.5}$$

The definition of the newly introduced symbols are recapitulated in Table C.1.

Table C.1: Symbols Appearing in the General State-Space Representation of Equation C.5

	x_i	z_i	m_i
$i = u$	$\frac{V}{\bar{c}}\frac{C_{X_u}}{2\mu_c}$	$\frac{V}{\bar{c}}\frac{C_{Z_u}}{2\mu_c - C_{Z_{\dot{\alpha}}}}$	$\frac{V}{\bar{c}}\frac{C_{m_u} + C_{Z_u}\frac{C_{m_{\dot{\alpha}}}}{2\mu_c - C_{Z_{\dot{\alpha}}}}}{2\mu_c K_Y^2}$
$i = \alpha$	$\frac{V}{\bar{c}}\frac{C_{X_\alpha}}{2\mu_c}$	$\frac{V}{\bar{c}}\frac{C_{Z_\alpha}}{2\mu_c - C_{Z_{\dot{\alpha}}}}$	$\frac{V}{\bar{c}}\frac{C_{m_\alpha} + C_{Z_\alpha}\frac{C_{m_{\dot{\alpha}}}}{2\mu_c - C_{Z_{\dot{\alpha}}}}}{2\mu_c K_Y^2}$
$i = \theta$	$\frac{V}{\bar{c}}\frac{C_{Z_0}}{2\mu_c}$	$-\frac{V}{\bar{c}}\frac{C_{X_0}}{2\mu_c - C_{Z_{\dot{\alpha}}}}$	$-\frac{V}{\bar{c}}\frac{C_{X_0}\frac{C_{m_{\dot{\alpha}}}}{2\mu_c - C_{Z_{\dot{\alpha}}}}}{2\mu_c K_Y^2}$
$i = q$	$\frac{V}{\bar{c}}\frac{C_{X_q}}{2\mu_c}$	$\frac{V}{\bar{c}}\frac{2\mu_c + C_{Z_q}}{2\mu_c - C_{Z_{\dot{\alpha}}}}$	$\frac{V}{\bar{c}}\frac{C_{m_q} + C_{m_{\dot{\alpha}}}\frac{2\mu_c + C_{Z_q}}{2\mu_c - C_{Z_{\dot{\alpha}}}}}{2\mu_c K_Y^2}$
$i = \delta_e$	$\frac{V}{\bar{c}}\frac{C_{X_{\delta_e}}}{2\mu_c}$	$\frac{V}{\bar{c}}\frac{C_{Z_{\delta_e}}}{2\mu_c - C_{Z_{\dot{\alpha}}}}$	$\frac{V}{\bar{c}}\frac{C_{m_{\delta_e}} + C_{Z_{\delta_e}}\frac{C_{m_{\dot{\alpha}}}}{2\mu_c - C_{Z_{\dot{\alpha}}}}}{2\mu_c K_Y^2}$
$i = \delta_t$	$\frac{V}{\bar{c}}\frac{C_{X_{\delta_t}}}{2\mu_c}$	$\frac{V}{\bar{c}}\frac{C_{Z_{\delta_t}}}{2\mu_c - C_{Z_{\dot{\alpha}}}}$	$\frac{V}{\bar{c}}\frac{C_{m_{\delta_t}} + C_{Z_{\delta_t}}\frac{C_{m_{\dot{\alpha}}}}{2\mu_c - C_{Z_{\dot{\alpha}}}}}{2\mu_c K_Y^2}$

The states in the state-space system in Equation C.5 are non-dimensional. However, for the continuation of this chapter these states are made dimensional by realizing the following relationships:

$$\hat{u} = \frac{u}{V} \qquad \dot{\hat{u}} = \frac{\dot{u}}{V}$$
$$\alpha = \frac{w}{V} \qquad \dot{\alpha} = \frac{\dot{w}}{V}$$
$$q = \frac{V}{\bar{c}}\frac{q\bar{c}}{V}$$

Applying these to the non-dimensional state-space of Equation C.5 yields a dimensional state-space system, Equation C.6. It must be mentioned that this system is defined in the stability frame and, therefore, will require a transformation to body frame later on.

$$\begin{bmatrix} \Delta\dot{u}_s \\ \Delta\dot{w}_s \\ \Delta\dot{\theta} \\ \Delta\dot{q} \end{bmatrix} = \begin{bmatrix} x_u & x_\alpha & x_\theta \cdot V & x_q \cdot \bar{c} \\ z_u & z_\alpha & z_\theta \cdot V & z_q \cdot \bar{c} \\ 0 & 0 & 0 & 1 \\ \frac{m_u}{\bar{c}} & \frac{m_\alpha}{\bar{c}} & \frac{V}{\bar{c}} m_\theta & \frac{V}{\bar{c}} m_q \end{bmatrix} \begin{bmatrix} \Delta u_s \\ \Delta w_s \\ \Delta\theta \\ \Delta q \end{bmatrix} + \begin{bmatrix} x_{\delta_e} \cdot V & x_{\delta_t} \cdot V \\ z_{\delta_e} \cdot V & z_{\delta_t} \cdot V \\ 0 & 0 \\ m_{\delta_e} \frac{V}{\bar{c}} & m_{\delta_t} \frac{V}{\bar{c}} \end{bmatrix} \begin{bmatrix} \Delta\delta_e \\ \Delta\delta_t \end{bmatrix} \tag{C.6}$$

As been mentioned, the derived state-space system in Equation C.6 assumes a steady, straight, symmetric flight condition with a flat non-rotating Earth, for this the following trim conditions were imposed:

$$u_{s_0} = V \tag{C.7}$$
$$w_{s_0} = 0 \tag{C.8}$$
$$\gamma_0 = 0 \tag{C.9}$$
$$\theta_0 = \arcsin\left(\frac{C_{X_0}\frac{1}{2}\rho V^2 S}{W}\right) \tag{C.10}$$
$$\alpha_0 = \theta_0 - \gamma_0 \tag{C.11}$$

The next step is to formulate the specific forces as experienced at pilot position. Specific force is defined as the non-gravitational force per unit mass, which can be formulated as:

$$\boldsymbol{f}^b_{cg} = \boldsymbol{a}^b - \boldsymbol{g}_S \tag{C.12}$$

where (see Figure C.1):

$$\boldsymbol{g}_S = \begin{bmatrix} -g\sin\theta \\ g\cos\theta \end{bmatrix} \tag{C.13}$$

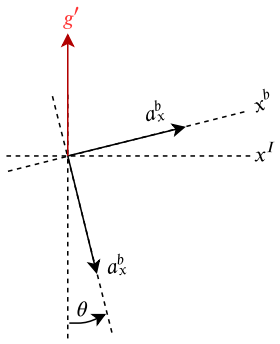

Figure C.1: Relation between Inertial and Body Axis

In order to formulate the specific forces, the accelerations need to be determined first, after which the gravitational components can be subtracted. The accelerations defined in body frame are:

$$a_x^b = \dot{u}_b + q_b w_b \tag{C.14}$$

$$a_z^b = \dot{w}_b - q_b u_b \tag{C.15}$$

As now is directly clear, a transformation between stability and body frame is required as the specific forces and accelerations are defined in body frame. These states in stability frame can easily be transformed to body frame using:

$$u_b = u_s \cos\alpha - w_s \sin\alpha \tag{C.16}$$

$$w_b = u_s \sin\alpha + w_s \cos\alpha \tag{C.17}$$

Combining Equations C.12 to C.17 yields the specific forces in body frame at the centre of gravity:

$$f_{x_{cg}}^b = \dot{u}_s \cos\alpha - \dot{w}_s \sin\alpha + q_b u_s \sin\alpha + q_b w_s \cos\alpha + g\sin\theta \tag{C.18}$$

$$f_{z_{cg}}^b = \dot{u}_s \sin\alpha + \dot{w}_s \cos\alpha - q_b u_s \cos\alpha + q_b w_s \sin\alpha - g\cos\theta \tag{C.19}$$

The next step is to express these specific forces at pilot position. This transformation becomes increasingly important as the aircraft gets bigger. For example, if the aircraft gets bigger, the distance between centre of gravity and cockpit increases as well. This increased distance acts as a moment arm giving additional experienced specific forces due to a pitch rate. For light aircraft the pilot is sitting close to the centre of gravity, which implies that this transformation is not very important. However, for the Cessna Citation 500 this distance is not negligible. The translation from centre of gravity to pilot position is given in Equations C.20 and C.21. For the Cessna Citation the moment arms are $l_x = 3.2$ $[m]$ and $l_z = 1$ $[m]$, for horizontal and vertical distance, respectively.

$$f_{x_p} = f_{x_{cg}}^b - \dot{q}_b l_z \tag{C.20}$$

$$f_{z_p} = f_{z_{cg}}^b - \dot{q}_b l_x \tag{C.21}$$

Finally, by combining Equations C.12 to C.21 an expression for the specific forces at pilot position using the states of the EOM state-space system is formulated. This expression is formulated as:

$$f_{x_p} = \dot{u}_s \cos\alpha - \dot{w}_s \sin\alpha + q_b u_s \sin\alpha + q_b w_s \cos\alpha + g\sin\theta - \dot{q}_b l_z \tag{C.22}$$

$$f_{z_p} = \dot{u}_s \sin\alpha + \dot{w}_s \cos\alpha - q_b u_s \cos\alpha + q_b w_s \sin\alpha - g\cos\theta - \dot{q}_b l_x \tag{C.23}$$

The advantage of this formulation is that effect of aircraft size can easily be analyzed simply by choosing different values for the moment arms l_x and l_z. The next step is to formulate an output vector of the form $y = Cx + Du$. Unfortunately, the current formulation of this specific force does not allow this formulation as of the non-linearity's. Luckily, after linearizing Equations C.22 and C.23 this output vector formulation becomes possible. Important to realize is that due to this linearization the region of validity is limited. Next the linearization surge specific force are visualized, the same steps apply for the heave specific force.

$$\Delta f_{x_p} = \left.\frac{\partial f_{x_p}}{\partial u_s}\right|_0 \Delta u_s + \left.\frac{\partial f_{x_p}}{\partial w_s}\right|_0 \Delta w_s + \left.\frac{\partial f_{x_p}}{\partial \dot{u}_s}\right|_0 \Delta \dot{u}_s + \left.\frac{\partial f_{x_p}}{\partial \dot{w}_s}\right|_0 \Delta \dot{w}_s + \left.\frac{\partial f_{x_p}}{\partial \theta}\right|_0 \Delta\theta + \left.\frac{\partial f_{x_p}}{\partial q_b}\right|_0 \Delta q_b + \left.\frac{\partial f_{x_p}}{\partial \dot{q}_b}\right|_0 \Delta \dot{q}_b + \left.\frac{\partial f_{x_p}}{\partial \alpha}\right|_0 \Delta\alpha \tag{C.24}$$

where:

$$\left.\frac{\partial f_{x_p}}{\partial u_s}\right|_0 = q_{b_0}\sin\alpha_0 \qquad \left.\frac{\partial f_{x_p}}{\partial \theta}\right|_0 = g\cos\theta_0$$
$$\left.\frac{\partial f_{x_p}}{\partial w_s}\right|_0 = q_{b_0}\cos\alpha_0 \qquad \left.\frac{\partial f_{x_p}}{\partial q_b}\right|_0 = u_{s_0}\sin\alpha_0 + w_{s_0}\cos\alpha_0$$
$$\left.\frac{\partial f_{x_p}}{\partial \dot{u}_s}\right|_0 = \cos\alpha_0 \qquad \left.\frac{\partial f_{x_p}}{\partial \dot{q}_b}\right|_0 = -l_z$$
$$\left.\frac{\partial f_{x_p}}{\partial \dot{w}_s}\right|_0 = -\sin\alpha_0 \qquad \left.\frac{\partial f_{x_p}}{\partial \alpha}\right|_0 = -\dot{u}_{s_0}\sin\alpha_0 - \dot{w}_{s_0}\cos\alpha_0 + q_{b_0}u_{s_0}\cos\alpha_0 - q_{b_0}w_{s_0}\sin\alpha_0$$

These partial derivatives can be simplified by imposing the following conditions:

$$u_{s_0} \neq 0 \qquad \dot{u}_{s_0} = 0$$
$$w_{s_0} = 0 \qquad \dot{w}_{s_0} = 0$$
$$\theta_0 \neq 0 \qquad q_{b_0} = 0$$
$$\alpha_0 \neq 0$$

After performing the exact same steps for the heave specific forces yields the following linearized specific forces:

$$\Delta f_{x_p} = \Delta\dot{u}_s\cos\alpha_0 - \Delta\dot{w}_s\sin\alpha_0 + u_{s_0}\sin\alpha_0\Delta q_b + g\cos\theta_0\Delta\theta - l_z\Delta\dot{q}_b \tag{C.25}$$
$$\Delta f_{z_p} = \Delta\dot{u}_s\sin\alpha_0 - \Delta\dot{w}_s\cos\alpha_0 - u_{s_0}\cos\alpha_0\Delta q_b + g\sin\theta_0\Delta\theta - l_x\Delta\dot{q}_b \tag{C.26}$$

As a final step it is assumed that the the θ_0 and α_0 angles are small, which allows for a small angle approximation. This assumption is reasonable, as the EMD analysis is performed at cruise conditions. Finally, the length of equations and number of states increases vastly, therefore, the Δ notation is for the remainder of the report dropped from the inputs, outputs and states. The linearized specific forces now become:

$$f_{x_p} = \dot{u}_s - \dot{w}_s\alpha_0 + u_{s_0}\alpha_0 q_b + g\theta - l_z\dot{q}_b \tag{C.27}$$
$$f_{z_p} = \dot{u}_s\alpha_0 - \dot{w}_s - u_{s_0}q_b + g\theta_0\theta - l_x\dot{q}_b \tag{C.28}$$

The next step is to actually formulate the output vector and its C- and D matrices. To simplify this step the individual appearing states in above equations are illustrated next:

$$\dot{u}_s = \begin{bmatrix} x_u & x_\alpha & x_\theta V & x_q\bar{c}\end{bmatrix}\boldsymbol{x} + \begin{bmatrix} x_{\delta_e}V & x_{\delta_t}V\end{bmatrix}\boldsymbol{u} \tag{C.29}$$
$$\dot{w}_s = \begin{bmatrix} z_u & x_\alpha & z_\theta V & z_q\bar{c}\end{bmatrix}\boldsymbol{x} + \begin{bmatrix} z_{\delta_e}V & z_{\delta_t}V\end{bmatrix}\boldsymbol{u} \tag{C.30}$$
$$\theta = \begin{bmatrix} 0 & 0 & 1 & 0\end{bmatrix}\boldsymbol{x} + \begin{bmatrix} 0 & 0\end{bmatrix}\boldsymbol{u} \tag{C.31}$$
$$q_b = \begin{bmatrix} 0 & 0 & 0 & 1\end{bmatrix}\boldsymbol{x} + \begin{bmatrix} 0 & 0\end{bmatrix}\boldsymbol{u} \tag{C.32}$$
$$\dot{q}_b = \begin{bmatrix} \frac{m_u}{\bar{c}} & \frac{m_\alpha}{\bar{c}} & \frac{V}{\bar{c}}m_\theta & \frac{V}{\bar{c}}m_q\end{bmatrix}\boldsymbol{x} + \begin{bmatrix} m_{\delta_e}\frac{V}{\bar{c}} & m_{\delta_t}\frac{V}{\bar{c}}\end{bmatrix}\boldsymbol{u} \tag{C.33}$$

Now by combining the knowledge of Equations C.27 to C.33 the final output vector can be formulated.

$$\boldsymbol{y}^{EOM} = \begin{pmatrix} f_{x_p}^{EOM} \\ f_{z_p}^{EOM} \\ q^{EOM}\end{pmatrix} = \begin{bmatrix} C_{f_xu} & C_{f_xw} & C_{f_x\theta} & C_{f_xq} \\ C_{f_zu} & C_{f_zw} & C_{f_z\theta} & C_{f_zq} \\ 0 & 0 & 0 & 1\end{bmatrix}\boldsymbol{x} + \begin{bmatrix} D_{f_x\delta_e} & D_{f_x\delta_t} \\ D_{f_z\delta_e} & D_{f_z\delta_t} \\ 0 & 0\end{bmatrix}\boldsymbol{u} \tag{C.34}$$

This concludes the derivation of the specific forces and pitch rate experienced at pilot position. The definition of the newly introduced symbols of Equation C.34 are recapitulated in Table C.2.

Table C.2: Symbols Appearing in the Output Vector State-Space Representation of Equation C.34

	$C_{f_x i}$	$C_{f_z i}$	$C_{\dot{q} i}$
$i = u$	$x_u - \alpha_0 z_u - l_z \frac{m_u}{\bar{c}}$	$\alpha_0 x_u + z_u - l_x \frac{m_u}{\bar{c}}$	$\frac{m_u}{\bar{c}}$
$i = w$	$x_\alpha - \alpha_0 z_\alpha - l_z \frac{m_\alpha}{\bar{c}}$	$\alpha_0 x_\alpha + z_\alpha - l_x \frac{m_\alpha}{\bar{c}}$	$\frac{m_\alpha}{\bar{c}}$
$i = \theta$	$x_\theta V - \alpha_0 z_\theta V + g - l_z \frac{V}{\bar{c}} m_\theta$	$\alpha_0 x_\theta V + z_\theta V + g\theta_0 - l_x \frac{V}{\bar{c}} m_\theta$	$\frac{V}{\bar{c}} m_\theta$
$i = q$	$x_q \bar{c} - \alpha_0 z_q \bar{c} + u_{s_0} \alpha_0 - l_z \frac{V}{\bar{c}} m_q$	$\alpha_0 x_q \bar{c} + z_q \bar{c} + u_{s_0} - l_x \frac{V}{\bar{c}} m_q$	$\frac{V}{\bar{c}} m_q$

	$D_{f_x i}$	$D_{f_z i}$	$D_{\dot{q} i}$
$i = \delta_e$	$x_{\delta_e} V - \alpha_0 z_{\delta_e} V - l_z m_{\delta_e} \frac{V}{\bar{c}}$	$\alpha_0 x_{\delta_e} V + z_{\delta_e} V - l_x \frac{V}{\bar{c}} m_{\delta_e}$	$\frac{V}{\bar{c}} m_{\delta_e}$
$i = \delta_t$	$x_{\delta_t} V - \alpha_0 z_{\delta_t} V - l_z m_{\delta_t} \frac{V}{\bar{c}}$	$\alpha_0 x_{\delta_t} V + z_{\delta_t} V - l_x \frac{V}{\bar{c}} m_{\delta_t}$	$\frac{V}{\bar{c}} m_{\delta_t}$

C.2. Linearization of the Motion Cueing Algorithm

As have been explained in Chapter 2 the MCA usually gives simulator positions and angles for controlling the motion platform driving the simulator. However, for this study those outputs are of no relevance. In the SRS a CWA is used as MCA. This CWA is therefore adapted to output specific forces rather than positions. Figure C.2 illustrates this adapted CWA for longitudinal motions. As this section only covers the longitudinal motions, the following assumptions were imposed for the adaptation of this CWA: $\phi_{sim} = \psi_{sim} = 0$. As been covered, this MCA is highly non-linear, because of the components, such as, transformations and rate limiters, and is therefore linearized in this section. Previous section linearized the EOM which are inputs to the CWA, as of this linearization these inputs now represent deviations from an initial condition.

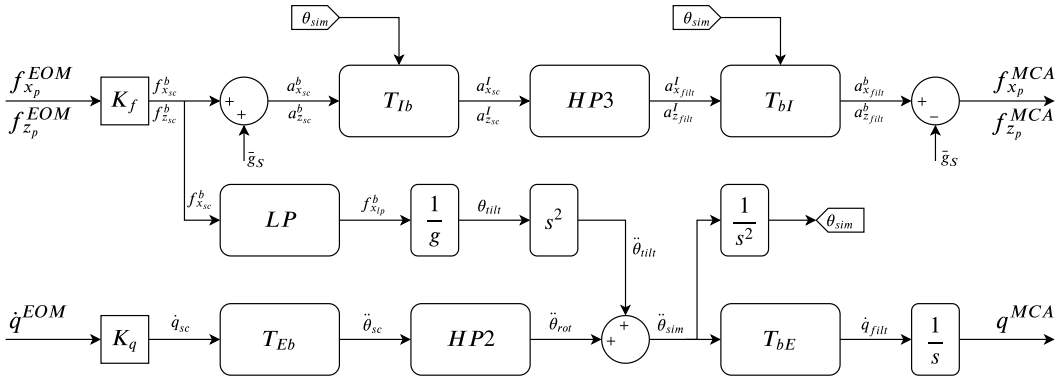

Figure C.2: Classical Washout Algorithm Adapted for Longitudinal EMD [16]

The different components of the CWA, indicated in Figure C.2, are presented in Equations C.35 to C.39.

$$T_{Ib} = \begin{bmatrix} \cos\theta_{sim} & \sin\theta_{sim} \\ -\sin\theta_{sim} & \cos\theta_{sim} \end{bmatrix} \qquad T_{bI} = \begin{bmatrix} \cos\theta_{sim} & -\sin\theta_{sim} \\ \sin\theta_{sim} & \cos\theta_{sim} \end{bmatrix} \tag{C.35}$$

$$T_{Eb} = \cos\phi = 1 \qquad T_{bE} = \cos\phi = 1 \tag{C.36}$$

$$HP3_i = \frac{s^2}{s^2 + 2\zeta_i \omega_{n_i} s + \omega_{n_i}^2} \frac{s}{s + \omega_{b_i}} \rightarrow \frac{s^3}{s^3 + A_i s^2 + B_i s + C_i} \tag{C.37}$$

where: $i = f_x$ and $i = f_z$ for the specific force x- and z-channel, respectively.

$$HP2 = \frac{s^2}{s^2 + 2\zeta_q \omega_{n_q} s + \omega_{n_q}^2} \rightarrow \frac{s^2}{s^2 + A_q s + B_q} \tag{C.38}$$

$$LP = \frac{\omega_{n_t}^2}{s^2 + 2\zeta_t \omega_{n_t} s + \omega_{n_t}^2} \rightarrow \frac{B_t}{s^2 + A_t s + B_t} \tag{C.39}$$

Now that all components of the CWA are covered, it can be linearized and written in state-space notation. This linearization and state-space formulation is considered basic knowledge and is therefore illustrated for the specific force x-channel only. This specific force channel is depicted as block diagram in Figure C.3.

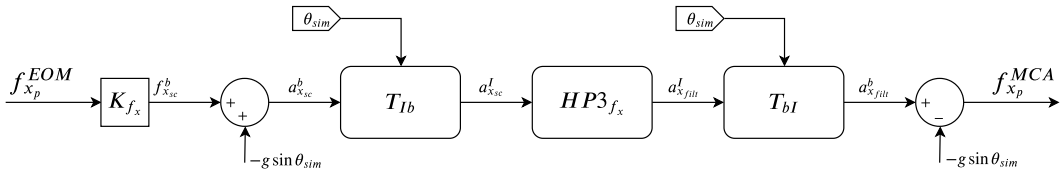

Figure C.3: CWA Specific Force x Channel Adapted for Longitudinal EMD

The first step for writing this channel in state-space formulation is to write the high-pass filter, denoted as $HP3$, in state-space formulation. For the specific force x-channel this high-pass filter is formulated as:

$$HP3_{f_x} = \frac{s^3}{s^3 + A_{f_x} s^2 + B_{f_x} s + C_{f_x}} \tag{C.40}$$

In order to write this transfer function into state-space formulation, the polynomial degree of the numerator must be strictly smaller than the polynomial degree of the denominator. This is, however, not the case and therefore the following trick is used:

$$\begin{aligned} HP3_{f_x} &= \frac{s^3}{s^3 + A_{f_x} s^2 + B_{f_x} s + C_{f_x}} - \frac{s^3 + A_{f_x} s^2 + B_{f_x} s + C_{f_x}}{s^3 + A_{f_x} s^2 + B_{f_x} s + C_{f_x}} + 1 \\ &= \frac{-A_{f_x} s^2 - B_{f_x} s - C_{f_x}}{s^3 + A_{f_x} s^2 + B_{f_x} s + C_{f_x}} + 1 = \frac{a_{x_{filt}}^I}{a_{x_{sc}}^I} \end{aligned} \tag{C.41}$$

The effect of this trick is visualized in Figure C.4. As can be seen here, this high-pass filter has a direct feed-through part, which will eventually result in a non-zero D-matrix.

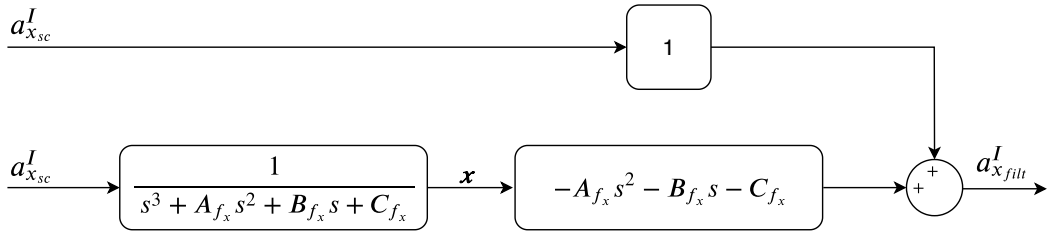

Figure C.4: Visualization of HP3 Transfer Function

The first block of Figure C.4 can easily be written in state-space formulation. In this state-space the state $\boldsymbol{x}$ represent the A_x^I, S_x^I and V_x^I, which are the simulator absement, displacement and velocity in inertial surge direction, respectively.

$$\begin{bmatrix} \dot{A}_x^I \\ \dot{S}_x^I \\ \dot{V}_x^I \end{bmatrix} = \begin{bmatrix} 0 & 1 & 0 \\ 0 & 0 & 1 \\ -C_{f_x} & -B_{f_x} & -A_{f_x} \end{bmatrix} \begin{bmatrix} A_x^I \\ S_x^I \\ V_x^I \end{bmatrix} + \begin{bmatrix} 0 \\ 0 \\ 1 \end{bmatrix} a_{x_{sc}}^I \tag{C.42}$$

The input to this high-pass filter is the x-acceleration expressed in inertial frame. This acceleration is linearized and can be expressed such that it inputs the $f_{x_p}^{EOM}$, which is the specific force resulting from the EOM. This is illustrated with next equation:

$$\begin{aligned} a_{x_{sc}}^I &= a_{x_{sc}}^b \cos\theta_{sim} + a_{z_{sc}}^b \sin\theta_{sim} \\ &\approx a_{x_{sc}}^b = f_{x_{sc}}^b - g\sin\theta_{sim} \approx K_{f_x} f_{x_p}^{EOM} - g\theta_{sim} \end{aligned} \tag{C.43}$$

Substituting Equation C.43 into Equation C.42, yields:

$$\begin{bmatrix} \dot{A}_x^I \\ \dot{S}_x^I \\ \dot{V}_x^I \\ \dot{\theta}_{sim} \end{bmatrix} = \begin{bmatrix} 0 & 1 & 0 & 0 \\ 0 & 0 & 1 & 0 \\ -C_{f_x} & -B_{f_x} & -A_{f_x} & -g \\ \cdot & \cdot & \cdot & \cdot \end{bmatrix} \begin{bmatrix} A_x^I \\ S_x^I \\ V_x^I \\ \theta_{sim} \end{bmatrix} + \begin{bmatrix} 0 \\ 0 \\ K_{f_x} \\ \cdot \end{bmatrix} f_{x_p}^{EOM} \tag{C.44}$$

This gives the state-space representation of the A- and B-matrices of the specific force x-channel. Important to note is that an exact formulation of the $\dot{\theta}_{sim}$ cannot be given at this point as this depends on both the tilt coordination and rotational channel and is therefore left blank.
The next step is to construct the output vector, looking at Figure C.4 the output, $a_{x_{filt}}^I$, is a combination of the state ($\boldsymbol{x}$) and input ($a_{x_{sc}}^I$), which can be written as:

$$a_{x_{filt}}^I = a_{x_{sc}}^I - A_{f_x} V_x^I - B_{f_x} S_x^I - C_{f_x} A_x^I = \begin{bmatrix} -C_{f_x} & -B_{f_x} & -A_{f_x} \end{bmatrix} \begin{bmatrix} A_x^I \\ S_x^I \\ V_x^I \end{bmatrix} + \begin{bmatrix} 1 \end{bmatrix} a_{x_{sc}}^I \tag{C.45}$$

For this study it is essential to output the specific forces $f_{x_p}^{MCA}$, which can be related to the filtered acceleration output $a_{x_{filt}}^I$ using the following:

$$f_{x_p}^{MCA} = a_{x_{filt}}^b + g\sin\theta_{sim} = a_{x_{filt}}^I \cos\theta_{sim} - a_{z_{filt}}^I \sin\theta_{sim} + g\sin\theta_{sim} \approx a_{x_{filt}}^I + g\theta_{sim} \tag{C.46}$$

Finally, substituting Equations C.43 and C.46 into Equation C.45 gives the state-space formulation of the C- and D-matrices, which are:

$$f_{x_p}^{MCA} = \begin{bmatrix} -C_{f_x} & -B_{f_x} & -A_{f_x} \end{bmatrix} \begin{bmatrix} A_x^I \\ S_x^I \\ V_x^I \end{bmatrix} + \begin{bmatrix} K_{f_x} \end{bmatrix} f_{x_p}^{EOM} \tag{C.47}$$

Previous steps illustrated how specific force x-channel can be linearized and formulated in state-space format. Applying these same steps to the remaining channels of the CWA yields a complete state-space representation of the CWA, which can be written in the form:

$$\dot{\boldsymbol{x}}^{MCA} = A^{MCA} \boldsymbol{x}^{MCA} + B^{MCA} \boldsymbol{u}^{MCA} \tag{C.48}$$

where the state vector and input vector are:

$$\boldsymbol{x}^{MCA} = \begin{bmatrix} A_x^I & S_x^I & V_x^I & A_z^I & S_z^I & V_z^I & \theta_{rot} & \dot{\theta}_{rot} & \theta_{tilt} & \dot{\theta}_{tilt} & \theta_{sim} & \dot{\theta}_{sim} \end{bmatrix}^T \tag{C.49}$$

$$\boldsymbol{u}^{MCA} = \begin{bmatrix} f_x^{EOM} & f_z^{EOM} & \dot{q}^{EOM} \end{bmatrix}^T \tag{C.50}$$

$$A^{MCA} = \begin{bmatrix} 0 & 1 & 0 & 0 & 0 & 0 & 0 & 0 & 0 & 0 & 0 & 0 \\ 0 & 0 & 1 & 0 & 0 & 0 & 0 & 0 & 0 & 0 & 0 & 0 \\ -C_{f_x} & -B_{f_x} & -A_{f_x} & 0 & 0 & 0 & 0 & 0 & 0 & 0 & -g & 0 \\ 0 & 0 & 0 & 0 & 1 & 0 & 0 & 0 & 0 & 0 & 0 & 0 \\ 0 & 0 & 0 & 0 & 0 & 1 & 0 & 0 & 0 & 0 & 0 & 0 \\ 0 & 0 & 0 & -C_{f_z} & -B_{f_z} & -A_{f_z} & 0 & 0 & 0 & 0 & 0 & 0 \\ 0 & 0 & 0 & 0 & 0 & 0 & 0 & 1 & 0 & 0 & 0 & 0 \\ 0 & 0 & 0 & 0 & 0 & 0 & -B_q & -A_q & 0 & 0 & 0 & 0 \\ 0 & 0 & 0 & 0 & 0 & 0 & 0 & 0 & 0 & 1 & 0 & 0 \\ 0 & 0 & 0 & 0 & 0 & 0 & 0 & 0 & -B_t & -A_t & 0 & 0 \\ 0 & 0 & 0 & 0 & 0 & 0 & 0 & 0 & 0 & 0 & 0 & 1 \\ 0 & 0 & 0 & 0 & 0 & 0 & -B_q & -A_q & -B_t^2 & -A_t B_t & 0 & 0 \end{bmatrix} \tag{C.51}$$

$$B^{MCA} = \begin{bmatrix} 0 & 0 & 0 \\ 0 & 0 & 0 \\ K_{f_x} & 0 & 0 \\ 0 & 0 & 0 \\ 0 & 0 & 0 \\ 0 & K_{f_z} & 0 \\ 0 & 0 & 0 \\ 0 & 0 & K_q \\ 0 & 0 & 0 \\ \frac{K_{f_x}}{g} & 0 & 0 \\ 0 & 0 & 0 \\ \frac{K_{f_x} B_t}{g} & 0 & K_q \end{bmatrix} \tag{C.52}$$

As illustrated in Figure C.2, the MCA is adapted to output specific forces and pitch rate, this results in the following formulation of the output vector:

$$\boldsymbol{y}^{MCA} = \begin{pmatrix} f_{x_p}^{MCA} \\ f_{z_p}^{MCA} \\ q^{MCA} \end{pmatrix} = C^{MCA}\,\boldsymbol{x}^{MCA} + D^{MCA}\,\boldsymbol{u}^{MCA} \tag{C.53}$$

$$C^{MCA} = \begin{bmatrix} -C_{f_x} & -B_{f_x} & -A_{f_x} & 0 & 0 & 0 & 0 & 0 & 0 & 0 & 0 & 0 \\ 0 & 0 & 0 & -C_{f_z} & -B_{f_z} & -A_{f_z} & 0 & 0 & 0 & 0 & 0 & 0 \\ 0 & 0 & 0 & 0 & 0 & 0 & 0 & 0 & 0 & 0 & 0 & 1 \end{bmatrix} \tag{C.54}$$

$$D^{MCA} = \begin{bmatrix} K_{f_x} & 0 & 0 \\ 0 & K_{f_z} & 0 \\ 0 & 0 & 0 \end{bmatrix} \tag{C.55}$$

This concludes the derivation of the specific forces and pitch rate filtered by the MCA which are experienced by the pilot in the flight simulator.

C.3. System Coupling

In order to make the EMD analysis possible, the linear model of the EOM and the MCA must be combined into one single linear system that is only exited by pilot inputs. These pilot inputs are the control surface deflections. The relation between the EOM and the MCA is illustrated in Figure C.5.

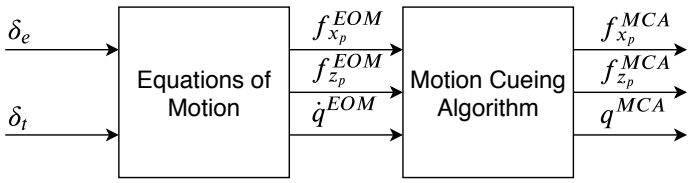

Figure C.5: EOM and MCA Relation

As evident from this figure, the outputs of the EOM are the inputs to the MCA. The goal is now to express the MCA inputs in EOM states and pilot inputs, which eventually yields a single state-space of the form:

$$\dot{\boldsymbol{x}}^{EMD} = A^{EMD}\,\boldsymbol{x}^{EMD} + B^{EMD}\,\boldsymbol{u}^{EMD} \tag{C.56}$$

where the state vector and input vector are:

$$\boldsymbol{x}^{EMD} = \begin{bmatrix} u_s & w_s & \theta & q_b & A_x^I & S_x^I & V_x^I & A_z^I & S_z^I & V_z^I & \theta_{rot} & \dot{\theta}_{rot} & \theta_{tilt} & \dot{\theta}_{tilt} & \theta_{sim} & \dot{\theta}_{sim} \end{bmatrix}^T \tag{C.57}$$

$$\boldsymbol{u}^{EMD} = \begin{bmatrix} \delta_e & \delta_t \end{bmatrix}^T \tag{C.58}$$

Equations C.52 and C.55 use the EOM outputs as inputs. In order to make a single state-space representation, these equations must be transformed. This transformation is referred to as system coupling, as it couples the EOM with the MCA. The complete system can be written as

$$A^{EMD} = \begin{bmatrix} A^{EOM} & 0 \\ A^{COUP} & A^{MCA} \end{bmatrix} \tag{C.59}$$

$$B^{EMD} = \begin{bmatrix} B^{EOM} \\ B^{COUP} \end{bmatrix} \tag{C.60}$$

$$\boldsymbol{y}^{EMD} = \begin{pmatrix} f_{x_p}^{EOM} \\ f_{z_p}^{EOM} \\ q^{EOM} \\ f_{x_p}^{MCA} \\ f_{z_p}^{MCA} \\ q^{MCA} \end{pmatrix} = \begin{bmatrix} C^{EOM} & 0 \\ C^{COUP} & C^{MCA} \end{bmatrix} \boldsymbol{x}^{EMD} + \begin{bmatrix} D^{EOM} \\ D^{COUP} \end{bmatrix} \boldsymbol{u}^{EMD} \tag{C.61}$$

In here Equation C.52, B^{MCA}, which uses the EOM outputs as input, is re-formulated as A^{COUP} and B^{COUP}, which expresses these EOM outputs using the EOM states and pilot inputs. The same is done for Equation C.55, D^{MCA}, which is in its turn transformed into

C^{COUP} and D^{COUP} for the same reason. The resulting coupling matrices are:

$$A^{COUP} = \begin{bmatrix} 0 & 0 & 0 & 0 \\ 0 & 0 & 0 & 0 \\ K_{f_x}C_{f_xu} & K_{f_x}C_{f_xw} & K_{f_x}C_{f_x\theta} & K_{f_x}C_{f_xq} \\ 0 & 0 & 0 & 0 \\ 0 & 0 & 0 & 0 \\ K_{f_z}C_{f_zu} & K_{f_z}C_{f_zw} & K_{f_z}C_{f_z\theta} & K_{f_z}C_{f_zq} \\ 0 & 0 & 0 & 0 \\ K_qC_{\dot{q}u} & K_qC_{\dot{q}w} & K_qC_{\dot{q}\theta} & K_qC_{\dot{q}q} \\ 0 & 0 & 0 & 0 \\ \frac{K_{f_x}}{g}C_{f_xu} & \frac{K_{f_x}}{g}C_{f_xw} & \frac{K_{f_x}}{g}C_{f_x\theta} & \frac{K_{f_x}}{g}C_{f_xq} \\ 0 & 0 & 0 & 0 \\ \frac{K_{f_x}B_t}{g}C_{f_xu} + K_qC_{\dot{q}u} & \frac{K_{f_x}B_t}{g}C_{f_xw} + K_qC_{\dot{q}w} & \frac{K_{f_x}B_t}{g}C_{f_x\theta} + K_qC_{\dot{q}\theta} & \frac{K_{f_x}B_t}{g}C_{f_xq} + K_qC_{\dot{q}q} \end{bmatrix} \tag{C.62}$$

$$B^{COUP} = \begin{bmatrix} 0 & 0 \\ 0 & 0 \\ K_{f_x}D_{f_x\delta_e} & K_{f_x}D_{f_x\delta_t} \\ 0 & 0 \\ 0 & 0 \\ K_{f_z}D_{f_z\delta_e} & K_{f_z}D_{f_z\delta_t} \\ 0 & 0 \\ K_qD_{\dot{q}\delta_e} & K_qD_{\dot{q}\delta_t} \\ 0 & 0 \\ \frac{K_{f_x}}{g}D_{f_x\delta_e} & \frac{K_{f_x}}{g}D_{f_x\delta_t} \\ 0 & 0 \\ \frac{K_{f_x}B_t}{g}D_{f_x\delta_e} + K_qD_{\dot{q}\delta_e} & \frac{K_{f_x}B_t}{g}D_{f_x\delta_t} + K_qD_{\dot{q}\delta_t} \end{bmatrix} \tag{C.63}$$

$$C^{COUP} = \begin{bmatrix} K_{f_x}C_{f_xu} & K_{f_x}C_{f_xw} & K_{f_x}C_{f_x\theta} & K_{f_x}C_{f_xq} \\ K_{f_z}C_{f_zu} & K_{f_z}C_{f_zw} & K_{f_z}C_{f_z\theta} & K_{f_z}C_{f_zq} \\ 0 & 0 & 0 & 0 \end{bmatrix} \tag{C.64}$$

$$D^{COUP} = \begin{bmatrix} K_{f_x}D_{f_x\delta_e} & K_{f_x}D_{f_x\delta_t} \\ K_{f_z}D_{f_z\delta_e} & K_{f_z}D_{f_z\delta_t} \\ 0 & 0 \end{bmatrix} \tag{C.65}$$

This concludes the derivation of the complete state-space system. This system is now ready for the actual EMD analysis.

D

Motion Platform Geometry

Table D.1: Platform Characteristics SRS

Upper Circle Radius	A_r	1600 [mm]
Lower Circle Radius	B_r	1650 [mm]
Upper Gimbal Spacing	$2P$	200 [mm]
Lower Gimbal Spacing	$2D$	600 [mm]

Table D.2: Actuator Characteristics SRS

Retracted Length	L_{min}	2081 [mm]
Maximum Length	L_{max}	3331 [mm]
Stroke	S	1250 [mm]
Lower Buffers	B_l	50 [mm]
Upper Buffers	B_u	50 [mm]
Maximum Operational Length	$L_{max,o}$	3281 [mm]
Minimum Operational Length	$L_{min,o}$	2131 [mm]
Operational Stroke	S_o	1150 [mm]
Maximum Speed	v_{max}	0.8 [m/s]
Maximum Acceleration	a_{max}	1.0 [g]

$$\begin{aligned} P &= A_r \sin(\gamma_p) \\ D &= B_r \sin(\gamma_b) \end{aligned} \tag{D.1}$$

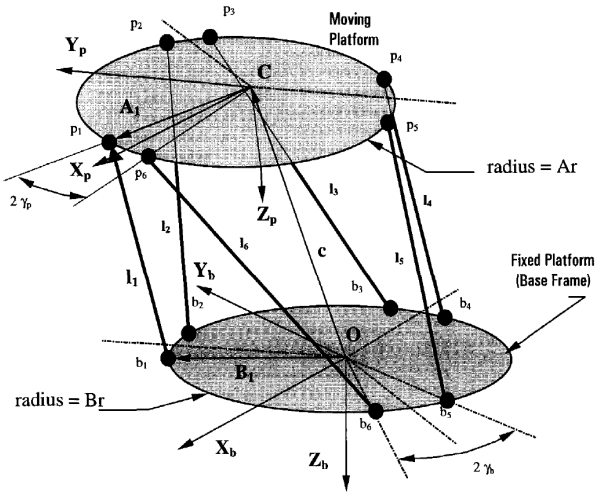

Figure D.1: Geometry Definition of Stewart Platform [25]

This page is intentionally left blank.

E

Verification and Validation

Verification and validation is an essential part to ensure a correct implementation of the design. This appendix contains the verification and validation for the lateral model derived in throughout the report.

E.1. Verification

The derivation of the complete EMD model is quite extensive and due to the different couplings prone to errors. In order to ensure that the derivation is done correctly, verification is an essential step. In Figure E.1 the Simulink verification environment is illustrated. In here the outputs of **1** are from the non-linear MCA, which is also illustrated in Figure E.2. During the EMD derivation this non-linear MCA is linearized, in the verification environment this linearized MCA is represented with **2**. To check whether this linearization is performed correctly, the outputs of **1** and **2** must be identical. Another essential step in the derivation of the complete EMD system is to couple the EOM and MCA. To verify that this system coupling is performed correctly, the responses of **2** and **3** must be identical.

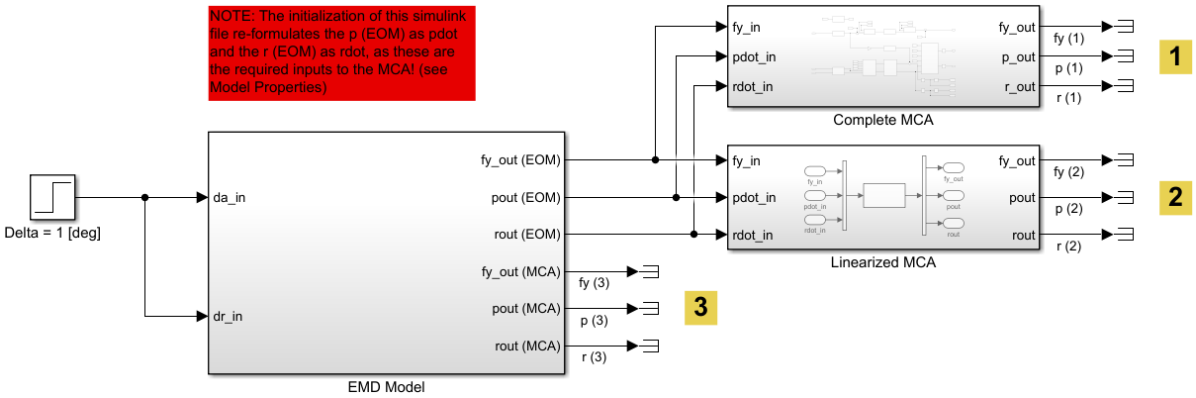

Figure E.1: Verification Environment in Simulink

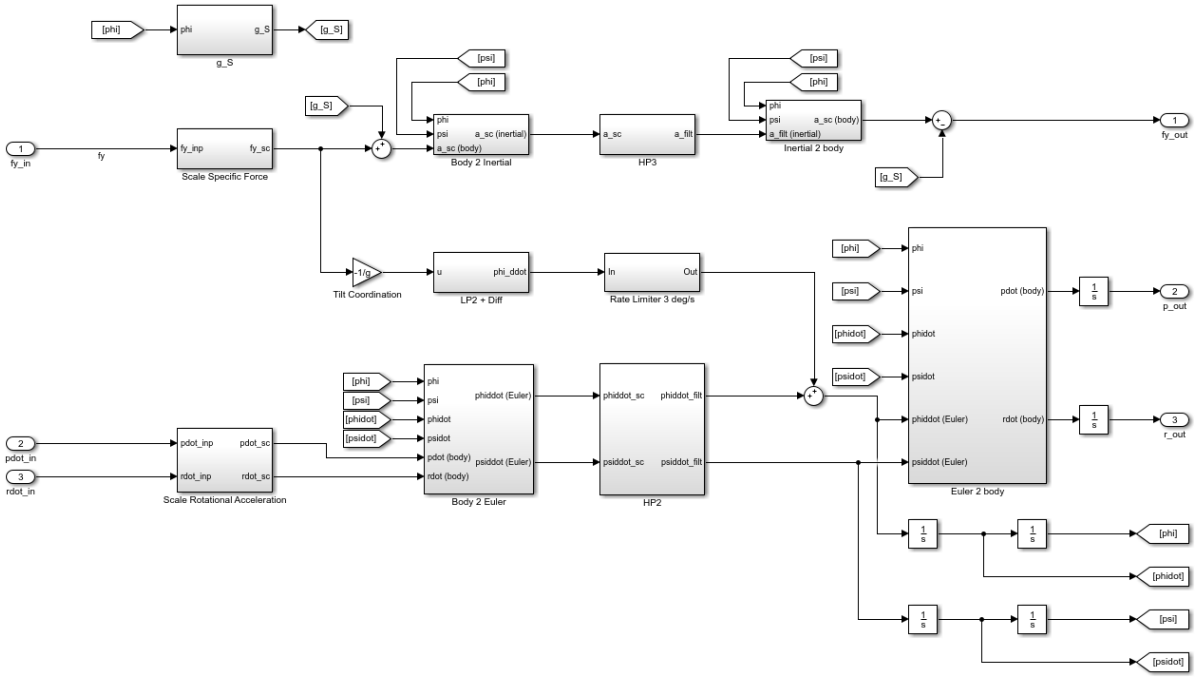

Figure E.2: Non-linear Simulink Model of the Classical Washout Algorithm
(sub-system 1 of Figure E.1)

Figure E.3 depicts the response to an aileron and rudder step input of 1 degree. As is clearly evident the response of **1**, **2** and **3** are identical. From here it can be verified that the derivation and implementation of the EMD system is performed correctly.

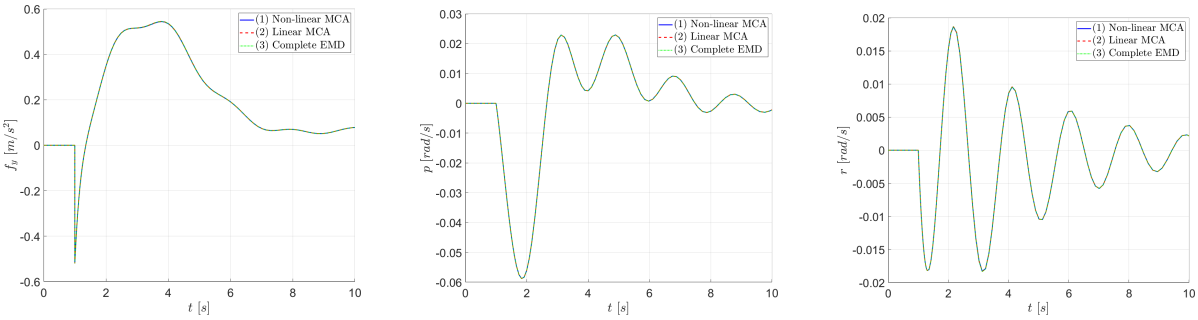

Figure E.3: Verification of the Motion Cues

E.2. Validation

In order to validate that the right model is implemented of the Cessna Citation 500, a simulation is performed. In this simulation the responses of the complete Cessna Citation are compared with the responses of the linear (simplified) model.

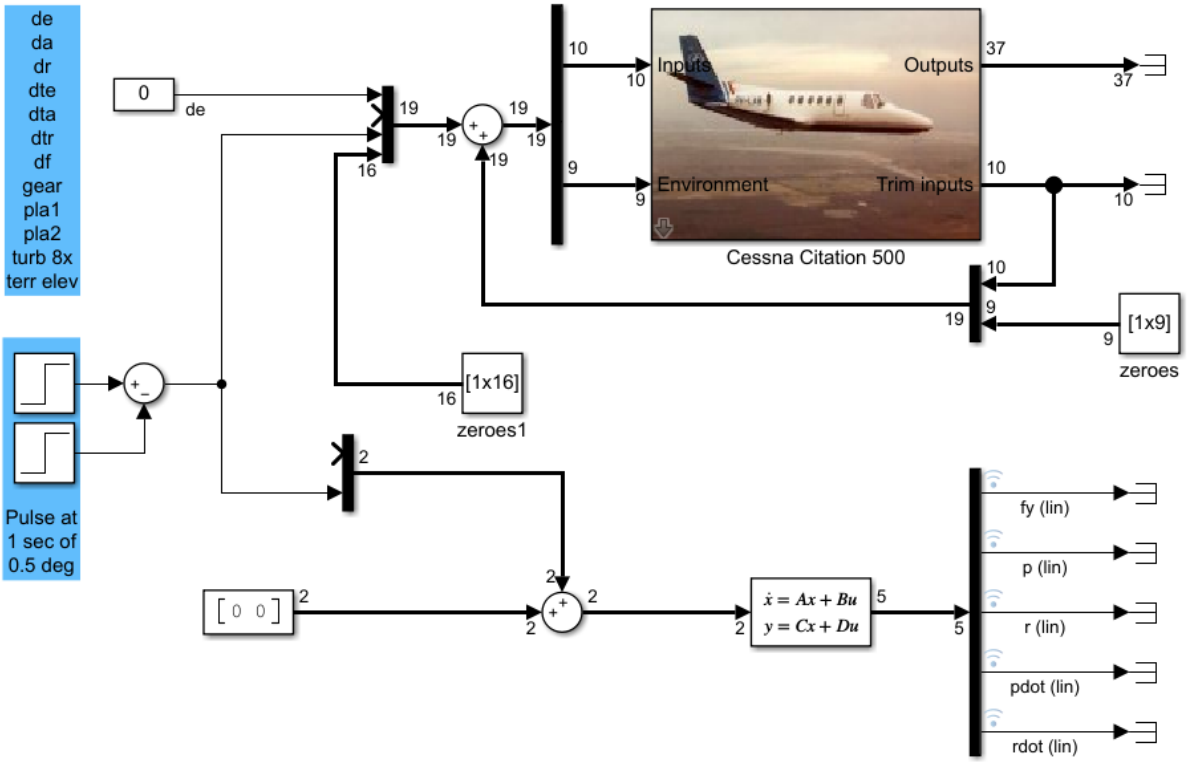

Figure E.4: Validation Model of Cessna Citation 500

Figure E.5 depicts the response to an rudder pulse input of 0.5 degrees. As can be seen from this figure, the responses of the different motion cues of the linear EOM resemble the complete EOM to a high degree. Therefore, it is concluded that the correct model of the Cessna Citation 500 is implemented.

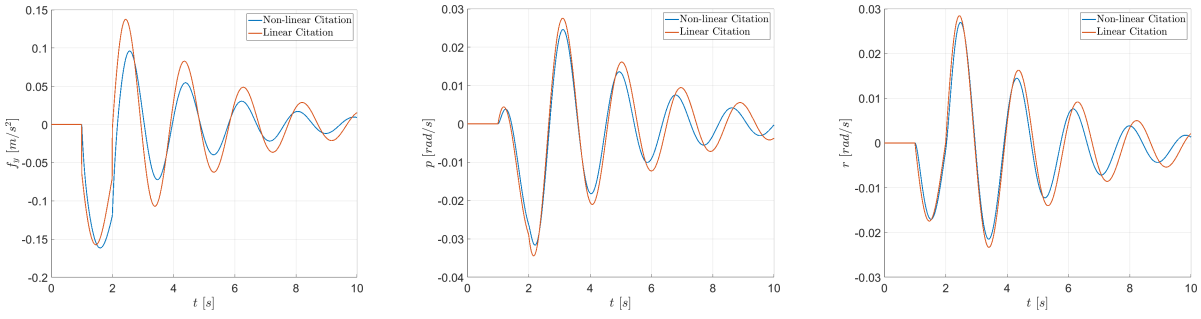

Figure E.5: Validation of the Motion Cues

This page is intentionally left blank.

F

OMCT Test Plan

Table F.1: Input signal and transfer functions per OMCT test [19]

OMCT Test 1: Pitch response to pitch input	
Input signal	Transfer function
$f_{PA}^z = -g$ $\dot{q}_{PA} = -A\omega^2 \sin(\omega t)$	$H_1(\omega) = \frac{\dot{q}_{PS}}{\dot{q}_{PA}}(\omega)$
OMCT Test 2: Surge response to pitch input	
Input signal	Transfer function
$f_{PA}^x = g\sin(\theta_{PA}(t))$ $f_{PA}^z = -g$ $\dot{q}_{PA} = -A\omega^2 \sin(\omega t)$	$H_2(\omega) = \frac{f_{PS}^x - g\sin(\theta_{PS})}{\dot{q}_{PA}}(\omega)$
OMCT Test 3: Roll response to roll input	
Input signal	Transfer function
$f_{PA}^z = -g$ $\dot{p}_{PA} = -A\omega^2 \sin(\omega t)$	$H_3(\omega) = \frac{\dot{p}_{PS}}{\dot{p}_{PA}}(\omega)$
OMCT Test 4: Sway response to roll input	
Input signal	Transfer function
$f_{PA}^z = -g$ $\dot{p}_{PA} = -A\omega^2 \sin(\omega t)$	$H_4(\omega) = \frac{f_{PS}^y}{\dot{p}_{PA}}(\omega)$
OMCT Test 5: Yaw response to yaw input	
Input signal	Transfer function
$f_{PA}^z = -g$ $\dot{r}_{PA} = -A\omega^2 \sin(\omega t)$	$H_5(\omega) = \frac{\dot{r}_{PS}}{\dot{r}_{PA}}(\omega)$
OMCT Test 6: Surge response to surge input	
Input signal	Transfer function
$f_{PA}^x = A\sin(\omega t)$ $f_{PA}^z = -g$	$H_6(\omega) = \frac{f_{PS}^x}{f_{PA}^x}(\omega)$
OMCT Test 7: Pitch response to surge input	
Input signal	Transfer function
$f_{PA}^x = A\sin(\omega t)$ $f_{PA}^z = -g$	$H_7(\omega) = \frac{\theta_{PS}}{f_{PA}^x}(\omega)$
OMCT Test 8: Sway response to sway input	
Input signal	Transfer function
$f_{PA}^y = A\sin(\omega t)$ $f_{PA}^z = -g$	$H_8(\omega) = \frac{f_{PS}^y}{f_{PA}^y}(\omega)$
OMCT Test 9: Roll response to sway input	
Input signal	Transfer function
$f_{PA}^y = A\sin(\omega t)$ $f_{PA}^z = -g$	$H_9(\omega) = \frac{\phi_{PS}}{f_{PA}^y}(\omega)$
OMCT Test 10: Heave response to heave input	
Input signal	Transfer function
$f_{PA}^z = A\sin(\omega t) - g$	$H_{10}(\omega) = \frac{f_{PS}^z}{f_{PA}^z}(\omega)$

This page is intentionally left blank.

G
Baseline Configuration

Table G.1: *B* Classical Washout Algorithm Filter Parameters

$K_{f_y} = 0.70$	$\omega_{b_{f_y}} = 0.00$	$K_p = 0.70$	$K_r = 0.70$
$\omega_{n_{f_y}} = 0.80$	$\omega_{n_t} = 2.00$	$\omega_{n_p} = 0.80$	$\omega_{n_r} = 0.80$
$\zeta_{f_y} = 1.00$	$\zeta_t = 1.00$	$\zeta_p = 1.00$	$\zeta_r = 1.00$

Table G.2: Resulting Distortions for *B* Configuration

	$\lvert f_y \rvert$ [−]	$\lvert \angle f_y \rvert$ [◦]	$\lvert p \rvert$ [−]	$\lvert \angle p \rvert$ [◦]	$r \rvert$ [−]	$\lvert \angle r \rvert$ [◦]
Dutch Roll	0.535	13.077	0.651	3.076	0.687	27.929
Aperiodic Roll	0.921	0.0	0.911	180.0	1.084	0.0

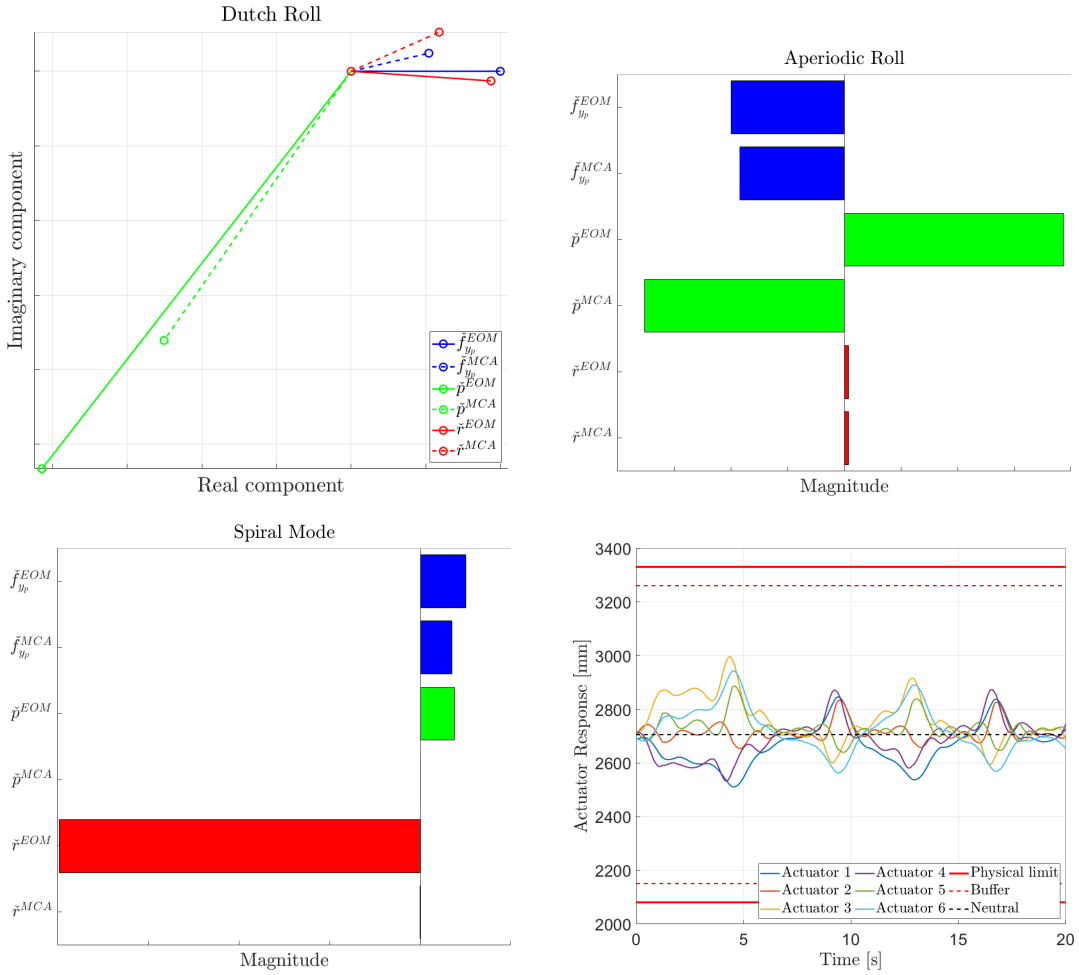

Figure G.1: Eigenvector Distortions and Actuator Responses

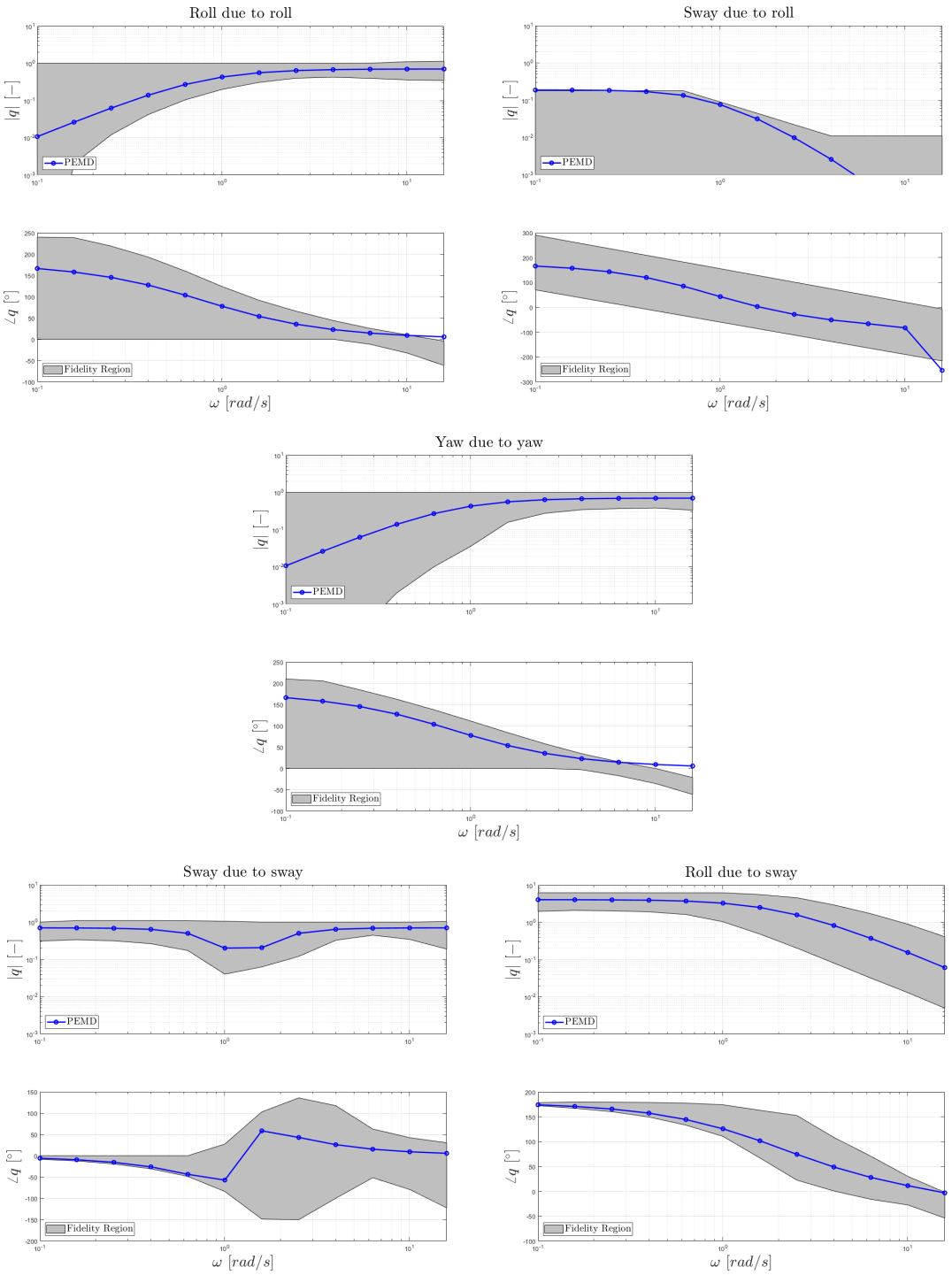

Figure G.2: Objective Motion Cueing Test Results

OMCT Tuned Configuration

Table H.1: *O* Classical Washout Algorithm Filter Parameters

$K_{f_y} = 0.60$	$\omega_{b_{f_y}} = 0.00$	$K_p = 0.60$	$K_r = 0.70$
$\omega_{n_{f_y}} = 1.00$	$\omega_{n_t} = 2.00$	$\omega_{n_p} = 0.80$	$\omega_{n_r} = 0.80$
$\zeta_{f_y} = 1.00$	$\zeta_t = 1.00$	$\zeta_p = 0.80$	$\zeta_r = 1.00$

Table H.2: Resulting Distortions for *O* Configuration

	$\lvert f_y \rvert$ [−]	$\lvert \angle f_y \rvert$ [◦]	$\lvert p \rvert$ [−]	$\lvert \angle p \rvert$ [◦]	$r \rvert$ [−]	$\lvert \angle r \rvert$ [◦]
Dutch Roll	0.393	14.768	0.599	0.976	0.687	27.929
Aperiodic Roll	0.836	0.0	0.882	180.0	1.084	0.0

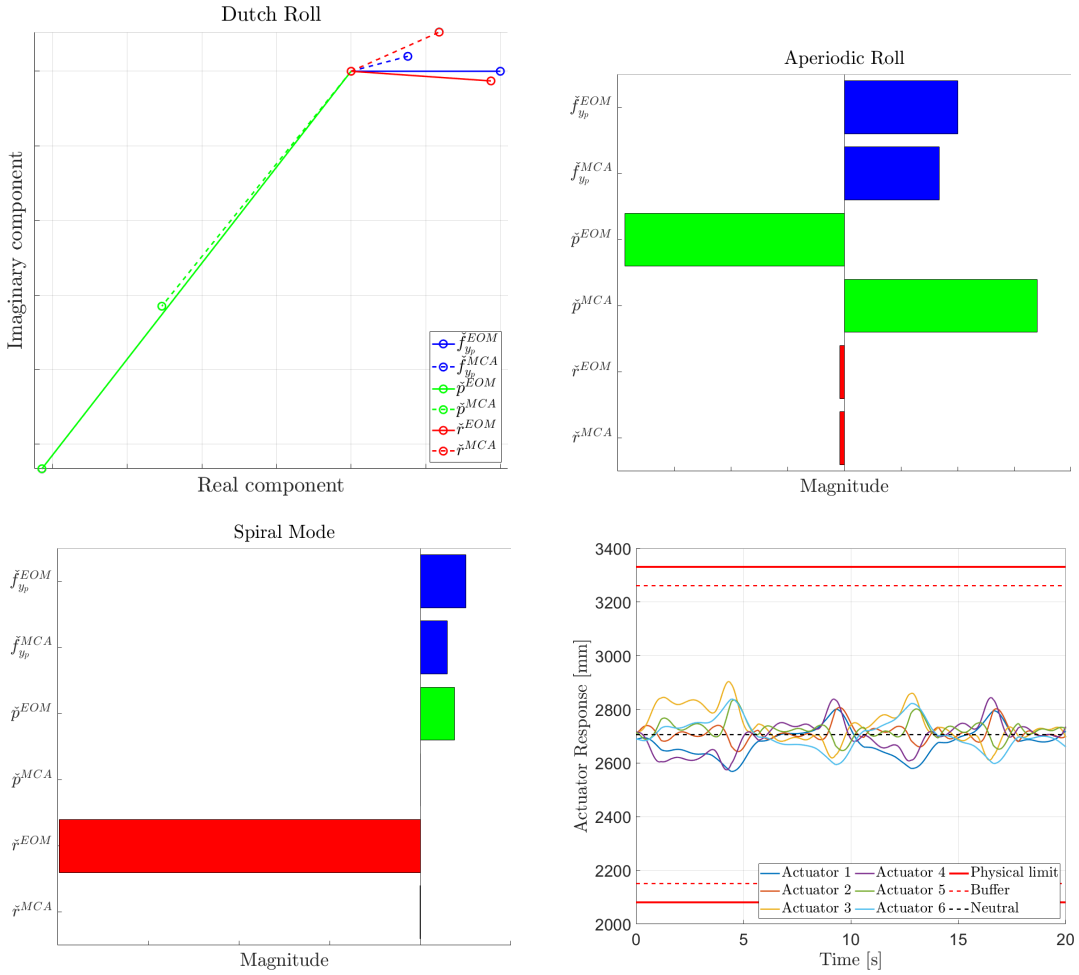

Figure H.1: Eigenvector Distortions and Actuator Responses

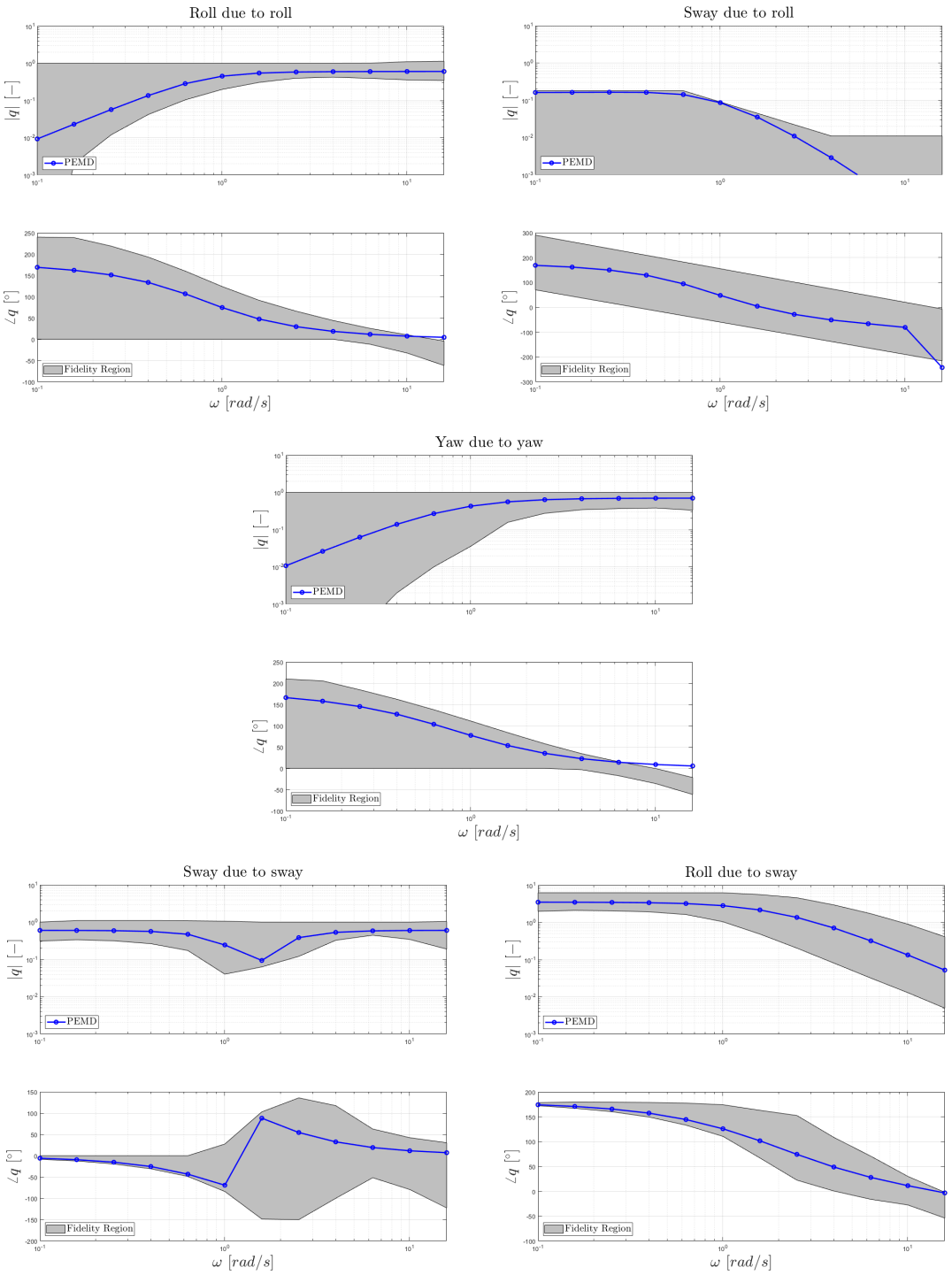

Figure H.2: Objective Motion Cueing Test Results

PEMD Tuned Configuration

Table I.1: P Classical Washout Algorithm Filter Parameters

$K_{f_y} = 0.600$	$\omega_{b_{f_y}} = 0.00$	$K_p = 1.067$	$K_r = 0.70$
$\omega_{n_{f_y}} = 0.750$	$\omega_{n_t} = 1.500$	$\omega_{n_p} = 0.928$	$\omega_{n_r} = 0.80$
$\zeta_{f_y} = 0.911$	$\zeta_t = 0.800$	$\zeta_p = 0.700$	$\zeta_r = 1.00$

Table I.2: Resulting Distortions for P Configuration

	$\lvert f_y \rvert$ [−]	$\lvert \angle f_y \rvert$ [◦]	$\lvert p \rvert$ [−]	$\lvert \angle p \rvert$ [◦]	$r \rvert$ [−]	$\lvert \angle r \rvert$ [◦]
Dutch Roll	0.472	5.089	1.010	15.305	0.687	27.929
Aperiodic Roll	1.000	0.0	1.000	0.0	1.084	0.0

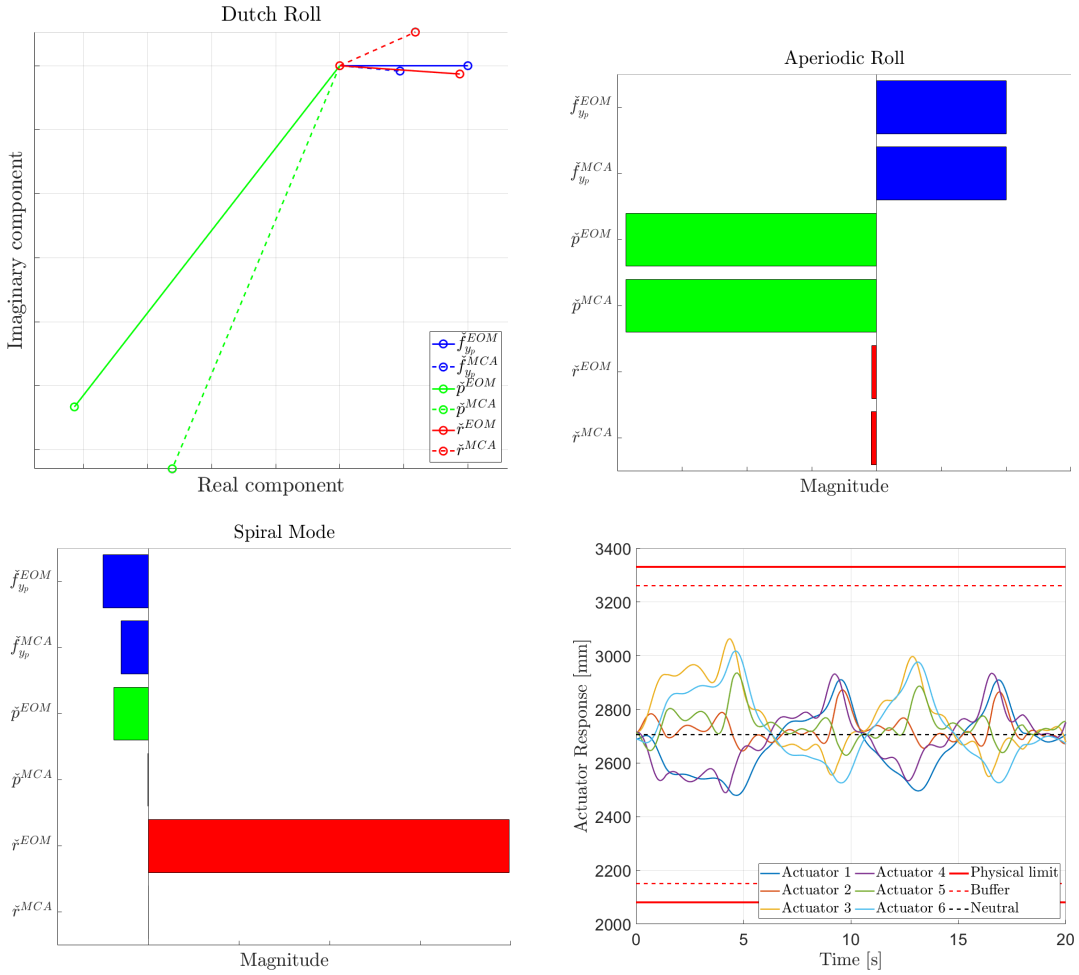

Figure I.1: Eigenvector Distortions and Actuator Responses

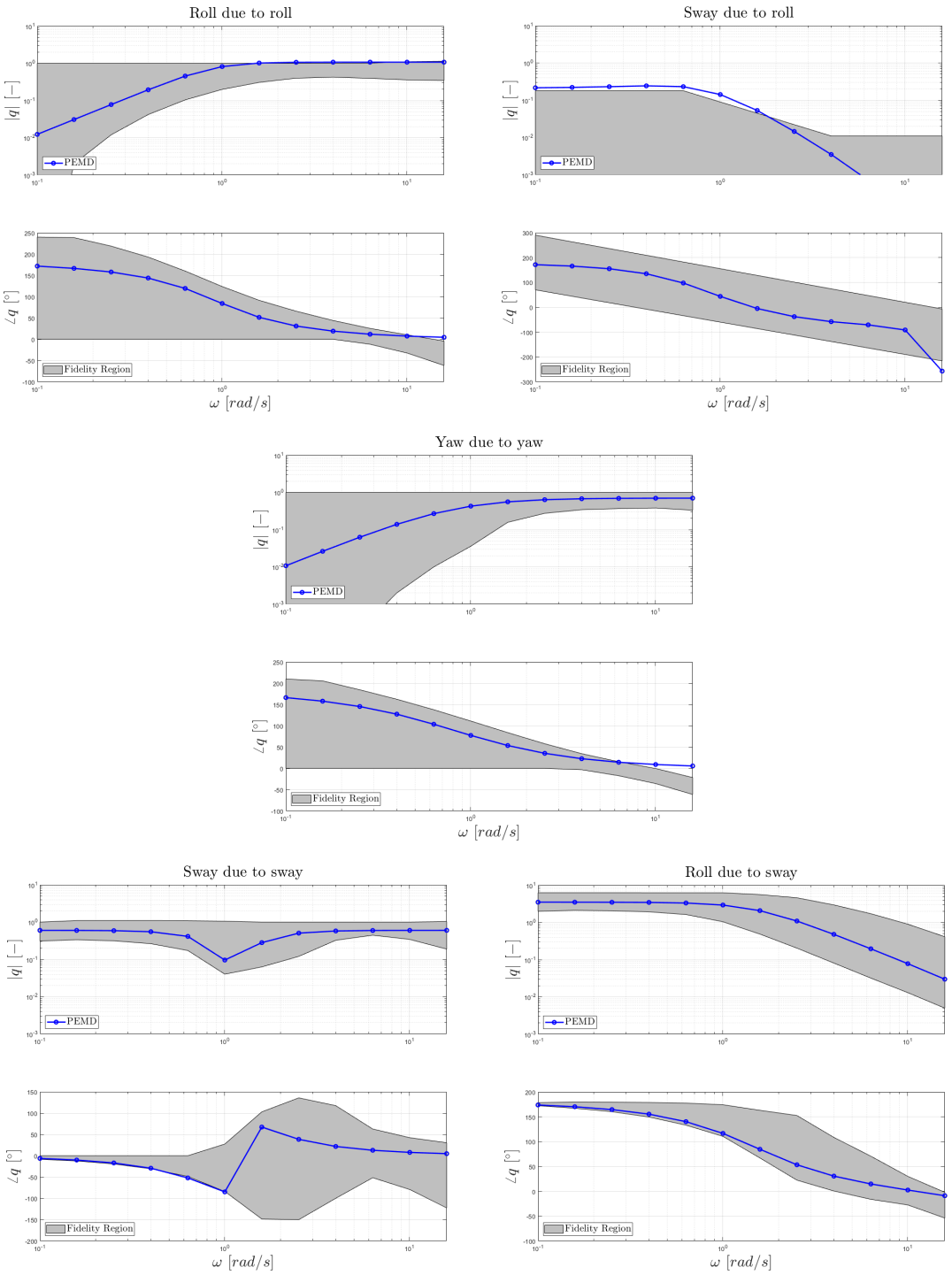

Figure I.2: Objective Motion Cueing Test Results